In situ Surface X-Ray Diffraction Studies of the Copper-Electrolyte Interface:

Atomic Structure and Homoepitaxial Growth

Dissertation

zur Erlangung des Doktorgrades
Doctor Rerum Naturalium
der Mathematisch-Naturwissenschaftlichen Fakultät
der Christian-Albrechts-Universität zu Kiel

vorgelegt von

Frederik Golks

Kiel & Grenoble, 2011

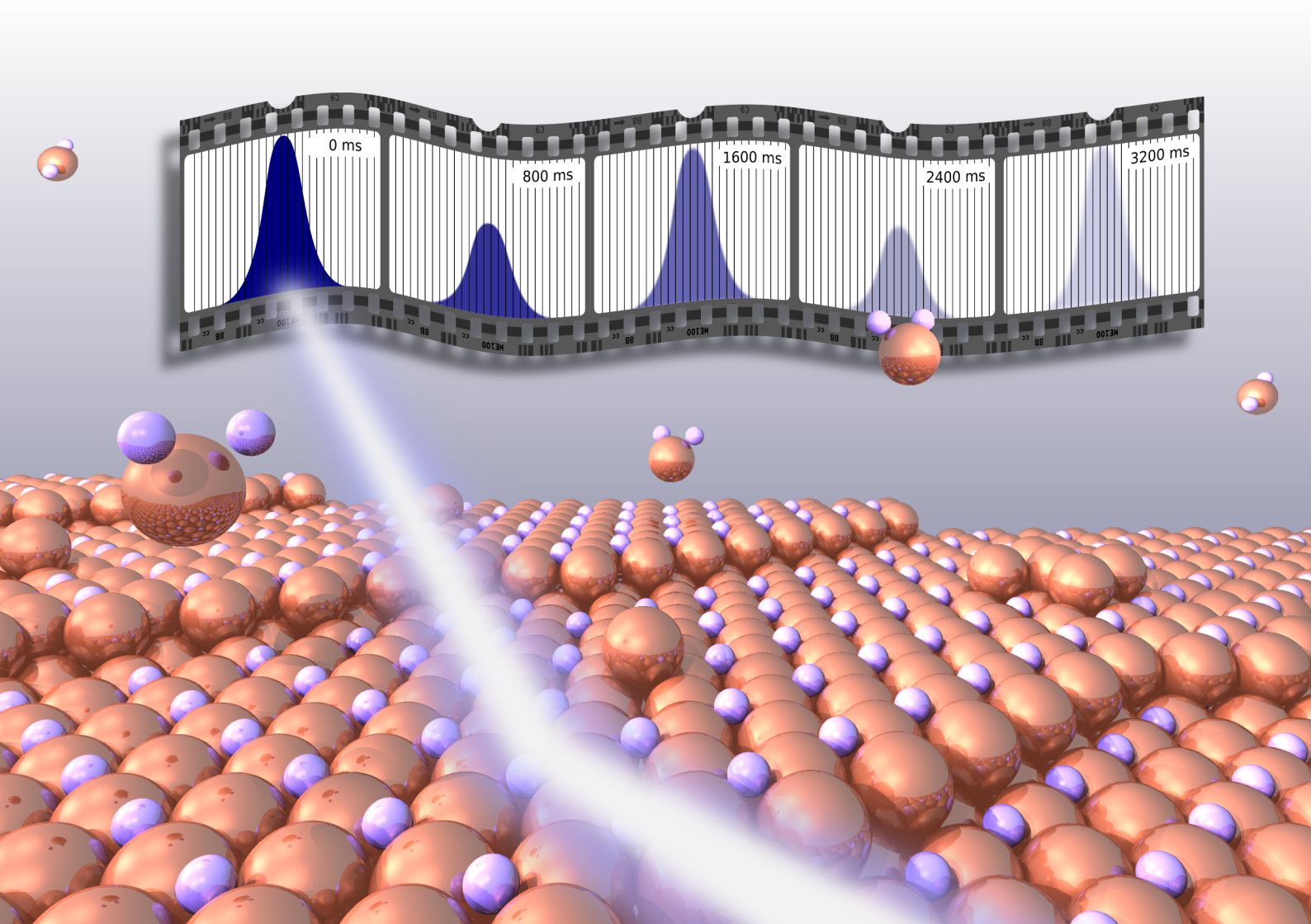

In situ Surface X-Ray Diffraction Studies of the Copper-Electrolyte Interface:

Atomic Structure and Homoepitaxial Growth

Dissertation

zur Erlangung des Doktorgrades
Doctor Rerum Naturalium
der Mathematisch-Naturwissenschaftlichen Fakultät
der Christian-Albrechts-Universität zu Kiel

vorgelegt von

Frederik Golks

Kiel & Grenoble, 2011

Die vorliegende Arbeit wurde im Rahmen eines Gemeinschaftsprojektes der Arbeitsgruppen von Prof. Dr. O. M. Magnussen, Universität Kiel, und Priv.-Doz. Dr. J. Zegenhagen, European Synchrotron Radiation Facility, Grenoble, angefertigt. Je zur Hälfte der Dissertation war der Arbeitsplatz in Kiel bzw. in Grenoble.

Referent: ..... Prof. Dr. Olaf M. Magnussen

Korreferent: ..... Priv.-Doz. Dr. Jörg Zegenhagen

Ort und Tag der Disputation: ..... Kiel, 19. Mai 2011

Zum Druck genehmigt: ..... Kiel, 19. Mai 2011

gez. Prof. Dr. Lutz Kipp, Dekan

Abstract

Copper electrodeposition is the predominantly used technique for on-chip wiring in the fabrication of ultra-large scale integrated (ULSI) microchips. In this 'damascene copper electroplating' process, multicomponent electrolytes containing organic additives realize void-free filling of trenches with high aspect ratio ('superconformal deposition'). Despite manifold studies, motivated by the continuous trend to shrink wiring dimensions and thus the demand of optimized plating baths, detailed knowledge on the growth mechanism - in presence and absence of additives - is still lacking.

Using a recently developed hanging meniscus x-ray transmission cell, brilliant synchrotron x-rays and a fast, one-dimensional detector system, unique real-time *in situ* surface x-ray diffraction studies of copper electrodeposition were performed under realistic reaction conditions, approaching rates of technological relevance. Preparatory measurements of the electrochemical dissolution of Au(001) in chloride-containing electrolyte demonstrated the capability of this powerful technique, specifically the possibility to follow atomic-scale deposition or dissolution processes with a time resolution down to five milliseconds.

The electrochemical as well as structural characterization of the Cu(001)- and Cu(111)-electrolyte interfaces provided detailed insight into the complex atomic-scale structures in presence of specifically adsorbed chloride on these surfaces. The interface of Cu(001) in chloride-containing electrolyte exhibits a continuous surface phase transition of a disordered Cl adlayer to a c(2×2) Cl adlayer with increasing potential. The latter was found to induce a small vertical corrugation of substrate atoms, which can be ascribed to lattice relaxations induced by the presence of coadsorbed water molecules and cations in the outer part of the electrochemical double layer. The study of the specific adsorption of chloride on Cu(111) from acidic aqueous electrolyte revealed a hexagonal, rotated adlayer structure, which was not reported before for this system. In comparison to other halide-metal(111) systems, the potential dependence of this structure suggests a strong adsorbate-adsorbate interaction.

Operating under diffusion-limited conditions, *i.e.*, at constant deposition rate, homoepitaxial growth of the Cu(001) single crystal electrode in chloride-containing solution has been investigated *in situ* for 1 and 5 mM Cu ion concentrations as a function of deposition overpotential. Detailed insight into the complex relationship between the atomic-scale structure of the solid-liquid interface, the growth behavior, and the resulting surface morphology was gained, revealing a pronounced mutual interaction of the Cu growth process and the Cl adlayer order. Depending on the latter, transitions from step-flow to layer-by-layer to 3D growth are observed, attributed to a reduction in the Cu surface mobility with increasing order. The kinetics of the c(2 × 2) adlayer ordering, in turn, are strongly affected during Cu deposition as compared to results obtained in Cu-free solution. Moreover, an oscillatory average strain in the surface layer is observed during layer-by-layer growth, indicating an expansion of the topmost layer occurring periodically for fractional coverages.

Addition of polyethylene glycol (PEG), a commonly used inhibitor in the industrial damascene process, considerably changes the growth conditions. The chloride ordering kinetics are influenced such that the c(2 × 2) covered phase is stabilized in a widened potential regime. The onset of the transition to 3D growth is observed at more negative potentials, limiting the occurrence of layering oscillations to a narrower potential regime. Compared to the PEG-free electrolyte, the deposition rate is notably slowed down by a factor of approximately 3. The present study reports new direct experimental observations of the growth mechanisms at electrochemical interfaces on the atomic-scale.

Zusammenfassung

Die elektrochemische Abscheidung von Kupfer ist die vorherrschende Methode zur Herstellung von Leiterbahnen in integrierten Schaltungen moderner Mikrochips. Im sog. Damaszener-Verfahren wird durch Elektrolyte, die diverse organische Additive enthalten, das lückenlose Füllen von Gräben mit hohen Aspektverhältnissen realisiert. Trotz vieler Studien, - motiviert durch die Notwendigkeit Abscheidebäder zu optimieren -, fehlen detaillierte Einblicke in den Wachstumsmechanismus, sowohl mit als auch ohne beigefügte Additive.

Durch Verwendung einer neuartigen elektrochemischen Röntgentransmissionszelle, brillianter Synchrotronstrahlung und eines schnellen 1D-Detektorsystems wurden einzigartige Studien der Elektrodeposition unter realistischen, sich technologischen Verhältnissen annähernden Reaktionsbedingungen mittels oberflächensensitiver Röntgenbeugung möglich. Vorbereitende Messungen der elektrochemischen Auflösung von Au(001) in chlorhaltigem Elektrolyt demonstrierten das Potential dieser leistungsstarken Technik, speziell die Möglichkeit, Abscheide- und Auflöseprozesse auf atomarer Skala mit einer Zeitauflösung von bis zu fünf Millisekunden zu verfolgen.

Die elektrochemische und strukturelle Charakterisierung von Cu(001)- und Cu(111)-Elektrolyt-Grenzflächen ermöglichte einen detaillierten Einblick in die komplexe atomare Struktur in Gegenwart von spezifisch adsorbiertem Chlor auf diesen Oberflächen. Die Cu(001) Grenzschicht in 10 mM HCl weist mit ansteigendem Potential einen kontinuierlichen Phasenübergang von einer ungeordneten zu einer geordneten c(2×2) Cl Adschicht auf. Dabei verursacht letztere eine vertikale Welligkeit (Relaxation) der Substratoberfläche, induziert durch Anlagerung von Wassermolekülen und Kationen in der äußeren Doppelschicht. Die Untersuchung der Adsorption von Chlor auf Cu(111) in saurem Elektrolyt zeigte eine bisher unbekannte hexagonale, rotierte Adschichtstruktur. Im Vergleich mit anderen Halogen-Metall(111)-Systemen lässt die Potentialabhängigkeit dieser Struktur auf eine starke Adsorbat-Adsorbat-Wechselwirkung schließen.

Das homoepitaktische Wachstum von Cu(001)-Einkristallelektroden wurde in Cl-haltigem Elektrolyt unter diffusionslimitierten Bedingungen für 1 und 5 mM Cu Ionenkonzentration als Funktion des Abscheidepotentials untersucht. Dabei wurden detaillierte Einblicke in den komplexen Zusammenhang von atomarer Struktur der Fest-Flüssig-Grenzfläche, Wachstumsverhalten und der daraus resultierenden Oberflächenmorphologie gewonnen. Eine starke Wechselwirkung zwischen Wachstumsprozess und der Cl Adschicht wurde beobachtet. Zum einen werden abhängig vom Cl Ordnungsgrad Übergänge von Stufenfluss- zu lagenweisem zu 3D-Wachstum induziert, die mit einer Abnahme der Cu Adatommobilität mit zunehmender Ordnung erklärt wird. Zum anderen ist die c(2×2) Ordnungskinetik im Vergleich zu Beobachtungen in Cu-freien Elektrolyten während des Wachstums stark beeinflusst. Während des lagenweisen Wachstums wurde darüber hinaus eine bedeckungsabhängige periodische Verspannung der Oberfläche beobachtet, die zu einer Expansion der obersten abgeschiedenen Schicht führt.

Durch Zugabe von Polyethylenglykol (PEG), eines in der Industrie häufig verwendeten Inhibitors, werden die Wachstumsbedingungen stark verändert. Die Cl-Umordnungskinetik ist beeinflusst, sodass die c(2×2) bedeckte Phase in einem erweiterten Potentialbereich stabilisiert wird. Der Übergang zum 3D-Multilagen-Wachstum ist zu negativen Potentialen verschoben und das Auftreten von Wachstumsoszillationen auf einen engeren Potentialbereich limitiert. Im Vergleich zum PEG-freien Elektrolyt ist die Abscheiderate auf ca. 30% verlangsamt.

Contents

Introduction

Electrodeposition as an industrial process is an integral part of the modern society for more than 200 years [1]. Starting with the first applications in electroforming of printing plates [2], electroplating gained major importance as the predominant surface finishing technique both for decorative as well as protective coatings (*e.g.*, jewelry, chromium plating, nickel-plated steel) [1]. In particular, the electrodeposition of copper is nowadays extensively used in electroforming, electrorefining, and electroplating [3] with widely spread technological applications. These include, amongst others, the refinement of produced copper - more than 80% of the copper production is refined electrolytically [3] - as well as the fabrication of electrical cables, lightning rods, heat exchangers, reflectors, electromagnets, electrical relays, busbars, and switches. Moreover, copper electrodeposition rose to fundamental importance in today's electronics industry, as the modern integrated circuit (IC) technology is the basis of all contemporary electronic devices and consequently of the modern information society [4].

The continuous, rapidly increasing demand for higher electron mobility interconnects, which permit faster signal transmission, shorter delay times and less power consumption, led in the late 1990s to the transition from an aluminum- to a copper-based interconnect technology. The more and more complex microchips in today's ultra-large scale integrated (ULSI) technology demand a strongly enhanced integrated circuit performance, which includes, *e.g.*, circuit switching speed, number of interconnects per interconnect level, number of interconnect levels, and chip area[1]. Contemporary industrial mass production features 45 nm wide interconnect wires with extreme height-to-width aspect ratios up to 15 [6]. A further shrinking in patterning down to 15-22 nm in width is expected within the next ten years [4].

The interconnect wires are produced using the 'damascene copper electroplating' process, in which multicomponent electrolytes ensure the realization of defect-free filling of trenches in a patterned silicon substrate ('superconformal deposition' or 'superfilling') [7, 8]. State-of-the-art plating baths, which effect faster growth of the deposit at the bottom of the trenches as compared to the walls, contain different organic additives. These are typically an empiric mixture of a polyether and an organosulfur compound used in combination with chloride ions [9–11].

Despite its success, the application of electrochemistry to the nano-scale dimensions in the ULSI technology was and is not effortless: The continuously shrinking wiring dimensions and the resulting quest for optimized plating baths continues to challenge scientists and engineers around the world. An in-depth understanding of the electrochemical processes, specifically of the fundamental atomic-scale processes during electrodeposition of copper under superconformal growth conditions, is indispensable in order to allow for further improvement of the deposit morphology. The role of the additives in the electroplating process

[1] According to 'Moore's law', the time-dependent improvement of these properties occurs exponentially since the last 30 years [5].

has been investigated intensely in numerous studies by diverse electrochemical methods as well as by spectroscopic techniques and *ex situ* electron microscopy (*e.g.* [7, 9, 12–15]). These studies delivered a detailed microscopic picture of the functionality of superfilling, in which the polyether molecules in combination with halide ions form an overlayer on the copper surface, which substantially inhibits the electrodeposition process. In contrast, the organosulfur compound accelerates the deposition reaction by disrupting the inhibiting film. The competition between both compounds, together with locally sensitive effects such as reaction kinetics and material transport in the electrolyte, is responsible for the shape evolution of the copper deposit in the plating process [9, 15–18].

However, a precise understanding of the influence of the additives on the elementary atomic-scale steps of the growth process is still lacking. In general, homoepitaxial growth in electrochemical environment has been studied only sparsely by *in situ* structure sensitive methods. For deposition from the gas phase under ultra-high vacuum conditions, direct studies by diffraction methods revealed a profound understanding of the basic mechanisms which determine thin film growth [19, 20], and thus allowed to establish the experimental fundament for kinetic growth theory [21]. In contrast, similar fundamental atomic-scale structural data has not yet been obtained in electrochemical environment. This is mainly related to the common problem of investigating such growth processes *in situ*. Although numerous excellent tools for obtaining atomic-scale structural data are available today, *in situ* studies under realistic reaction conditions are often hampered by a limited functionality or the applicability of these instruments in electrochemical environment. In particular, electrodeposition studies under conditions involving high current densities and substantial atomic mass transport in the electrolyte with scanning probe techniques are often compromised due to obstruction by the scanning tip [22, 23]. Such inherent drawbacks may be overcome by using synchrotron radiation based techniques, *e.g.*, surface x-ray diffraction (SXRD) [24, 25].

In situ SXRD using synchrotron sources has been shown to provide high precision data both on the in-plane as well as on the surface-normal interface structure [24–28]. However, studies of copper electrodeposition by this technique are very seldom and were primarily carried out for the characterization of crystal structures of *ex situ* grown deposits (*e.g.* [29]). Despite some attempts of *in situ* investigations of heteroepitaxial deposition of copper (*e.g.*, on GaAs [30, 31]), to my knowledge, no *in situ* SXRD studies of the homoepitaxial electrodeposition of copper have been reported up to now.

New methods and instrumentation for *in situ* SXRD studies of electrochemical deposition processes were developed recently. A new cell design employing a transmission geometry where the beam travels through the electrolyte volume of several millimeters thickness [24, 32–34], allowed to overcome the inherent drawbacks of previously used thin layer cells[2]. In detail, unrestricted mass transport and a low cell resistance of the developed cell geometry allowed for high-quality *in situ* investigations of electrochemical growth processes under realistic reaction conditions, *i.e.*, at high deposition rates. The successful applicability to studies of homoepitaxial deposition on metal surfaces was reported for gold electrodes [34, 36–41]. Specifically, potential-dependent measurements of the diffusion-

[2] for earlier attempts *cf.* references [33, 35], however, these cell designs were not optimized for *in situ* growth studies

controlled deposition processes revealed that the kinetic growth behavior of the system, *i.e.*, step-flow, layer-by-layer, or 3D growth, could be directly followed up to growth rates of several monolayers per minute (ML/min).

The aim of the present thesis was to apply these recent developments to fundamental atomic-scale studies of copper electrodeposition - in terms of promoting the fundamental understanding of atomic-scale growth in electrochemical environment and, in particular, in terms of deepening the understanding of the processes occurring under superconformal growth conditions. Concretely, the atomic-scale structure of the electrochemical interface between the low index copper electrode surfaces Cu(001) and Cu(111) and chloride-containing electrolyte has been investigated by combined SXRD and electrochemical measurements. As the project aimed at clarifying the homoepitaxial growth process of copper, the growth behavior of Cu(001) in simple inorganic plating solutions, *i.e.*, in presence of copper and chloride ions, and in the presence of the inhibiting polyethylene glycol/chloride complex (PEG/Cl) was investigated. This allowed to clarify the complex interdependence of the surface morphology, the influence of these species, and the growth behavior during electrodeposition under diffusion-limited conditions. For the understanding of realistic superconformal growth processes, the time-resolution of our SXRD experiments had to be increased into the millisecond time regime in order to be able to resolve growth oscillations at technologically relevant deposition rates, typically around 5 to 20 ML/s. For this purpose, a fast 1D detector system has been employed and data analysis software for automated fitting of the intensity transients has been developed.

The thesis is divided in eight chapters. The first chapter introduces fundamentals of the electrodeposition process. In particular, reaction kinetics at the interface as well as nucleation and growth processes during electrodeposition from solutions containing metal-ions are treated. The chapter concludes with the discussion of the influence of additives on the deposition reaction and the introduction of the copper damascene plating process.

The subsequent chapter 2 briefly summarizes the basics of surface sensitive x-ray diffraction and explains the potential of this technique for *in situ* investigations of solid-liquid interfaces.

The details of the experimental techniques and preparation methods are given in chapter 3. After a description of the beamline and the diffractometer, the 1D detector system employed in the measurements is introduced. Subsequently, the electrochemical setup, the sample preparation method as well as cleaning procedures for the used equipment are presented.

The experimental results are given in the chapters 4-7. Starting with chapter 4, the powerful capabilities of SXRD employing the novel 1D detector are demonstrated. In particular, preparatory *in situ* SXRD studies of the electrochemical dissolution of Au(001) electrodes are presented, which were performed in order to explore the lower limit in time resolution with which electrodeposition and electrodissolution processes may be investigated.

The characterization of the Cu(001) and Cu(111) interface structures in chloride-containing electrolytes are subject of chapter 5. Generally, specifically adsorbed halides are known to form ordered adlayers on many low-index fcc metal single crystal electrodes [25]. The results obtained within the present study will provide new insight in both adlayer structure and phase transitions from the ordered to the disordered chloride adlayers on Cu(001) and

Cu(111) and will be discussed with respect to modern theories (density functional theory (DFT) and halide adlayer theories, respectively).

Detailed studies of the homoepitaxial growth of Cu(001) in electrolytes containing 1 and 5 mM $Cu(ClO_4)_2$ by simultaneous SXRD and electrochemical measurements are presented in chapter 6. Time-dependent changes in the scattered x-ray signal were recorded with the one-dimensional detector system at selected reciprocal space positions as a function of the electrode potential, providing first direct observation of the atomic-scale growth processes on the copper single crystal electrode in chloride-containing electrolytes. The interdependence of the growth process and the chloride adlayer will be addressed in detail as well as the evolution of surface strain during the growth process.

In continuation of these fundamental studies, homoepitaxial growth studies of Cu(001) in presence of the PEG/chloride complex were performed and will be presented in chapter 7. The influencing effect upon the addition of PEG on the chloride adlayer phase formation as well as on the resulting growth will be examined.

Finally, a conclusion and outlook is given in chapter 8. Some details regarding technical aspects and theoretical background are presented in the appendix of this thesis.

1 Electrodeposition

This chapter focuses on the fundamentals of electrodeposition which will be indispensable for the understanding of the results and discussions presented in this work. More comprehensive descriptions are found in standard electrochemistry textbooks and in application oriented publications (*e.g.* [4,42–50]) as well as in numerous excellent review articles (*e.g.* [51–54]).

1.1 Introduction

As shown in figure 1.1, the principle of a simple electrodeposition cell is the analogous to a galvanic cell acting in reverse. An external power supply drives an electrical current through two conducting electrodes immersed in an electrolyte containing ions of a metal species to be deposited. The dissolved metal ions are reduced and deposited as metal atoms at the interface between the solution and the cathode, following the reduction reaction

$$\mathrm{Me}^{n+}_{(\mathrm{aq.})} + ne^- \xrightarrow{\text{reduction}} \mathrm{Me}_{(\mathrm{sol.})}\,, \tag{1.1}$$

where n describes the valence of the metal species, *e.g.* Cu^{2+}, and e^- is an electron.

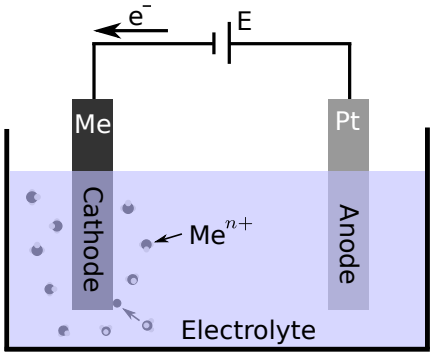

Figure 1.1: Schematic diagram of an electrodeposition cell. Under the influence of an external power supply, metal ions Me^{n+} are reduced at the cathode to solid metal atoms following the cathode reaction (1.1).

Thus, the cathode, which is also referred to as working electrode, serves as substrate for the electrodeposited film. In the growth studies presented in this thesis, copper single-crystals with (001) surface orientation were employed. At the second electrode, also called anode or counter electrode, an oxidation reaction compensates for the electron loss and completes the current circuit. Instead of controlling the current passing through the working electrode, which is referred to as galvanostatic electrodeposition, we usually used a potentiostatic control by fixing the potential applied to the substrate. Since high currents as well as ohmic drops in the electrolyte may influence the potential of the anode and therefore distort the electrochemical measurements, a third electrode, the reference electrode, is used to measure the relative potential reliably (three electrode configuration) [43]. The current passing through the reference electrode is minimized, resulting in a well-defined potential (so-called unpolarized reference electrode).

1.2 Equilibrium Potential

In equilibrium, the working electrode is generally subject to deposition and dissolution at the same time. In addition to the deposition reaction, the reverse metal dissolution reaction occurs and equation (1.1) may be adapted as

$$\mathrm{Me}^{n+}_{(\mathrm{aq.})} + ne^- \underset{\text{oxidation}}{\overset{\text{reduction}}{\rightleftharpoons}} \mathrm{Me}_{(\mathrm{sol.})} \tag{1.2}$$

for the generalized metal redox reaction (electron transfer reaction). For a more negative potential of the cathode, the reducing reaction given by equation (1.2) increases, whereas for more positive potentials, the oxidizing rate increases. The driving force which determines the predominant direction of the redox reaction - and thus of the processes taking place at the interface - is the electrochemical potential $\tilde{\mu}_i$ for the corresponding free particle (electron/ion) [43, 55, 56],

$$\tilde{\mu}_i = \mu_i + n_i F \Phi_i = \mu_i^0 + RT \ln a_i + n_i F \Phi_i \,. \tag{1.3}$$

The electrochemical potential $\tilde{\mu}_i$ is the sum of the chemical potential μ_i and an additional term which takes the electrical potential difference Φ_i between the electrode and the potential at the site of the particle i into account (Galvani potential) [55, 56]. $R = N_a k_B$ is the gas constant (product of Avogadro constant N_a and Boltzmann's constant k_B), T is the temperature, $F = N_a e_0$ is the Faraday constant (product of Avogadro constant N_a and elementary charge e_0), a_i is the chemical activity (which is a measure for the effective concentration), μ_i^0 is the chemical standard potential (for $a_i = 1$) and n_i is the charge transfer number of the electron transfer reaction.

From equation (1.3), the Nernst equation is derived, which gives the equilibrium potential of the electrode at which both reducing and oxidizing reaction rates are equal:

$$E_{\mathrm{eq.}} = E_0 + \frac{RT}{nF} \cdot \ln a_{\mathrm{Me}^{n+}} \,. \tag{1.4}$$

The equilibrium potential depends solely on the effective concentration $a_{\mathrm{Me}^{n+}}$ of the metal ions in the electrolyte at the working electrode, however, it is not necessarily equal to the bulk concentration of Me^{n+} (*cf.* section 1.3.2). The constant E_0 is referred to as standard galvani potential and denotes the potential difference between the galvani potentials of both phases for the effective concentration $a_{\mathrm{Me}^{n+}} = 1$. Employing a reference electrode, this potential difference can be referred to the standard electrode potential, which equals $E_{\mathrm{eq.}}$ if $a_{\mathrm{Me}^{n+}} = 1$. Its absolute value then depends on the employed reference electrode (*cf.* tables in [49]). For instance, the Nernst equilibrium potential of the copper electrode in 1 mM Cu^{2+}-containing electrolyte versus Ag/AgCl reference electrode is given by $E_{\mathrm{eq.}} = 0.056\,\mathrm{V}$ ($E_0 = 0.143\,\mathrm{V}$).

1.3 Interfaces under Non-Equilibrium Conditions

1.3.1 Electrode Reaction Kinetics

The rate of metal deposition in an electrolytic cell is controlled by the overpotential $\eta = E - E_{\mathrm{eq.}}$, where E is the external potential applied to the working electrode. The

overpotential forces electrode reactions to proceed at a required rate, leading to a current flow through the interface. Disregarding overpotentials influenced by a limited mass transport of reactants from the bulk solution to the surface or caused by a limited reaction rate before or after the electron transfer, the overpotential is mainly determined by the electron transfer overpotential. In this case, the current density is given by the Butler-Volmer-equation [43]

$$j(\eta) = j_+ + j_- = nFk_0c_{\text{red.}} \cdot \exp\left(\frac{\alpha nF}{RT} \cdot E\right) - nFk_0c_{\text{ox.}} \cdot \exp\left(-\frac{(1-\alpha)nF}{RT} \cdot E\right) . \quad (1.5)$$

Therein, j_+ and j_- are the anodic and cathodic current densities, respectively, n is the charge transfer number, and α is an asymmetry parameter with $0 < \alpha < 1$. The concentrations of the oxidized and reduced species are given by $c_{\text{ox.}}$ and $c_{\text{red.}}$, respectively.

Assuming that the plating overpotential and thus the applied electrode potential is sufficiently negative (*i.e.*, $(\alpha - 1)FE/RT \gg 1$), the dissolution rate becomes negligible and equation (1.5) yields an exponential dependence of j on E, which is known as Tafel-behavior [57]:

$$j(\eta) = -nFk_0c_{\text{ox.}} \cdot \exp\left(-\frac{(1-\alpha)nF}{RT} \cdot E\right) . \quad (1.6)$$

In contrast, for small overpotentials (*i.e.*, $|\alpha FE/RT| \ll 1$), the exponential functions of equation (1.5) yield a linear dependence of the deposition current density on E,

$$j(\eta) \propto \frac{nF}{RT} \cdot E . \quad (1.7)$$

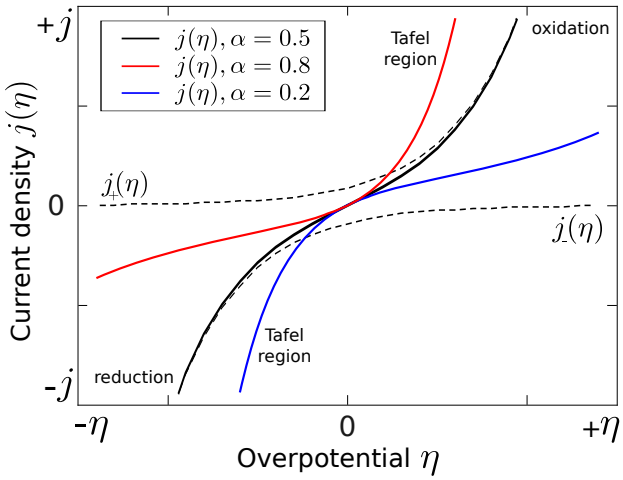

Figure 1.2: Simulated current density - overpotential dependence according to the Butler-Volmer equation (1.5). Curves are shown for different asymmetry parameter values of α. The dashed lines show the partial anodic (j_+) and cathodic (j_-) current densities for $\alpha = 0.5$.

Figure 1.2 depicts the Butler-Volmer-equation (1.5) for three different asymmetry parameters α and the partial anodic (j_+) and cathodic (j_-) current densities for $\alpha = 0.5$. Since the derivation of the Butler-Volmer-equation does not consider effects such as diffusion of reactants or rate limiting chemical reactions, it usually gives good first order approximations, however, it does not entirely describe the kinetic processes at the electrochemical

interface. Beside the electron transfer reaction given in equation (1.2), the cathodic electrodeposition of metals is often accompanied by further processes which will be discussed in the following section.

1.3.2 Diffusion-Limited Reaction Kinetics

In an electrolytic system, which is supposed to be unstirred and held at the open circuit potential (OCP), *i.e.*, under equilibrium conditions with vanishing current, the ion concentration c_0 is constant all over the electrolyte. Upon applying a negative potential to the working electrode, the metal deposition reaction is initiated (eq. (1.1)), leading to an adsorption of cations from the electrolyte on the surface. Consequently, the electrolyte at the interface depletes of Me^{n+}. A time-dependent concentration gradient profile evolves until a steady-state equilibrium of diffusion and depletion is reached. In a distance $> \delta_N$ from the cathode, the Nernst diffusion layer thickness, the ion concentration maintains its bulk value due to natural convection caused by, *e.g.*, variations in the temperature (*cf.* chapter 1.3.3). This behavior is illustrated in figure 1.3a for the cases of low ① and high ② overpotentials.

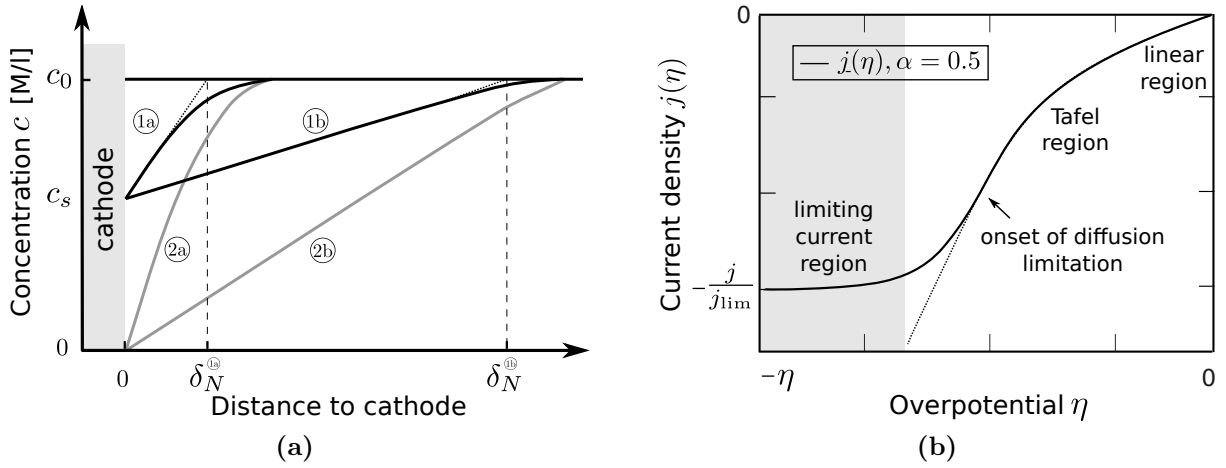

Figure 1.3: (a) Illustration of the time- and distance-dependent concentration gradient during electrodeposition in an unstirred electrolyte. c_0 and c_s denote the metal ion concentration in the bulk electrolyte and at the surface, respectively. Concentration gradients are shown for some seconds after initiation of current flow (index 'a') and under equilibrium conditions (index 'b'). (b) Simulation of the deviation of the cathodic current density $-j/j_{\mathrm{lim}}$ from the Butler-Volmer-equation (eq. (1.5)) due to diffusion limitation. The limiting current region is shaded.

The electrical current density due to diffusion of metal ions to the cathode is given by Fick's first law

$$j_D = nF\Psi_D = -nFD\nabla c_{\mathrm{Me}^{n+}} \overset{*}{=} -nFD\frac{\partial}{\partial x}c_{\mathrm{Me}^{n+}} = -nFD\frac{\left[c_{\mathrm{Me}^{n+}}\right]_0 - \left[c_{\mathrm{Me}^{n+}}\right]_{\mathrm{s}}}{\delta_N}\,, \qquad (1.8)$$

with the diffusion flux Ψ_D, the ion diffusivity coefficient D of the metal species in the electrolyte, the number of transferred electrons n per ion and the 'Nernst diffusion layer' $\delta_N = (c_0 - c_s)/((\partial c/\partial x)_{\mathrm{x=0}})$. In the step labeled with $*$, the gradient was replaced by the

one-dimensional partial derivative. The indices 0 and s denote the metal ion concentration in the bulk electrolyte and at the surface, respectively. Within the diffusion layer δ_N, the concentration gradient is non-zero and diffusion determines the transport of ions to the surface. δ_N strongly depends on the hydrodynamic conditions in the electrolyte and usually does not exceed $\sim 0.5\,\mathrm{mm}$ [43]. Typical time scales for the evolution of a diffusion equilibrium in non-stirred electrolytes, as it is the case throughout this work, are approximately 30 to 60 s (the time dependence is given by $\delta_N = \sqrt{\pi D t}$ [49]).

In case of a vanishing concentration of metal ions at the cathode, *i.e.*, at high overpotentials, j_D yields the condition for the diffusion-limited current density

$$j_D^{\mathrm{lim.}} = -nFD\frac{c_0}{\delta_N}\,. \tag{1.9}$$

Electrochemical reactions proceed very fast in the range where j_D equals $j_D^{\mathrm{lim.}}$. Combining equations (1.8) and (1.9) with the Nernst equation (eq. (1.4)), *i.e.*,

$$\eta_D = \frac{RT}{nF}\cdot\ln\frac{c_s}{c_0}\,, \tag{1.10}$$

the diffusion overpotential can be calculated as a function of the ratio between actual and limiting current density [58]

$$\eta_D = \frac{RT}{nF}\cdot\ln\left(1-\frac{j}{j_{\mathrm{lim.}}}\right)\,. \tag{1.11}$$

Within the limiting current region, which is shown in figure 1.3b as shaded region, the metal ion flux to the cathode is solely depending on the ion concentration in the solution, the temperature-dependent diffusion coefficient, and the hydrodynamic conditions. Specifically, diffusion-limited deposition allows to decouple potential-induced surface processes from changes in the deposition rate. It allows to study metal deposition under well-defined, kinetically controlled conditions, where the deposition rate is solely given by the potential-independent transport of metal ions to the electrode surface. Consequently, potential-dependent surface processes can be clearly separated from diffusion kinetics for a wide potential range [36, 59], as will be essential prerequisite for the growth behavior studies presented in chapters 6 and 7.

1.3.3 Transport Processes in the Electrolyte

In electrochemical environment three basic transport mechanisms are distinguished, each of them induced by a different driving force. Migration denotes the transport of charged particles due to the electric field. The concentration gradient, which evolves in vicinity of the electrode surface (*cf.* 1.3.2), induces diffusion processes. The third mechanism is convection, typically caused by variations in the temperature. In stagnant solution, convection is assumed to be negligible in vicinity to the electrode. Thus, the approach of the negatively charged metal complex to the cathode is only possible if the diffusion due to the concentration gradient compensates for the diffusion due to the electromigration (repulsive

force). The total current density in dependence of diffusion, migration and convection rates is given by the Planck-Nernst equation

$$\begin{aligned} j_i &= j_i^{\text{dif.}} + j_i^{\text{mig.}} + j_i^{\text{conv.}} \\ &\approx j_i^{\text{dif.}} + j_i^{\text{mig.}} \\ &= -n_i F \left(c_i u_i \nabla \Phi + D_i \nabla c_i \right) \\ &< 0 \qquad \text{for} \quad |c_i u_i \nabla \Phi| < |D_i \nabla c_i| \,. \end{aligned} \tag{1.12}$$

Therein, n_i is the number of transferred electrons, c_i the concentration of the species i in the solution, and D_i and u_i its diffusion constant and ionic mobility, respectively.

In the electrodeposition experiments presented in this work (chapters 6 and 7), a supporting electrolyte is used, which enhances the conductivity in the electrolyte by several orders of magnitude [43] and thus decreases the potential gradient, so that the constraint of (1.12) is fulfilled and deposition proceeds.

1.4 Nucleation and Crystal Growth

Crystal growth is the addition of atoms into the characteristic arrangement of a crystalline structure, specifically the incorporation of metal atoms from the environment (ultra-high vacuum or electrolyte) into the solid surface exhibiting a defined crystallographic orientation. Since at Nernst equilibrium (given by equation (1.4)), dissolution and deposition processes occur at equal rates, crystal growth can only proceed under the influence of a (negative) overpotential in non-equilibrium.

1.4.1 Cathodic Deposition of Metal Complexes

In order to understand how the negatively charged metal complex can be deposited on the cathode, *i.e.*, on the electrode carrying charge of the same polarity, a simplified model, depicting the atomic-scale processes within a nanometer to the surface, will be discussed in the following.

The approach of the solvated atom or metal-complex from the bulk electrolyte to the cathode is schematically shown in figure 1.4. According to equation (1.12), the complex

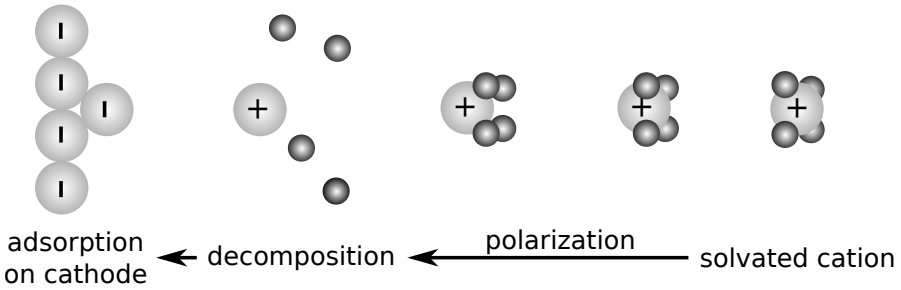

Figure 1.4: Illustration of the atomic-scale deposition process from solution (from [60]). With decreasing distance to the electrode, the negatively charged metal complex is polarized, resulting in the stripping of the ligans and an enhanced attraction of the positively charged metal ion. Subsequently, the metal ion is neutralized.

diffuses to the cathode due to the concentration gradient evolved in vicinity of the surface. With decreasing distance of the complex to the negatively charged electrode, the electric field Φ polarizes the metal ligand complex, leading to a stronger attraction of the metal ion. Close to the surface, *i.e.* in a distance of several Å, the complex decomposes and the freed metal cation is adsorbed on the surface, *i.e.*, deposited. A desorption process back into the solution can be neglected for electrode potentials far from equilibrium.

1.4.2 Nucleation Processes on the Atomic Scale

For an atomistic view of crystal growth [61–65] several sub-processes have to be taken into account, each of them proceeding at a distinct rate and depending on system parameters such as temperature and electrode potential. According to ref. [51], metal deposition is characterized by the attachment of adatoms to energetically favorable surface sites (defects), which act as sites for growth. In terms of epitaxial deposition, kink sites [66, 67] can basically be considered as the main sites of growth or dissolution of the crystal. The incorporation of an adatom at a kink site results in a new, adjacent kink site with the same properties, which are characterized by half the coordination number compared to bulk atoms. Consequently, the binding energy of these lattice positions is substantially enhanced compared to adatom positions on top of terraces, making the incorporation energetically favorable. The recreation of the kink sites leads to a preferential one-dimensional crystal growth along step edges [68]. Figure 1.5 summarizes schematically surface defects on a cubic lattice crystal.

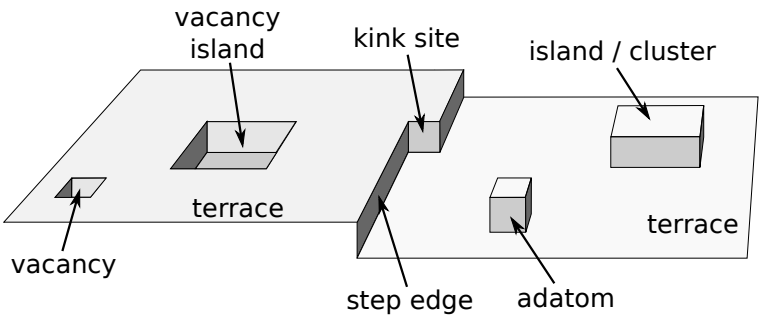

Figure 1.5: Illustration of a metal surface exhibiting different kinds of defects.

Deposited adatoms in the center of terraces are located at adsorption sites with a minimized potential energy (*e.g.*, fourfold hollow sites on a squared fcc(001) surface). If the thermal activation energy exceeds the activation barrier E_m for the transition of an adatom to the neighboring adsorption site (see also figure 1.7c), the adatom diffuses over the surface and becomes either incorporated to step-edges or participates in the formation of nuclei. In figure 1.6 the different atomic processes in 2D film deposition are depicted. The rates of these processes strongly depend on system parameters [63] such as material, crystalline order, growth rate, temperature, interface structure, and applied electrode potential [36].

In a more precise treatment, the thermally activated diffusion of adatoms across the surface and also across step edges may proceed via two different mechanisms, jumps and

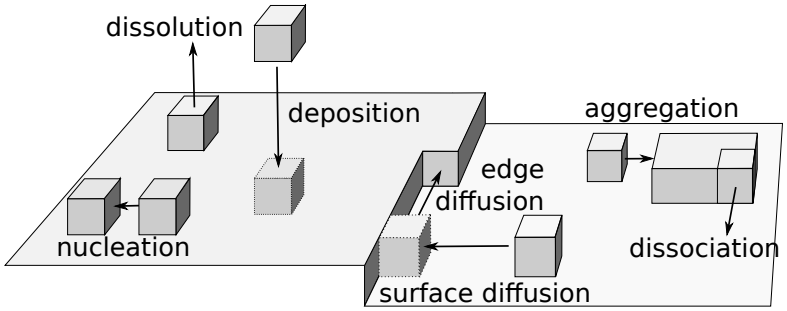

Figure 1.6: Illustration of kinetic atomic processes occurring during 2D crystal growth.

site exchange (figures 1.7a and 1.7b, respectively) [69–72], with a diffusion frequency given by

$$\nu = \nu_0 \cdot \exp\left(-E_m/k_B T\right) . \tag{1.13}$$

The attempt frequency ν_0 is comparable to typical lattice vibrations frequencies ($\sim 10^{12} - 10^{13}$ Hz). k_B is the Boltzmann constant. However, the adatom diffusion across step edges is energetically hindered by a bidirectional enhanced potential barrier E_{ESB} (Ehrlich-Schwoebel-barrier, ESB) [73–75], as illustrated in figure 1.7c. This barrier has to be overcome by thermal activation of the adatom in order to diffuse across the step edge. In contrast to deposition experiments in ultra-high vacuum, where numerous studies showed evidence for the existence of the ESB, no direct observations of the ESB had been reported in electrochemical environment until 2002 [76, 77]. In this environment as well, the probability for adatoms to cross a step edge can be described by the Boltzmann probability distribution

$$\gamma = \exp\left(-E_{\mathrm{ESB}}/k_B T\right) . \tag{1.14}$$

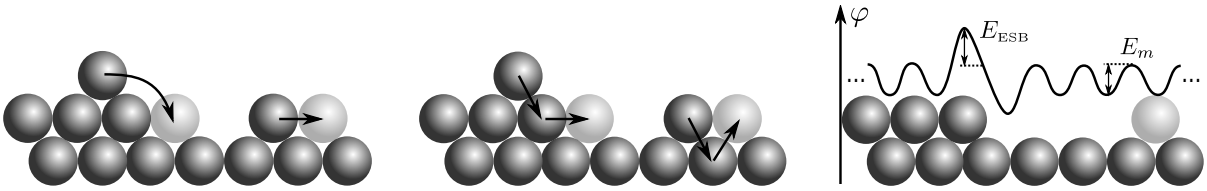

(a) jumping **(b)** site exchange **(c)** diffusion barriers

Figure 1.7: Adatom diffusion mechanisms via (a) jumping and (b) site exchange processes. (c) Illustration of surface diffusion barriers for adatom diffusion on terraces (E_m) and across step edges (E_{ESB}).

1.4.3 Kinetic Growth Modes in Electrodeposition

The thermodynamic growth modes for the deposition of metal atoms on surfaces close to equilibrium depend on the balancing of the surface free energies of the deposited film,

the substrate and the film-substrate interface. A distinction between three different growth modes is generally accepted [78], however, in case of crystal growth far from equilibrium, the deposit morphology becomes more dependent on the complex interplay of atomic diffusion processes. Since in reality, a clear separation between energetic and kinetic effects is not always possible, a full description of thin film growth within the thermodynamic theory is usually difficult. For example, the thermodynamic theory predicts layer-by-layer growth for homoepitaxial deposition of metals, whereas studies on rather simple systems revealed the occurrence of different growth behavior (*e.g.* [36]), thus indicating the importance of kinetic effects.

A different approach for homoepitaxial growth considers the two processes of adatom diffusion on a flat terrace (intralayer mass transport) and diffusion of adatoms across step edges onto the lower terrace (interlayer mass transport). The ratio of these rates determines three different kinetic growth modes, referred to as step-flow growth, layer-by-layer growth and 3D growth. Figure 1.8 depicts the time-dependent surface morphology for all three cases.

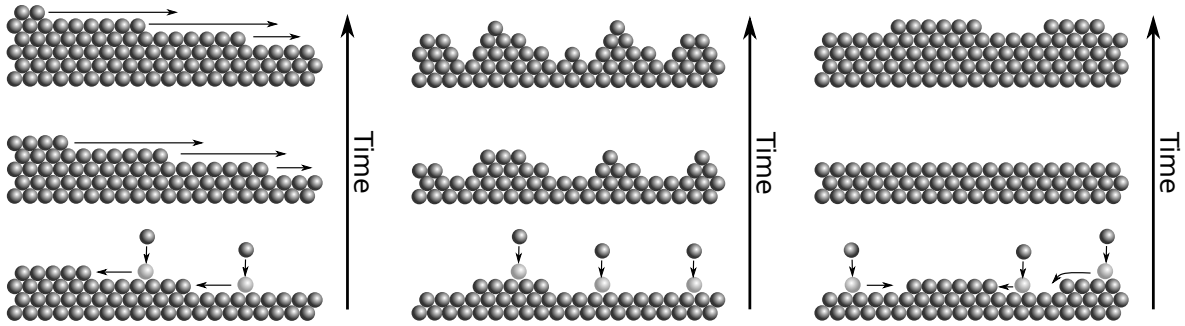

(a) Step-flow-growth **(b)** 3D-growth **(c)** Layer-by-layer-growth

Figure 1.8: Illustration of the three kinetic growth mechanisms step-flow growth, 3D growth, and layer-by-layer growth and the corresponding evolution of the surface morphology. With proceeding time (bottom to top), the amount of deposited material increases.

Step-flow growth is the kinetic growth mode which is often found in vicinity of equilibrium. Due to a rapid intralayer (and typically negligible interlayer) mass transport, the diffusing adatoms reach step edges before they can form a nucleus with other diffusing adatoms. Consequently, the probability for the formation of stable nuclei is low. Once diffused to the step edge, the adatoms are incorporated into the crystal structure, resulting in simultaneous growth of all terraces (figure 1.8a).

With increasing deposition rate, *i.e.* far from equilibrium, the adatom density and thus the nucleation probability on the surface is enhanced. If the adatom density becomes large enough, growth of adatom islands starts. In contrast to step-flow growth, now the decisive parameter for the resulting growth morphology is the interlayer mass transport. The Ehrlich-Schwoebel-barrier E_{ESB} mainly determines the growth behavior observed far from equilibrium as it controls the rate of interlayer mass transport.

According to equation (1.14), an infinite high ESB would lead to a vanishing interlayer mass transport and consequently to multilayer island growth, also referred to as 3D growth

(figure 1.8b). The number of exposed layers increases with increasing amount of deposited material and follows a Poisson distribution [79, 80], yielding very rough surfaces.

In contrast, if the surface exhibits steady, rapid interlayer and intralayer mass transport processes, and if the deposition rate is not too high, ideally all atoms randomly deposited on top of growing islands reach the island step edges and subsequently jump to the lower layers. The resulting growth proceeds via successive layer-by-layer growth, which is characterized by a periodic change of the surface morphology between a flat surface (full coverage of the topmost layer) and a rougher surface (fractional coverage of topmost layer) with increasing amount of deposited atoms [19]. This is shown in figure 1.8c. Both conditions of vanishing and infinite ESB are extreme cases. Real growth far from equilibrium proceeds in-between these extreme growth modes [19]. For instance, Trofimov and coworkers postulated an intermediate kinetic growth behavior between ideal layer-by-layer and ideal multilayer growth. In this so-called 'smooth multilayer growth' [39, 81, 82], the growth front consists of two to three simultaneously growing monolayers, leading to a saturating rms-roughness.

However, these models are not always accurate. For instance, if E_{ESB} is very small, not necessarily ideal layer-by-layer growth can be predicted. A more precise definition of growth modes, which takes the interlayer mass transport and surface roughness into account, is given by Rosenfeld *et al.* [19]. The comparison of the critical coverage $\theta_{\mathrm{crit.}}$, at which nucleation on top of growing islands sets in, with the coverage $\theta_{\mathrm{coal.}}$, at which islands coalesce to form a connected layer, yields a criterion for the quantitative distinction of 2D and 3D growth

$$\begin{aligned} \theta_{\mathrm{crit.}} &> \theta_{\mathrm{coal.}} \quad \rightarrow \quad \text{2D growth} \\ \theta_{\mathrm{crit.}} &< \theta_{\mathrm{coal.}} \quad \rightarrow \quad \text{3D growth}\,. \end{aligned} \tag{1.15}$$

Furthermore, Rosenfeld *et al.* derived expressions which describe the transition line between 2D and 3D growth and between 2D and step-flow growth. Both equations are given in (1.16) and (1.17), respectively [19].

$$R_{\mathrm{2D/3D}} = \lambda_0^{2(i+2)/i} \cdot \exp\left(-\frac{E_i/i + E_m + E_{\mathrm{ESB}} \cdot 2(i+2)/i}{k_B T}\right) \tag{1.16}$$

$$R_{\mathrm{2D/SF}} = \left(\frac{\lambda_0}{L}\right)^{2(i+2)/i} \cdot \exp\left(-\frac{E_i/i + E_m}{k_B T}\right) \tag{1.17}$$

Therein, R is the deposition rate, λ_0 is a constant related to island separation, i is the size of the critical nucleus, E_i is the binding energy of the critical cluster, E_m is the activation energy for terrace diffusion, k_B is the Boltzmann constant, T is the temperature, and L is the step separation distance.

Figure 1.9 illustrates the interpretation of the transitions for the simplified case of fixed energies (*e.g.*, as deposited from the gas phase) and temperature independent island sizes i as a function of the temperature. In case of a vanishing ESB, the Arrhenius plot of equations (1.16) and (1.17) shows parallel transition lines. Assuming thermal mobility of the adatoms, the transition line between 2D and 3D growth vanishes (dashed line) and only 2D and step-flow growth are observed (figure 1.9a). In contrast, the presence of an

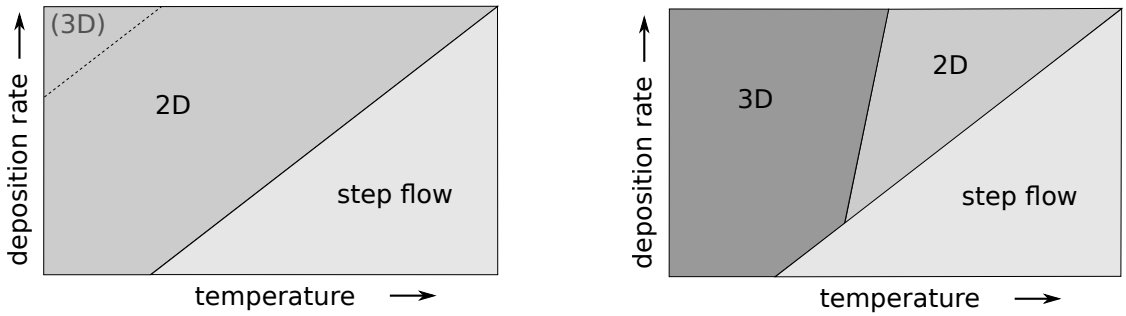

(a) $E_{\mathrm{ESB}} = 0$ **(b)** $E_{\mathrm{ESB}} > 0$

Figure 1.9: Illustration of the transition lines defined by equations (1.16) and (1.17) in an Arrhenius plot for different E_{ESB} in dependence of the substrate temperature. Shown is the simplest case of fixed energies E_i, E_m, and E_{ESB} as valid for deposition from the gas phase. From [19].

edge barrier $E_{\mathrm{ESB}} > 0$ modifies the behavior and the transition lines are not parallel any more. Consequently, a transition between different growth behavior may be observed with increasing temperature (at constant deposition rate), figure 1.9b, occurring from 3D to 2D to step-flow growth or directly from 3D to step-flow growth.

In case of deposition from electrolyte, the energies E_i, E_m, and E_{ESB} are potential-dependent, whereas the temperature is constant. Consequently, the transition lines exhibit a potential-dependent shape. As the knowledge about the potential-dependence of these energies is still limited, no precise predictions can be made for deposition in electrochemical environment. Experimental studies, for instance growth mode studies performed for homoepitaxial growth of Au(001) [36, 41] (*cf.* chapter 6), deepen this knowledge.

1.4.4 Influence of Additives

Additives are components which are admixed, beside the Me^{n+} ions, to the plating electrolyte with the purpose of influencing the electrodeposition reaction by adsorbing on the electrode surface. The most commonly used and simplest additives are anions, which adsorb, depending on the applied electrode potential, with varying strength on the surface. For instance, chloride anions, which play an important role in copper electrodeposition, are known to form ordered adlayers on the low-index copper single crystal surfaces (*cf.* chapter 5) [83, 84]. Vogt *et al.* reported that the formation of a c(2×2) chloride adlayer on Cu(001) leads to a preferred step orientation parallel to the [010] and [100] crystal directions [85, 86]. Moreover, the adlayer induced fourfold alignment of the step edges profoundly affects the morphology of the copper deposit, giving rise to the formation of pyramidal mounds and blocks [87, 88]. A detailed discussion about the Cu(001)-chloride system will be given in chapter 5.1.

In addition to anionic species, organic molecules are widely employed as additives in industrially used electroplating baths. Commonly accepted theory explains their functionality by the adsorption of the molecule on the surface accompanied by blocking of specific, *e.g.*, kink or step sites, or non-specific lattice sites. That way, growth may be influenced either directly by preventing or accelerating the incorporation of new metal atoms at kink or step sites, or indirectly by inhibiting or accelerating surface diffusion [89, 90]. These mode

of actions may be further classified, according to Oniciu *et al.* [91], as diffusion-controlled or non-diffusion-controlled, depending on the rate determining step which is influenced by the additive. Examples for the former are the influence of the diffusion of the metal ion or of other species to or on the surface. The latter, in contrast, includes influences on the charge transfer or the incorporation of the adatom into the crystal structure.

Literature about electrodeposition usually refers to additives by means of the observed effect, *e.g.*, additives leading to surface smoothing are typically referred to as 'levelers' or 'brighteners'. However, the precise mode of operation is largely not understood and depends strongly on the electrochemical system in use. In particular, the same additive may act in diverse ways in different systems. Thus, not only different mechanisms were suggested as explanation for the action of different additives [89], but the proposed mechanisms even diverged for the deposition of the same metal under different working conditions [91].

Furthermore, in many commercially used processes the electrolytes contain an assortment of more than one additive and in such cases also the interactions between the additives become important (*e.g.* [9, 13, 92]). An example is the copper damascene plating process [7, 8], which will be introduced in the following section.

1.4.5 Copper Damascene Plating

Copper damascene plating is the key process in the production of ultra-large scale integrated (ULSI) interconnects in today's microelectronics industry [7, 8, 93, 94]. As illustrated in figure 1.10, the process begins with the deposition of a dielectric material (a), usually SiO_2, followed by the etching of trenches or vias[1] into the layer (b). Subsequently, the entire surface is covered by an electroconductive barrier layer of TaN or TiN, which is essential to prevent copper from diffusing into the substrate. An additional copper seed layer, deposited on top of the TaN layer, serves as counter electrode for the deposition process (c) (usually deposited by chemical vapor deposition (CVD)). In the electrodeposition process (d), copper is deposited onto the conducting substrate including the trenches and vias. Excessive metal deposited outside of trenches and vias is removed in a subsequent step using chemical-mechanical polishing (CMP) (e) [8].

The challenging step in the production of these ULSI microchips is the defect-free filling of the approximately 65 nm narrow trenches, which typically exhibit depth-to-width aspect

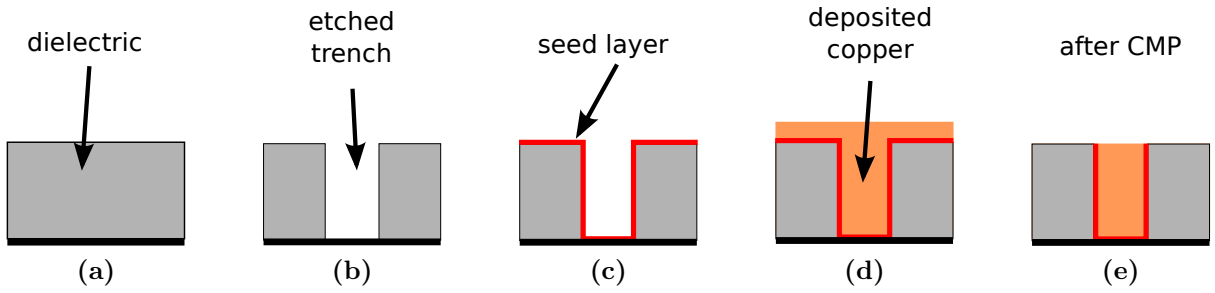

Figure 1.10: Illustration of the partial steps in the copper damascene plating process. Explanations of the steps are given in the text.

[1] 'via' is also used as abbreviation for 'vertical interconnect access'

ratios of up to 15 [6]. The specific type of filling, that meets these requirements without void formation, is called 'superconformal growth' or 'superfilling'. As depicted in figure 1.11, an enhanced deposition rate in the trench or via, which is achieved by a sophisticated interplay of various accelerator and inhibitor additives [7, 11, 95–97], leads to the prevention of voids or seams in the feature. Typically, modern copper plating baths contain the inhibitor polyethylene glycol (PEG), chloride and sufonate-terminated disulfides such as 3-mercapto-1-propane sulfonic acid (MPSA) or bis(3-sulfopropyl) disulfide (SPS) as accelerators [9–11].

Whereas PEG in combination with chloride hinders the electrodeposition of copper [10, 98–102], the two latter counteract the inhibiting effect by catalyzing the deposition reaction [9–11, 99, 103, 104]. However, a precise understanding of how these additives influence the deposition reaction, especially on the atomic scale, is still lacking and subject to lively discussion. A more detailed overview of the current state of research will be given in chapter 7.

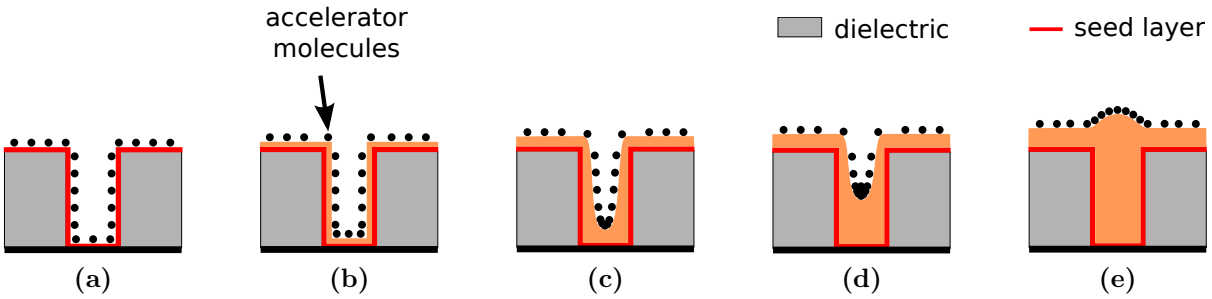

Figure 1.11: Illustration of the time-dependence of superconformal growth according to the curvature enhanced accelerator coverage model. Each single image represents successive stages of the deposition process. Due to an increasing accelerator concentration at the bottom of the feature, the deposition rate is significantly enhanced with respect to the deposition rate on flat or convex areas.

According to the curvature enhanced accelerator coverage (CEAC) model introduced by T. Moffat *et al.* [14, 17, 105], the local copper reduction rate in superconformal growth is controlled by the coverage of the accelerator. During the deposition process, the accelerator remains segregated at the interface, similar to surfactants. As shown in figure 1.11, the accelerator coverage on the seed layer is initially uniform (a). During deposition, the coverage at concave areas in trenches or vias increases as the surface area decreases, leading to locally enhanced deposition rates with respect to the deposition rate on flat or convex areas (b) - (d). This behavior may even lead to bump formation over the trench (e), which is removed in the CMP process.

The CEAC model allows for accurate quantitative simulations of the superfilling process as approved by comparison with experimental observations [9]. Besides the CEAC model, different approaches to explain the superfilling process have been proposed, but will not be discussed here.

2 Surface X-Ray Diffraction

After the first attempts in the 1950s [106] and much effort during the last 30 years [107–111], surface x-ray diffraction (SXRD) is nowadays a well-established technique for the characterization of surfaces and surface processes. Due to their small scattering cross section, *ergo* a weak interaction with matter, x-rays exhibit a large penetration depth compared to other surface sensitive scattering techniques such as electron or helium atom diffraction. Thus, buried interfaces may be investigated, including solid-liquid and solid-gas interfaces[1], to which common UHV based and scanning probe techniques are not applicable. As multiple scattering processes are typically negligible, a description of the scattering theory within a kinematical approach is often sufficient to analyze the data. However, the small amount of scattering atoms at the interface ($\sim 10^{15}\,\mathrm{cm}^{-2}$) leads to a very low scattered intensity signal as compared to the scattered intensity from a bulk crystal. Highly brilliant synchrotron radiation is thus indispensable in order to provide sufficient counting statistics and short counting times. Furthermore, the penetration depth of the x-ray beam has to be limited by using grazing incidence of the impinging beam with respect to the surface plane [112,113]. Otherwise, the signal from the crystal bulk becomes too strong and overlays the signal from the interface, which is already superposed by a high background intensity due to scattering from the solution bulk. In addition, enhanced surface sensitivity can be achieved by measuring the scattered intensity at the so-called anti-Bragg condition of crystal truncation rods.

In this chapter, a brief overview of the fundamentals of surface x-ray diffraction will be given. For a more detailed discussion of the basic principles of x-ray scattering, scattering from crystal surfaces and/or the description of surface sensitive x-ray techniques in general, the reader is referred to the comprehensive literature [111,114–120]. Excellent introductions to the application of SXRD to the investigation of electrochemical interfaces are given in [24–28, 121, 122].

2.1 Single Crystal X-Ray Diffraction

A crystal is characterized by the three real space lattice vectors $\vec{a}_1 = (a_1, 0, 0)$, $\vec{a}_2 = (0, a_2, 0)$, and $\vec{a}_3 = (0, 0, a_3)$, corresponding to three lattice vectors $\vec{a}_1^*$, $\vec{a}_2^*$, and $\vec{a}_3^*$ in reciprocal space. The diffraction of x-rays by the crystal is described in good approximation using the kinematical scattering theory. Specifically, singular, elastic scattering processes and the negligibility of interference phenomena of incoming and scattered beam (*e.g.* standing waves) are assumed. It is $|\vec{k}_i| = |\vec{k}_f| = k = 2\pi/\lambda$, with the incident and the scattered wave vectors, $\vec{k}_i$ and $\vec{k}_f$, respectively. k denotes the wave number and λ the wavelength of the monochromatic beam. Dynamical effects such as inelastic scattering, extinction and

[1] In the following, the terms 'surface' and (electrochemical) 'interface' will be used synonymously as both are treated equally with respect to x-ray diffraction.

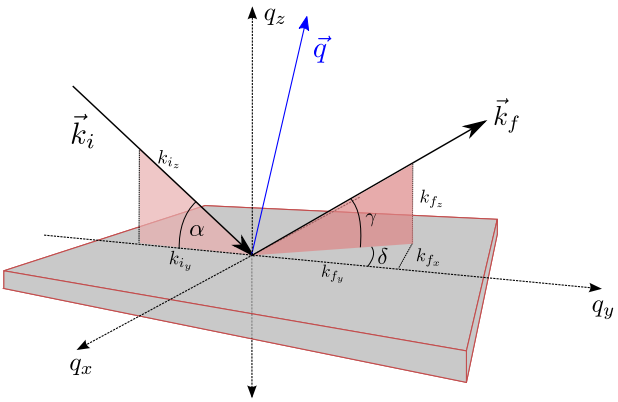

Figure 2.1: Scattering geometry in a typical surface x-ray diffraction experiment. $\vec{k}_i$ and $\vec{k}_f$ are the wave vectors of the incoming and scattered beam, respectively. Their difference defines the scattering vector $\vec{q}$.

refraction will be neglected. The scattering vector or momentum transfer $\vec{q} = (q_1, q_2, q_3)$ is defined by

$$\vec{q} = \vec{k}_f - \vec{k}_i = H \cdot \vec{a}_1^* + K \cdot \vec{a}_2^* + L \cdot \vec{a}_3^* \,, \tag{2.1}$$

and is referenced to the reciprocal lattice basis by the indices H, K and L. In case of integer H, K and L values, these indices are called Miller indices. Figure 2.1 illustrates the geometry of a typical (surface) x-ray diffraction experiment.
At a fixed position in reciprocal space, the scattered intensity of a crystal, which consists of N_i unit cells in the appropriate directions $\vec{a}_i$ of the real space lattice, is proportional to the square of the structure factor of the crystal [116],

$$\begin{aligned}
I(\vec{q}) \;&\propto\; |F_{\text{cryst.}}(\vec{q})|^2 \\
&= \left| \underbrace{\sum_{j_1=1}^{N_1}\sum_{j_2=1}^{N_2}\sum_{j_3=1}^{N_3}}_{\text{sum over unit cells}} \underbrace{\sum_{j=1}^{N} f_j(\vec{q}) \cdot e^{2\pi i\, \vec{q}\cdot\vec{r}_j} \cdot \underbrace{e^{-B_j \vec{q}^{\,2}/(4\pi)^2}}_{\text{Debye-Waller}} \cdot e^{2\pi i\, \vec{q}\cdot(j_1\vec{a}_1 + j_2\vec{a}_2 + j_3\vec{a}_3)}}_{F_{\text{u}}(\vec{q})} \right|^2 && (2.2) \\
&= |F_{\text{u}}(\vec{q})|^2 \cdot \left| \sum_{j_1=1}^{N_1}\sum_{j_2=1}^{N_2}\sum_{j_3=1}^{N_3} e^{2\pi i\, \vec{q}\cdot(j_1\vec{a}_1 + j_2\vec{a}_2 + j_3\vec{a}_3)} \right|^2 && (2.3) \\
&= |F_{\text{u}}(\vec{q})|^2 \cdot \frac{\sin^2(\frac{1}{2} N_1\, \vec{q}\,\vec{a}_1)}{\sin^2(\frac{1}{2}\, \vec{q}\,\vec{a}_1)} \cdot \frac{\sin^2(\frac{1}{2} N_2\, \vec{q}\,\vec{a}_2)}{\sin^2(\frac{1}{2}\, \vec{q}\,\vec{a}_2)} \cdot \frac{\sin^2(\frac{1}{2} N_3\, \vec{q}\,\vec{a}_3)}{\sin^2(\frac{1}{2}\, \vec{q}\,\vec{a}_3)} && (2.4) \\
&\to |F_{\text{u}}(\vec{q})|^2 \cdot N_1^2 \cdot N_2^2 \cdot N_3^2, \qquad \text{for large} \quad N_1, N_2, N_3 \,. && (2.5)
\end{aligned}$$

$F_{\text{u}}(\vec{q})$ is the structure factor of the unit cell, itself dependent on the atomic scattering factors $f_j(\vec{q})$ of the N atoms subscripted with j in that unit cell. $f_j(\vec{q})$ is given by the Fourier transformation of the electron density ρ_j of the atoms at positions $\vec{r}_j$ in the unit cell:

$$f_j(\vec{q}) = \int_{\text{cell}} \rho_j(\vec{r}) e^{i\,\vec{q}\cdot\vec{r}}\, d^3\vec{r}. \tag{2.6}$$

Thermal vibrations and static displacements (disorder) of the atom at $\vec{r}_j$ are taken into account by the Debye-Waller factor $\exp(-B_j\vec{q}^{\,2}/(4\pi)^2)$. Therein, the isotropic displacement

from the equilibrium position is given by $B_j = 8\pi^2\langle(x_j - \overline{x}_j)^2\rangle$ [119]. In case of anisotropic displacements, which are expected for surface atoms, B_j is replaced by a tensor $\tau(\vec{r}_j)$. The atomic displacements result in a blurring of crystalline reflections, a stronger decrease of the peak intensity with increasing $|\vec{q}|$ and an enhanced diffuse scattering.

The summations in the second factor in equation (2.3), *i.e.*, in the interference function, are performed over the N_i unit cells in the appropriate directions $\vec{a}_i$ of the real space lattice, respectively. Evaluation of equation (2.2) gives rise to a discrete diffraction pattern in reciprocal space with Bragg reflections at integer (H, K, L) values, defined by the three Laue equations

$$\vec{q}\cdot\vec{a}_1 = 2\pi H \qquad \vec{q}\cdot\vec{a}_2 = 2\pi K \qquad \vec{q}\cdot\vec{a}_3 = 2\pi L\,. \tag{2.7}$$

If the crystal is infinitely large in the direction of $\vec{a}_i$, *i.e.*, $N_i \to \infty$, the according Bragg diffraction peak is described by a Dirac δ function. Each Bragg reflection can be allocated to the diffraction from the corresponding lattice planes in real space with a lattice spacing

$$d_{\mathrm{HKL}} = \frac{a}{\sqrt{H^2 + K^2 + L^2}}, \qquad a = |\vec{a}_i| \tag{2.8}$$

for the case of an fcc crystal.

2.2 X-Ray Diffraction from Surfaces and Interfaces

2.2.1 Grazing Incidence Geometry

With the introduction of the surface, we now consider a truncated crystal and assume $\vec{q}_3 = \vec{q}_z$ with z as the coordinate perpendicular to the surface.

In order to separate the weak surface scattering signal from the strong contribution of the crystal bulk, the sample surface is aligned at a glancing incidence angle α_i with respect to the impinging x-ray beam [113]. In this grazing incidence geometry, schematically shown in figure 2.1, effects of refraction at the surface have to be considered [123]. According to

$$n = 1 - \delta - i\beta = 1 - \frac{\lambda^2}{2\pi} r_e \rho_e - i\frac{\lambda}{4\pi}\mu\,, \tag{2.9}$$

the complex refractive index n of x-rays is slightly less than unity. The imaginary part β and the real part δ are dependent on the x-ray wavelength λ, the electron density ρ_e and the photoelectric absorption coefficient μ of the material. r_e denotes the Thomson radius of the electron.

Consequently, the transmitted beam is refracted towards the surface. If the angle of incidence α_i is smaller than the critical angle defined by $\alpha_c \approx \sqrt{2\delta}$, the beam is totally reflected at the interface. In this case, an evanescent wave travels in parallel to the surface and decays exponentially into the crystal. Figure 2.2 shows the calculated scattering depth Λ as a function of α_i for a copper crystal and a photon energy of 22.5 keV, according to

$$\Lambda \approx (\sqrt{2}k)^{-1} \cdot \left(\sqrt{(\alpha_c^2 - \alpha_i^2)^2 + 4\beta^2} + \alpha_c^2 - \alpha_i^2\right)^{-1/2}\,. \tag{2.10}$$

For $\alpha_i < \alpha_c$, the evanescent wave is damped into the crystal within some tens of angstroms. However, it increases rapidly to thousands of angstroms if $\alpha_i > \alpha_c$. Thus, controlling the angle of incidence allows to select the scattering depth contributing to a given measurement. From figure 2.2 a penetration depth of $\sim 3400\,\text{Å}$, corresponding to ~ 1900 atomic copper layers, is deduced for the incident angle $\alpha_i = 0.437°$, which was commonly used throughout this work. This value is largely overestimated, as for larger penetration depths adsorption effects become dominat.

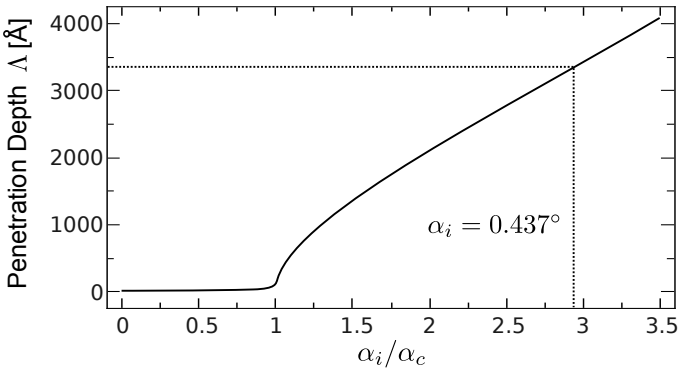

Figure 2.2: Scattering depth Λ as a function of the angle of incidence α_i according to equation (2.10) for copper and $\lambda = 0.55\,\text{nm}$ (22.5 keV). $\alpha_c = 0.149°$ denotes the critical angle for this energy. A scattering depth of approximately 3400 Å is obtained for an incidence angle of $\alpha_i = 0.437°$.

2.2.2 Crystal Truncation Rods

The introduction of a perfectly flat, bulk terminated crystal surface leads to a substantial change of the periodicity of the electron density. As illustrated in figure 2.3a, the electron density variation as a function of z can be represented by a Heaviside step function. Inside the crystal, its value is given by ρ_{bulk}, whereas outside of the crystal its value vanishes.

Thus, the structure factor of the coherently illuminated volume V of the truncated crystal is given by the convolution of the structure factor of the infinite crystal, eq. (2.4), and the Fourier transformation of the electron density step function (sketched in figure 2.3b). The results are crystal truncation rods (CTR) at integer in-plane Miller indices H and K, *i.e.*, diffuse streaks of intensity perpendicular to the surface [110, 124–128]. This is illustrated in figure 2.3c. The intensity modulation in-between two Bragg peaks, which varies over several orders of magnitude, is determined by the structure factor of the surface layer, $F_{\text{surf.}}(\vec{q})$. The structure factor of the surface layer and of the bulk (equation (2.4)) contribute to the total scattered intensity [111, 117] according to

$$I(\vec{q}) = |F(\vec{q})|^2 = |F_{\text{surf.}}(\vec{q}) + F_{\text{bulk}}(\vec{q})|^2 \,. \tag{2.11}$$

The scattered intensity variation as a function of q_z can then be calculated as:

$$\begin{aligned} I^{\text{CTR}}(\vec{q}) &= |F(2\pi H/a_1, 2\pi K/a_2, q_z)|^2 \\ &= |F_{\text{u}}(\vec{q}_{\text{CTR}})|^2 \cdot \frac{\sin^2(\frac{1}{2}N_1\,\vec{q}\,\vec{a}_1)}{\sin^2(\frac{1}{2}\,\vec{q}\,\vec{a}_1)} \cdot \frac{\sin^2(\frac{1}{2}N_2\,\vec{q}\,\vec{a}_2)}{\sin^2(\frac{1}{2}\,\vec{q}\,\vec{a}_2)} \cdot \frac{1}{2\sin^2(\frac{1}{2}\,\vec{q}\,\vec{a}_3)} \\ &\rightarrow |F_{\text{u}}(\vec{q}_{\text{CTR}})|^2 \cdot N_1^2 \cdot N_2^2 \cdot \frac{1}{2\sin^2(\frac{1}{2}\,\vec{q}\,\vec{a}_3)} \qquad \text{for large} \quad N_1, N_2 \,. \end{aligned} \tag{2.12}$$

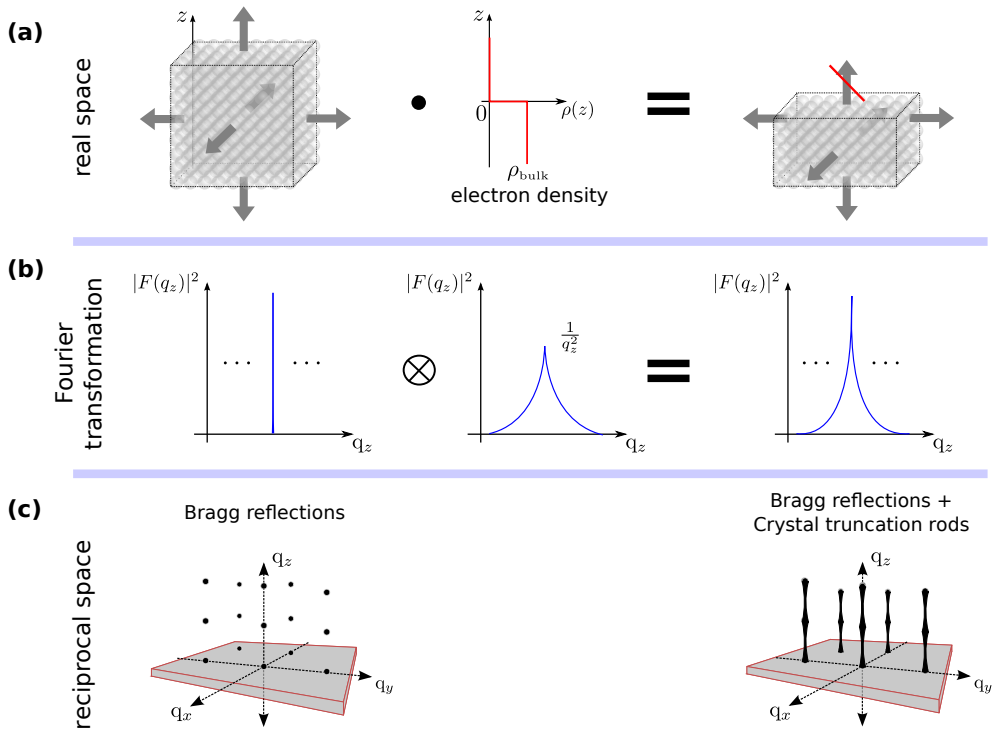

Figure 2.3: Illustration of the physical origin of crystal truncation rods. (a) By multiplying the infinite crystal in real space with an electron density step function $\rho(z)$, a truncated crystal can be generated. (b) The multiplication operation in real space equates to a convolution of the periodic Dirac δ-peaks with the Fourier transform of the Heaviside step function $\rho(z)$ in reciprocal space, which is proportional to $1/q_z$. (c) The resulting reciprocal space consists of periodic Bragg-reflections originating from the bulk lattice, extended by tails of intensity towards lower and higher q_z values.

For integer values of L, equation (2.12) yields the intensity of Bragg peaks. Moreover, close to the Bragg peaks, a $1/q_z^2$-dependence of the scattered intensity is obtained due to the Fourier transform of the Heaviside step function. The intensity at the anti-Bragg position, *i.e.*, halfway between two Bragg peaks, is very sensitive to structural changes at the surface [129]. Thus, for the investigation of homoepitaxial growth, time-dependent intensity transients at the anti-Bragg position may reveal important information about changes in the surface morphology, allowing for conclusions about, *e.g.*, growth behavior (*cf.* chapter 4), evolution of surface roughness as well as adsorption and desorption of species on the surface.

For an extensive structural analysis, a set of CTRs is recorded by performing rocking scans at different, usually equidistant positions along several rods. In order to take the scattering geometry into account, several correction factors are applied to the L-dependent integrated intensity (*cf.* annex A.4.1) [130]. Subsequent model calculations, which base on assumptions for the real space atomic arrangement at the surface or interface, may reveal the underlying structure. Such a detailed analysis will be reported for the Cu(001)-electrolyte interface in chapter 5.1.

2.2.3 Scattering from Relaxed and Reconstructed Surfaces

Crystals are generally not terminated by a perfectly flat surface. In addition to thermal vibrations, the surface structure, *i.e.*, surface roughness, relaxation and reconstruction of the topmost atom layers as well as adsorbed adlayers strongly influence the intensity distribution of the CTRs. Figure 2.4 shows simulated intensity curves for the specular CTR of a Cu(001) surface with an ideally truncated, a relaxed and a rough surface, respectively. The relaxation of the topmost layer leads to an asymmetry in the intensity distribution between two Bragg peaks, which depends on the amount and the direction of the relaxation (expansion or contraction). Whereas the non-specular CTRs are sensitive to the electron density distribution within the surface plane, the specular CTR has no in-plane wave-vector component and thus reflects solely the atomic arrangement in the direction perpendicular to the surface.

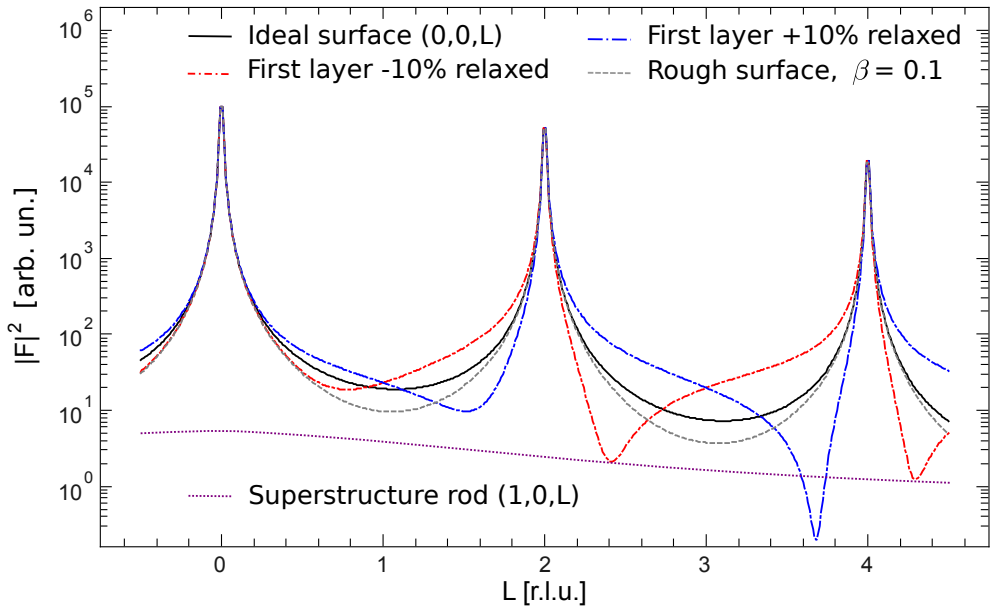

Figure 2.4: Intensity variation of the specular crystal truncation rod as a function of L for different Cu(001) surface morphologies. The solid curve shows the CTR profile for a perfectly sharp terminated surface as calculated by eq. (2.12). The two dash-dotted CTR curves are calculated for a topmost layer which is relaxed inward (-) or outward (+) by 10%, respectively. The dashed line shows the intensity distribution for the case of a rough surface with a roughness parameter of $\beta = 0.1$. For comparison, the c(2×2)-Cl superstructure rod (1,0,L) intensity is shown as dotted line at the bottom (*cf.* chapter 5.1).

A two-dimensional layer, *i.e.*, a reconstructed surface or an adsorbed layer, gives rise to additional superstructure rods in reciprocal space. As the electron density in z-direction is sharply localized, its Fourier transform yields a broad, homogeneous intensity distribution perpendicular to the surface, as shown in figure 2.4 (dotted line). These rods contain only information on the two-dimensional lateral structure and their intensity variation in

dependence of L is solely determined by the z-dependence of the superstructure, *i.e.*, the z-coordinates of the atoms within the unit cell[2] (as compared to equations (2.5) and (2.12)):

$$I^{\mathrm{2D}}(\vec{q}) \;=\; |F_{\mathrm{u}}^{\mathrm{2D}}(\vec{q})|^2 \cdot N_1^2 \cdot N_2^2 \,. \tag{2.13}$$

Reconstructed surface layers have a different in-plane lattice constant (surface unit cell) with respect to the substrate structure and may also exhibit a different electron density distribution. Thus, beside superstructure rods which overlap with bulk truncation rods, superstructure rods may occur at fractional Miller indices H and K. For instance, referring to the surface unit cell of a fcc(001) terminated crystal, a c(2×2) reconstructed superstructure will give rise to superstructure rods at $H, K = n + 1/2$, n integer (*cf.* chapter 5.1). The intensity of $I^{\mathrm{2D}}(\vec{q})$ is comparable to the diffracted intensity of the CTR at anti-Bragg condition [131], as visible in figure 2.4.

2.2.4 Roughness

By replacing the electron density step function in section 2.2.2 with a less abrupt function, atomic-scale surface roughness may be taken into account for the modeling of the CTR. With the occupancy parameter Θ_j of an atomic plane located at $z = j \cdot a_3$, $j \in \mathbb{Z}$, the surface structure factor is described by

$$F_{\mathrm{surf.}}^{\mathrm{rough}}(\vec{q}) \;=\; \sum_j f_j(\vec{q}) \cdot \Theta_j \cdot e^{-B_j \vec{q}^{\,2}/(4\pi)^2} \cdot e^{2\pi i\, \vec{q}\cdot\vec{r}_j} \,. \tag{2.14}$$

A commonly used approach is to assume an exponential roughness model [110], in which the occupancy of the j^{th} layer on top of the ideally terminated surface is given by

$$\Theta_j = \beta^j \quad \text{for} \quad j > 0, \qquad \Theta_j \overset{*}{=} 1 \quad \text{for} \quad j < 0, \qquad \text{with} \quad 0 < \beta < 1 \,. \tag{2.15}$$

The relation marked with $*$ accounts for the contribution of scattered intensity from layers within the finite penetration depth of the x-ray beam in the crystal (where the occupancy is 1). Consequently, the diffracted intensity from a rough or stepped fcc crystal surface yields [110]

$$I_{\mathrm{rough}}^{\mathrm{CTR}}(\vec{q}) \;=\; |F_{\mathrm{u}}(\vec{q})|^2 \cdot N_1^2 N_2^2 \cdot \left| \sum_{j=-\infty}^{\infty} \Theta_j \cdot e^{i\vec{q}\,\vec{a}_3} \right|^2 \tag{2.16}$$

$$\;=\; |F_{\mathrm{u}}(\vec{q})|^2 \cdot N_1^2 N_2^2 \cdot \frac{(1-\beta)^2}{(1+\beta^2-2\beta\cos(\vec{q}\,\vec{a}_3))} \cdot \frac{1}{2\sin^2(\frac{1}{2}\,\vec{q}\,\vec{a}_3)} \,. \tag{2.17}$$

In addition to the perfectly sharp surface, figure 2.4 shows a crystal truncation rod simulated with an exponential roughness parameter of $\beta = 0.1$ (gray dashed line). In-between two Bragg peaks, the intensity is substantially reduced with respect to the ideally terminated surface, due to destructive interference of the successive layers.

[2] as will be discussed in chapter 5.1, the intensity of the superstructure rod may be influenced due to interference phenomena of waves scattered at atomic layers, which are parallel to the superstructure and which have the same lateral periodicity

According to I.K. Robinson [110], a more convenient and intuitive expression for the surface roughness is given by the root-mean square roughness

$$\sigma_{\mathrm{rms}} = \frac{\sqrt{\beta}}{1-\beta} \cdot d_{\perp} \,, \tag{2.18}$$

where $d_{\perp}$ is the lattice spacing perpendicular to the surface.

3 Experimental Techniques

3.1 SXRD Experiments at the ESRF

The surface x-ray diffraction experiments described in this work were carried out at the European Synchrotron Radiation Facility (ESRF) in Grenoble, France. As one of the most powerful (third generation [132]) synchrotron light sources in the world, the ESRF provides x-ray beams with intense flux and high brilliance[1] (*cf.* table A.1). The ID32 beamline, which is optimized for surface and interface studies by x-ray diffraction, was chosen to carry out the experiments and will be described in detail in the following two sections. Afterwards, the one-dimensional detector Mythen 1K will be introduced, which was implemented into the diffractometer setup in the scope of this thesis (section 3.1.3). The chapter concludes with a brief presentation of the software which was developed and used for analyzing the data (section 3.1.4).

3.1.1 Beamline ID32

The ID32 beamline is a highly specialized, high resolution beamline dedicated to experiments for surface and interface studies by x-ray techniques. Zegenhagen *et al.* recently presented in detail the actual setup in reference [133]. A schematic sketch of the beamline is shown in figure 3.1.

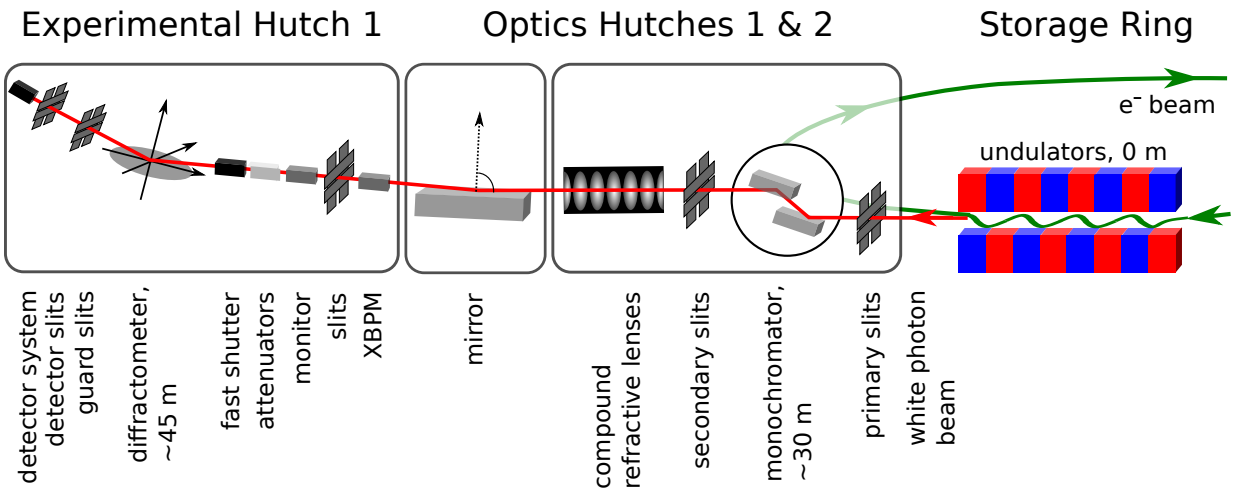

Figure 3.1: Schematic sketch of the beamline ID32 at the European Synchrotron Radiation Facility. The x-ray beam (red), generated by the undulators in the storage ring, passes several optical elements before impinging on the sample at the diffractometer.

[1] Brilliance is defined as the number of x-ray photons emitted per area of the source (mm^2), per solid angle ($mrad^2$), per second and per spectral interval (0.1 % bandwidth) [119].

Two undulators situated in the electron storage ring provide an x-ray beam which is linearly polarized in the horizontal ring plane. At a distance of 45 m from the source, a maximum photon flux of $\sim 10^{15}$ photons s^{-1} mm^{-2} at 20 keV (bandwidth 0.1%) is achieved with the focused beam. Table A.1 in the appendix summarizes the characteristic properties of the x-ray source, the undulators and the optical components at ID32 (status 2008 - 2010).

Throughout the entire beamline, the x-ray beam travels in ultra-high vacuum from the source to close to the sample in the experimental hutch 1. In the first optics hutch (OH1), the beam is monochromized by a LN_2 cooled high-heat-load monochromator, which consists of a pair of Si(111) crystals. Typically, the gap between both crystals is tracked as a function of the Bragg angle in order to ensure a constant height of the exiting beam. Subsequently, the monochromated x-ray beam passes a set of up to 15 two-dimensional parabolic beryllium compound refractive lenses (CRL), which are dispersive optical elements. A demagnification of the source by a factor of two is achieved, allowing to focus the beam down to a width of ∼20 µm in vertical direction at the sample. In the second optics hutch an x-ray mirror (coated with SiO_2-, Ni-, and Pd-stripes) is installed which acts as a low-pass filter for higher harmonics transmitted by the monochromator. For the studies presented in this work, an x-ray beam of 22.5 keV ($\lambda = 0.55$ Å) was used, usually focused by 15 CRLs and the Pd mirror. In order to avoid beam drift due to the thermal load on the optical components, an x-ray beam positioning monitor (XBPM) is installed which automatically stabilizes the beam via a feedback loop connected with the monochromator vertical and horizontal angle piezos. The latter control the fine adjustment of the monochromator. This way, the beam position on the sample can be kept constant with an accuracy of about 1 µm. A pair of horizontal (hg) and vertical slits (vg) defines the physical width and angular divergence of the beam impinging on the sample surface. In order to illuminate the entire sample length (in beam direction) in grazing incidence geometry (sample diameter typically 4 mm, angle of incidence ∼0.437°) usually a slit size of 50 µm was chosen in vertical direction. In horizontal direction a slit size of about 200 µm ensured enough intensity. Between the slits and the sample, the intensity of the monochromized and focused x-ray beam is monitored by using an ionization chamber. That way, the diffracted intensity measured by the detector can be normalized to the intensity of the incident beam. The irradiated intensity can be reduced by an attenuator arrangement or completely blocked by a fast shutter while no data is taken. Both protect the detector from saturation and minimize beam induced radiolytic effects at the solid-liquid interface (*e.g.* photoelectrons from the metal surface).

3.1.2 Six-Circle Diffractometer

The first experimental hutch houses a six-circle kappa diffractometer (Huber [134]) designed for high resolution surface x-ray diffraction experiments. A detailed presentation including geometry specific angle calculations, which link reciprocal space coordinates to a set of motor positions, are given by Lohmeyer and Vlieg [130, 135] and are summarized in A.3.1.

In figure 3.2a the diffractometer together with the used 'Huber tower' is shown. Figure 3.2b shows the schematic geometry of its six circles. Three of these circles are used for sample positioning (χ, φ, ϑ), two for in- and out-of-plane detector positioning (δ, γ, respectively) and one rotation (α) enables to set the grazing incidence angle via tilting the entire diffractometer by about $\pm 1°$ with respect to the incident x-ray beam. The rotation

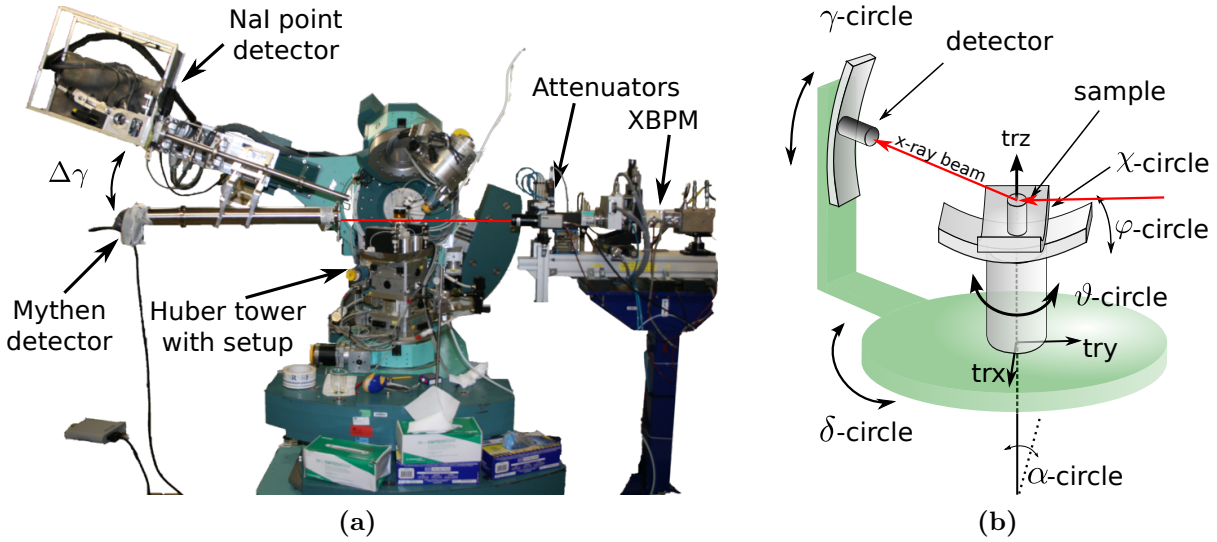

Figure 3.2: (a) Picture of the six-circle diffractometer at ID32 together with the experimental setup and the Mythen detector. (b) Schematic representation of the six circles of the used diffractometer. The red line indicates the x-ray beam.

axes of the six circles ideally coincide in one pivot point, the center of rotation, which in turn is the point where the sample surface is situated. The sample itself is mounted on top of the Huber tower which allows additional sample alignment via three perpendicular translation directions (trx, try, trz). The control of the instrument is performed using the SPEC™ control software [136].

In this work mainly in-plane measurements are carried out, *i.e.*, measurements at a constant q_z, typically equivalent to $L = 0.1$ reciprocal lattice units (r.l.u.). Therefore, first the sample normal was aligned to be in axis with the diffractometer sample rotation axis (ϑ axis) using the circles χ and φ. After fixing their positions, the orientation matrix was calculated from the angular sets of two aligned, linearly independent reflexes close to the surface (usually (2,0,0.1) and (1,1,1)). Details on this calculation can be found in A.3.1 in the appendix and in ref. [135].

Beside a new one-dimensional detector, which will be introduced in the following section, the diffracted intensity from the sample surface can alternatively be recorded by a Cyberstar point detector. This NaI detector is mounted in a distance of ∼1.1 m from the center of rotation and exhibits a 84 cm long evacuated flight tube. Sample guard slits at the upstream end of the flight tube (fixed aperture, 1 (h) × 5 (v) mm^2) reduce unwanted diffuse scattering which contributes to the background intensity. Additional pairs of horizontal (dhs) and vertical (dvs) slits are installed directly in front of the detector and can be varied from 0.5 to 5 mm aperture size. Their widths determine the detector resolution, as will be discussed in A.4.2 in the appendix. Via a graphite analyzer crystal in front of the detector, ineleastic contributions (fluorescence x-rays), that might be emitted from the sample, are suppressed.

3.1.3 Mythen 1K Detector

In the scope of this work, a novel one-dimensional detector system, the 'Dectris Mythen 1K detector', was implemented into the diffractometer setup [137]. The detector sensor consists of 1280 independent single-photon-counting silicon microstrip channels with a width of 50 µm and a length of 8 mm, summing up to an active area of $64 \times 8\,\mathrm{mm}^2$. Originally developed at the Swiss Light Source for time-resolved powder diffraction experiments [138], the Mythen detector has been a well suited instrument for our time-resolved and dose-critical measurements due to the principal advantages of simultaneous detection of x-rays and the fast readout time of 0.3 ms [139]. The dramatically reduced time needed to record a full peak cross section compared to measurements with the NaI point detector allows to investigate processes on time scales which are of industrial relevance, *e.g.*, the deposition of copper with growth rates of up to several ML/s, as will be shown in chapter 4. Furthermore, this development was essential prerequisite in order to minimize the exposure time in our studies of the influence of organic compounds on the growth process of Cu(001) (*cp.* chapter 7). B. Schmitt *et al.* give a detailed technical description of the detector system in [138]. Measurements performed by A. Bergamaschi *et al.* showed that the quality of the obtained data is comparable with that of traditional high-resolution point detectors (crystal-analyzer setup) in terms of FWHM resolution and peak profile shape [140]. The most important technical details of the microstrip detector are listed in the appendix in table A.1.

As can be seen in figure 3.2a, the detector is mounted on an additional detector arm under a certain angle $\Delta\gamma$ (and an unavoidable small in-plane angle $\Delta\delta$) below the existing NaI point detector with a distance of 1 m between the sample and the detector. This setup, developed and constructed in the scope of this work, allows to switch easily between both detectors and to access the same positions in reciprocal space as with the point detector. The orientation of the extended detector axis is parallel to the sample surface. A flight tube with 8 cm in diameter suppresses diffuse scattering (*e.g.*, from air) and provides the possibility to mount both sample guard and detector slits with the aperture sizes of 0.5 to 8 mm in vertical direction (horizontal direction remains open). In our diffraction experiments we chose the 2 mm guard slit as a compromise between high scattered intensity and reduced diffuse scattering from the bulk electrolyte. For triggering purposes, *i.e.*, to be able to start the detector measurements in parallel to the electrochemical experiments, the detector is connected via an impedance converter to the triggering output of the Ivium potentiostat.

For the sake of completeness, a brief alignment procedure of the Mythen 1K is given in A.3.2.

3.1.4 Mythen 1K Analyzing Software and Crosslinking to `SPEC`

As the one-dimensional detector is not implemented in `SPEC`, the provided software 'Mythen GUI' of the Dectris company was used for data acquisition. For a preliminary, quick analysis of the measured data, *i.e.*, the plotting of the integrated intensity as a function of time, a homemade command line based software was used ('Mythen Data Analysis tool' (MDA), written in Python). After specifying a range of interest (ROI) and subtracting a polynomial background, the software allows to determine the integrated intensity via the numerical sum of the discrete intensities obtained for the channels. The resulting intensity-time plot was

usually indistinguishable from an intensity-time plot obtained after fitting the data with either Lorentzian, Gaussian, or pseudo-Voigt functions. Thus, time-consuming and more complex least-square fits were only performed when necessary. An advanced graphical user interface software ('Mythen Data Analysis Pro' (MDAPro), written in Python) combines all of these analysis methods including the possibility to browse the recorded scans and frames. Moreover, it adds further analysis functions, *e.g.*, the export of time-channel-intensity maps and cyclic diffractograms (x-ray intensity measured during potential cycles, *cf.* chapter 5.1 or 7). In addition, routines for the statistical calculation of peak position, width and skewness via standardized moments were implemented, allowing to analyze also asymmetric peak profiles which cannot be fitted using simple model functions (*cf.* section A.5).

In order to be able to record crystal truncation rods with the Mythen detector, a crosslink connection between the `SPEC`-hosting computer and the Mythen control computer was established via a secure shell script. Further details are given in the appendix A.2. The entire integration of the Mythen 1K into the existing experimental setup as well as the development of functional data analysis tools was part of the present work.

3.2 Electrochemical Setup

For the *in situ* SXRD measurements a recently developed hanging meniscus transmission cell was used. Compared to commonly used thin-layer cells (*e.g.* [24,141]), this cell geometry combines the advantage of a minimized electrical resistance (estimated as $R_{cell} \approx 7\,\Omega$ [40]) and nearly unrestricted mass transport since a homogeneous diffusion of charge to the electrode surface is possible (in contrast to rather slow diffusion in case of thin-layer cells [142]). Recent SXRD studies on diverse electrochemical systems, *e.g.*, the electrodeposition and electrodissolution of gold surfaces in aqueous electrolyte, proved the perfect applicability of the cell for the investigation of dynamic interface processes at the electrolyte-metal interface [34, 36, 37, 40, 143]. Thus, using this cell geometry, it is possible to combine *in situ* SXRD studies with high quality electrochemical measurements performed in parallel.

In the following, a brief introduction to the used cell setup including the remote controlled pump exchange system will be given. A more comprehensive discussion can be found in references [38, 40]. The principle of the hanging meniscus transmission cell resembles cell geometries commonly used in single crystal electrochemistry (*e.g.* [24, 144]). Figure 3.3a shows a cross sectional sketch of the cell, which was used in all experiments presented in this work.

The tripartite cell body, made of chemical inert Kel-F™ (polychlorotrifluoroethylene, PCTFE), holds a glass capillary which is filled with approximately 1 ml electrolyte. From the open end of the glass tube ($\varnothing_{inner} = 3\,mm$) a free standing, almost cylindrical and ∼50 µl-containing meniscus establishes the contact to the electrode surface. Via an additional, inner capillary and incorporated electrolyte inlet and outlet, made of Teflon™ (polytetrafluoroethylene, PTFE), the electrochemical cell allows exchange of the electrolyte in the meniscus. The cell is connected to a remote-controlled pump system consisting of two synchronized syringe pumps (Hamilton™PSD3). That way an exchange can be performed even during the SXRD measurements and the meniscus size can be kept constant with µl precision (figures 3.3b and 3.4).

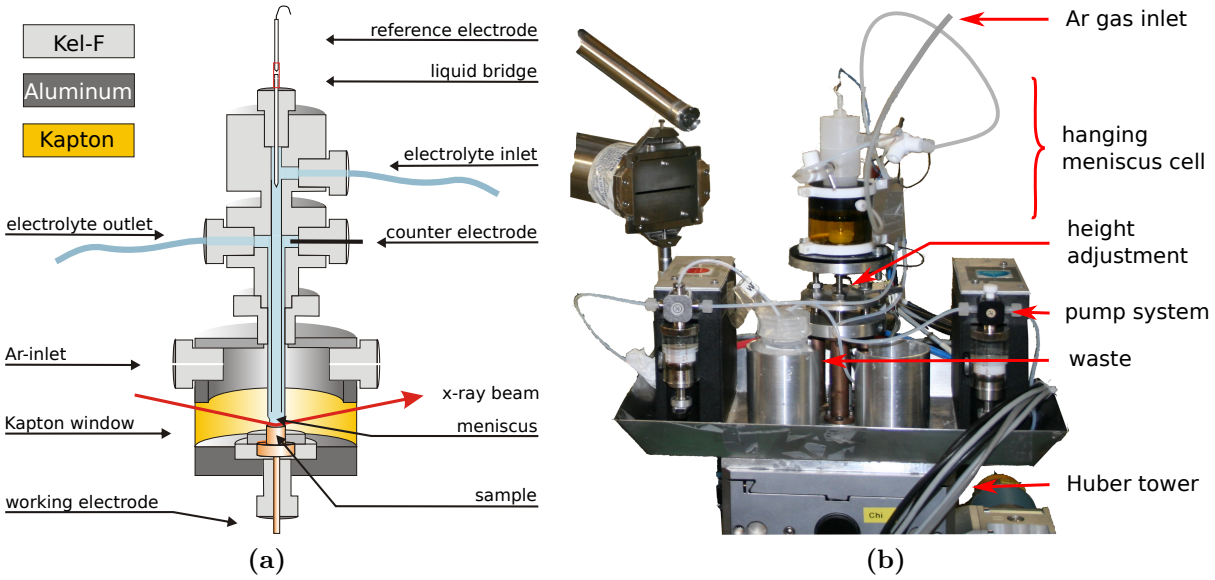

Figure 3.3: (a) Schematic cross section of the complete hanging meniscus transmission cell used for the SXRD experiments including a single crystal working electrode. (b) Picture of the experimental setup on the x-ray diffractometer. The labels identify the important parts of the setup (descriptions see text).

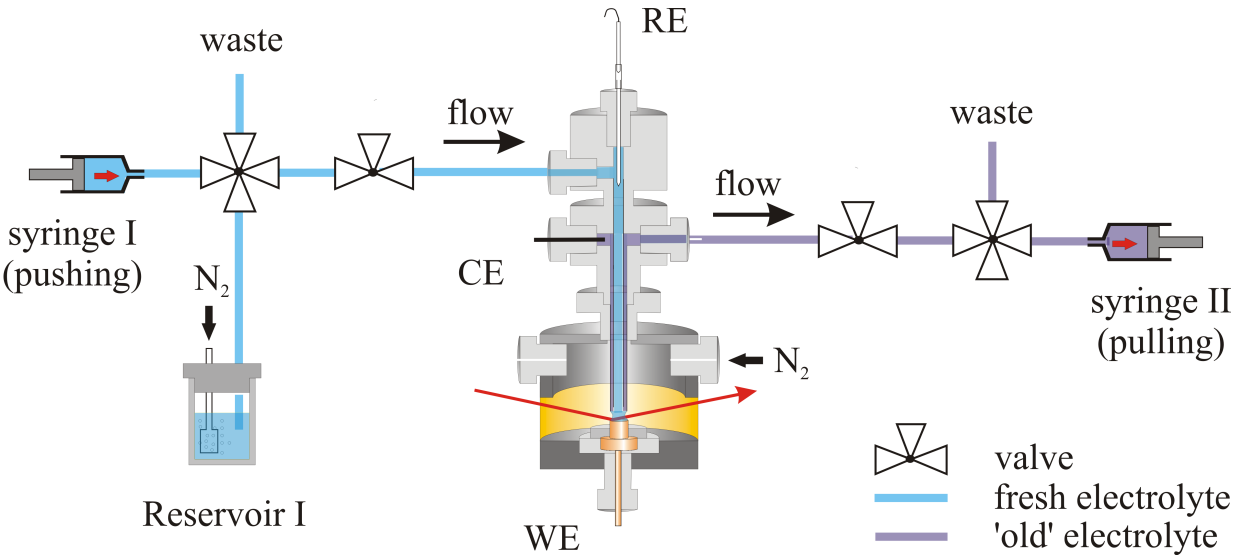

Figure 3.4: Schematic diagram showing the principal implementation of hanging meniscus cell and electrolyte exchange system. The latter consists of two motor-driven syringe pumps, with syringe I serving as inlet and syringe II as outlet. Both syringes are connected via 4-way selector valves and Teflon™ tubes to the cell.

The three electrode configuration used for the experiments consists of an ideal non-polarizable Ag/AgCl (3 M KCl) reference electrode (RE) and a Pt counter electrode (CE). The latter was chosen to be about eight times larger in interface area than the sample surface in order to prevent characteristic electrode reactions at the CE. Both electrodes are situated in the inlet and outlet of the cell, respectively, with the inner capillary serving as Luggin capillary for the RE. In order to limit the current density at the RE, the RE is connected via a high input impedance to a digital potentiostat (Ivium Technologies, CompactStat™ [145]) so that the current passing through the reference electrode is negligible. The potentiostat handles potentiostatic as well as galvanostatic control of the sample, but in the experiments reported in this work mainly potentiostatic control was employed.

Continuous argon flow through the cell holding compartment keeps the meniscus free from contaminations from the surrounding gas (*e.g.* oxygen). The cell is mounted on the diffractometer Huber tower in upright geometry, as shown in figure 3.3b. Using this electrochemical setup allowed to perform experiments under stable conditions of more than 12 hours.

The red arrow in figures 3.3a and 3.4 indicates the x-ray beam which is solely scattered by the sample surface and the electrolyte solution in this 'wall-free geometry' (neglecting scattering by the thin Kapton window). Thus, only the liquid structure factor contributes to the scattered background intensity. Moreover, problems caused by beam damage of the window material, such as cell leakage or contamination of the electrolyte, are avoided [24]. The transmissivity of the x-ray beam through the electrolyte is given by the Beer-Lambert absorption law as 81% for a photon energy of 22.5 keV.

3.3 Sample Preparation

All hat-shaped Cu(001), Cu(111), and Au(001) single crystals used throughout this work were delivered from Mateck [146] with a miscut smaller than 0.1°, a specified roughness of less than 0.03 µm and a purity of at least 99.999%. The dimensions of the crystals are given by a total height of 6 mm, a 2 mm brim and a circular surface of either 4 mm (Cu(111), Cu(001), Au(001)) or 6 mm in diameter (Cu(001)).

Before each experiment the copper single crystals were prepared using electropolishing in 60-70% orthophosphoric acid for at least 10 seconds. Up to 10 polishing cycles were performed when deemed necessary. Thereby, a potential of about + 2 V between the copper electrode and a $\sim$6 cm^2 platinum sheet was applied [86], leading to dissolution of the copper crystal accompanied by the removal of surface impurities. While immersed into the polishing solution the crystal was steadily moved with rapid movements. Subsequent to each polishing cycle the entire crystal was rinsed with Milli-Q water before it was covered with a water droplet and mounted in the sample holder [86]. Using this method, usually high quality copper surfaces were obtained as verified by surface diffraction. However, if the crystal showed already a high degree of roughness (by direct visual inspection), the electropolishing procedure even enhanced this roughness, leading to worse surfaces. In this case the crystal was judged unsuitable for SXRD and was replaced by a better one.

The preparation of the Au(001) crystal electrodes was done by flame annealing in a butane gas flame for approximately 5 to 10 minutes at light yellow glow (approximately

800 °C). Similar as reported for flame annealing of platinum crystals [147], the enhanced mobility of the atoms at high temperatures leads to the removal of surface adsorbates and a flattening of the surface. After several minutes of cooling down in air, the crystals were transfered into the electrochemical cell. Surfaces prepared by this technique proofed to be suitable for x-ray diffraction experiments as discussed in ref. [40].

3.4 Preparation of Electrolytes

Except for the case of PEG-containing electrolytes, all solutions were prepared from ultra-pure chemicals and ultra-pure water (Milli-Q, 18.2 MΩ, impurities < 8 ppb). Table 3.1 lists all used chemicals, their specifications and their provider. PEG was obtained in technical purity (95%) and was not further purified.

IUPAC Name	Product	Purity	Provider
Hydrochloric acid	HCl, 30%, Suprapur	> 99.999%	Merck
Perchloric acid	$HClO_4$, UPA, 65-71%	> 99.999%	Romil
Copper(II) perchlorate	$Cu(ClO_4)_2{\cdot}6H_2O$	> 99.999%	Alfa Aesar
Chloroauric acid	$HAuCl_4$ aq. solution, 40% Au		Chempur
Sodium perchlorate	$NaClO_4$	> 99.99%	Sigma-Aldrich
Polyethylene glycol	$HC(C_2H_4O)_nH$, 3000 M	≈ 95%	Merck
Potassium chloride	KCl SigmaUltra	> 99.0%	Sigma-Aldrich
	KCl Suprapur	> 99.999%	Merck
Sulfuric acid	H_2SO_4, pA, 95-98%, ISO 1	> 99.0%	Sigma-Aldrich, Merck
Hydrogen peroxide	H_2O_2, pA, 35% in H_2O	> 99.0%	Sigma-Aldrich
	H_2O_2, pA, 30% in H_2O	> 99.0%	Merck
Orthophosphoric acid	H_3PO_4, pA, 85%	> 99.0%	Sigma-Aldrich, Merck
Argon gas	Ar BIP or Premier	> 5.0	Air Products

Table 3.1: Overview of all used chemicals, specifying product specifications and providers.

3.5 Cleaning Procedure of Glassware and Equipment

In order to avoid impurities in the electrochemical experiments, all parts of the setup, which had direct contact with the electrolyte or the sample, were cleaned thoroughly by immersion into the strong oxidative peroxymonosulfuric acid ('Caro's acid', H_2SO_5, mixture of H_2SO_4 and H_2O_2 at the ratio of 3:1) for at least two days. Afterwards, the glassware was cooked in Milli-Q water several times in order to remove remaining SO_5^{3-} ions. As Kel-F™ and Teflon™ parts are not heat resistant, those parts were cleaned in Milli-Q water in an ultrasonic bath (T = 60°). Syringes, tubes, etc. were flushed repeatedly with Caro's acid and Milli-Q water. The counter electrode was cleaned by electrochemical stripping and subsequent flame annealing in a butane gas flame.

Notation Conventions

Throughout this thesis, all potentials are referred to the silver/silver-chloride reference electrode (Ag/AgCl, 3 M KCl) unless otherwise noted. Concentrations are given in mol or milli-mol per liter, abbreviated as 'M' and 'mM', respectively. Superstructures are noted in consistency with the appropriate publications - typically with respect to the surface unit cell - even if different from the conventional 'Wood's notation' (*e.g.*, the commonly used notation c(2×2) will be preferred to the notation $(\sqrt{2} \times \sqrt{2})$R45°).

4 Preparatory Measurements: High-Speed SXRD Studies of the Electrochemical Dissolution of Au(001)

Industrially employed current densities in technological electroplating in the copper damascene process are typically in the range of $10\,\mathrm{mA/cm^2}$, which corresponds to local growth rates of more than 10 ML/s. As the deposition rate influences the growth behavior and consequently the resulting deposit morphology [19,21,63], detailed insight into the atomic-scale growth process at these rates is highly desirable in order to deepen the fundamental understanding of the deposition process as well as to optimize the plating baths in today's industry. Thus, key requirement to studies of the electrodeposition processes at technologically relevant rates is to increase the time resolution of contemporary *in situ* instruments for the structure-sensitive investigation of electrochemical atomic-scale processes.

In situ scanning tunneling and atomic force microscopy (STM, AFM) as well as synchrotron-based methods such as surface x-ray diffraction are the favorable techniques to achieve this goal. Since the development of these high-resolution structure-sensitive *in situ* methods, which allowed for manifold structural studies at solid-liquid interfaces [24–28, 85, 110, 111,117,148–163], they have become an essential tool in modern interface science. In combination with electrochemical analytical methods, the modern atomic level understanding of electrode surfaces was greatly spurred. Specifically, it is possible to directly study electrode surfaces in dependence of the applied potential and to correlate structural changes with observations made in electrochemical measurements, *e.g.*, in the electrochemical current recorded in parallel. Such kind of studies will be presented for the Cu(001) and Cu(111) surfaces in chloride-containing electrolyte in chapter 5.

In addition, these techniques contributed enormously to an in-depth understanding of electrochemical interface processes during crystal growth and dissolution by revealing detailed information on the mechanisms of nucleation and growth on the atomic scale. Kinetic growth mode studies allowed to observe the dependence of the growth behavior on the applied electrode potential during the early stages of deposition or dissolution and to clarify the interdependence with the resulting surface morphology [36, 37, 39–41]. In addition, studies of the influence of surface defects and heterogeneities on the initial nucleation process were possible, demonstrating how the substrate as well as anionic or organic adsorbates affect the homogeneous nucleation densities and the shape of monolayer or vacancy islands. Vogt *et al.*, Polewska *et al.*, and Magnussen *et al.* were even able to directly follow the propagation of individual kinks along step edges during growth or dissolution at low overpotentials by *in situ* STM [86, 164–168].

However, despite the unquestionable importance of these results for nanoscale electrochemistry, *in situ* studies with scanning probe or SXRD techniques are currently limited to growth rates of up to 1 ML/s and thus preclude *in situ* investigations of faster processes. In case of high-resolution scanning probe microscopy, these limitations are caused by the low image acquisition rate (maximum speed of modern video STMs is around 10 to 20 images

per second [169–171]) and influence of the scanning tip on the electrochemical processes of interest. Whereas the time resolution is, in principle, a solvable problem [168], the influence of the scanning tip is an inherent fundamental problem. In detail, shielding effects by the tip in vicinity of the scanned area lead to significant lower local growth rates [22,23], therefore the observed growth behavior may differ from the actually occurring growth behavior under identical conditions in absence of the tip.

In case of synchrotron-based techniques, these inherent drawbacks do not exist. However, commonly used thin layer electrochemical cells, in which the sample surface is covered by an electrolyte layer of a few ten micrometer thickness, typically exhibit a high solution resistance (RC constant) and low transportation rates from the solution to the surface. Thus, the applicability of SXRD employing such cells is strongly limited to studies of slow kinetics and processes which do not require substantial mass transport in the electrolyte. Both these drawback were overcome by the development of a new cell design, a 'thick layer' cell, by Scherb and coworkers [141], which exhibits a hemispherical fused silica dome serving as x-ray window. Employing a wall-free cell geometry, Tamura *et al.* reported in 2004 for the first time combined SXRD and electrochemical studies of structural phase transitions during Bi underpotential deposition (UPD) on Au(111) on a millisecond time scale [33]. The high temporal resolution was achieved by summing the scattered intensity signal during several thousand periodic potential cycles using a multichannel scaler. Specifically, they were able to demonstrate that the two phase transitions from zero-coverage to a commensurate (2×2)-Bi adlayer to a high-coverage incommensurate (p×3)-2Bi phase with increasing amount of deposited material proceed on different time scales. Whereas the former occurs on the millisecond time scale, the latter is three orders of magnitude slower. In contrast to this study, where reversible processes are averaged for a large number of repeatedly performed equivalent measurements, (irreversible) processes, which strongly depend on the experimental procedure ('sample history'), have to be measured in one single experiment ('one-shot experiment') and can not be averaged to gain higher temporal resolution. Especially for the intended growth (and here dissolution) studies of the present work, the reversibility of the processes is strongly limited, thus requiring a different approach.

The same cell principle, also featuring unrestricted mass transport and time constants comparable to conventional electrochemical cells, was implemented in a 'hanging-meniscus cell' in transmission geometry [24, 32–34, 38] (for a detailed description see section 3.2). Using this setup, Krug *et al.* and Kaminski *et al.* investigated the atomic-scale electrodeposition and dissolution processes on gold single crystal electrodes in chloride containing electrolyte by SXRD [36, 37, 39–41]. They demonstrated that the kinetic growth behavior, *i.e.* step-flow, layer-by-layer, and 3D growth, can be directly determined from time-dependent intensity transients recorded at the anti-Bragg out-of-phase condition for scattering from consecutive layers. As shown in figure 4.1, for 3D multilayer growth, the scattered intensity decays to low values, usually background level, with deposited amount due to increasing surface roughness (*cf.* discussion in section 1.4.3). For the layer-by-layer growth mechanism the x-ray intensity transient reflects the successive growth of single monolayers, *i.e.*, the electrode surface is either perfectly terminated or covered by a fraction of a monolayer, resulting in oscillation maxima and minima, which arise from constructive and destructive interference of the scattered waves, respectively. In case of step-flow growth, the terraces grow simultaneously, hence the overall surface morphology does not change with time,

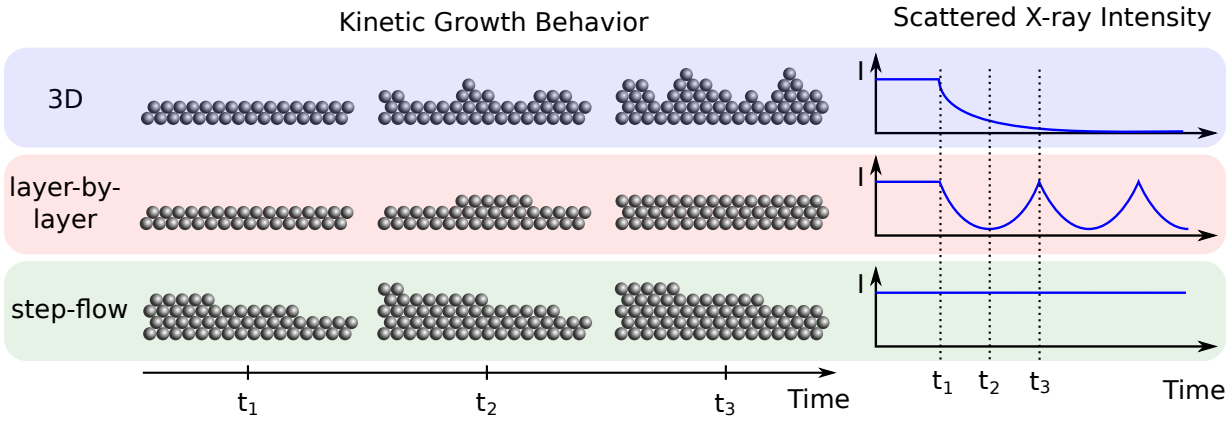

Figure 4.1: Illustration of the three kinetic growth behaviors (according to section 1.4.3) and the corresponding time-dependent scattered x-ray intensities at the anti-Bragg out-of-phase condition (ideal theoretical curve shapes). In case of crystal dissolution, the same behavior may be distinguished, resulting in the same time-dependence of the intensity transients.

yielding a time-independent scattered signal at a constant high level. The same principles are also valid in case of crystal dissolution [39].

Up to growth rates of several monolayers per minute (ML/min), Krug *et al.* investigated the growth behavior for the homoepitaxial electrodeposition of Au on Au(001) as a function of the applied electrode potential and diffusion-limited deposition rate [36, 40]. Their measurements revealed a complex, potential-dependent growth behavior, exhibiting transitions from step-flow to layer-by-layer to 3D and again to (reentrant) layer-by-layer growth with increasing potential (*cf.* in more detail in chapter 6). Equivalent studies of the electrochemical dissolution of Au(111), which were performed within the scope of this thesis and served as basis for the following experiments, showed a layer-by-layer dissolution mechanism for the entire active dissolution regime up to the onset of passivation [39, 40].

In order to resolve growth or dissolution oscillations occurring at even higher rates, improved counting statistics with data acquisition times of a few milliseconds are crucial to provide enough data sampling in 'one-shot' experiments. Due to the low scattered intensities at the anti-Bragg condition (*cf.* section 2.2.2, typical signal to background ratios are around 2-5), such improvements become only possible by integrating the scattered, background corrected intensity of the full reflection over a defined range of in-plane detector angles instead of recording the maximum intensity at the peak center. This task can be significantly accelerated by employing a one-dimensional detector as compared to performing time-consuming in-plane scans with a point detector. Within the scope of the present thesis, the fast Mythen 1K detector system, which is described in detail in section 3.1.3, was implemented into the existing beamline setup (*cf.* also A.1 – A.3), resulting in a fast data acquisition system for simultaneous recording of 1D intensity scans and electrochemical data. In addition to the high data acquisition rate of up to 600 Hz, the simultaneous recording of the full diffraction peak cross-section allows also to determine transients of the full width at half maximum (FWHM) and peak position either via fitting model functions to the data or by calculating the standardized moments within a statistical approach (*cf.* sections 3.1.4 and A.5). Thus, information on the lateral surface structure during the

one-shot experiments may be obtained, as will be sketched in the following publication. A detailed analysis of those transients will be presented for the homoepitaxial growth of Cu(001) in chapter 6.

In the following, *in situ* surface x-ray diffraction studies will be presented, which aimed at testing the Mythen 1D detector system under reaction conditions of technological relevance. These studies were performed using the electrochemical dissolution of Au(001) in chloride-containing electrolyte as an example. This model system has already been investigated in detail [36,37,40,172–179], thus the surface structure, the adsorbate structure and potential-dependent changes are well-known.

In figure 4.2 a cyclic voltammogram of Au(001) in 0.1 M HCl is shown, which is in accordance with literature [172]. A characteristic peak at $\sim 0\,\mathrm{V}$ (versus Ag/AgCl reference electrode) in the anodic sweep indicates the transition from a hexagonal reconstructed to an unreconstructed surface phase. Both reconstruction lifting and formation in this electrolyte have been studied in detail using various experimental techniques [173, 175, 178, 179]. The two additional current peaks at $\sim 0.6\,\mathrm{V}$ are related to an order-disorder phase transition of the chloride adlayer. In particular, STM studies by Cuesta *et al.* revealed an uniaxially, incommensurate c(2×p)R45° structure for potentials more positive than 0.6 V, with a potential-dependent p ranging from 2.3 to 2.5 [177]. From the growth studies reported in ref. [36], it is known that adatom surface transport processes are enhanced at the potential of 0.6 V as compared to more negative potentials, resulting in rapid smoothing of the surface. Due to this smoothing effect, which ensures reproducible starting conditions for all measurements during the experiment, the Au(001) electrode surface in chloride-containing electrolyte was judged to be well-suited for the intended dissolution experiments.

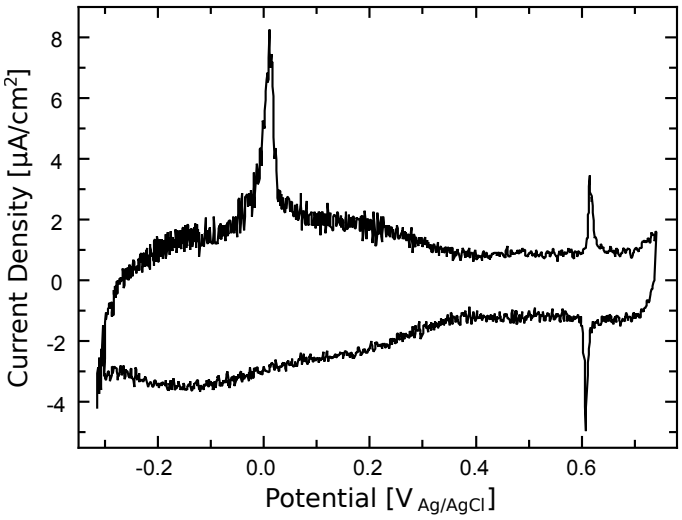

Figure 4.2: Cyclic voltammogram of Au(001) in 0.1 M HCl ($\mathrm{dE/dt} = 20\,\mathrm{mV/s}$), showing three characteristic current peaks: With increasing potential, the transition from the hexagonal reconstructed to the unreconstructed surface is observable at $\sim 0\,\mathrm{V}$ and the disorder to c(2×p)R45° order phase transition of the chloride adlayer at $\sim 0.6\,\mathrm{V}$.

As Ye *et al.* determined in an electrochemical quartz crystal microbalance (EQCM) study, the dissolution of gold in chloride-containing electrolyte proceeds via the formation of a stable gold-chloride complex in a three electron oxidation process [180, 181],

$$\mathrm{Au} + 4\mathrm{Cl}^- \rightarrow \mathrm{AuCl}_4^- + 3e^- \,, \tag{4.1}$$

for potentials between approximately 1.0 and 1.2 V. For higher anodic potentials the dissolution is strongly hindered by passivation caused by the formation of gold oxide [182]. Earlier

atomic-scale studies of the anodic dissolution of gold single crystal electrodes, specifically of the Au(111) and Au(001) electrodes in 0.1 M $HClO_4$ + Cl^--containing electrolyte, were performed by Ye *et al.* using electrochemical as well as scanning probe methods [181,183,184]. These studies were performed at much lower dissolution rates (< 1 ML/min) as compared to the following experiments.

In figure 4.3, the *in situ* STM images of the study of Ye *et al.* are shown [184]. In (a), an overview image of $1 \times 1\,\mu m^2$ obtained at 0.54 V shows large, stable terraces and step edges, which are parallel to the [110] direction of the Au(001) surface[1]. The image sequence (b)-(f) shows a detail of the image shown in (a) during a dissolution experiment ($0.5 \times 0.5\,\mu m^2$). In (b), the initial Au(001) surface at 0.84 V is shown, where the step edges seem to be more straight and sharper as compared to the image obtained for 0.54 V (especially terraces on the left site of the image). This is explained by the enhanced mobility of the gold atoms at this potential. Upon sweeping the potential into the active dissolution regime at 1.04 V (c), etching of the step edges sets in, observable in the formation of numerous kinks. While the dissolution proceeds with time, the direction of step edges changes from a preferred direction along [110] ((b)-(c)) to a preferred direction along [100] ((d)-(f)).

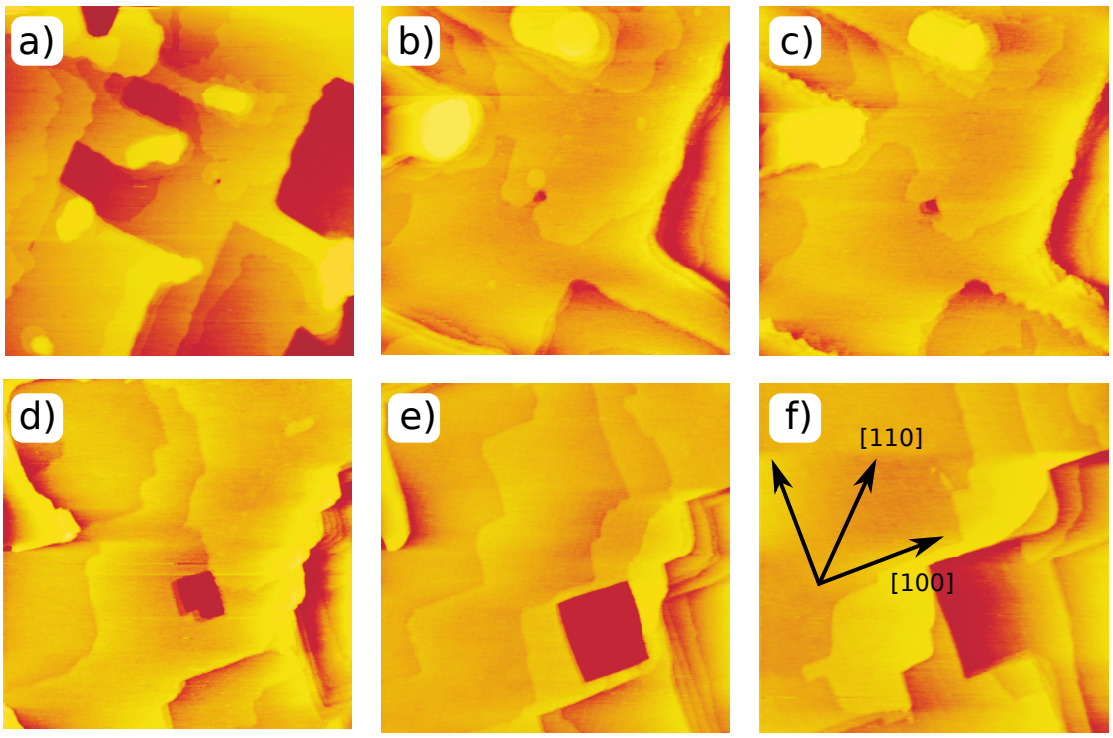

Figure 4.3: *In situ* STM images of Au(001) in 0.1 M $HClO_4$ + 1 mM Cl^- taken from reference [184]. (a) Overview image obtained at 0.54 V ($1 \times 1\,\mu m^2$). Enlarged detail ($0.5 \times 0.5\,\mu m^2$) measured (b) at 0.84 V, and (c) 0 min, (d) 10 min, (e) 20 min, (f) 40 min after the potential was swept to 1.04 V. $E_{tip} = 1.40$ V, $I_{tunnel} = 3$ nA. Credit [185].

[1]The potential values given by Ye *et al.* (recorded vs. the reversible hydrogen electrode (RHE)) were converted according to $E_{Ag/AgCl} = E_{RHE} + 0.0591 \cdot \log_{10}[H^+] - 0.1976$ V).

From these results, Ye and coworkers conclude that the anodic dissolution of Au(001) proceeds anisotropically in a step flow etching process in which the steps exhibit a preferential orientation along the [100] directions of the gold substrate. This anisotropy of the dissolution process is attributed to a stabilization of atomic rows along the [100] directions, induced by the chloride adlayers on the electrode surface.

Noteworthy, the dissolution on the terrace seems to occur at defect sites. For instance, a pit in the center of the image, which is already observable in (a) and (b), grows to a vacancy island with increasing time, suggesting that the dissolution proceeds rather in a a layer-by-layer mechanism.

The new methodical approach to fast *in situ* SXRD measurements fills the gap in reaction rates between fundamental atomic-scale studies and technologically relevant conditions. Consequently, apart from the importance for the experiments on copper electrodeposition (*cf.* chapters 6 and 7), it is of general interest for time-resolved studies of surface processes of all kinds. In summary, the substantial progress in the time resolution allows for studies in a new time domain for single-shot surface diffraction experiments.

JACS
JOURNAL OF THE AMERICAN CHEMICAL SOCIETY

COMMUNICATION

pubs.acs.org/JACS

High-Speed *in situ* Surface X-ray Diffraction Studies of the Electrochemical Dissolution of Au(001)

Frederik Golks,[†,‡] Klaus Krug,[†,§] Yvonne Gründer,[†,#] Jörg Zegenhagen,[‡] Jochim Stettner,[†] and Olaf M. Magnussen*[,†]

[†]Institut für Experimentelle und Angewandte Physik, Universität Kiel, Leibnizstrasse 19, 24098 Kiel, Germany

[‡]European Synchrotron Radiation Facility, 6 Rue Jules Horowitz, 38000 Grenoble, France

ABSTRACT: We present *in situ* X-ray surface diffraction studies of interface processes with data acquisition rates in the millisecond regime, using the electrochemical dissolution of Au(001) in Cl-containing solution as an example. This progress in time resolution permits monitoring of atomic-scale growth and etching processes at solid−liquid interfaces at technologically relevant rates. Au etching was found to proceed via a layer-by-layer mechanism in the entire active dissolution regime up to rates of ∼20 ML/s. Furthermore, we demonstrate that information on the lateral surface morphology and in-plane lattice strain during the electrochemical process can be obtained.

High-resolution *in situ* studies of solid−liquid interfaces by structure-sensitive methods, such as scanning probe microscopy and synchrotron-based techniques, have become an indispensable tool in modern interface science. Specifically, they have contributed enormously to the in-depth understanding of the complex interface processes in crystal growth and dissolution by revealing in detail the mechanisms of nucleation and growth on the atomic scale. For example, in the field of electrochemical deposition or dissolution, these studies clarified the potential-dependent growth behavior and resulting nanoscale morphology in the early stages of deposition or dissolution. They revealed the influence of surface defects and heterogeneities on the initial nucleation in the submonolayer regime. Furthermore, they showed how the substrate as well as anionic or organic adsorbates affect the homogeneous nucleation densities and the shape of monolayer or vacancy islands, and allowed even the propagation of individual kinks to be followed along steps during growth or dissolution.[1,2]

Despite the unquestionable importance of these results for nanoscale electrochemistry, a common general problem of all of these studies is the low growth rates, which are at most a couple of monolayers (ML) per minute, but typically much lower. In contrast, the minimum current densities typically employed in technological electroplating, e.g., in the copper damascene process used in ULSI manufacturing,[3] are in the range of 10 $mA \cdot cm^{-2}$, corresponding to local growth rates of ≥10 ML/s. Hence, like in heterogeneous catalysis, where industrial processes and scientific model studies under ultra-high vacuum-conditions are separated by a huge "pressure gap", a substantial "current density gap" exists between atomic-resolution *in situ* studies and applications. Since the deposition rate (i.e., the flux of particles to the crystal surface) is a central parameter in kinetic growth theory and influences the growth behavior as well as the resulting deposit morphology,[4−6] this is a serious drawback in clarifying the mechanisms of real-world electrodeposition processes.

in situ studies at high growth rates by high-resolution scanning probe microscopy are difficult due to the inherently low image acquisition rates and the influence of the scanning tip. The former can be somewhat mitigated by progress in increasing the time resolution.[7] The latter is a fundamental problem, leading to significant shielding of the scanned area and consequently to orders of magnitude lower local growth rates.[8,9] In contrast, studies by photon-based methods, such as X-ray diffraction, are in principle not plagued by such interference by the experimental probe. However, before now most studies have been performed in thin-layer electrochemical cells, where the sample surface is covered by an electrolyte layer of only a few tens micrometers thickness. This results not only in a large ohmic drop but also in strongly hindered transport to the electrode surface. Thus, true *in situ* studies during electrochemical growth processes are not possible in this way.

As we recently demonstrated for the case of Au electrochemical deposition and dissolution in Cl-containing solution,[10−12] the growth behavior and interface structure can be directly followed by surface X-ray scattering (SXS) using synchrotron radiation. By employing a transmission geometry, electrochemical cells can be realized that — contrary to thin-layer SXS cells — feature unrestricted mass transport and time constants comparable to those achieved with conventional electrochemical cells. *in situ* measurements during growth or dissolution at moderate rates (a few seconds per ML) were possible with such cells, with the local microscopic rates being almost identical to the macroscopic rates derived from the current density. These studies revealed a layer-by-layer dissolution mechanism for the electrochemical dissolution of Au(111) up to the onset of passivation[12] and a complex, potential-dependent growth behavior, featuring step-flow, layer-by-layer, 3D, and re-entrant layer-by-layer growth, for the homoepitaxial electrodeposition of Au on Au(001).[10,11]

Here we demonstrate for the case of electrochemical dissolution of Au(001) that, even at rates approaching those employed in technological deposition and dissolution processes, atomic-scale data can be obtained by *in situ* surface X-ray diffraction. Key to this improvement was the implementation of a fast 1D X-ray detector (Dectris Mythen 1K). It permits a much higher data

Received: December 23, 2010
Published: February 22, 2011

dx.doi.org/10.1021/ja1115748 | *J. Am. Chem. Soc.* 2011, 133, 3772–3775

Journal of the American Chemical Society COMMUNICATION

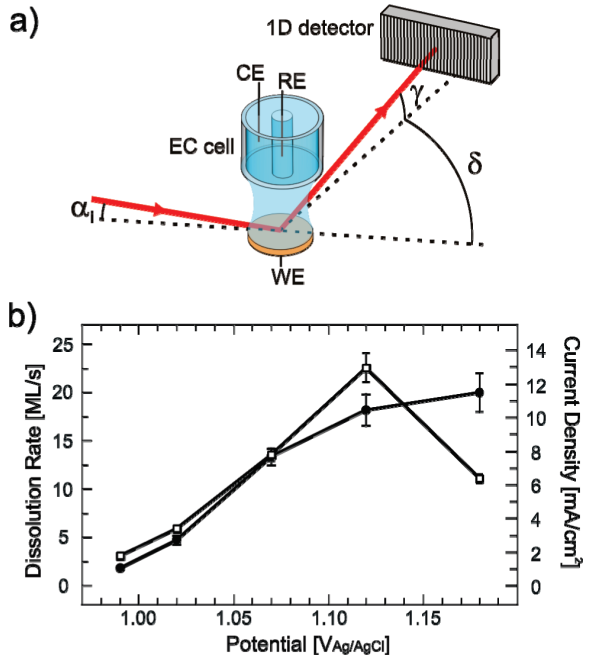

Figure 1. (a) Schematic scattering geometry of the *in situ* SXS experiments. (b) Potential-dependent microscopic dissolution rates obtained from the SXS experiments (filled circles) and from the simultaneously measured average electrochemical current density (open squares).

acquisition rate (up to 600 Hz) as compared to a conventional NaI point detector (maximum acquisition rate ~10 Hz). Furthermore, it allows simultaneously recording of the full diffraction peak cross section and the background scattering. As will be shown below, this enables measurements with millisecond data acquisition times, even at reciprocal space positions close to the surface-sensitive anti-Bragg position of the crystal truncation rod (CTR), where the intensity is minimal. This substantial progress in time resolution permits studies in a new time domain for single-shot surface diffraction experiments.

The measurements were performed using the six-circle diffractometer of beamline ID32 of the European Synchrotron Radiation Facility (ESRF) and the "hanging meniscus" X-ray transmission cell described in ref 13. The electrolyte is in contact with the sample electrode via a freestanding meniscus kept in an argon atmosphere (see scheme in Figure 1a). The incident X-ray beam (photon energy 22.5 keV), which is defined by vertical and horizontal slits of 10 and 300 μm, respectively, impinged at a grazing incident angle $\alpha_i = 0.384°$ onto the center of the electrode surface (corresponding to an illuminated sample area of 1.49×0.30 mm^2). Due to this wall-free geometry, the beam is only scattered by the sample and the electrolyte solution, and the background scattering is predominantly given by the smoothly varying liquid structure factor of the electrolyte solution. In order to minimize possible radiolytic effects, a fast photon shutter assured that the sample was only illuminated by the X-ray beam when recording the scattered intensity.

A NaI point detector was mounted together with the 1D detector on the same detector arm, which allows the former to be used for sample alignment and subsequently the latter for the time-resolved measurements. The 1D detector was oriented with the 1D pixel line parallel to the surface plane (see Figure 1a), covering an in-plane angular range of 3.66°. The spacing of the individual 50 μm wide pixels defined an angular resolution of $\Delta\delta = 2.865 \times 10^{-3}$°. Their height of 8 mm covered an angular range of $\Delta\gamma = 0.458°$ relative to the surface plane, over which the scattered intensity was integrated. In the time-resolved measurements, the Mythen detector was triggered by the potentiostat (Ivium, CompactStat), providing a precise temporal correlation of the X-ray time scan and the electrochemical data.

The samples used were 4 mm diameter Au(001) single crystals (Mateck) with a miscut <0.1° and a mosaic spread <0.013°, prepared by flame annealing prior to the experiment. The employed 0.1 M HCl + 0.5 mM $HAuCl_4$ electrolyte solution was prepared from HCl (Merck Ultrapur, 30%), $HAuCl_4$ aqueous solution (Chempur, 40% Au), and Milli-Q water. Potentials were measured versus a Ag/AgCl (3 M KCl) reference electrode. As coordinate system the common fcc Au unit cell with lattice constant $a = 4.08$ Å was employed.

The SXS studies were performed at the (1,1,0.1) position, i.e., close to the anti-Bragg position of the (1 1 l) crystal truncation rod. At this point in reciprocal space, the scattered intensity is highly sensitive to the surface morphology, specifically the atomic-scale roughness, and consequently provides insight into the growth or dissolution behavior in time-resolved measurements.[6,10−12] In the experiments, the sample was initially kept at 0.6 V, i.e., clearly below the Nernst potential of 0.83 V. The Au surface transport in this potential regime is fast, resulting in rapid smoothing of the surface.[10] SXS measurements at 0.6 V reveal a pronounced peak at (1,1,0.1) in the 1D detector frames with a height $>2 \times 10^4$ counts/s, allowing statistically significant single-shot measurements even at acquisition times of 5 ms (Figure 2a, inset).

The electrochemical Au dissolution was studied by stepping the potential to values in the range from 0.99 to 1.18 V, corresponding to overpotentials ≥160 mV and dissolution currents >1 mA·cm^{-2} (Figure 1b). As illustrated in Figure 2a, for a potential step to 1.07 V this resulted in dramatic changes in the initially constant integrated background-corrected intensity obtained from the 1D detector frames. In particular, regular oscillations in intensity are observed as a function of dissolution time, which are characteristic for a layer-by-layer dissolution mechanism. Similar oscillations were obtained up to dissolution potentials of 1.18 V but were most pronounced at the lowest overpotentials (see Figure 2b). Toward more positive potentials the SXS intensity rapidly decays with time (see Figure 2a), indicating an increasing surface roughening at higher dissolution rates, i.e., an imperfect layer-by-layer dissolution mechanism. A similar behavior was found in previous SXS studies of Au(111) performed at lower dissolution rates.[12] The microscopic dissolution rates, derived from the oscillation period, are in accordance with the simultaneously obtained electrochemical current densities (Figure 1b). The discrepancy at the most positive potentials is related to the onset of Au passivation in that range.

Atomic-scale data on Au(100) dissolution in chloride-containing electrolyte were also obtained in an earlier *in situ* STM study by Ye et al.,[14] albeit at much lower dissolution rates (<0.1 ML/min). In this work dissolution occurred predominantly by step flow etching, with the steps in the dissolution regime exhibiting a strong preferential orientation along the [100] directions of the Au substrate. Our results indicate a transition toward layer-by-layer or smooth multilayer (see ref 12) dissolution at higher overpotentials, illustrating the importance of *in situ* studies at realistic current densities.

dx.doi.org/10.1021/ja1115748 |*J. Am. Chem. Soc.* 2011, 133, 3772–3775

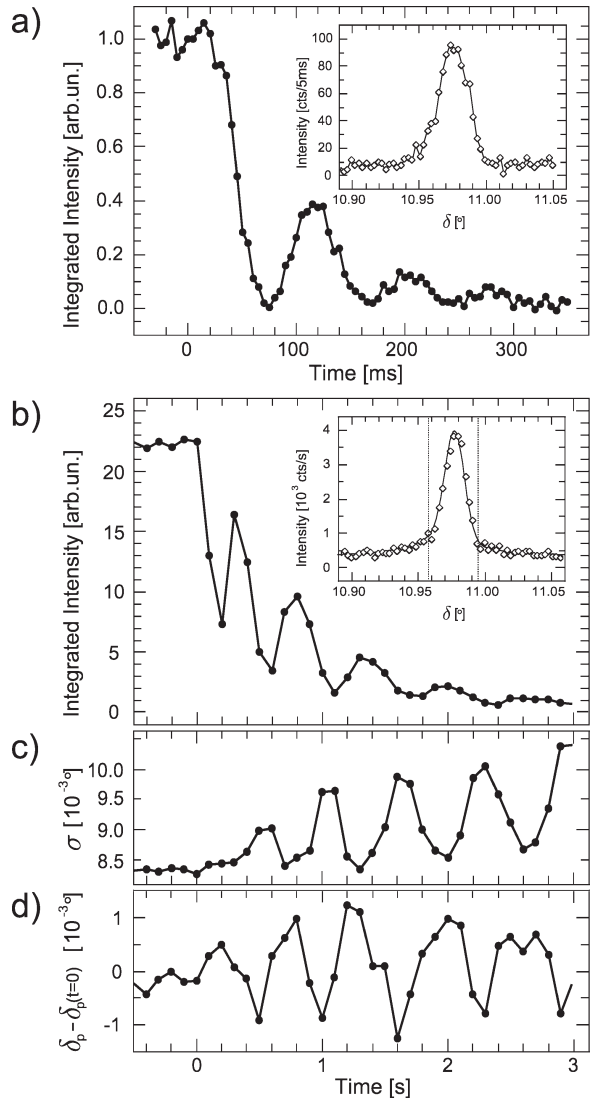

Figure 2. *in situ* SXS intensity of Au(001) in 0.1 M HCl + 0.5 mM $HAuCl_4$ at (1,1,0.1) during potential steps from 0.6 to (a) 1.07 (200 frames/s) and (b−d) 0.99 V (10 frames/s), showing growth oscillations in the Au dissolution regime (filled circles). Insets show selected single frames of the 1D detector obtained at (a) t = 15 ms and (b) t = 1.9 s (the dashed line indicates the limited range used for the determination of σ and δ_p). In addition, for the step to 0.99 V, (c) the peak width σ and (d) the peak position δ_p of the (1,1,0.1) peak are shown.

Each frame of the 1D detector provides not only the integrated peak intensity but also additional structural information with the same temporal resolution. This is illustrated by results of a dissolution experiment at 0.99 V (recorded with 100 ms/frame to improve the counting statistics), where in addition to the peak intensity the peak position δ_p and peak width σ were determined as a function of dissolution time (Figure 2b−d). Due to a slight asymmetry in the peak shape (see below), the latter two values were determined by calculating the first and second moment (mean value and its standard deviation, respectively) of the δ-dependent intensity distribution (limited to the range indicated by the dashed lines in the inset in Figure 2b to reduce the effect of the broad background peak). Fits of the peak by a Gaussian resulted in peak positions and heights with a qualitatively very similar behavior; i.e., the results discussed below are robust with respect to the analysis method.

As clearly visible, not only the intensity but also the width of the CTR peak oscillate in the dissolution regime (Figure 2c), with maxima and minima in intensity corresponding to particularly narrow and broad peaks, respectively. The oscillating peak width indicates the changes in the size of the coherently scattering regions on the sample surface and agrees well with expectations for layer-by-layer growth: at maxima in intensity, the topmost layer is approximately closed (coverage close to 1) and the X-ray correlation length is determined (apart from the instrumental resolution) by the average size of the terraces between atomic steps in the substrate. In contrast, the minima in intensity correspond to a surface covered by approximately half a monolayer of Au etch pits ("vacancy islands"), and the correlation length is given by the average size of the pits and the (comparably sized) areas between them. The correlation length hence is significantly smaller than the terrace size, resulting in a larger peak width.

Also the peak position δ_p oscillates in-phase with the peak intensity, indicating oscillations in the lattice spacing (Figure 2d). This behavior can be rationalized by an in-plane lattice expansion in the topmost Au layer at partial coverage. Under these conditions, the finite extension of the remaining Au islands between the etch pits allows lateral relaxation. From the minima in δ_p, a strain of the order of 10^{-4} is calculated for the experiment in Figure 2b. Similar observations with even larger lattice expansions were reported for vapor-phase Cu(001) homoepitaxial growth.[15] A more detailed analysis suggests the presence of two overlapping peaks at slightly different positions, resulting in an asymmetric peak shape. A similar behavior was reported previously in SXS studies of vapor-phase epitaxial growth.[16] The peak asymmetry also oscillates in-phase with the intensity oscillations (manifested in oscillations in the third moment of the intensity distribution), indicating different responses of the two peaks to the morphological changes during dissolution. A more detailed quantitative analysis of such effects will be presented elsewhere.

These preliminary studies illustrate the potential of *in situ* SXS for gaining detailed structural information on the growth interface during realistic deposition conditions. In fact, a clear diffraction peak at (1,1,0.1) was even observable at an acquisition rate of 500 Hz, which means that *in situ* measurements at deposition or dissolution rates up to 100 ML/s are, in principle, feasible. Systematic studies of this type will provide fundamental insight into technologically relevant electrochemical processes. Furthermore, they will allow experimental testing of the applicability of modern growth theories to electrochemical deposition and dissolution processes.

AUTHOR INFORMATION

Corresponding Author
magnussen@physik.uni-kiel.de

Present Addresses
[§]Department of Chemical Engineering, National Cheng Kung University, Tainan 70101, Taiwan.
[#]The School of Chemistry, The University of Manchester, Oxford Road, Manchester M13 9PL, UK.

Journal of the American Chemical Society COMMUNICATION

■ ACKNOWLEDGMENT

We thank the DFG for financial support via MA1618/13-3 and the staff of ID 32 for technical assistance. We acknowledge the European Synchrotron Radiation Facility for provision of synchrotron radiation facilities.

■ REFERENCES

(1) Itaya, K. *Prog. Surf. Sci.* **1998**, *58*, 121.
(2) Magnussen, O. M.; Behm, R. J. *J. Electroanal. Chem.* **1999**, *467*, 258.
(3) Andricacos, P. C.; Uzoh, C.; Dukovic, J. O.; Horkans, J.; Deligianni, H. *IBM J. Res. Develop.* **1998**, *42*, 567.
(4) Venables, J. A.; Spiller, G. D. T.; Hanbrücken, M. *Rep. Prog. Phys.* **1984**, *47*, 399.
(5) Brune, H. *Surf. Sci. Reports* **1998**, *31*, 121.
(6) Rosenfeld, G.; Poelsema, B.; Comsa, G. In *Growth and properties of ultrathin epitaxial layers*; King, D. A., Woodruff, D. P., Eds.; Elsevier Science B.V.: Amsterdam, 1999; Vol. 8, p 66.
(7) Polewska, W.; Behm, R. J.; Magnussen, O. M. *Electrochim. Acta* **2003**, *48*, 2915.
(8) Divisek, J.; Steffen, B.; Stimming, U.; Schmickler, W. *J. Electroanal. Chem.* **1997**, *440*, 169.
(9) Skylar, O.; Treutler, T. H.; Vlachopoulos, N.; Wittstock, G. *Surf. Sci.* **2005**, *597*, 181.
(10) Krug, K.; Stettner, J.; Magnussen, O. M. *Phys. Rev. Lett.* **2006**, *96*, 246101–1.
(11) Kaminski, D.; Krug, K.; Golks, F.; Stettner, J.; Magnussen, O. M. *J. Phys. Chem. C* **2007**, *111*, 17067.
(12) Krug, K.; Kaminski, D.; Golks, F.; Stettner, J.; Magnussen, O. M. *J. Phys. Chem. C* **2010**, *114*, 18634.
(13) Magnussen, O. M.; Krug, K.; Ayyad, A. H.; Stettner, J. *Electrochim. Acta* **2008**, *53*, 3449.
(14) Ye, S.; Ishibashi, C.; Uosaki, K. *Proc. Electrochem. Soc.* **2000**, *PV2000-35*, 133.
(15) Fassbender, J.; May, U.; Schirmer, B.; Jungblut, R. M.; Hillebrands, B.; Güntherodt, G. *Phys. Rev. Lett.* **1995**, *75*, 4476.
(16) Braun, W.; Kaganer, V. M.; Jenichen, B.; Satapathy, D. K.; Guo, X.; Tinkham, B. P.; Ploog, K. H. *J. Cryst. Growth* **2005**, *278*, 449–457.

5 Surface Structure of Copper Electrodes in Chloride-Containing Electrolyte

The interaction of halide ions with metal surfaces is of great interest both for scientific and technological reasons [25]. For instance, the adsorption behavior and adlayer structure of chloride on copper electrode surfaces is of central importance for technological processes related to the fabrication of metal interconnections in modern microelectronic devices [187, 188] (*cf.* Introduction). Manifold studies of the atomic-scale structure of specifically adsorbed halide ions on different metal single crystal surfaces, performed in ultra-high vacuum (UHV) as well as electrochemical environment, have been carried out using *ex situ* and *in situ* structure-sensitive techniques, electrochemical methods as well as theoretical methods (*e.g.* [25, 83, 84, 188–196]).

These studies revealed in detail the complex, potential-dependent two-dimensional adlayer phase behavior, which is known to significantly influence electrochemical reactions such as electrochemical deposition, dissolution, corrosion, and electrocatalytic processes [25]. The addition of chloride ions to acidic Cu-ion-containing electrolytes, for example, leads to an increase in the copper deposition rate proportional to the added concentration [197, 198]. This effect is assumed to be caused by an enhanced electron transfer reaction caused by inner sphere bridge bondings which result from the adsorption of the Cl^- species at the surface [196, 197].

In general, a vast variety of halide adlayer structures were reported, including simple low-order commensurate superstructures, commensurate structures with larger unit cells, uniaxial-incommensurate structures, as well as entirely incommensurate superstructures (reference [25] and references therein). The latter two are typically accompanied by electrocompression effects, *i.e.*, the halide adlayer lattice spacing depends on the applied electrode potential. Surprisingly, quite often the adlayer structures observed in UHV and electrochemical environment resemble each other, although pronounced differences in the charge distribution in vicinity of the surface are expected, *e.g.*, due to the presence of physisorbed species such as coadsorbed water or cations in electrochemical environment [199,200]. Studies, which directly compare structural data measured likewise for interfaces in electrochemical environment and their equivalent under UHV conditions, are still seldom [201–206]. Such a comparative study will be presented in the subsequent section for the Cu(001)-Cl system. Beyond highly precise atomic-scale structural data on the potential-dependent chloride adlayer, this study contributes to the understanding of how the presence of the outer part of the double layer alters the chemical bonding of the chemisorbed inner adsorbate layer to the surface and the near surface structure of the metal electrode. This, in turn, may develop a better understanding of the complex interplay among the interactions of the various species at the interface, the charge distribution, and the interface structure.

Typical copper electroplating baths, *e.g.*, used in the damascene process (*cf.* Introduction and section 1.4.5), contain between 0.2 and 1.5 mM concentration of chloride ions [10].

Significantly higher concentrations than 1 mM Cl^- in the solution may exceed the solubility product of $CuCl_{solid}$, resulting in its precipitation at the interface [207–209]. In the potential regime which is of relevance for the damascene process, the low index surfaces Cu(001), Cu(110), and Cu(111) exhibit well-defined, densely packed Cl^- adlayers [25,83,85,210–214], as will be discussed in the following two sections. The importance of these adlayer structures for the electrodeposition process of copper is reflected in the strong influence of the ordered adlayer on surface step orientations during growth and subsequent coarsening [25, 85, 210–214]. For instance, Wu and Barkey reported in an AFM study that the fourfold symmetry of the chloride adsorbate in case of Cu(001) stabilizes planar regions on the surface, which are separated by steps along the {100} direction, giving rise to the formation of pyramidal mounds and blocks [87, 88]. This faceted growth was explained by a pronounced anisotropy of the step edge energies and the appropriate activation energy for the corresponding adatom surface transport processes caused by the chloride adlayer (*cf.* figure 5.2).

Moreover, under chemical conditions employed for copper superconformal growth, *i.e.*, in presence of the organic additive polyethylene glycol (PEG) (*cf.* sections 1.4.4, 1.4.5 and chapter 7), the chloride adlayers play a key role as they seem to act as the bridging ligand between PEG and the electrode surface [215] and consequently allow for the formation of the deposition reaction inhibiting film [10,98–102,216,217]. A more fundamental understanding of the chloride adlayer structure, its formation, potential-dependence and nature of binding will thus not only deliver deeper insight into the copper electrodeposition process, but also into the interrelation of the chloride adlayer and the organic additives used in the damascene plating process. The study of the interdependence of chloride and PEG adsorption as well as of the influence of the inhibiting PEG/chloride-complex on the atomic-scale processes during copper homoepitaxial electrodeposition is subject of chapter 7.

Thus, in order to achieve a better understanding of halide adsorption on metals and especially the interactions that influence the observed structures, high-precision data on the potential-dependent structure of the adlayers are required. The investigation of the Cu(001) surface in chloride-containing electrolyte, which will be presented in the subsequent section, serves as the base with respect to the growth studies performed in the scope of this work (chapters 6 and 7). In addition, an *in situ* SXRD study of chloride adsorption on the Cu(111) electrode surface will be presented in section 5.2, focusing on the (potential-dependent) in-plane structure of the ordered Cl^- adlayer.

The attempt to investigate the chloride adlayer structure on the third low-index copper surface, Cu(110), in electrolyte containing 1 mM HCl (pH value of 3) was hampered by the formation of crystalline copper oxide. This is somehow surprising, as according to Pourbaix [209], the equilibrium potentials for the possible oxidation reactions, given in equation (5.1), are much higher than the maximal applied potential of -0.11 V in the experiments. Thus, no oxide phases of Cu are expected to be stable at the potentials applied during the measurements.

$$\begin{aligned} 2Cu_{solid} + H_2O &\rightleftharpoons Cu_2O + 2H^+ + 2e^- \qquad E_{eq.} = 96.7\,mV \\ Cu_{solid} + H_2O &\rightleftharpoons CuO + 2H^+ + 2e^- \qquad E_{eq.} = 195.7\,mV \end{aligned} \tag{5.1}$$

A detailed description both of the experiments and the results are given in reference [218].

5.1 Surface Structure of Cu(001) in Chloride-Containing Electrolyte

Most halide adlayers on (001) oriented fcc crystals exhibit a commensurate c(2×2) structure, where the adsorbates reside in the energetically strongly preferred fourfold-hollow sites of the metal substrate lattice [195, 219–223]. Due to its importance for the copper electrodeposition process, the adsorption of Cl on Cu(001) is an extensively studied example of such a c(2×2) adlayer. It has been reported for chloride adlayers under UHV conditions [84, 224–230] as well as in chloride-containing electrolytes [85, 158, 203, 204, 231]. The first observations of the existence of the c(2×2) chloride adlayer structure on Cu(001) in HCl solution, at electrode potentials below the onset of dissolution, have been reported by Suggs and Bard [231], based on *in situ* STM measurements. Vogt *et al.* additionally observed the (1×1) substrate at potentials more negative than -0.4 V [86], suggesting either chloride adsorption or a potential-induced phase transition from a dilute adlayer of highly mobile chloride ('lattice gas') to an ordered c(2×2)-Cl structure with increasing potential [85, 86]. In figure 5.1, 3D STM images of the Cu(001) equilibrium surface structure at -0.21 V are shown, recorded in 1 mM HCl (taken from ref. [85]). The long-range surface morphology exhibits extremely straight steps, which are oriented with an angle of 90° with respect to each other (a). The high-resolution image of the atomic structure shows that the step edges are well aligned with the c(2×2) structure, *i.e.*, the step edges lie in the [010] and [100] directions (b). According to Vogt and coworkers, the local step edge positions are rather stable, on time scales of several minutes, in contrast to a much higher mobility of atoms at the step edges in case of the (1×1) phase (estimated 3-4 orders of magnitude higher).

As depicted in the model in figure 5.2, the c(2 × 2) chloride adlayers on top of the two shown terraces are phase shifted with respect to each other. This results in an antiphase

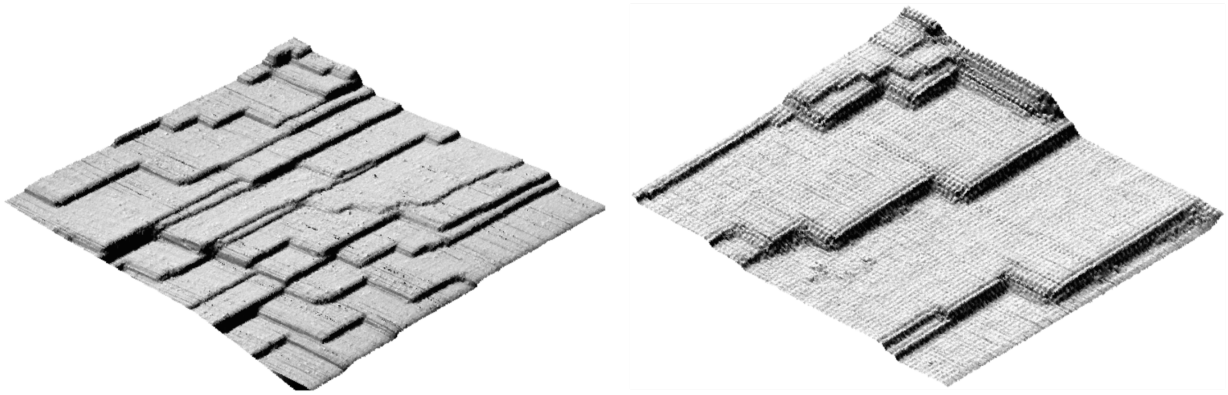

(a) **(b)**

Figure 5.1: *In situ* STM images of the Cu(001) surface in 1 mM HCl at -0.21 V electrode potential (after waiting for 3 h), taken from reference [85]. The observed surface morphology shows the c(2×2) chloride adlayer structure which is present at this potential. (a) Overview image showing extremely straight steps (740 Å × 740 Å, $I_t = 2.3$ nA). (b) The image of the atomic-scale structure reveals that the step edges are well-aligned with the c(2×2) Cl adlayer along the [010] and [100] directions (260 Å × 260 Å, $I_{tunnel} = 4.8$ nA). Credit [232].

shifted alignment of chloride rows on both sides of the [010]-oriented step and an in-phase alignment of chloride rows on both sides of the [100]-oriented step or vice versa. The obtained difference in the structure in vicinity of the step edges, specifically the different coordination of copper and chloride atoms at these sites, yields an anisotropy in the step edge energies and the appropriate activation energies for adatom surface transport processes across the step edges. Consequently, the ordered chloride adlayer is expected to strongly influence growth and dissolution processes, *e.g.*, observable in the aforementioned faceted growth reported by Wu *et al.* [88].

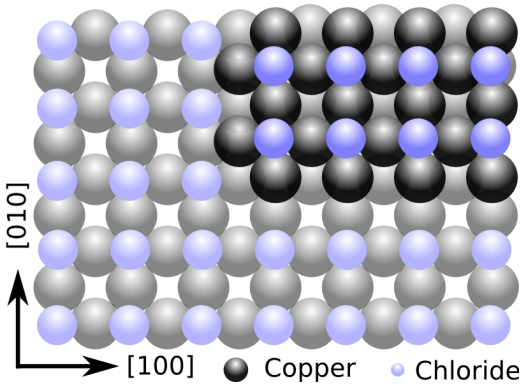

Figure 5.2: Schematic model of two Cu(001) terraces covered by the c(2 × 2) chloride adlayer. The phase shift of the adlayer on the lower terrace (light colors) with respect to the adlayer on the upper terrace (dark colors) results in a strong anisotropy of the [100]- and [010]-oriented step edges.

In the following work, detailed *in situ* SXRD and complementary DFT results on the adsorption behavior and interface structure of Cu(001) electrodes in chloride-containing electrolyte will be presented. In addition to the investigation of the potential-induced chloride adlayer structural changes, also the surface-normal interface structure of the c(2×2) adlayer and the substrate, studied by CTR measurements, will be discussed. Specifically, the results of these studies in electrochemical environment, performed in presence of the ordered and the disordered adlayer, are directly compared with corresponding data recently reported by Tolentino *et al.* for the chloride/Cu(001)-system under UHV conditions [233].

PHYSICAL REVIEW B **81**, 174114 (2010)

Reversal of chloride-induced Cu(001) subsurface buckling in the electrochemical environment: An *in situ* surface x-ray diffraction and density functional theory study

Y. Gründer, D. Kaminski,* F. Golks, K. Krug, J. Stettner, and O. M. Magnussen
Institut für Experimentelle und Angewandte Physik, Universität Kiel, Olshausenstr. 40, 24098 Kiel, Germany

A. Franke, J. Stremme, and E. Pehlke
Institut für Theoretische Physik und Astrophysik, Universität Kiel, Olshausenstr. 40, 24098 Kiel, Germany
(Received 20 October 2009; published 20 May 2010)

The interface of Cu(001) electrode surfaces in 10 mM HCl solution was studied by *in situ* surface x-ray diffraction and density functional theory, focusing on the precise structure of the $c(2\times2)$ Cl adlayer formed at positive potentials. Crystal truncation rod measurements in this adsorbate phase at a potential of −0.20 $V_{Ag/AgCl}$ reveal distinct differences to corresponding data by Tolentino *et al.* [Surf. Sci. **601**, 2962 (2007)] for the $c(2\times2)$ Cl structure formed at the Cu(001)-vacuum interface. Although in both environments, the atoms in the second Cu layer exhibit a small vertical corrugation, the sign of this corrugation is reversed. Furthermore, also the Cu-Cl bond distance and the average Cu interlayer spacings at the surface differ. *Ab initio* calculations performed for this adsorbate system reproduce these effects—specifically the reversal of the subsurface second-layer buckling caused in the presence of coadsorbed water molecules and cations in the outer part of the electrochemical double layer. In addition, studies at more negative potentials reveal a continuous surface phase transition to a disordered Cl adlayer at −0.62 $V_{Ag/AgCl}$, but indicate a substantial Cl coverage even at the onset of hydrogen evolution.

DOI: 10.1103/PhysRevB.81.174114 PACS number(s): 61.05.cf, 68.08.−p, 68.43.−h, 71.15.Mb

I. INTRODUCTION

The atomic-scale structure of the metal-electrolyte interface is a topic of central importance to interfacial electrochemistry and has been studied extensively by electrochemical measurements, structure-sensitive *in situ* techniques, as well as by theoretical methods. In particular, adsorbate layers of strongly chemically bound ("specifically adsorbed") anions, such as halide or sulfate, have been investigated in great detail, revealing a complex, potential-dependent two-dimensional (2D) phase behavior, which can significantly affect electrochemical reactions such as galvanic deposition, etching, corrosion, and electrocatalytic processes.[1] Often very similar superstructures are observed as those found in studies under ultrahigh vacuum (UHV) conditions after adsorption of the corresponding gaseous species from the gas phase. Nevertheless, complete structural agreement is not expected since in electrochemical environment the presence of physisorbed species in the so-called diffuse double layer—notably coadsorbed water and cations—leads to pronounced changes in the electrostatic potential drop at the interface, as revealed by UHV model studies on simulated double layers.[2,3] The precise influence of these effects on the interface structure is still unclear. Specifically, up to now only a few studies have presented detailed measurements of the bond lengths at electrochemical interfaces that could be directly compared to structural data on corresponding anionic adlayer structures under UHV conditions.[4–9] Such comparative studies allow to clarify how the presence of the outer part of the double layer alters the chemical bonding of the chemisorbed inner adsorbate layer to the surface and the near surface structure of the metal electrode, which in turn may throw light on the interplay among the interactions of the various species at the interface, the charge distribution, and the interface structure. Here we present a combined surface x-ray diffraction (SXRD) and density-functional theory (DFT) study of Cu(001) in hydrochloric acid which reveals that the presence of water and cations in the outer double layer not only introduces relaxations in the spacing of the chemisorbed chloride and the first metal layers but also a reversal of a subsurface lattice modulation as compared to that observed in UHV. For better understanding of the structural differences in UHV and in electrochemical environment, we estimate the difference of the work function introduced by the electrolyte and discuss its influence on the structure of the adsorbate complex.[10]

Halide adlayers in electrochemical environment[1] as well as the corresponding halogen adlayers formed in the gas phase[11] adsorb on the (001) surface of most fcc metals in form of a simple low-order commensurate $c(2\times2)$ structure with $P4mm$ symmetry, where the adsorbates reside in the energetically strongly preferred fourfold-hollow sites of the metal substrate lattice.[12–15] A prototypical system for halide adsorption on fcc(001) surfaces and for which the adsorption process has been studied by SXRD and by electrochemical methods is Br on Ag(001).[10,16,17] For increasing potential a second-order phase transition from a lattice gas to an ordered $c(2\times2)$ structure has been found for the bromine adlayer. Also the adsorption of Cl on Cu(001) is an important, well-studied example of this $c(2\times2)$ adlayer. It has been reported for chlorine adlayers under UHV conditions[18–25] as well as in chloride-containing electrolytes.[6,7,26–31] However, at the electrochemical interface the $c(2\times2)$ structure was observed only positive of a critical potential (−0.4 $V_{Ag/AgCl}$ at a Cl concentration of 10^{-3} M) by *in situ* STM, whereas at more negative potentials the (1×1) substrate lattice was visible, suggesting a potential-induced order-disorder phase transition into a dilute adlayer of highly mobile chloride.[28,30] More

recently, the surface-normal interface structure of the $c(2\times2)$ adlayers of Cl and Br on Cu(001) was studied by *in situ* SXRD, focusing on the halide-copper interlayer spacing.[6,7] Specifically, the dependence of the Br adlayer spacing on potential was found to be stronger than that of the Cl adlayer, which was attributed to a more ionic character of the Cl and an almost discharged Br adsorbate, respectively. Similar SXRD measurements of Cl on Cu(001) surfaces under UHV conditions by Tolentino *et al.*[18] as well as earlier angle-resolved photoemission studies by Wang *et al.*[32] indicated that the $c(2\times2)$ superstructure extends to the second atomic copper layer in form of a small subsurface buckling, an effect that was also reported for the $c(2\times2)$ Br adlayer in the *in situ* SXRD study by Saracino *et al.*[6,7]

In this work we present detailed *in situ* SXRD and complementary DFT results on the adsorption behavior and interface structure of Cu(001) electrodes in chloride-containing electrolyte, focusing on the buckling in the second Cu layer. These studies allow to directly compare the Cu surface structure in the presence of the $c(2\times2)$ Cl adlayer and after disordering and partial desorption of the Cl with corresponding data for Cl-covered and clean Cu(001) surfaces under UHV conditions, respectively. In particular, the influence of the electrochemical environment on the copper subsurface buckling will be discussed. As reference for the surface structure of the $c(2\times2)$ Cl adlayer at the Cu(001)-vacuum interface we will use the recent SXRD study by Tolentino *et al.*[18] SXRD provides direct, highly accurate structural data that can be modeled on the basis of simple kinematic diffraction theory. Results by this technique therefore seem more reliable than those obtained by electron diffraction methods, where more complex modeling by dynamic scattering theory is required.

II. EXPERIMENTAL

A. Surface x-ray diffraction

The x-ray scattering experiments were performed at the ID 32 beamline of the European Synchrotron Radiation Facility in Grenoble using a photon energy of 22.5 keV and a grazing incidence angle of 0.44°. The Cu(001) single-crystal sample (Mateck, 99.999%, 4 mm diameter, miscut $<0.1°$) was prepared prior to the experiments by electropolishing in 70% orthophosphoric acid. Subsequently, the sample was covered by a droplet of milli-Q water and mounted into the electrochemical hanging meniscus cell described in Ref. 33. In all experiments 10 mM HCl solution prepared from suprapur hydrochloric acid (Merck) and milli-Q water was used as electrolyte. All potentials were measured versus a Ag/AgCl (3 M KCl) reference electrode. During the measurements the liquid meniscus in contact with the surface was kept under high-purity nitrogen (air liquid, 99.999%) to remove dissolved oxygen from the electrolyte.

In the crystal truncation rod (CTR) studies the integrated intensities $|F_{hkl}|^2$ (where F_{hkl} is the structure factor) of different reflections (hkl) were measured in z axis geometry by rotating the sample about its surface normal. The background-subtracted integrated intensities were corrected for the Lorentz factor, polarization factor, active sample area, and the rod interception appropriate for the z axis geometry.[34] Since the specular rod was recorded in $(\theta\text{-}2\theta)$ geometry, for which different corrections for the active sample area and the rod interception have to be applied than for the nonspecular CTRs, its intensity distribution had to be corrected by an additional scaling factor. Errors due to photon statistics and systematic errors in data acquisition are taken into account. The latter was estimated from deviation of measured integrated intensities of symmetry equivalent reflections to 20% and is the dominating contribution. The structure was determined by a fit of the simulated square of the structure factors to the experimental ones and a χ^2 minimization using the code "fit" (Ref. 35) which allows a three dimensional structural refinement of the SXRD data.[36–38] *The parameter error* Δx *of the best fit value* x *is determined by* $\chi^2(x+\Delta x)=\chi^2(x)+1$.

Standard bulk coordinates of the Cu(0 0 1) surface ($a_1=a_2=a_3=3.615$ Å, $\alpha=\beta=\gamma=90°$) are used in the following. The momentum-transfer vector is then defined by $Q=Hb_1+Kb_2+Lb_3$ with $a_ib_i=2\pi\delta_{ij}$ where H, K, L, are the diffraction indices. The index L is along the direction perpendicular to the surface. The indices of the crystal truncation rods are given by $(H+K=2n)$ and the ones for rods from the reconstructed surface are determined by $(H+K=2n+1)$.

B. Density functional theory

The density functional theory (DFT) calculations were performed using the Vienna *ab initio* simulation program (VASP) developed at the Institut für Materialphysik of the Universität Wien.[39–42] The generalized gradient approximation by Perdew and Wang (PW91-GGA) (Ref. 43) is applied to the exchange-correlation energy-functional. All atoms except Ca are described by projector augmented wave (PAW) pseudopotentials as introduced by Blöchl *et al.*[44] Ca atoms are described by ultrasoft pseudopotentials. The potentials for VASP from the database are used.[45]

The Cu(001) surface is simulated by a slab geometry with a supercell containing 15 Cu layers and a $p(2\times2)$ surface unit cell. The theoretical lattice constant for Cu of $c=3.636$ Å is assumed, which is slightly larger than the experimental lattice constant $c=3.615$ Å. The Cl atoms are adsorbed on both sides of the slab forming a $c(2\times2)$ superstructure, with the Cl atoms occupying hollow positions of the Cu(001) surface. The kinetic-energy cutoff of the plane-wave basis set has been chosen equal to 280 eV, and the integrals over the Brillouin zone are approximated by sums over special **k** points. We use a 6×6 Monkhorst-Pack set of equidistant **k** points[46] parallel to the surface. Atomic positions were relaxed until the residual forces acting on the Cu and Cl atoms are less than 1 meV/Å. The maximum allowed residual force has been chosen rather small because the atomic displacements of interest in this work are only of the order of few mÅ. In this way, the surface structure under UHV conditions can be calculated.

The Cu(001)-$c(2\times2)$ Cl surface becomes much more difficult to describe when in contact with an electrolyte. Different approaches to simulate electrochemical interfaces have been developed and are described in the literature.[7,47–52] Here

we follow two different simple approaches in order to obtain a qualitative impression of the effects on the Cu surface relaxation induced by the presence of the electrolyte: (i) a homogeneous electric field of the order of 0.3–0.9 V/Å is applied perpendicular to the slab[53] to simulate the electric field in the Helmholtz layer. In the bulk the electric field is screened by the induced surface charge density. The electrostatic potential has a discontinuity in the middle of the vacuum region. In this way the perturbing potential can be taken to be periodic. We monitor the additional displacement of the Cl and the Cu atoms induced by the electric field together with its induced screening charge density. (ii) Following the method described (and already applied to Cu(001)/halogen/electrolyte interfaces) by Saracino *et al.*,[7] two Ca atoms are placed in the middle of the vacuum region within each supercell. They are located atop the two Cl atoms in the $p(2\times2)$ surface unit cell, but in view of the large separation between the Ca and the surface atoms we expect displacement of the Ca atoms parallel to the surface to be of only minor importance for the effects investigated here. Electrons are transferred from the Ca atomic layer to the metal-halogen slab. This charge transfer results in an electric field in front of the metal. Furthermore, two pairs of water molecules, located on top of each other, have been added to each side of the slab. As in Ref. 7, the H-atoms point toward the surface, and the O atoms lie above the Cl atoms. During the subsequent relaxation, the Cl atoms and the Cu atoms in the outermost six layers of the slab as well as the H and O atoms of the water molecule are allowed to move, with each O-atom being restricted to an axis perpendicular to the surface. The residual forces acting on the water molecules are less than 3 meV/Å. In order to control the pressure exerted on the surface, calculations have been carried through for different thickness of the region between the slabs.

III. RESULTS

A. Surface x-ray diffraction

In the initial phase of the experiments the Cu(001) surface was characterized by cyclic voltammetry, recorded in the SXRD cell, and parallel measurements of the scattered x-ray intensity at selected positions along the substrate's CTRs and $c(2\times2)$ superstructure rods (Fig. 1). Specifically, the potential-dependent intensity at (1, 0, 0.1) and (1, 1, 0.1), i.e., the $c(2\times2)$ superstructure rod and the anti-Bragg position of the lowest-order Cu(001) CTR, was monitored. The intensity measured at (1, 0, 0.1) is proportional to the square of the coverage of the Cl induced $c(2\times2)$ superstructure, whereas data monitored at the anti-Bragg position (1, 1, 0.1) is sensitive to the coverage of all Cu-hollow sites occupied with Cl atoms, independent of the degree of order.[17] Recording the potential dependent intensity of both the superstructure rod and the anti-Bragg position is therefore indispensable to determine independently the coverages for both adlayer phases, the two-dimensional lattice gas as well as the Cl $c(2\times2)$ superstructure. In the voltammogram, Cl adsorption and desorption manifests in form of broad peaks between ≈−0.35 V and the onset of hydrogen evolution near −0.70 V (the additional cathodic current in this potential range may be related to the reduction of small amounts of residual oxygen in the cell). During the chloride adsorption process the intensity at the anti-Bragg position decreases while the intensity at the superstructure rod increases from zero at the negative potential limit to a saturation value at potentials positive of ≈−0.35 V. Potential-step experiments show that the intensity change occurs on time scales shorter than the time resolution of the SXRD experiments (0.5 s) and is highly reversible (as also seen in the potential-sweep experiment in Fig. 1). Such a behavior can only be attributed to the desorption and disordering of the chloride adlayer, whereas other structural changes such as potential-induced variations in the surface roughness can be excluded. Furthermore, no evidence of other ordered Cl adlayer structures was found in in-plane scans along high-symmetry directions. The latter as well as the absence of potential-induced surface roughening is in excellent agreement with the extensive previous *in situ* STM studies of this system.

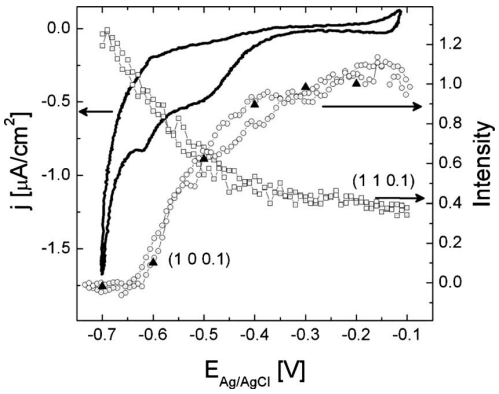

FIG. 1. Cyclic voltammogram (scan rate 10mV/s) of Cu(001) in 10 mM HCl (solid line) as well as potential-dependent intensity of the Cl superstructure rod at (1, 0, 0.1) and the Cu CTR at (1, 1, 0.1). In addition, the intensities measured after a step from −0.2 V to different potentials are indicated (filled triangles).

According to these measurements, residual $c(2\times2)$ ordering exists down to potentials close to the onset of hydrogen evolution and only completely disappears at −0.62 V. This $c(2\times2)\leftrightarrow(1\times1)$ transition manifests in form of small peaks in the cyclic voltammogram and occurs at substantially more negative potentials than those where the $c(2\times2)$ structure was observed by *in situ* STM.[28,30] The latter most likely is caused by a high adsorbate mobility in the potential regime where the surface is only partially covered by the ordered adlayer structure, inducing rapid fluctuations in the $c(2\times2)$ domain network on time scales beyond the temporal resolution in the earlier STM studies. Indeed, in very recent *in situ* video-STM observations positional changes of the Cl adsorbates at domain boundaries faster than 10^{-4} s were inferred.[54] The intensity curves at (1, 0, 0.1) and (1, 1, 0.1) are identical for potential sweeps in positive and in negative direction, indicating a highly reversible process as expected for anion adsorption. Furthermore, in potential jump experiments the same steady-state intensities were obtained after the potential step (Fig. 1, filled triangles), typically faster than the experimental time resolution (1 s). Consequently,

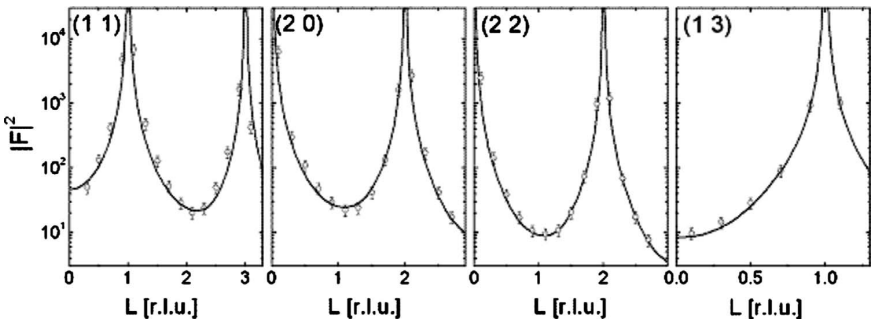

FIG. 2. Experimental crystal truncation rods of Cu(001) in 10 mM HCl at −0.70 V (circles) and best fit based on a relaxed bulk like structure (lines).

the curves in Fig. 1 represent the potential-dependent equilibrium state of this adsorbate system.

These results are at variance with recent SXRD experiments on Cu(001) in Br-containing solution by Saracino *et al.*[7] In that study the intensity at (1, 0, 0.1) on the superstructure rod was found to be nearly constant over the entire double layer potential range, even at negative potentials, where the corresponding voltammogram exhibited similar Br adsorption and desorption peaks as visible in Fig. 1. The reason for this discrepancy, not only to our SXRD results but also to the electrochemical and previous *in situ* STM data,[28] is currently unclear. However, the behavior observed in this study is almost identical to that found by *in situ* SXRD for bromide and chloride adsorption on Ag(001) electrodes, where likewise a continuous order-disorder transition to a $c(2\times2)$ phase with very similar x-ray intensity curves was reported.[10,16,17] Specifically, for Br on Ag(001) the intensity at (1, 1, 0.1) was found to increase toward more negative potentials, as in the system studied here, reaching a saturation value only 300 mV negative of the potential where the $c(2\times2)$ superstructure peak disappeared. This behavior was attributed to the presence of a disordered 2D lattice gas of adsorbates which partly occupy fourfold hollow and partly other adsorption sites. Also for Cl on Cu(001) an analogous lattice gas most likely exists negative of the phase transition potential, although the complete desorption of the anion adlayer apparently only occurs deep within the hydrogen evolution regime and hence was not accessible in the SXRD experiments. The chloride desorption process on Cu(001) with a remaining $c(2\times2)$ structure is stretched over a range of 300 mV, whereas the Br desorption process on Ag(001) with a remaining $c(2\times2)$ structure only takes place over a potential range of 200 mV. This indicates that the desorption process is slower for Cl on Cu(001) than for Br on Ag(001) which can be explained by the less noble character of the copper substrate compared to silver and the higher ionicity of the chloride compared to bromide inducing a stronger binding with larger attractive interaction between the substrate and adsorbate.

Detailed studies of the interface structure were performed at −0.20 V, where the surface is fully covered by the $c(2\times2)$ Cl superstructure (Fig. 2), and at −0.70 V, i.e., ≈100 mV negative of the order-disorder phase transition potential (Fig. 3). At both potentials we measured the (1, 1, *L*), (2, 0, *L*), (2, 2, *L*) and (1, 3, *L*) CTRs and obtained a set of 48 nonequivalent reflections. At −0.20 V in addition the specular rod and the (1, 0, *L*) and (1, 2, *L*) superstructure rods were recorded, with in total 44 integrated intensities $|F_{hkl}|^2$ at nonequivalent reciprocal space positions (hkl). The *L* dependent diffuse background of the (1, 0, *L*) superstructure rod was determined carefully and subtracted. Due to the errors associated with this procedure, the errors of the integrated intensities of the (1, 0, *L*) rod increase at lower *L*. The integrated intensities of the rods recorded at the two different potentials were taken in the same geometry on the same sample. The CTR data at both potentials is fully consistent with the potential dependence of the x-ray intensity shown in Fig. 1.

The CTRs obtained at −0.70 V were fitted to a structural model assuming a Cu(001)-(1×1) surface and a relaxation of the layer spacing d_{12} between the copper surface layer and the underlying bulk lattice (for all following Cu layers the Cu bulk spacing was used). In addition, the anisotropic Debye-Waller factors for the first two Cu layers, an isotropic Debye-Waller factor for the third layer and an overall scale factor were optimized in the fit. In analogy to the Br/Ag(001) adsorbate system[10,16] a partial occupation of the fourfold-hollow sites with Cl adsorbates was assumed to model the disordered 2D lattice gas of chloride. Models without this disordered Cl adlayer also provided good fits of the experimental data and resulted in very similar vertical relaxations, but led to unusually small Debye-Waller factors of the Cu surface layer. The parameters for the best fit ($\chi^2=2.37$), which describes well the measured CTRs (Fig. 2, solid lines), are shown in Table I, together with the parameters obtained in SXRD measurements by Mironets *et al.* for a bare Cu(001) surface in UHV.[55] The Cl coverage 80 mV negative of the order-disorder transition is 0.15 ML which is in good agreement with the values found for Br on Ag(001) (Refs. 10 and 16) at corresponding potentials, i.e., 55 mV negative of the order-disorder transition taking into account the broader desorption regime of the chloride. However, this observation differs strongly from the zero coverage reported by Huemann *et al.* for the same system at the negative end of the double layer regime.[6] In the latter study a decrease rather than an increase in the intensity at (2, 0, *L*) was found toward negative potentials, contrary to our experimental data. This is probably the main cause of the different results in that study.

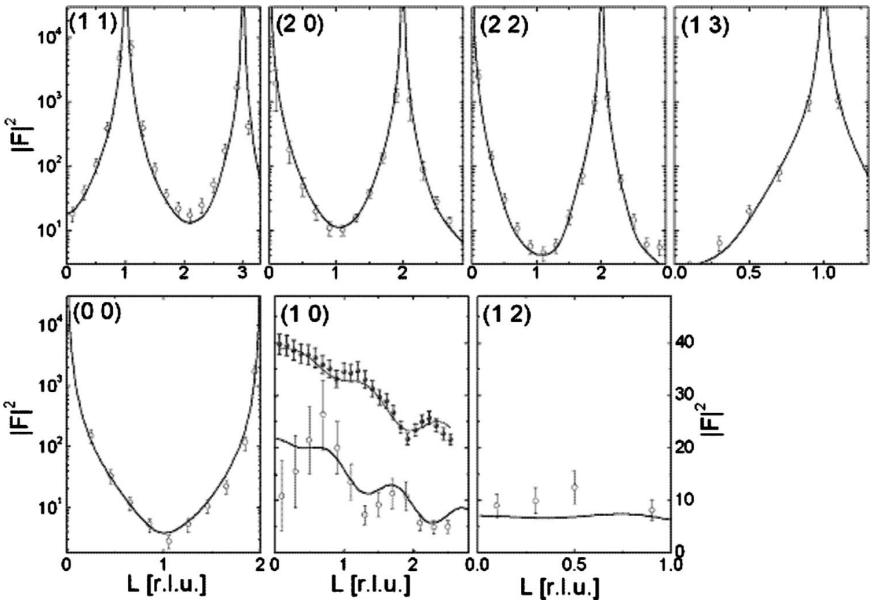

FIG. 3. Experimental crystal truncation rods and the lowest-order $c(2\times2)$ superstructure rod for Cu(001) in 10 mM HCl at −0.20 V (circles), together with the best fit based on the structural model described in the text (lines). Shown in the figures are also the measured (1, 0, L) superstructure rod of the $c(2\times2)$ Cl structure in UHV (from Ref. 18, filled symbols), which is antiphase shifted relative to the data obtained in electrochemical environment.

Unfortunately, only the (2, 0, L) CTR was measured at the negative limit, prohibiting a more detailed comparison. For the first layer a slight inward relaxation of 1.0% is found in our analysis, which directly manifests in the experimental data as a shift of the CTRs minima toward higher L. Within the experimental errors this relaxation is identical to that obtained for clean copper in UHV.[55]

Fits of the data measured at −0.20 V employed a model of a $c(2\times2)$ Cl adlayer as confirmed by STM measurements in chloride containing electrolytes[6,25–28] and supported by in-plane scans along high-symmetry directions of the Cu(001) surface. The spacing between the Cl adlayer and the Cu surface layer d_{Cl} as well as the topmost two layer spacings in the Cu substrate d_{12} and d_{23} were allowed to relax (see also Fig. 4). Furthermore due to the presence of distinct intensity oscillations in the (1, 0, L) superstructure rod (see Fig. 3) we allow in the second Cu layer different vertical positions for atoms directly below the Cl adsorbate atoms and the Cu atoms in between those. This small subsurface buckling of amplitude Δ_2 will be the focus of the following section. Qualitatively speaking, the intensity oscillations in the (1, 0, L) rod are caused by the interference of waves scattered at atomic layers, which are parallel to the surface plane and have a defined vertical distance as well as a phase difference between each other. The lateral periodicity within these layers has to be identical to that of the superstructure, with the Cl adsorbates on top of the Cu(001) forming the upper layer. The second layer has to result from a subsurface modulation with the same $c(2\times2)$ symmetry. It can be unambiguously identified as the buckling of the second layer, as the period of the oscillations of the superstructure rod is approximately one reciprocal lattice unit (see Fig. 3), corresponding to a vertical distance of 3.615 Å. This model is additionally sup-

TABLE I. Fit parameters for Cu(001)-(1×1) in 10 mM HCl at −0.70 V (this work) and under UHV conditions at 160 K (from Ref. 55). The values were given in Ref. 55 as rms vibrational amplitudes in Å and converted to Debye-Waller factors via $\langle u_s^2\rangle = B_j/(16\pi^2)$.

	(1×1) at −0.70 V	(1×1) in UHV (Ref. 55)
d_{Cl}(Å)	1.782 ± 0.030	
d_{12}(Å)	1.785 ± 0.020	1.777 ± 0.028
d_{23}(Å)	1.808 ± 0.020	1.806 ± 0.026
d_{34}(Å)	1.808 ± 0.020	1.809 ± 0.026
d_{45}(Å)	1.808 ± 0.020	1.807 ± 0.018
DW(Cl)	2.8 ± 0.1	
DW($\mathrm{Cu}_{1\parallel}$)	1.75 ± 0.05	1.876 ± 0.036
DW($\mathrm{Cu}_{1\perp}$)	1.18 ± 0.11	2.052 ± 0.098
DW($\mathrm{Cu}_{2\parallel}$)	0.74 ± 0.08	1.087 ± 0.010

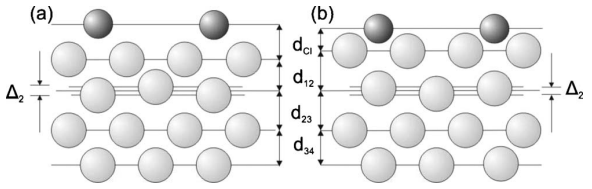

FIG. 4. Side view of the structural model for the $c(2\times2)$ Cl adlayer on Cu(001) in (a) electrochemical environment and (b) at the metal-vacuum interface, illustrating schematically the lattice relaxation and the buckling of the second Cu layer.

TABLE II. Fit parameters for $c(2\times2)$ Cl-covered Cu(001) in 10 mM HCl at −0.20 V (this work) and under UHV conditions (Ref. 18).

	$c(2\times2)$ at −0.20 V	$c(2\times2)$ in UHV (Ref. 18)
d_{Cl}(Å)	1.856 ± 0.015	1.585 ± 0.006
d_{12}(Å)	1.794 ± 0.015	1.839 ± 0.005
d_{23}(Å)	1.822 ± 0.025	1.825 ± 0.003
Δ_2(Å)	$+0.025\pm0.0070$	-0.012 ± 0.003
DW($Cl_{\parallel}$)	2.39 ± 0.17	2.61
DW($Cl_{\perp}$)	2.05 ± 0.19	0.44
DW($Cu_{1\parallel}$)	1.64 ± 0.03	1.39
DW($Cu_{1\perp}$)	0.35 ± 0.06	
DW(Cu_2)	0.70 ± 0.03	0.7

ported by symmetry arguments: the $c(2\times2)$ superstructure exhibits $p4mm$ symmetry with two perpendicular mirror planes crossing at the free hollow site of the Cu(001) bulk unit cell and a fourfold rotation axis also located at the free hollow site. All atoms of the unit cell are located at high-symmetry positions and therefore lateral displacements are forbidden by the symmetry. In addition all copper atoms of the first (or in fact any odd) Cu layer are equivalent and therefore a buckling in those layers is forbidden. Additional free fit parameters were anisotropic Debye-Waller factors for the first two Cu layers, an isotropic Debye-Waller factor for the third Cu layer, and the overall scale factor. The latter was found to be within 2% of the scale factor determined by the fit of the data at −0.70 V, indicating a consistent fit of the two surface structures. Table II summarized the parameters of the best fit ($\chi^2=2.85$) together with those obtained by Tolentino *et al.* for this adsorbate system under UHV conditions;[18] the corresponding calculated CTRs and superstructure rods are included in Fig. 3 (solid lines) and obviously provide a good quantitative description of the experimental data. The structural parameters of the $c(2\times2)$ Cl superstructure in the two environments strongly differ, as will be discussed in more detail in the following sections. Specifically, the second-layer Cu atoms located directly below the Cl adsorbates are at lower vertical positions than the atoms in between the adsorbed Cl, opposite to the observations at the metal-vacuum interface.[18]

The presence and qualitative behavior of this subsurface buckling can be directly seen in the experimental data. As shown in Fig. 3, the (1, 0, L) superstructure rods measured in vacuum and electrochemical environment exhibit a clear difference, namely, a phase shift of the oscillations relative to each other by 0.5 reciprocal lattice units. In the following we will show that this phase shift is the direct result of a reversal in the second Cu layer buckling at the electrochemical interface as compared to that found in UHV. The intensity of the superstructure rod is due only to scattering from atoms obeying the symmetry of the superstructure, i.e., the adsorbate layer and the second copper layer within our model. Placing these atoms at $\vec{r}_{Cu\ a}=\binom{0}{\Delta_2/2}$, $\vec{r}_{Cu\ b}=\binom{a_1/\sqrt{2}}{-\Delta_2/2}$ and $\vec{r}_{Cl}=\binom{0}{d}$, where $d=d_{Cl}+d_{12}$ is the vertical distance of the chloride adlayer to the average vertical positions of the second-layer Cu atoms and the buckling amplitude Δ_2 is positive if the copper atom beneath the chloride atom is lifted, the intensity distribution along the (1, 0, L) rod is given by

$$I \propto |f_{Cl}e^{i\cdot q_z\cdot d}+f_{Cu}(e^{iq_z\Delta_2/2}+e^{i\pi}e^{-iq_z\Delta_2/2})|^2$$
$$\approx f_{Cl}^2+f_{Cu}^2(q_z\Delta_2)^2+2f_{Cu}f_{Cl}q_z\Delta_2\sin(q_zd). \quad (1)$$

Here the Debye-Waller factor is included in the structure factors for chloride (f_{Cl}) and copper (f_{Cu}) and Δ_2 is assumed to be much smaller than d. The oscillations of the intensity of the superstructure rod are represented by the third summand in Eq. (1), which includes the term $\sin(d\ q_z)$. This simple calculation in kinematical approximation shows clearly that exclusively the buckling amplitude Δ_2 and the vertical distance d between the second Cu layer and the Cl adlayer affect the amplitude and the period, respectively, of the intensity oscillation of the superstructure rod. This implies especially that a significant correlation between the parameter pair (Δ_2 d) and the remaining structural parameters can be excluded. For that reason, this small effect can be unambiguously detected, although the buckling amplitude is similar to the errors in the interlayer spacings. The above consideration also confirms the assumed model: the extension of the superstructure to another Cu layer than the second would affect the oscillation period and an additional layer would result in additional oscillations with different period. Reversal of the buckling, i.e., inversion of the sign of Δ_2, causes an antiphase shift in the oscillations. Hence, the two central qualitative observations for the (1, 0, L) rod—the extension of the $c(2\times2)$ to the second Cu layer and the different sign of the buckling in UHV and electrochemical environment—can already be deduced from this simplified analysis. In addition, the CTR analysis indicates a 17% expansion of the Cl-Cu interlayer spacing as compared to that found in UHV,[18] in agreement with the *in situ* SXRD results by Huemann *et al.*[6]

B. Calculation of second-layer Cu-atom buckling

In this section we argue that the reversal of the sign of the corrugation of the second-layer Cu atoms at the electrochemical interface, as opposed to UHV, can be reproduced by density functional calculations. DFT calculations for this system have been carried through by Saracino *et al.*,[7] who mentions a small buckling to result from their calculations. Here we focus on this subsurface buckling, which was not quantified explicitly in the previous DFT work. In order to relate to literature we will also quote our calculated Cl-Cu and Cu-Cu interlayer separations. Initial calculations for the clean Cl-free Cu(001) surface yield an interlayer separation of the two topmost Cu layers of 1.76 Å, which corresponds to a 3% contraction with respect to the bulk value. This agrees within the error bars with previous theoretical (GGA or LDA) results,[14,56] and it is consistent with the experimental SXRD results for a clean Cu(001) surface under UHV conditions[55] and in 10 mM HCl at −0.70 V (see Table I). For the $c(2\times2)$ Cl covered Cu(001) surface in the absence of external electric fields or additional species, i.e., the surface under UHV conditions, we obtain a Cl-Cu interlayer separation $d_{Cl}=1.667\pm0.012$ Å in agreement with Ref. 7 and an average spacing between the two topmost Cu layers d_{12}

TABLE III. Calculated surface atomic geometry of $c(2\times2)$ Cl-covered Cu(001) in the presence of external applied electric fields, additional water molecules, and water and Ca counter ions. For the latter case also the height L_z of the supercell is given. Vac denotes a vacuum layer. The estimated error of the second Cu layer corrugation is 0.004 Å.

	L_z (Å)	d_{Cl} (Å)	d_{12} (Å)	Δ_2 (Å)
$c(2\times2)$-Cl at 0 V/Å	Vac	1.67	1.82	−0.006
$c(2\times2)$-Cl at 0.3 V/Å	Vac	1.68	1.82	−0.005
$c(2\times2)$-Cl at 0.9 V/Å	Vac	1.71	1.82	−0.004
$c(2\times2)$-Cl+H_2O	44.27	1.70	1.80	−0.002
$c(2\times2)$-Cl+H_2O+Ca	44.27	1.79	1.77	+0.006
$c(2\times2)$-Cl+H_2O+Ca	45.27	1.81	1.79	+0.0034
$c(2\times2)$-Cl+H_2O+Ca	46.27	1.82	1.81	+0.0026

$=1.817\pm0.01$ Å. Saracino *et al.* have reported a first Cu-Cu layer spacing 0.6% larger than the bulk value,[7] which is within the error bar of our calculation. The 3% contraction of the interlayer separation between the topmost two Cu layers of the clean Cu(001) surface vanishes upon Cl adsorption, which is ascribed to the charge transfer from the Cu surface to the negatively charged Cl ions.[57] The buckling amplitude of the second Cu layer is $\Delta_2=-0.006$ Å, with a convergence error of about ±0.004 Å estimated from additional calculations with different number of Cu layers, vacuum thickness, k-point sets, and cutoff energy. This value is compatible with the experimental corrugation under UHV conditions found in the SXRD measurements by Tolentino *et al.*,[18] taking the errors in the experimental and DFT studies into account.

In a first approach, the effect of the outer part of the electrochemical double layer on the Cu surface relaxation was simulated by applying a homogeneous electric field to the $c(2\times2)$ Cl slab. The electric field vector is parallel to the surface normal and points toward the Cu surface. This corresponds to an induced negative screening charge at that surface. In response to the applied electric field the corrugation of the second-layer Cu atoms decreases, as can be seen in Table III. However, the applied fields in the range of 0.3 V/Å–0.9 V/Å are not sufficiently strong to reverse the buckling. The average interlayer separation between the two first metal layers d_{12} decreases only insignificantly as the electric field is switched on, while the Cl-Cu separation increases in agreement with the trend reported in Ref. 7. The qualitative trends are thus the same as derived from the comparison of the present SXRD experiments with the data by Tolentino *et al.*[18] but the effect is too small, at least for the electric field strengths considered here.

In all following DFT calculations the electrochemical interface was modeled by additionally introducing species of the outer Helmholtz layer—specifically water and counter ions—into the supercell, whose height was chosen equal to 44.27 Å. If solely water molecules are added to the system the corrugation decreases to $\Delta_2=-0.002$ Å while the Cl-Cu interlayer separation increases (in comparison to the surface in UHV) to $d_{Cl}=1.70$ Å and the topmost Cu interlayer separation contracts to $d_{12}=1.80$ Å. This trend fits to the conception that the Cl ion is partially screened by the water dipoles, thereby weakening the Cl-Cu bond and strengthening the attractive interaction between the two topmost Cu layers.[50]

Finally, we have added both the water molecules and Ca atoms into the vacuum region between the slabs. For this system occurs a charge transfer from the Ca atoms to the slab, which results in an electric field in the electrolyte region. Upon structural optimization of the $c(2\times2)$ Cl surface as described above (see Sec. II B), the relaxation pattern changes distinctly more pronounced than in the calculations where the electric field was directly applied. The results are summarized in Table III for different size L_z of the supercell in the direction perpendicular to the surface. We note that the total energy adopts a minimum between $L_z=45$ and 46 Å, corresponding to the condition of zero pressure. Additional calculations at different L_z but frozen position of the top layer Cu and Cl atomic positions corroborate the interpretation that a significant part of the variation in Δ_2 in Table III is related to the different amount of charge transfer as a function of L_z. The largest effect on the Cu corrugation Δ_2 can be observed for $L_z=44.27$ Å (for which, however, the pressure does not vanish). In this case, the Cl-Cu interlayer separation further increases to $d_{Cl}=1.79$ Å whereas the average spacing between the first two Cu layers decreases. Most notably, the corrugation of the second-layer Cu atoms reverses its sign as compared to the surface under UHV conditions and becomes $\Delta_2=0.006$ Å. Hence, our DFT calculations reproduce the intriguing effect of the electrolyte on the subsurface buckling of the second Cu layer. To relate this result for $L_z=44.27$ Å to the relaxations caused by an electric field (Table III, top 3 rows) we note that the screening charge density at the Cu surface atoms is roughly a factor of four larger than in case of the 0.9[V/ Å] electric field. The larger effect may therefore be a consequence of the larger induced charge density.

IV. DISCUSSION

As already discussed in the previous studies by Huemann *et al.*[6] and Saracino *et al.*,[7] the interface structures of the $c(2\times2)$ Cl adlayer on Cu(001) in electrochemical environment and at the metal-vacuum interface exhibit notable differences, which can be attributed to the presence of the outer Helmholtz layer. They are schematically indicated in the structural models shown in Figs. 4(a) and 4(b). In agreement with the previous *in situ* SXRD results[6] the Cu-Cl interlayer spacing of 1.856 Å and the corresponding Cu-Cl bond length of 2.59 ± 0.01 Å are 17% larger than that observed in UHV.[18] As already pointed out by Huemann[6] the spacing in electrochemical environment is close to that expected for ionic bonding (2.58 Å),[58] whereas the bond-length deduced from the SXRD data in UHV is closer to the bond-length expected for a covalent bonding (2.35 Å).[59] Furthermore, also the out-of-plane Debye-Waller factor of the chloride layers, corresponding to the chloride's vibrations perpendicular to the surface, is clearly increased at the electrochemical interface, whereas all other vibrational amplitudes are comparable in the two environments. Both effects can be attributed to a reduced binding of the Cl layer in the presence of the

electrolyte solution, caused by the solvation of the anionic adsorbates and the presence of counter ions in the diffuse layer.

Of particular interest in the present study is the small, but clearly detectable corrugation of the second copper layer. Under UHV conditions the Cu atoms below the Cl atoms are displaced toward the surface and those without Cl on top are closer to the Cu bulk [Fig. 4(b)].[18] This was explained by a partial charge transfer between the copper atoms in the first copper layer and the chloride atoms, resulting in an ionic bond between the chloride and the second-layer copper atoms underneath those adsorbates. In contrast, for the $c(2\times2)$ structure at the electrochemical interface our *in situ* SXRD data unambiguously indicates an upward displacement of the second-layer Cu atoms situated between the Cl adsorbate positions [Fig. 4(a)], i.e., a reversal of this subsurface buckling. A buckling of the same type as in our study and with similar corrugation amplitude (0.004–0.008 Å, depending on the potential) was also found by Saracino *et al.* for the $c(2\times2)$ structure of bromide on Cu(001).[7] Our DFT calculations strongly suggest that the corrugation reversal is a clear consequence of the presence of the electrolyte and apparently requires both the solvation of the Cl adsorbates by coadsorbed water as well as the electric field generated by cations in the outer Helmholtz layer. These effects modify the charge distribution in the chemisorbed adlayer and the adjacent Cu surface, which in turn may influence the structural relaxation of the top copper layers.

To better understand the relationship of $c(2\times2)$ Cl on Cu(001) in UHV and in electrochemical environment we estimate the potential shift introduced by the electrolyte. The potential of the metal electrode E_{Me} is given by[60]

$$E_{\mathrm{Me}} = \Phi_{\mathrm{Me}}/e - E_{\mathrm{ref}} + E_{\mathrm{sol}}. \tag{2}$$

Here Φ_{Me} is the electron work function of the metal in UHV and E_{ref} is the "absolute potential" of the reference electrode. The absolute potential of the standard hydrogen electrode is approximately $E_{\mathrm{SHE}}=4.5$ eV,[61,62] which corresponds to an "absolute potential" of the Ag/AgCl electrode of $E_{\mathrm{Ag/AgCl}}=4.7$ eV. The term E_{sol} contains potential shifts due to the contact of the electrode with electrolyte solution, which are (i) the modification of the work function when the electrode is brought in contact with the solution, (ii) the contribution of any preferentially oriented solvent molecules, and (iii) the potential drop due to the presence of free charges close to the interface. The work function of the bare Cu(001) surface is $\Phi_{001}=4.48$ eV, however, the adsorption of Cl into a $c(2\times2)$ superstructure introduces a work function shift of $\Delta\Phi_{c(2\times2)}=+1.1$ eV.[63] Consequently, the difference between the Cu(001) electrode in 10 mM HCl at an applied potential of −0.2 V and the $c(2\times2)$ Cl in UHV corresponds to

$$E_{\mathrm{sol}} = E_{\mathrm{Me}} - (\phi_{001} + \Delta\phi_{c(2\times2)})/e + E_{\mathrm{Ag/AgCl}} = -1.1\ \mathrm{V}. \tag{3}$$

Hence, the Cu(001)-$c(2\times2)$ surface in HCl solution is substantially negatively charged as compared to the $c(2\times2)$ Cl structure in UHV. This charge on the electrode side is compensated by a corresponding charge formed by cations in the outer Helmholtz layer and results in an electric field toward the Cu surface, as introduced in the calculations. Assuming the additional negative charge of the Cu(001)-$c(2\times2)$ in the electrochemical environment to be located on the Cl adlayer, this would correspond to a more ionic character of halide, resulting from the electrostatic screening of the chemisorbed Cl by the coadsorbed water and cations, which is supported by the consideration of the difference in bond lengths above. A higher ionicity of adsorbed halide ions under these conditions was already proposed in previous studies[6–9] to explain the expanded halide-copper bond at electrochemical interfaces. Furthermore, Saracino *et al.* suggested a less ionic character of $c(2\times2)$ Br on Cu(001),[7] which by analog reasoning as above can be attributed to the smaller work function shift [$\Delta\Phi_{c(2\times2)}=+0.9$ eV (Ref. 64)] induced by the Br adlayer.

Finally, we compare the structural data for the $c(2\times2)$ Cl-covered Cu surface at −0.20 V and the Cu(001)-(1×1) surface at −0.70 V, where the Cl adlayer is disordered. In both cases we find very similar values for the first Cu interlayer spacing, specifically an ≈1% inward relaxation. This agrees well with the relaxation of the clean Cu(001) surface,[55] but clearly differs from that of the Cu(001)-$c(2\times2)$ Cl in UHV,[18] which points again to pronounced changes in the nature of the adsorbate's bond as suggested previously.[6–9] The Cl vibration amplitudes at −0.70 V are increased in comparison to those at −0.20 V, in agreement with a disordering of the adlayer at negative potentials. The Cu-Cl spacing at −0.70 V appears smaller than that at −0.20 V, suggesting a slight change in the metal-halide bond. This is not unexpected since already under UHV conditions the adsorbate's coverage influences its charge state. For adsorbates in electrochemical environment this effect is even stronger due to the different hydration of the adsorbates in the low coverage phases at negative potentials as compared to that in the close-packed structures at more positive potentials, where the solvent is largely displaced from the metal surface and the adlayer is partly discharged.[1,10] However, following the arguments given previously,[6,7] the Cl-Cu bond length should increase at more negative potentials, where the adsorbate is expected to be more ionic, or be potential independent, assuming that the Cl adsorbate on Cu(001) is largely ionic even in the $c(2\times2)$ phase.[6,7] A similar effect was observed for Cl adsorption on Au(111), where the existence of a weaker bond with a longer distance at more negative potentials was revealed by x-ray absorption fine structure.[65]

V. CONCLUSION

In this work we have presented detailed structural results obtained by *in situ* SXRD measurements and DFT calculations for the chloride adlayer on Cu(001) as well as discussed those data in relationship to previous studies of this and related adsorbate systems. Although Cl adsorption at the electrochemical interfaces and Cl_2 adsorption under UHV conditions result in the same $c(2\times2)$ superstructure, the presence of the electrolyte induces a corrugation reversal in the buckling of the second Cu layer. The subsurface struc-

tural reversal can be reproduced in the calculations by taking the outer part of the electrochemical double layer into account. The estimation of the difference in work function in electrochemical and UHV environment points toward a more negatively charged Cu(001)-$c(2\times2)$ surface in solution and consequently to a more ionic bonding.

In addition, potential dependent x-ray scattering measurements reveal that the $c(2\times2)$ structure exists down to potentials close to the onset of hydrogen evolution, where a phase transition from the $c(2\times2)$ structure to a disordered 2D lattice gas of chloride is observed. The disordered Cl adlayer was found to exhibit a substantial coverage even at potentials as negative as 0.7 V vs Ag/AgCl. This behavior is analogous to that of Cl and Br on Ag(001) electrodes, where a qualitatively identical continuous order-disorder transition was reported.[10,16,17]

In general, the $c(2\times2)$ phases of anionic adsorbates on (001)-oriented metal surfaces represent particularly simple, but important cases and therefore are well suited as model systems to further a true quantum theoretical understanding of electrochemical interfaces and their relationship to surfaces under UHV conditions. Detailed surface crystallographic studies as presented here as well as in a few previous publications[6–9] provide experimental data that can be directly compared to calculations, thus allowing to test and guide the development of *ab initio* theories for the description of electrochemical phase boundaries.

ACKNOWLEDGMENTS

We thank the Deutsche Forschungsgemeinschaft for financial support via Grant No. Ma 1618/13. Calculations have been carried through at the Rechenzentrum der Universität Kiel. We acknowledge the ESRF for providing synchrotron radiation facilities and thank the ID 32 beamline staff for the technical support.

*Present address: University of Life Sciences in Lublin, Faculty of Food Science and Biotechnology, Skromna 8, 20-704 Lublin, Poland.

[1] O. M. Magnussen, Chem. Rev. **102**, 679 (2002).
[2] J. K. Sass and K. Bange, in *Electrochemical Surface Science*, edited by M. P. Soriaga (American Chemical Society, Washington, 1988), Chap. 4, p. 54.
[3] J. K. Sass, D. Lackey, J. Schott, and B. Straehler, Surf. Sci. **247**, 239 (1991).
[4] J. Wang, B. M. Ocko, A. J. Davenport, and H. S. Isaacs, Phys. Rev. B **46**, 10321 (1992).
[5] C. A. Lucas, N. M. Markovic, and P. N. Ross, Phys. Rev. B **55**, 7964 (1997).
[6] S. Huemann, N. T. M. Hai, P. Broekmann, and K. Wandelt, J. Phys. Chem. B **110**, 24955 (2006).
[7] M. Saracino, P. Broekmann, K. Gentz, M. Becker, H. Keller, F. Janetzko, T. Bredow, K. Wandelt, and H. Dosch, Phys. Rev. B **79**, 115448 (2009).
[8] O. Endo, M. Kiguchia, T. Yokoyamaa, M. Ito, and T. Ohta, J. Electroanal. Chem. **473**, 19 (1999).
[9] O. Endo, H. Kondoh, Y. Yonamoto, T. Yokoyama, and T. Ohta, Surf. Sci. **463**, 135 (2000).
[10] Th. Wandlowski, J. X. Wang, and B. M. Ocko, J. Electroanal. Chem. **500**, 418 (2001).
[11] P. A. Dowben, CRC Crit. Rev. Solid State Mater. Sci. **13**, 191 (1987).
[12] T. Kramar, D. Vogtenhuber, R. Podloucky, and A. Neckel, Electrochim. Acta **40**, 43 (1995).
[13] A. Ignaczak and J. A. N. F. Gomes, J. Electroanal. Chem. **420**, 71 (1997).
[14] A. Migani, C. Sousa, and F. Illas, Surf. Sci. **574**, 297 (2005).
[15] A. Migani and F. Illas, J. Phys. Chem. B **110**, 11894 (2006).
[16] B. M. Ocko, J. X. Wang, and T. Wandlowski, Phys. Rev. Lett. **79**, 1511 (1997).
[17] J. X. Wang, T. Wandlowski, and B. M. Ocko, in *Proceedings of the Symposium on the Electrochemical Double Layer*, edited by C. Korzeniewski and B. E. Conway (The Electrochemical Society, Pennington, NJ, 1997), p. 293.
[18] H. C. N. Tolentino, M. De Santis, Y. Gauthier, and V. Langlais, Surf. Sci. **601**, 2962 (2007).
[19] D. Westphal and A. Goldmann, Solid State Commun. **35**, 437 (1980).
[20] D. Westphal, A. Goldmann, F. Jona, and P. M. Marcus, Solid State Commun. **44**, 685 (1982).
[21] K. N. Eltsov *et al.*, JETP Lett. **62**, 444 (1995).
[22] M. Galeotti, B. Cortigiani, M. Torrini, U. Bardi, B. Andryushechkin, A. Klimov, and K. Eltsov, Surf. Sci. **349**, L164 (1996).
[23] M. Kiguchi, T. Yokoyama, S. Terada, M. Sakano, Y. Okamoto, T. Ohta, Y. Kitajima, and H. Kuroda, Phys. Rev. B **56**, 1561 (1997).
[24] C. Y. Nakakura, V. M. Phanse, and E. I. Altman, Surf. Sci. **370**, L149 (1997).
[25] C. Y. Nakakura, G. Zheng, and E. I. Altman, Surf. Sci. **401**, 173 (1998).
[26] I. Villegas, C. B. Ehlers, and J. L. Stickney, J. Electrochem. Soc. **137**, 3143 (1990).
[27] D. W. Suggs and A. J. Bard, J. Phys. Chem. **99**, 8349 (1995).
[28] M. R. Vogt, F. A. Möller, C. M. Schilz, O. M. Magnussen, and R. J. Behm, Surf. Sci. **367**, L33 (1996).
[29] T. P. Moffat, J. Phys. Chem. B **102**, 10020 (1998).
[30] M. R. Vogt, A. Lachenwitzer, O. M. Magnussen, and R. J. Behm, Surf. Sci. **399**, 49 (1998).
[31] O. M. Magnussen, L. Zitzler, B. Gleich, M. R. Vogt, and R. J. Behm, Electrochim. Acta **46**, 3725 (2001).
[32] L.-Q. Wang, A. E. Schach von Wittenau, Z. G. Ji, L. S. Wang, Z. Q. Huang, and D. A. Shirley, Phys. Rev. B **44**, 1292 (1991).
[33] O. M. Magnussen, K. Krug, A. H. Ayyad, and J. Stettner, Electrochim. Acta **53**, 3449 (2008).
[34] E. Vlieg, J. Appl. Crystallogr. **30**, 532 (1997).
[35] http://www.sub.uni-hamburg.de/opus/volltexte/1999/99/
[36] C. Kumpf, A. Müller, W. Weigand, E. Umbach, J. Wagner, V. Wagner, S. Gundel, L. Hansen, J. Geurts, J. H. Zeysing, F. Wu, and R. L. Johnson, Phys. Rev. B **68**, 035339 (2003).
[37] R. Herger, P. R. Willmott, O. Bunk, C. M. Schlepütz, B. D.

Patterson, B. Delley, V. L. Shneerson, P. F. Lyman, and D. K. Saldin, Phys. Rev. B **76**, 195435 (2007).
[38] A. Hirnet, K. Schroeder, S. Blügel, X. Torrelles, M. Albrecht, B. Jenichen, M. Gierer, and W. Moritz, Phys. Rev. Lett. **88**, 226102 (2002).
[39] G. Kresse and J. Hafner, Phys. Rev. B **47**, 558 (1993).
[40] G. Kresse and J. Hafner, Phys. Rev. B **49**, 14251 (1994).
[41] G. Kresse and J. Furthmuller, Comput. Mater. Sci. **6**, 15 (1996).
[42] G. Kresse and J. Furthmuller, Phys. Rev. B **54**, 11169 (1996).
[43] J. P. Perdew, J. A. Chevary, S. H. Vosko, K. A. Jackson, M. R. Pederson, D. J. Singh, and C. Fiolhais, Phys. Rev. B **46**, 6671 (1992).
[44] P. E. Blöchl, Phys. Rev. B **50**, 17953 (1994).
[45] G. Kresse and D. Joubert, Phys. Rev. B **59**, 1758 (1999).
[46] H. J. Monkhorst and J. D. Pack, Phys. Rev. B **13**, 5188 (1976).
[47] A. Y. Lozovoi, A. Alavi, J. Kohanoff, and R. M. Lynden-Bell, J. Chem. Phys. **115**, 1661 (2001).
[48] S. Venkatachalam, P. Kaghazchi, L. A. Kibler, D. M. Kolb, and T. Jacob, Chem. Phys. Lett. **455**, 47 (2008).
[49] E. Skúlason, G. S. Karlberg, J. Rossmeisl, T. Bligaard, J. Greeley, H. Jónsson, and J. K. Nørskov, Phys. Chem. Chem. Phys. **9**, 3241 (2007).
[50] J. Rossmeisl, E. Skúlasona, M. E. Björketuna, V. Tripkovica, and J. K. Nørskova, Chem. Phys. Lett. **466**, 68 (2008).
[51] J. S. Filhol and M. Neurock, Angew. Chem. Int. Ed. **45**, 402 (2006).
[52] C. D. Taylor, S. A. Wasileski, J. S. Filhol, and M. Neurock, Phys. Rev. B **73**, 165402 (2006).
[53] J. Neugebauer and M. Scheffler, Phys. Rev. B **46**, 16067 (1992).
[54] T. Tansel, A. Taranovskyy, and O. M. Magnussen, Studies of Adsorbate Dynamics by In Situ Video-STM: Surface Diffusion, Adsorbate-Adsorbate Interactions, and Interactions with Defects, 2008.
[55] O. Mironets, H. L. Meyerheim, C. Tusche, P. Zschack, H. Hong, N. Jeutter, R. Felici, and J. Kirschner, Phys. Rev. B **78**, 153401 (2008).
[56] R. Pentcheva and M. Scheffler, Phys. Rev. B **61**, 2211 (2000).
[57] F. Sette, T. Hashizume, F. Comin, A. A. MacDowell, and P. H. Citrin, Phys. Rev. Lett. **61**, 1384 (1988).
[58] J. C. Slater, J. Chem. Phys. **41**, 3199 (1964).
[59] R. D. Shannon, Acta Crystallogr., Sect. A: Cryst. Phys., Diffr., Theor. Gen. Crystallogr. **32**, 751 (1976).
[60] S. Trasatti, J. Electroanal. Chem. **150**, 1 (1983).
[61] W. Schmickler, Chem. Rev. **96**, 3177 (1996).
[62] W. Schmickler, *Interfacial Electrochemistry* (Oxford University Press, New York; Oxford, 1996).
[63] D. Westphal and A. Goldmann, Surf. Sci. **131**, 113 (1983).
[64] N. V. Richardson and J. K. Sass, Surf. Sci. **103**, 496 (1981).
[65] O. Endo, D. Matsumura, K. Kohdate, M. Kiguchi, T. Yokoyama, and T. Ohta, J. Electroanal. Chem. **494**, 121 (2000).

5.2 Surface Structure of Cu(111) in Chloride-Containing Electrolyte

Similar to the chloride adlayer on Cu(001), the chloride adlayer on the Cu(111) electrode has been investigated both by *ex situ* [212,235,236] and *in situ* [156,212,236–238] structure-sensitive methods. First low energy electron diffraction studies, reported by Stickney and Ehlers in 1989, revealed a diffraction pattern which they interpreted as (12×12) structure, which consists of local $(\sqrt{3} \times \sqrt{3})$R30° arrangements with regular arrays of translational domain boundaries. 5 years later, the first *in situ* STM measurements by Suggs and Bard were published. In contrast to the observations in UHV, they reported the existence of a $(6\sqrt{3} \times 6\sqrt{3})$R30° ordered chloride adlayer structure over the whole potential region in HCl solution. Since then, even more divergent observations have been made, *e.g.*, reporting a simple $(\sqrt{3} \times \sqrt{3})$R30° structure [236–238] or an uniaxially electrocompressive chloride adlayer [212]. Table 5.1 summarizes the experimental observations. Up to now, no common agreement on the chloride adlayer structure on Cu(111) exists.

Electrolyte	**Structure & Stable Potential Regime**	**Coverage**	**Technique**	**Reference**
110 mM HCl, 110 mM KCl	$(6\sqrt{3} \times 6\sqrt{3})$R30° -0.55 to -0.05 V	0.454	STM	[156]
10 mM HCl	$(\sqrt{3} \times \sqrt{3})$R30° -0.50 to -0.05 V	1/3	STM	[236,237]
0.1 mM HCl + 10 mM $HClO_4$	c(p×$\sqrt{3}$), p = 2.53 - 2.48 -0.55 to 0 V	0.395-0.405	STM/LEED	[212]

Table 5.1: Summary of observed chloride adlayers on Cu(111).

The diversity of the observations may be related to the difficulty of drawing high-precision conclusions on the in-plane morphology based on studies by STM. Typically, small deviations from commensurate superstructures as well as potential-dependent shifts of the adlayer lattice parameters may not be resolved by STM and AFM [239, 240]. In this context, high resolution SXRD measurements often contributed to a deeper understanding by determining the unit cell parameters at the electrochemical interface with unsurpassed resolution [239, 240].

In the subsequent publication, a first *in situ* SXRD study of the chloride/Cu(111) system is reported, which focuses on a detailed investigation of the potential dependent in-plane structure of the ordered chloride adlayer. In contrast to the aforementioned studies, an incommensurate, potential dependent adlayer structure is observed. The comparison with similar halide adlayer structures on Au(111) and Ag(111) [25] shows clear differences in between these adsorbate systems, specifically in the potential dependence and epitaxial rotation of the adlayer. These findings will be discussed on the basis of theoretical studies of incommensurate adlayers, developed by Novaco and MacTague [241, 242] as well as Bohr and Grey [243, 244].

The subsequent publication has been sumitted to *Surface Science* (2011).

Structure and Electrocompression of Chloride Adlayers on Cu(111)

Yvonne Gründer[1,‡], Arne Drünkler[1], Frederik Golks[1,2], G. Wijts[1,2], Jochim Stettner[1], Jörg Zegenhagen[2], Olaf M. Magnussen[1]

[1]*Institut für Experimentelle und Angewandte Physik, Universität Kiel, Leibnizstraße 19, 24098, Kiel, Germany*
[2]*European Synchrotron Radiation Facility, 6 Rue Jules Horowitz, 38000 Grenoble, France*

The specific adsorption of chloride on Cu(111) from acidic aqueous electrolyte (pH 3) was investigated by *in-situ* surface X-ray diffraction, revealing an incommensurate hexagonal rotated adlayer. The structure and its potential dependence suggest a strong adsorbate-adsorbate interaction as compared to other halide adlayers on (111)-oriented metal electrode surfaces. The orientational epitaxy can be rationalized by the model suggested by Grey and Bohr (Europhys. Lett. **18**, 171, 1992), which is based on symmetry considerations.

1. Introduction

The adsorption behavior and adlayer structure of specifically adsorbed anions on metal electrode surfaces has been widely studied both due to fundamental interest and their importance for several technologically relevant processes [1]. The presence of specifically adsorbed anions can significantly affect the electrochemical reactivity of a metal electrode which is of major relevance for galvanic deposition, etching, corrosion, and electrocatalysis. Halides – the most simple type of anions and ubiquitous in natural and technological environments – are prototypic adsorbate systems and their adsorption on metal single crystal surfaces has been investigated in great detail. These studies have revealed a complex adlayer phase behavior with a wide variety of ordered structures over a wide potential range [1-6]. The range of observed structures includes simple low-order commensurate superstructures, such as adlayers with $(\sqrt{3}\times\sqrt{3})R30°$ structure, commensurate structures with larger unit cells, uniaxial-incommensurate structures, where the adlayer locks into the substrate lattice along one direction but is compressed along the other lattice direction, and 2D incommensurate (IC) superstructures. In the latter two cases the halide lattice spacings typically decrease and the coverage correspondingly increases continuously with the electrode potential, an effect termed electrocompression. The fact that the adlayer structures and phase transitions are highly reversible as a function of the applied electrode potential, makes these systems ideal models for studies of 2D phase behavior and epitaxy.

Chloride adlayers on copper electrodes are of major importance in corrosion and electroplating, in particular for the on-chip metallization of ULSI microchips, where chloride and organic additives form an inhibiting adsorbate layer that controls the growth process, leading to superconformal growth. For this reason, chloride adlayers on Cu(111) electrodes have been investigated by a number of *ex-situ* and *in-situ* structure-sensitive methods [7-12]. The earliest structural data was reported by Stickney and Ehlers who found a split diffraction pattern by *ex-situ* low energy electron diffraction (LEED), which was attributed to a (12×12) structure, consisting of a local $(\sqrt{3}\times\sqrt{3})R30°$ arrangement with a regular array of translational domain boundaries [7]. Direct *in-situ* STM observations of an ordered Cl adlayer phase on Cu(111) were published by Suggs and Bard, who proposed a $(6\sqrt{3}\times 6\sqrt{3})R30°$ structure [8]. In contrast, more recent *in-situ* STM and *ex-situ* LEED studies suggested a simple $(\sqrt{3}\times\sqrt{3})R30°$ structure [10-12] or a uniaxially compressed chloride adlayer [9]. In the latter study a 6° rotation of one high symmetry direction of the adlayer with respect to the substrate was reported. It is clear from these experimental studies, therefore, that a consistent picture of the Cl adlayer structure on Cu(111) is yet to emerge.

In order to develop a better understanding of halide adsorption on metal electrode surfaces and especially the different interactions that influence the observed structures, precise data for the potential-dependent structure of the adlayer is required. Due to its lower d-band energy, copper is expected to have less affinity for halide adsorption compared to the two other coinage group metals, Ag and Au [13]. Indeed, a more ionic state of Cl on copper electrode surfaces was deduced from the surface-normal Cl - Cu bond distances in previous studies of the $c(2\times2)$ structure on Cu(100) in Cl-containing solution [14-16]. On the energetically less corrugated (111) surface these effects can also affect the adlayer structure within the surface plane, providing a sensitive probe of the adsorbate nature and shedding light on the interplay of the adatom-substrate and adatom-adatom interactions on this more reactive surface.

In this letter we present an *in-situ* surface X-ray diffraction (SXRD) study of chloride adsorption on Cu(111), focusing on the in-plane structure of the ordered adlayer. SXRD allows determinination of the unit cell parameters at the electrochemical interface with high resolution, providing precise and unambiguous structural data. This was illustrated in comparable studies of halide adlayers on Au(111) and Ag(111), where small deviations from commensurate hexagonal structures as well as potential-dependent shifts of the lattice parameters were often not detected by STM/AFM [17,18]. In contrast to the previous studies of Cl/Cu(111), a 2D incommensurate adlayer is observed, similar to the halide adlayers formed on Au(111) and Ag(111) at saturation coverage [1]. However, the potential dependence and epitaxial rotation of Cl/Cu(111) exhibit clear differences to those adsorbate systems and these differences are discussed on the basis of theoretical studies of incommensurate adlayers.

2. Experimental

The X-ray scattering experiments were performed at the ID 32 beamline of the European Synchrotron Radiation Facility in Grenoble using a photon energy of 22.5 keV and a grazing incidence angle of 0.3°. The Cu(111) single crystal sample (Mateck, 99.999%, 4 mm diameter, miscut < 0.1°) was prepared prior to the experiments by electropolishing in 70% orthophosphoric acid. Subsequently, the sample was covered by a droplet of Milli-Q water and mounted in the electrochemical

‡ Current address: The School of Chemistry, The University of Manchester, Oxford Road, Manchester M13 9PL, UK

hanging meniscus cell described in Ref. [19]. All potentials were measured versus a Ag/AgCl (3 M KCl) reference electrode. The cell was filled with 0.1 M $NaClO_4$ + 1 mM HCl, prepared from suprapur hydrochloric acid (Merck), sodium perchlorate hydrate (Aldrich, 99.99%) and Milli-Q water. During the measurements the liquid meniscus in contact with the surface was kept under high purity argon (Air Products, 99.999%) to remove dissolved oxygen from the electrolyte.

Standard surface coordinates of the Cu(111) surface ($|\vec{a}_1| = |\vec{a}_2| = d_{Cu}$ = 2.56 Å, $|\vec{a}_3|$ = 6.21 Å, $\alpha = \beta = 90°$, $\gamma = 120°$, $\vec{a}_3 \| $ to the surface normal) are used in the following. The momentum transfer vector is given by $\vec{Q} = \vec{Q}_{\|} + \vec{Q}_{\perp}$ with $\vec{Q}_{\|} = H \cdot \vec{b}_1 + K \cdot \vec{b}_2$ and $\vec{Q}_{\perp} = L \cdot \vec{b}_3$, where $\vec{a}_i \cdot \vec{b}_i = 2\pi\delta_{ij}$ and *H, K, L* are the diffraction indices.

3. Results and discussion

Prior to the structural studies the electrochemical behavior of Cu(111) in 0.1 M $NaClO_4$ + 0.1 mM HCl was characterized by cyclic voltammetry (fig. 1). In accordance with previous studies a cathodic and an anodic peak at -0.68 V and -0.36 V, respectively, are observed, which are associated with chloride desorption and adsorption [10,12,20].

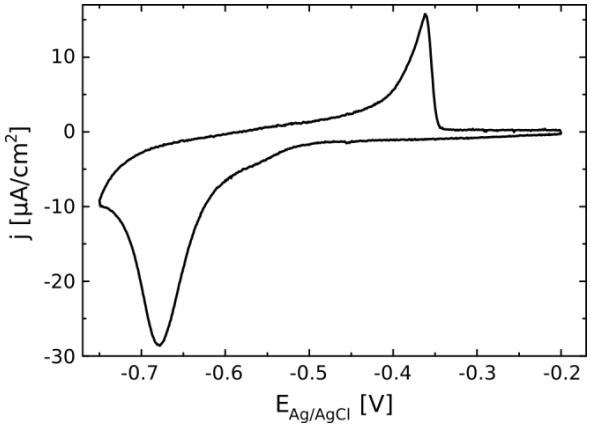

Fig. 1: Cyclic voltammogram of a Cu(111) surface in 0.1 M $NaClO_4$ + 0.1 mM HCl recorded at 10mV/s.

To investigate the structure of the chloride adlayer, *in-situ* SXRD measurements were performed at potentials positive of the anodic peak, where chloride is expected to be adsorbed. By scanning the reciprocal space at low surface-normal wave vector transfer (L = 0.15), the 2D order of the adlayer in the surface plane was studied. At a potential of -0.15 V an in-plane diffraction pattern as shown in fig. 2a was observed. In addition to the crystal truncation rods of the Cu(111) substrate, six low-order pairs of diffraction peaks were found, which are arranged in a hexagonal pattern and which we associate with diffraction rods resulting from a hexagonal-rotated 2D incommensurate chloride adlayer. The positions of these peaks are close to the low order positions expected for a *(√3×√3)R30°* superstructure (indicated by the vector $\vec{q}_S$ in fig. 2a), but exhibit a slightly larger momentum transfer $|\vec{q}_A| = 1.07 \cdot |\vec{q}_S|$. Furthermore, $\vec{q}_A$ is rotated by ±6° relative to $\vec{q}_S$, resulting in a pair of peaks. Corresponding chloride superstructure rods at symmetrically equivalent low-order positions, as well as at higher order positions, were also recorded. Apart from these peaks and the crystal truncation rods of the substrate no further peaks could be found, in particular along the axes defined by $\vec{b}_1$ or $\vec{q}_S$. This excludes the presence of a uniaxially incommensurate structure of the chloride adlayer as suggested by Inukai et al. [9], which would give rise to a similar diffraction pattern as the hexagonal-rotated structure with additional peaks along these high symmetry axes. The corresponding real space structure, deduced from the reciprocal peak positions, is shown in fig. 2b. The adlayer at -0.15 V is rotated by $\phi = 6.0°$ with respect to the high symmetry directions of the substrate (*e.g. (√3×√3)R30°*) and exhibits a chloride-chloride distance of 4.14 Å. Due to the mismatch of adsorbate and substrate lattice a moiré lattice emerges (unit cell indicated in Figure 2b), with a lattice spacing of $|\vec{r}_M| \approx 10\sqrt{3} \cdot d_{Cu} \approx 44$ Å at -0.15 V.

The potential dependence of the chloride adlayer structure was investigated by recording in-plane rocking (fig. 3a) and radial scans (fig. 3b) through the first order superstructure peaks. In

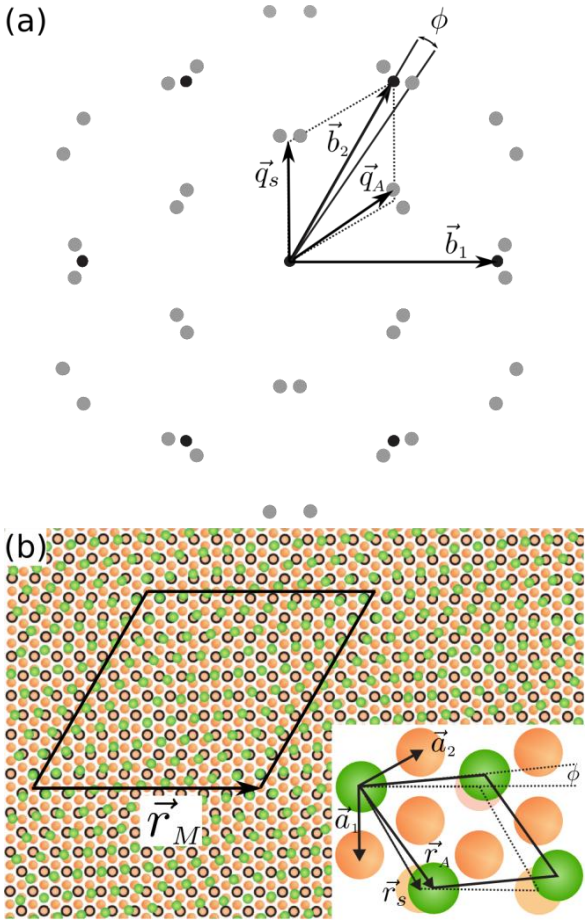

Fig. 2: (a) In-plane diffraction pattern of the hexagonal rotated chloride adlayer on Cu(111) at -0.15 V, showing the diffraction rods of the copper substrate (black) and of the Cl superstructure (grey). The reciprocal space vectors of the surface unit cell of the substrate surface ($\vec{b}_1, \vec{b}_2$), a first-order vector of the Cl adlayer structure ($\vec{q}_A$), and the reciprocal space position of the low-order commensurate *(√3×√3)R30°* structure ($\vec{q}_S$) are indicated by arrows. **(b)** Corresponding real space structure for the chloride adsorbate (green circles) on the Cu(111) surface (orange circles). For a better visibility of the expected moiré-pattern the *(√3×√3)R30°* superstructure is highlighted by black borders around the copper surface atoms and the unit cell of the moiré structure is shown. The surface unit cells of substrate, *(√3×√3)R30°* structure, and adlayer are shown in the inset.

these experiments the potential was first decreased in steps of 10 mV from -0.15 V to -0.30 V, where the superstructure peak disappeared. The disappearance of the superstructure peak is surprising in view of the absence of features in the voltammogram at this potential. However, structural phase transitions in anion adlayers often are indicated only by small spikes that strongly depend on the surface roughness. At potentials negative of -0.30 V no scattering from a similar or different superstructure (*e.g.* *(√3×√3)R30°* or uniaxially incommensurate structures) could be found, which is in contradiction to earlier *in-situ* STM observations where a *(√3×√3)R30°* adlayer structure was observed over almost the whole double layer potential range, down to the onset of hydrogen evolution [10,12]. Since no noticeable charge transfer occurs in the voltammogram at -0.30 V, the chloride coverage does not change significantly during the phase transition, *i.e.*, the chloride density in the adjacent phase at more negative potentials should be close to that in the hexagonal-rotated adlayer. Similar observations were reported for related adsorbate systems, *e.g.* bromide on Au(111) [1-3], and can be rationalized by a transition from the ordered hexagonal structure to a disordered liquid-like adsorbate layer of similar surface density.

Subsequently, the potential was increased again (in 20 mV steps) up to -0.12 V. At -0.28 V the superstructure peaks reappeared and were found at all subsequent potentials at nearly identical positions as during the potential steps in negative

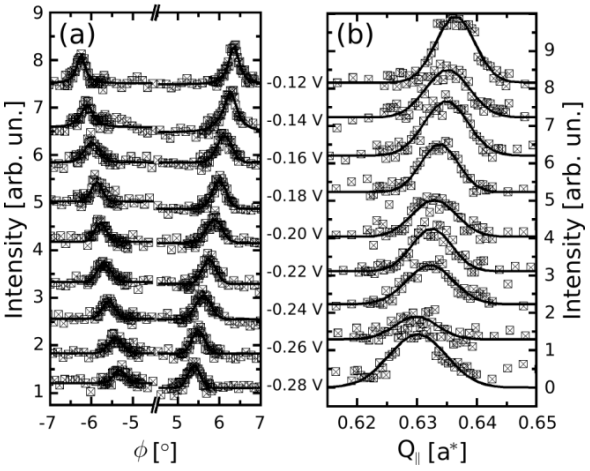

Fig. 3: Potential dependence of the first-order Cl superstructure peaks. **(a)** In-plane rocking scans through the superstructure rods, showing both rotational domains. **(b)** Radial in-plane scans through one of the domains. The rotation angle ϕ increases as the adlayer compresses.

direction, indicating that the potential-dependent chloride adlayer is highly reversible. Quantitative analysis of the peak positions reveals an approximately linear dependence of the adsorbate-adsorbate spacing d_{Cl} and of the rotation angle, ϕ, on the potential (fig. 4a,b), with ϕ changing from 5.3 to 6.3° and d_{Cl} from 4.17 to 4.13 Å between -0.29 and -0.12 V, respectively. The latter corresponds to a linear electrocompression of $0.76 \cdot 10^{14}$ cm^{-2} V^{-1}. The local Cl coverage in the hexagonal rotated phase, calculated via $\theta = (d_{Cu} / d_{Cl})^2$, varies between 0.375 and 0.383 over this range.

From these data we calculated the 2D isothermal compressibility

$$\kappa_{2D} = \frac{1}{Z_{ion} e_0} \left(\frac{dA}{dE} \right)$$

of the monolayer, where dA/dE is the change in area A per adsorbate atom with potential E and Z_{ion} is the valence state of the ion in solution. Assuming Z_{ion} = -1, a compressibility κ_{2D} = 1.726±0.050 Å^2/eV is obtained, which is much lower than the compressibility of 4.5 - 7 Å^2/eV found for iodide, bromide and chloride on Au(111) [2] and for chloride on Ag(111) [1] (see table 1), but in the range of those found for electrochemically deposited metal monolayers (1 - 2 Å^2/eV) [21-23].

For a surface covered completely by the hexagonal-rotated adlayer phase the integrated intensity of the superstructure rod would be proportional to the square of the local Cl coverage θ, *i.e.*, would change only slightly with potential. However, the measured intensity of the diffraction peaks (fig. 4d) shows a clearly different behavior at potentials negative of -0.20 V. Although the data exhibit a significant scatter due to the low peak intensities, a clear decrease towards more negative potentials is discernible in this region. This behavior is similar to that of chloride adsorption on Cu(001) electrodes, where the coverage of the ordered c(2x2) chlorine adlayer continuously decreases over a wide potential regime [16]. In analogy to the latter system we suggest that for the rotated-hexagonal Cl adlayer on Cu(111) the surface fraction covered by this phase continuously changes between -0.30 and -0.20 V. Most probably, the ordered hexagonal superstructure is gradually replaced by the adjacent (disordered) adlayer phase.

The Cl adlattice spacing d_{Cl} is noticeably larger on Cu(111) than on Au(111) and Ag(111) electrode surfaces [1,2]. Moreover, taking the different size of the adsorbate species into account, it is also larger than that of other incommensurate hexagonal halide adlayers on the (111) surfaces of noble metals, as illustrated in table 1 where we chose the potential E_0 of 2D phase formation (*i.e.*, the negative potential end of the IC phase) as the reference point. The halide spacings $d_X(E_0)$ at this potential is 19% larger than the corresponding Van-der-Waals diameter d_{VdW}, while the increase in all other adsorbate systems is typically only 13 to

	$d_X(E_0)$ [Å]	$\sqrt{3} \cdot d_{Me}$ [Å]	d_{VdW} [Å]	$d_X(E_0) / d_{VdW}$	$d_{VdW} / \sqrt{3} \cdot d_{Me}$	r_{AS}
Cl/Cu(111)	4.17	4.427	3.52	1.19	0.79	0.94
Cl/Ag(111)	4.00	5.003	3.52	1.14	0.70	0.80
Cl/Au(111)	4.03	4.996	3.52	1.14	0.70	0.81
Br/Au(111)	4.24	4.996	3.70	1.15	0.74	0.85
I/Au(111)	4.47	4.996	3.96	1.13	0.79	0.89
I/Ag(111)	4.48	5.003	3.96	1.13	0.79	0.89

Table 1: Structural data for 2D incommensurate hexagonal halide adlayers on the (111) surfaces of noble metal electrodes. $d_X(E_0)$, d_{VdW}, and d_{Me} denote the adsorbate-adsorbate spacing of halide species X at the negative potential limit of the incommensurate phase, the halide van-der-Waals diameter, and the nearest neighbor spacing of metal substrate atoms, respectively, $r_{AS} = d_X(E_0) / \sqrt{3} \cdot d_{Me}$ corresponds to the incommensurability parameter (data taken from Ref. [1,33] and this work).

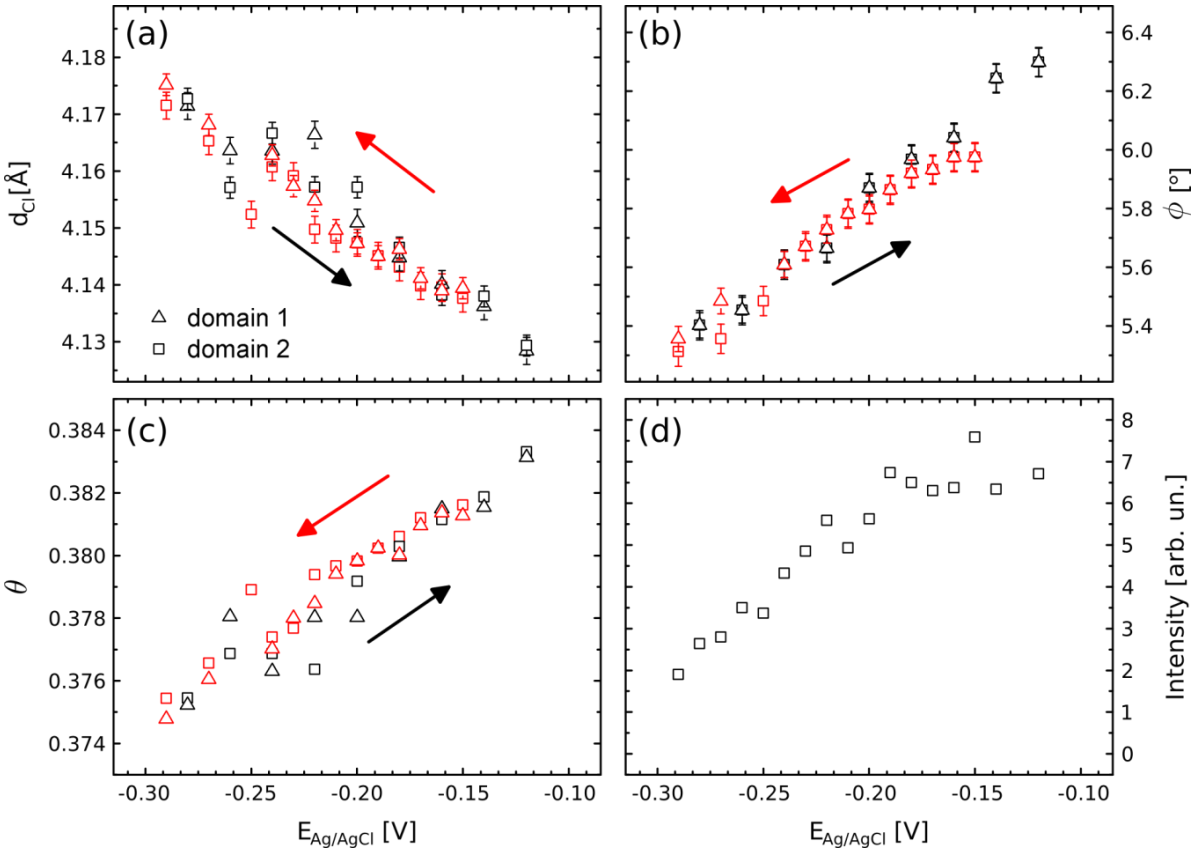

Fig. 4: Potential dependence of **(a)** the adsorbate spacing d_{Cl}, **(b)** the rotation angle ϕ relative to the substrate lattice of the chloride adlayer, **(c)** the local Cl coverage θ, calculated from d_{Cl}, and **(d)** the integrated intensity of the superstructure rods, shown for both studied domains (triangles and squares) and for potential steps in negative (red) and back in positive direction (black).

15%. In accordance with the suggestions of previous *in-situ* SXRD studies of Cl on Cu(100) electrodes [14-16], we attribute this to a more ionic character of adsorbed chloride on Cu(111) electrode surfaces, resulting in a stronger adsorbate repulsion. For the sake of completeness it should be noted that 2D incommensurate hexagonal adlayers were also found for Cu underpotential deposition on Au(111) [24,25] and Pt(111) [26] in the presence of Cl. In these systems salt-like CuCl layers were observed, which exhibited a much smaller Cl-Cl spacing of 3.6 Å. This spacing is close to the ionic radius of chloride and can be attributed to electrostatic screening of the adsorbates charges by the Cu coadsorbate.

From inspection of fig. 4a and b it is obvious that the rotation angle ϕ is a well defined function of the adsorbate spacing d_{Cl}. The phenomenon of epitaxial rotation is well known in adlayer systems and heteroepitaxial growth. For incommensurate adlayers the most well known quantitative theory was developed by Novaco and McTague [27,28], which was originally derived for adlayers on graphite [27,28], but also proved to be applicable to the hexagonal-rotated structures of iodine on Au(111) and Ag(111) [4]. Novaco and McTague showed that, for an infinite incommensurate adlayer, a rotation from a high symmetry, commensurate orientation is energetically preferred if the transverse strain in the adlayer is lower than the longitudinal strain. The rotation angle then depends linearly on the incommensurability and its slope on the ratio of the longitudinal to transverse sound velocities c_L/c_T. For iodine on Au(111) the rotation angle increases linearly with the incommensurability parameter $z = \sqrt{3}\, d_{Au}/d_{I\text{-}I}$ [4], which agrees with the Novaco-McTague theory [29,30]. Values of c_L/c_T between 1.49 and 1.52 incommensurability and its slope on the ratio of the longitudinal to transverse sound velocities c_L/c_T. For iodine on Au(111) the were determined, which are close to the expected value (c_L/c_T=*1.73*) for a self-bound Lennard-Jones system [29,30]. For the system investigated here, a linear dependence of the rotation angle on the incommensurability parameter ($z=\sqrt{3}\, d_{Cu}/d_{Cl}$) was also observed. However, the deduced c_L/c_T ratio is not approximately constant but varies from 2.8 at -0.29 V to 3.8 at -0.15 V. Both the change of this ratio with potential, as well as the high values, indicate that in the case of Cl/Cu(111) the adsorbate-adsorbate interaction is comparable to the adsorbate-substrate interaction which invalidates the assumption of a self-bound Lennard-Jones potential on which the Novaco-McTague model is based.

Much better suited to describe the chloride adlayer rotation seems to be an alternative model, developed by Bohr and Grey [31,32]. This theory is based on the assumption that a high-symmetry state of a system usually corresponds to an extremum,

maximum or minimum, in energy. An incommensurate adlayer leads to a domain structure or moiré pattern, which depends on the angle ϕ of the adlattice relative to the substrate (see fig. 2). Bohr and Grey suggested that the interfacial energy has a minimum when the high symmetry direction $\vec{r}_M$ of the formed moiré pattern either lies along one of the high symmetry directions of the substrate $\vec{r}_S$ or along one of the high symmetry directions of the adlayer $\vec{r}_A$ [31,32]. In the first case the angle Ψ_S between $\vec{r}_M$ and $\vec{r}_S$ will have a well-defined constant value, whereas in the second case the angle Ψ_A between $\vec{r}_M$ and $\vec{r}_A$ will have a well-defined constant angle. This assumption is based exclusively on symmetry considerations and cannot predict which of the two solutions nor which angles of Ψ_S or Ψ_A might be energetically favorable. The reciprocal lattice vector of the moiré-pattern, $\vec{q}_M$, corresponds to the difference $\vec{q}_M = \vec{q}_A - \vec{q}_S$ of the reciprocal lattice vectors of substrate $\vec{q}_S$ and adsorbate $\vec{q}_A$. The rotation angle ϕ can be calculated on the basis of simple geometric considerations and depends only on the ratio of the adsorbate and substrate lattice parameters $r_{AS} = |\vec{q}_S| / |\vec{q}_A| = |\vec{r}_A| / |\vec{r}_S|$. For the first case, where the moiré pattern is oriented parallel to the high symmetry directions of the substrate (*i.e.*, $\vec{r}_M \parallel \vec{r}_A$), ϕ depends on the lattice mismatch r_{AS} via:

$$\cos\phi = r_{AS}\sin^2\Psi_S + \cos\Psi_S\sqrt{1 - r_{AS}^2\sin^2\Psi_S}$$

In the second case the moiré pattern is oriented along the high symmetry directions of the adsorbate ($\vec{r}_M \parallel \vec{r}_A$) and:

$$\cos\phi = \frac{1}{r_{AS}}\sin^2\Psi_A + \cos\Psi_A\sqrt{1 - \left(\frac{1}{r_{AS}}\right)^2\sin^2\Psi_A}$$

Apart from the trivial case $\Psi_S = \Psi_A = 0$ where adsorbate and substrate lattice are aligned ($\phi = 0$), the high symmetry directions of a hexagonal lattice correspond to Ψ_S or Ψ_A values that are multiples of 30°, providing a number of possible functional relations $r_{AS}(\phi)$. For chloride on Cu(111) the relevant substrate lattice is given by the nearest commensurate structure, which is the $(\sqrt{3}\times\sqrt{3})R30°$ superstructure. Here $\vec{r}_S$ is as shown in fig. 2 and the lattice mismatch $r_{AS} = d_{Cl} / d_{(\sqrt{3}x\sqrt{3})R30°}$. The experimentally obtained rotation angles as function of r_{AS} are shown in fig. 5 together with the theoretical relations $\phi(r_{AS})$ for Ψ_S or Ψ_A of 30° and 60°. Obviously, the experimental data for Cl on Cu(111) are in excellent agreement with the case $\Psi_S = 60°$, corresponding to a moiré structure with its high symmetry axis $\vec{r}_M$ along the [1 1 2] direction of the Cu(111) substrate. This can be directly seen in fig. 2b, where the real space structure for a lattice mismatch of 0.95 and an adlayer rotation of 5.5° is shown.

For Cl on Au(111) and Ag(111) electrode surfaces the adlayer and substrate lattice are aligned, which is a (trivial) case allowed by the Bohr-Grey theory. The situation for other incommensurate hexagonal halide adlayers is difficult to assess, since reliable experimental results on $\phi(r_{AS})$ have only be published for iodine on Au(111) [4]. These data are shown for comparison in fig. 5 and are clearly not well described by the Bohr-Grey theory. The measured rotation angles for Br/Au(111) [3] exhibit pronounced hysteresis, but also all deviate noticeably from the theory. Why only Cl on Cu(111) follows a (non-trivial) theoretical Bohr-Grey dependence and why it is described by the case $\Psi_S = 60°$ is currently not clear; the lattice mismatch in these adsorbate systems may play a role in this. Based on the ratio of the halide Van-der-Waals diameters to the $(\sqrt{3}\times\sqrt{3})R30°$ lattice spacing, Cl on Cu(111) may be expected to show a comparable behavior to I on Ag(111) and I on Au(111) (see table 1). However, the

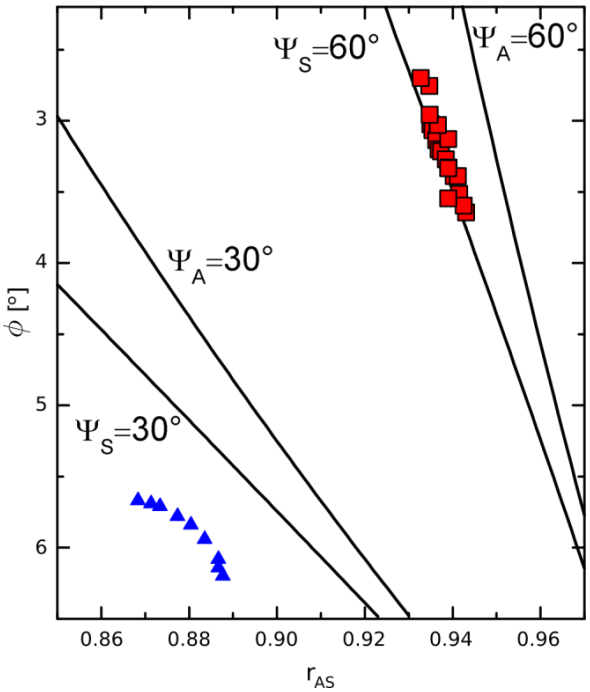

Fig. 5: Rotation angle as function of lattice mismatch r_{AS} for Cl on Cu(111) (squares) and theoretical behavior according to the theory of Bohr and Grey for a hexagonal surface lattice with different rotation angles Ψ=30° and 60° of the moiré structure relative to the substrate (S) or adsorbate (A) lattice. For comparison, also the experimental data for I on Au(111) is shown (triangles, taken from Ref. [4]).

experimentally measured mismatch is much smaller (*i.e.*, r_{AS} is much closer to 1) for Cl on Cu(111) than for the other halide on metal (111) systems, most probably due to a residual charge of the chloride adsorbate and resulting ionic repulsion (see above). We admit that this correlation may be coincidental, since the Bohr-Grey theory is solely based on symmetry arguments and establishing a causal relationship between the magnitude of the mismatch and the validity of the theory is not straightforward. Finally, we note that the Bohr-Grey theory also seems to be roughly compatible with the rotation angles of Tl and Pb on Ag(111) [21-23], although in this case the adlattice spacing exceeds that of the corresponding substrate, *i.e.*, the mismatch (relative to the (1×1) substrate lattice) is $r_{AS} > 1$.

In conclusion, our results identify unambiguously the structure of the ordered chloride adlayer on Cu(111), providing clear evidence for a 2D incommensurate adlayer with a rotated hexagonal structure. The larger adsorbate-adsorbate spacing as compared to related halide adlayers on (111)-oriented noble metal surfaces suggests, as for Cl on Cu(100), a more ionic bond of the chloride adlayer on copper. Surprisingly, the potential-dependent rotation and compressibility of the Cl adlayer on Cu(111) is much closer to the behavior observed for UPD metal adlayers than to other halide adlayers. These structural data provide a basis for understanding the interaction of chloride with copper electrode surfaces and are thus relevant to fundamental questions related to copper electrodeposition and corrosion.

Acknowledgements
We thank the ESRF for providing synchrotron radiation facilities and the ID 32 beamline staff for technical support. Financial

support by the Deutsche Forschungsgemeinschaft via Ma 1618/13-3 is gratefully acknowledged.

REFERENCES

[1] O.M.Magnussen, *Chem. Rev.* **102**, 679 (2002).
[2] O.M.Magnussen, B.M.Ocko, R.R.Adzic, J.Wang, *Phys. Rev. B* **51**, 5510 (1995).
[3] O.M.Magnussen, J.X.Wang, R.R.Adzic, B.M.Ocko, *J. Phys. Chem.* **100**, 5500 (1996).
[4] B.M.Ocko, G.M.Watson, J.Wang, *J. Phys. Chem.* **98**, 897 (1994).
[5] B.M.Ocko, O.M.Magnussen, R.R.Adzic, J.Wang, Z.Shi, J.Lipkowski, *J. Electroanal. Chem.* **376**, 35 (1994).
[6] B.M.Ocko, O.M.Magnussen, J.X.Wang, R.R.Adzic, *Physica B* **221**, 238 (1996).
[7] J.L.Stickney, C.B.Ehlers, *J. Vac. Sci. Technol. A* **7**, 1801 (1989).
[8] D.W.Suggs, A.J.Bard, *J. Am. Chem. Soc.* **116**, 10725 (1994).
[9] J.Inukai, Y.Osawa, K.Itaya, *J. Phys. Chem. B* **102**, 10034 (1998).
[10] M.Kruft, B.Wohlmann, C.Stuhlmann, K.Wandelt, *Surf. Sci.* **377-379**, 601 (1997).
[11] M.Wilms, P.Broekmann, M.Kruft, C.Stuhlmann, K.Wandelt, *Appl. Phys. A* **66**, S473 (1998).
[12] P.Broekmann, M.Wilms, M.Kruft, C.Stuhlmann, K.Wandelt, *J. Electroanal. Chem.* **467**, 307 (1999).
[13] M.T.M.Koper, R.A.van Santen, *Surf. Sci.* **422**, 118 (1999).
[14] S.Huemann, N.T.M.Hai, P.Broekmann, K.Wandelt, H.Zajonz, H.Dosch, *J. Phys. Chem. B* **110**, 24955 (2006).
[15] M.Saracino, P.Broekmann, K.Gentz, M.Becker, H.Keller, F.Janetzko, T.Bredow, K.Wandelt, *et al*, *Phys. Rev. B* **79**, 115448 (2009).
[16] Y.Gründer, D.Kaminski, F.Golks, K.Krug, J.Stettner, O.M.Magnussen, A.Franke, J.Stremme, *et al*, *Phys. Rev. B* **81**, 174114 (2010).
[17] W.Haiss, J.K.Sass, X.Gao, M.J.Weaver, *Surf. Sci.* **274**, L593 (1992).
[18] X.Gao, M.J.Weaver, *J. Am. Chem. Soc.* **114**, 8544 (1992).
[19] O.M.Magnussen, K.Krug, A.H.Ayyad, J.Stettner, *Electrochim. Acta* **53**, 3449 (2008).
[20] G.M.Brisard, N.Bertrand, V.Trepanier, P.N.Ross, N.M.Markovic, in: *Electrochemical Science and Technology of Copper*, P.Vanysek, M.Alodan, J.Lipkowski and O.M.Magnussen (eds.), The Electrochemical Society, (2000) p. 155.
[21] O.R.Melroy, M.F.Toney, G.L.Borges, M.G.Samant, J.B.Kortright, P.N.Ross, L.Blum, *Phys. Rev. B* **38**, 10962 (1988).
[22] O.R.Melroy, M.F.Toney, G.L.Borges, M.G.Samant, J.B.Kortright, P.N.Ross, L.Blum, *J. Electroanal. Chem.* **258**, 403 (1989).
[23] M.F.Toney, J.G.Gordon, M.G.Samant, G.L.Borges, O.R.Melroy, D.Yee, L.B.Sorensen, *Phys. Rev. B* **45**, 9362 (1992).
[24] J.Hotlos, O.M.Magnussen, R.J.Behm, *Surf. Sci.* **335**, 129 (1995).
[25] O.M.Magnussen, J.Hotlos, G.Beitel, D.M.Kolb, R.J.Behm, *J. Vac. Sci. Technol. B* **9**, 969 (1991).
[26] I.M.Tidswell, C.A.Lucas, N.Markovic, P.N.Ross, *Phys. Rev. B* **51**, 10205 (1995).
[27] A.D.Novaco, J.P.McTague, *Bulletin of the American Physical Soc* **23**, 293 (1978).
[28] A.D.Novaco, J.P.McTague, *Phys. Rev. B* **20**, 2469 (1979).
[29] J.P.McTague, A.D.Novaco, *Phys. Rev. B* **19**, 5299 (1979).
[30] A.D.Novaco, J.P.McTague, *Phys. Rev. Lett.* **38**, 1286 (1977).
[31] F.Grey, J.Bohr, *Europhys. Lett.* **18**, 717 (1992).
[32] F.Grey, J.Bohr, in: *Phase transitions in surface films 2*, H.Taub (ed.), Plenum Press, New York (1991) p. 83.
[33] R.D.Shannon, *Acta Cryst.* **A32**, 751 (1976).

6 Homoepitaxial Growth of Cu(001) in Chloride-Containing Electrolyte

The fundamental understanding of homoepitaxial electrochemical deposition of metals is of considerable interest not only in view of crystallographic aspects but also due to its importance for technological deposition processes. As described in the introduction and section 1.4.5, the electrodeposition of copper is of great importance in contemporary industrial processes, specifically, in copper metal refinement, electroplating of electronic circuit boards as well as for the fabrication of ultra-large scale integrated circuits.

Subject of this chapter is the investigation of the growth process of the Cu(001) single crystal electrode during homoepitaxial electrodeposition in the simple inorganic plating solution 0.1 M $HClO_4$ + 1 mM HCl + x mM $Cu(ClO_4)_2$ electrolyte, x = 1 and 5. In particular, the presented SXRD study aims at elucidating the precise interplay of the initial atomic-scale surface structure, the growth behavior and the temporal evolution of the nanometer-scale surface morphology as a function of the applied deposition overpotential.

In contrast to the scarcity of *in situ* studies of homoepitaxial growth processes in electrochemical environment, growth at the solid-vacuum interface by molecular beam epitaxy has been investigated in vast detail both by STM and diffraction techniques (*e.g.* [19, 20] and references therein). As discussed in section 1.4, experimental and theoretical studies [21] showed that homoepitaxial growth far from equilibrium is determined by the extrinsic factors temperature and deposition rate, *i.e.*, the flux of atoms to the surface, and the intrinsic rates of inter- and intralayer mass transport, themselves also depending on the temperature. The ratio of the two surface transport processes characterizes the three kinetic growth behavior step-flow, layer-by-layer and 3D multilayer growth. In general, most unreconstructed fcc(001) metal single crystal surfaces under UHV conditions exhibit fast interlayer mass transport [19], resulting in the observation of step-flow or layer-by-layer growth over a wide range of temperatures. In addition, the aforementioned studies revealed a comprehensive atomistic picture of crystal growth, in which deposited adatoms diffuse on the surface before they are incorporated into step edges or, upon reaching a critical saturation density, nucleate to form clusters. These nuclei, which develop to stable islands with proceeding deposition, act as sinks for diffusing adatoms, thus limiting their density [245]. The precise shape of the growing islands[1], which depends on the relative energy barriers for diffusion across different step-edge orientations and around island corners, is typically almost square for fcc(001) metal surfaces [247–251].

Homoepitaxial Deposition of Copper in UHV

The homoepitaxial deposition of copper on Cu(001) in UHV was subject of numerous extensive experimental as well as theoretical studies (*cf.* [252, 253], and references therein), serving as popular model system for the study of fcc metal(001) homoepitaxy [252]. In

[1] as well as vacancy islands and mounds occurring during multilayer growth [246]

detail, diffraction studies employing spot profile analyzing LEED (SPA-LEED), RHEED and helium atom scattering (HAS) revealed that growth on Cu(001) at room temperature proceeds in an imperfect layer-by-layer mechanism [253–257] on initially smooth terraces with averaged widths of approximately 850 Å [252]. As proposed by embedded atom method (EAM) calculations and confirmed by other *ab initio* calculations, surface diffusion of the copper adatoms proceeds via jumps ('hopping') in directions determined by the crystal lattice [253, 258–260]. The morphological information contained in the diffraction data was confirmed by STM results [252] as well as the almost square shape of adatom islands [247], which were found to exhibit a high degree of mobility at room temperature [252].

In figure 6.1, a sequence of STM images obtained for different coverages during homoepitaxial growth at room temperature is shown. The island density obtained at a coverage of 0.08 monolayer (a) slightly decreases with increasing amount of deposited material to 0.45 monolayer coverage. At this coverage (b), the onset of island coalescence can be observed, as well as first signs of second-layer growth. This phenomenon is frequently called 'smooth multilayer growth' [39, 81, 82], *cf.* section 1.4.3. At 0.7 monolayer coverage (c), island coalescence as well as second-layer growth are well advanced. Subsequent to growth, coarsening of the remaining islands alter the non-equilibrium morphology with time. STM studies clearly revealed that both vacancy [261, 262] and adatom islands [263, 264] move and Pai *et al.* suggested that this island coarsening at room temperature may occur via diffusion of large islands consisting of up to 700 copper atoms [263].

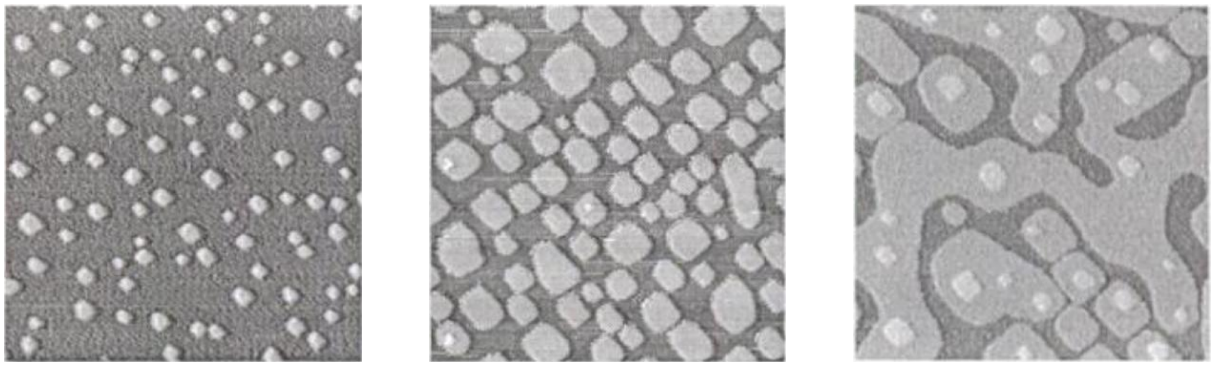

(a) **(b)** **(c)**

Figure 6.1: Sequence of STM images during homoepitaxial growth of Cu(001) in UHV at room temperature, taken from reference [252]. The images show the surface morphology for different coverages ($100\,\mathrm{nm} \times 100\,\mathrm{nm}$). The island density obtained at a coverage of 0.08 ML (a) slightly decreases with increasing amount of deposited material to 0.45 ML coverage. At this coverage (b), the onset of island coalescence can be observed, as well as first signs of second-layer growth. At 0.7 ML coverage (c), island coalescence as well as second-layer growth are well advanced. Credit [265].

Deposition in Electrochemical Environment

In electrochemical environment, fundamental *in situ* atomic-scale studies of electrodeposition concentrated mainly on heteroepitaxy of various metals [65, 155, 163, 266–270]. *In situ* studies of homoepitaxial growth processes have been reported only sparsely, for in-

stance, the homoepitaxial growth of silver single crystal electrodes was investigated employing electrochemical methods and optical microscopy [65,271,272]. Although no detailed atomic-scale structural information was obtained for the growth process, these measurements revealed that the attachment of silver adatoms during growth occurs at kink sites and anisotropically with respect to a preferred growth direction.

Recently, Krug *et al.* studied extensively the homoepitaxial electrodeposition of gold on Au(001) single crystal electrodes from diluted chloride- and $HAuCl_4$-containing electrolyte [36]. Employing time-resolved *in situ* surface x-ray diffraction, real-time studies of the diffusion-limited electrodeposition process were performed under realistic reaction conditions at large overpotentials. The experiments revealed a particularly interesting succession of growth mechanisms as a function of the applied electrode potential and gold concentration, as shown in figure 6.2. With decreasing potential, transitions from step-flow to layer-by-layer to multilayer growth and again to (re-entrant) layer-by-layer growth are observed[2]. The latter (unexpected) transition is attributed to an increased surface adatom

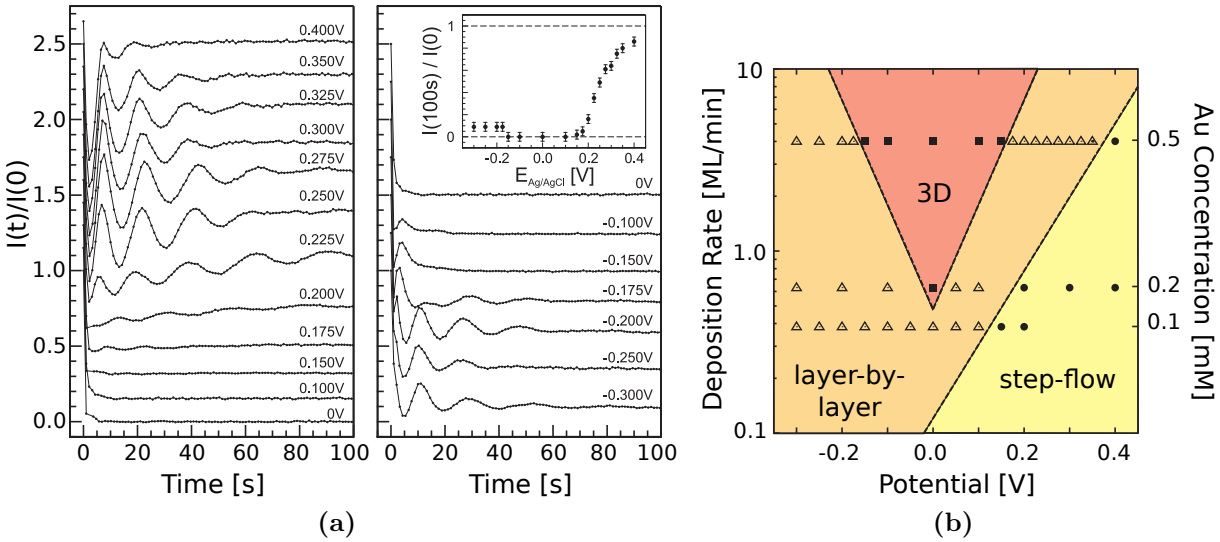

Figure 6.2: (a) Time resolved *in situ* SXRD data obtained during diffusion-limited homoepitaxial electrodeposition on Au(001) in 0.1 M HCl + 0.5 mM $HAuCl_4$. The scattered intensity at the (1,1,0.1) anti-Bragg reciprocal space position was recorded after potential steps from 0.6 V to different (indicated) potentials. The intensity curves are background-subtracted, normalized to the initial intensity and shifted with respect to each other to ensure visibility. The observed deposition mechanisms are layer-by-layer growth followed by step flow growth ($E \approx 0.4$ V), layer-by-layer growth ($0.33\,V < E < 0.2\,V$), 3D growth ($0.2\,V < E < 0\,V$) and re-entrant layer-by-layer growth ($E < -0.10$ V). The inset shows the steady-state intensity measured 100 s after the potential step, normalized on the initial intensity, versus the applied electrode potential. Values close to unity indicate smooth growth, whereas values close to zero indicate surface roughening during the growth process. For $E > -0.15$ V the Au(001) surface exhibits a (1×1) structure, for lower potential values the hexagonally reconstructed phase is present. (b) Kinetic growth mode diagram obtained from measurements of homoepitaxial deposition of Au(001) in 0.1 M HCl + x mM $HAuCl_4$ (x = 0.1, 0.2, 0.5). The occurrence of different growth behavior is related to the electrode potential and deposition rate (concentration). Taken from reference [36]. Credit [273].

[2]for classification of the intensity transients see chapter 4, figure 4.1 and corresponding text.

mobility with formation of the Au(001) hexagonal reconstruction at $E < -0.15\,V$. Clearly, these observations demonstrate the importance of the substrate structure for the growth behavior and for the resulting film morphology. In addition, a much faster formation of the reconstruction was observed under deposition conditions as compared to the very slow kinetics of this process in absence of gold in the electrolyte. Moreover, the reconstruction is found to compress reversibly and linearly with decreasing potential, in conjunction with an alignment of different domains by linear rotation [40]. Detailed insight into the complex formation kinetics of the hexagonal reconstruction under deposition conditions were reported by Kaminski *et al.*, also investigated by *in situ* SXRD [37]. These observations, which indicate the pronounced influence of the growth process on the reconstructed surface layer, underline the importance of *in situ* studies of electrodeposition in order to obtain an in-depth understanding of the processes occurring during crystal growth.

Deposition of Copper in Electrochemical Environment

In electrochemical environment, a two-step model for the electrodeposition of copper was developed based on electrochemical steady-state and transient experiments [274, 275],

$$Cu^{2+} + e^- \rightleftharpoons Cu^+_{(aq.)} \tag{6.1}$$

$$Cu^+_{(aq.)} + e^- \rightleftharpoons Cu_{(sol.)}\,. \tag{6.2}$$

The first reduction reaction is assumed to occur a thousand times slower than the second reaction, thus being the deposition rate determining step, whereas the latter reaction is considered to be at a local equilibrium. In addition to the existence of the solvated $Cu^+_{(aq.)}$ intermediate species, which has been proven by rotating disk experiments [274–277], an adsorbed $Cu^+_{(ads.)}$ surface intermediate has been proposed based on impedance measurements [98, 278]. However, no direct observation of the latter species has been provided.

The addition of chloride ions to the electrolyte, typically between 0.2 and 1.5 mM Cl^- (*cf.* discussion in chapter 5), accelerates the copper deposition reaction by enhancing the electron transfer in the rate-determining first step (6.1). This effect, which is linear with the chloride concentration in the electrolyte, is attributed to the rate-accelerating formation of inner sphere bonds that involve adsorbed chloride ions at the surface [196, 197]. Electrochemical studies showed that the dissolution of copper at low current densities in presence of chloride ions occurs via the formation of an adsorbed CuCl species with subsequent removal of $CuCl_2^-$ anions [279–282]. The pronounced influence of the ordered chloride adlayers on the surface morphology of the low index copper single crystal electrodes, especially on their step orientation, at potentials relevant for deposition was already addressed in the previous chapter. In case of Cu(001), the repulsive interactions between the chloride anions in the c(2×2) adlayer induce a strong anisotropy between the [010] and [100] step edges (*cf.* figure 5.2), leading to step faceting [283]. Moreover, the anisotropy is known to influence the deposit morphology, for instance yielding faceted growth reported by Wu and Barkey [88].

A systematic study of the deposit shape evolution, *i.e.*, a detailed roughness analysis on the nano- to micrometer scale, was performed by Schwarzacher *et al.* for polycrystalline copper deposits after immersion into the plating bath [284]. These *ex situ* atomic force and electron microscopy studies demonstrated a correlation of the electrolyte composition and

the scaling behavior of the growth morphology. In particular, anomalous scaling behavior of the roughness parameter is observed for chloride-containing copper sulfate solution, whereas deposition in absence of chloride yielded normal scaling behavior.

Direct *in situ* STM studies of the anodic dissolution of and electrodeposition on low-index copper single crystal electrodes in chloride-containing electrolyte have been reported by Suggs *et al.*, Vogt *et al.*, and Polewska *et al.* [85, 86, 156, 164–168, 231, 286]. The first studies of dissolution as well as (re)deposition of Cu(001) in 10 mM HCl at moderate rates (at -0.08 to -0.05 V and -0.30 V electrode potential, respectively) were performed by Suggs *et al.* who observed a step-flow dissolution mechanism and showed that the preferred reaction sites are located at step edges which are aligned in the {100} directions. Even for enhanced etching overpotentials (0.20 V electrode potential), the dissolution process was found to occur accelerated at the same sites. The preferential etching and deposition was explained by a higher density of kinks and the open structure of the copper {100} edges. Similar studies, performed for Cu(111) electrodes under comparable conditions, are given in [156]. Beyond that, the studies by Vogt *et al.* and Polewska *et al.* revealed a comprehensive atomic-scale picture of the processes occurring during dissolution and (re)deposition in vicinity of the Cu/Cu^{2+} equilibrium potential, determining the structure of active sites, the involved microscopic mechanisms, as well as the corresponding local

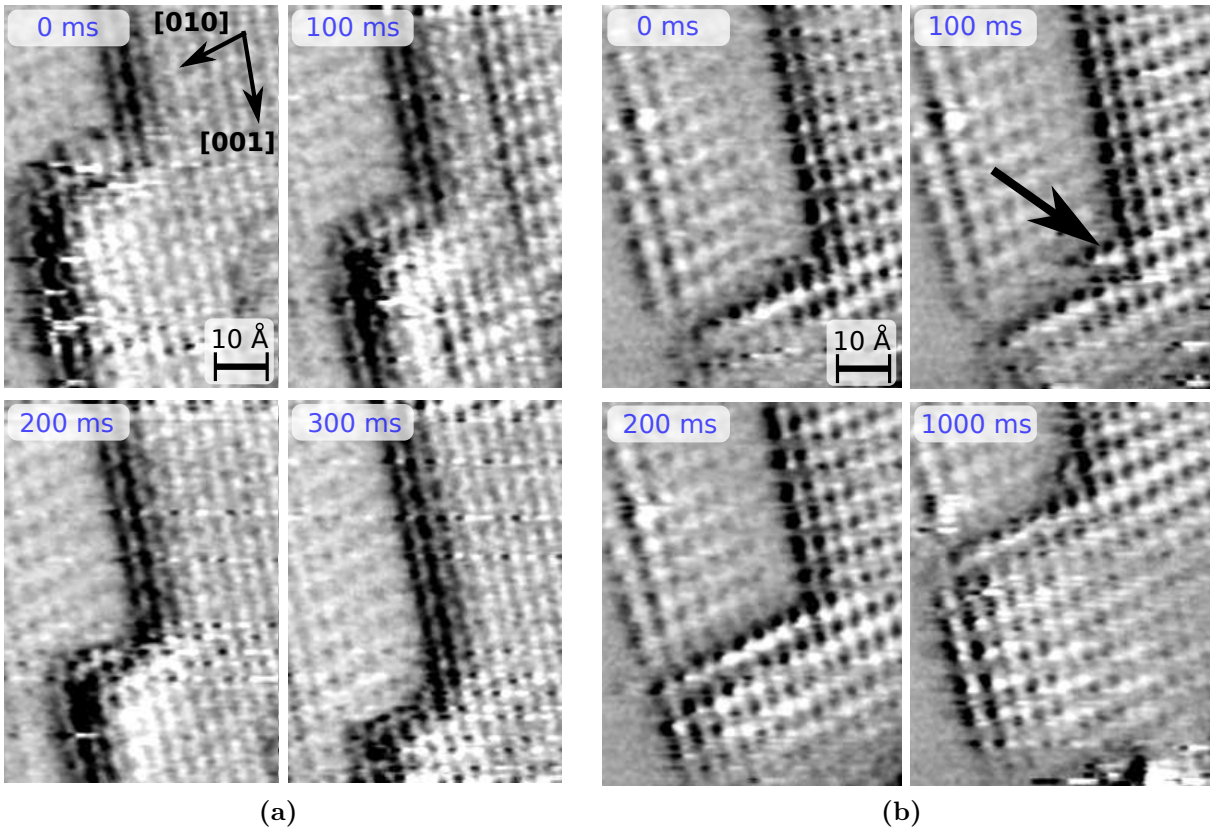

Figure 6.3: Sequence of *in situ* video-STM images during local dissolution (a) and growth (b) on Cu(001) in 10 mM HCl, demonstrating the anisotropic removal and attachment of several ($\sqrt{2} \times \sqrt{2}$)R45°-rows wide segments (approximately $5 \times 8\,\mathrm{nm}^2$, 10 Hz video). Taken from [171]. Credit [285].

rates. In detail, dissolution and growth on Cu(001) in 10 mM HCl in this potential regime is found to occur via removal of primitive $(\sqrt{2} \times \sqrt{2})$R45° surface unit cells [86, 168, 171], which contain two copper and an adsorbed chloride atom. Thereby, the c(2×2) chloride adlayer induces, as explained in section 5.1, an anisotropy which favors the deposition and dissolution processes at kink sites in the {001}-oriented monoatomically high steps, in accordance with Suggs *et al.*. In figure 6.3, a series of successive *in situ* video-STM images are shown [171], measured for Cu(001) in 10 mM HCl at -0.23 V. The local dissolution (a) and growth (b) of a several $(\sqrt{2} \times \sqrt{2})$R45°-rows wide segment of a terrace occurs solely along the [010] steps, as indicated by the arrow in (b).

UHV-STM studies on the structurally similar oxygen-covered Ni(001) surface, reported by Kopatzki and coworkers, revealed the formation of a c(2 × 2) adlayer structure, which was found to induce similar step faceting along the {100} directions [248, 287, 288]. For the Ni homoepitaxial growth processes on the c(2 × 2)-covered surface, also an anisotropic behavior is observed, which was rationalized by an energetical preference of the step edges exhibiting the out-of-phase shifted adlayers on upper and lower terrace (*cf.* figure 5.2).

In situ atomic-scale studies of the homoepitaxial growth of copper on Cu(001) at potentials far from equilibrium have not been reported yet, although, spurred by the technological importance of copper electrodeposition (*cf.* introduction), great interest in the fundamental steps of the deposition process exists. This deficiency is mainly related to the difficulty of making direct observations on the atomic scale under real reaction conditions with contemporary available techniques, as discussed in the introduction and in more detail in chapter 4. SXRD studies of copper electrodeposition in general mainly concentrated on post-deposition characterization of *ex situ* grown heteroepitaxial deposit crystal structures [29]. An exception is an *in situ* study by Gründer *et al.* of the electrodeposition of copper on As-terminated GaAs(001), revealing growth of eight equivalent domains of copper clusters, which are rotated and inclined with respect to the GaAs substrate lattice [30, 31, 289, 290].

The *in situ* atomic-scale studies of the homoepitaxial growth of copper on Cu(001) presented in the following aimed at a fundamental understanding of the processes during deposition, similar to the studies reported by Krug and coworkers. The well-known surface structure of the Cu(001)-chloride system is an excellent prerequisite for the intended studies. In addition, Vogt and coworkers observed a potential-dependent surface step edge mobility of the copper adatoms [86], which should clearly affect the growth behavior.

For the *in situ* SXRD studies, the electrochemical cell (chapter 3.2) and the new one-dimensional detector system (chapter 3.1.3, discussed in detail in chapter 4) were employed. The deposition experiments were performed in 0.1 M $HClO_4$ + 1 mM HCl + x mM $Cu(ClO_4)_2$ (x = 1 and 5) at high overpotentials under diffusion limitation of the metal species in the electrolyte solution. As described in section 1.3.2, this allows to decouple the deposition rate from potential changes at the sample surface and consequently to study solely the influence of the applied electrode potential on the atomic-scale surface transport[3] during electrodeposition [34]. The subsequent study will provide new insight into the important process of copper electrodeposition. In addition, the obtained detailed data in

[3]It should be emphasized that this approach, in which the surface morphology is investigated in dependence of the potential induced surface mobility, is in contrast to growth studies during molecular beam epitaxy in UHV, where the surface morphology is monitored during deposition at a fixed, temperature dependent surface mobility.

the additive-free solution will be indispensable, serving as a reference point for the subsequent investigations of the electrodeposition in presence of the inhibitor polyethylene glycol (chapter 7).

In situ Surface X-Ray Diffraction Studies of Homoepitaxial Growth on Cu(001) from Aqueous Acidic Electrolyte

F. Golks[1,2], Y. Gründer[1,‡], J. Stettner[1], K. Krug[1,†] , J. Zegenhagen[2], O. M. Magnussen[1]

[1]*Institut für Experimentelle und Angewandte Physik, Universität Kiel, Leibnizstraße 19, 24098, Kiel, Germany*
[2]*European Synchrotron Radiation Facility, 6 Rue Jules Horowitz, 38000 Grenoble, France*

We present first *in situ* surface x-ray scattering studies of homoepitaxial Cu electrodeposition on Cu(001) electrodes in electrolytes containing chloride and 1 mM or 5 mM $Cu(ClO_4)_2$. By time-resolved measurements, detailed insight into the underlying atomic-scale processes is gained up to growth rates of 38 ML/min, revealing a pronounced mutual interaction of the Cl adlayer order and Cu growth behavior. Whereas at the lower potential limit, where the Cl adlayer is disordered, step-flow growth is observed, with more positive potentials, in the regime of the c(2×2) Cl adlayer phase, a transition to layer-by-layer and 3D growth is found. In turn, the kinetics of the c(2×2) Cl adlayer ordering during Cu deposition is substantially slowed down as compared to Cu-free solution. Furthermore, from a detailed analysis of the anti-Bragg peak shape during layer-by-layer growth, an oscillatory average strain in the surface layer is deduced, which is tentatively rationalized by a model considering strain induced by step edges and adatoms.

1. Introduction

Since the successful implementation of copper as a silicon chip interconnect material in the 1990s [1,2], a renewed interest in the copper electroplating process encouraged manifold research. The advances achieved in the copper electrodeposition process play a major role in the down scaling of today's storage media, chip interconnects, microelectronic packaging, and micro-mechanical components (ref. [3] and references therein). Acidic plating baths have become the commonly used, cost-effective copper plating systems in the micro- and nano-electronics industry. Beside a copper ion source, an important constituent of the acidic plating bath are chloride ions in varying concentrations to influence the deposit properties. Small amounts of organic additives, such as polyethylene glycol (PEG) or 3-mercapto-1-propane sulfonic acid (MPSA), are typically added to the bath in order to achieve defect-free filling of sub-micrometer features ('superconformal deposition'), grain refining and suppression of dendritic deposition [4-9].

In this work, we have studied the influence of chloride on the atomic-scale interface processes during Cu electrodeposition on Cu(001). Chloride is known to form an ordered c(2×2) adlayer structure at potentials > -0.50 V (vs. Ag/AgCl), with a transition to a disordered phase with decreasing potential [10,11]. *In situ* scanning tunneling microscopy (STM) studies of the initial stages of corrosion of Cu(001) in hydrochloric acid revealed that the c(2×2) Cl adlayer induces a pronounced faceting of the Cu steps into straight {001} oriented segments with a very low kink density [10,12,13,14]. Atomic-scale studies of homoepitaxial growth in the vicinity of the Cu/Cu^+ equilibrium potential were performed by Polewska *et al.* for Cu(001) single crystal electrodes in chloride containing electrolyte by electrochemical video-STM [15]. The Cu growth process, performed at very low overpotentials and growth rates below 1 monolayer (ML) per minute, apparently occurs via a step-flow mechanism, involving attachment of units consisting of one surface unit cell (*i.e.*, two Cu and an adsorbed Cl atom [10,12,16]). During deposition parallel growth of either one or several units wide rows along the [010] and [100] oriented Cu steps was observed. High-resolution *in situ* STM studies were also performed on heteroepitaxial Cu electrodeposition [17]. However, in that case the mismatch to the substrate lattice has a decisive influence and strongly affects the nucleation and growth behavior.

Furthermore, the influence of chloride on the micrometer-scale deposit morphology was investigated by Wu and Barkey using atomic force microscopy (AFM) [18,19,20]. As reported in [19], Cu(001) in chloride-containing electrolyte may encounter adsorbate-induced roughening/faceting transitions. The faceting is already promoted by very low Cl concentrations and becomes more pronounced with increasing concentration. The fully ordered Cl overlayer was assumed to stabilize terraces with well-defined (100) edges. Huo and Schwarzacher investigated the kinetic roughening during copper electrodeposition by *ex situ* AFM [21]. By a detailed roughness analysis they demonstrated the dependence of the scaling behavior, *i.e.*, the evolution of the surface morphology during growth, on the electrolyte composition. Specifically, in contrast to Cl-free copper-sulfate electrolytes, a description within the normal Family-Vicsek approach is not possible in the presence of Cl. Instead, an extra scaling exponent is needed in order to describe the time-dependent local roughness by anomalous scaling.

Despite these fundamental studies and the considerable technological importance, an in-depth understanding of the homoepitaxial electrodeposition of copper on the atomic-scale is still lacking. In particular, previous atomic-resolution studies focused on the regime of low growth rates, where step-flow deposition prevails [15]. This restriction is a serious limitation: According to kinetic growth theory, growth behavior and the resulting deposit morphology are determined by the growth rate or, in other words, the adatom flux to the interface, and the rates of the intra- and interlayer mass transport processes [22]. The latter are largely unknown in electrochemical environment and often depend on potential and the electrolyte composition. A prediction of the growth behavior at higher flux is therefore not possible. For a better understanding of the electrodeposition behavior under technological conditions, fundamental data on the growth behavior at higher deposition rates is therefore in dire need.

Homoepitaxial growth on clean Cu single crystal surfaces under ultrahigh vacuum conditions has been extensively studied by experimental and theoretical methods (ref. [23,24] and

‡ Current address: The School of Chemistry, The University of Manchester, Oxford Road, Manchester M13 9PL, UK
† Current address: Department of Chemical Engineering, National Cheng Kung University, Tainan 70101, Taiwan

references therein). In detail, growth on Cu(001) at room temperature and with deposition rates in the range of several ML/min was found to proceed in an imperfect layer-by-layer mechanism [25,26]. As proposed by embedded atom method (EAM) calculations and confirmed by other *ab initio* calculations, surface diffusion of the copper adatoms proceeds via hopping between neighbor sites [24,27]. STM mesurements revealed a square shape of adatom islands with the steps predominantly oriented along the [110] directions [28], which were found to exhibit a high degree of mobility at room temperature [23]. In addition, coverage-dependent oscillations of the in-plane strain were reported during layer-by-layer growth [29]. Subsequent to growth, coarsening of the remaining islands alters the non-equilibrium morphology with time [30]. Similar investigations of the homoepitaxial deposition of copper in electrochemical environment are largely lacking.

The investigations presented here aim at clarifying the interface morphology during deposition at higher growth rates in order to determine the relationship between the atomic-scale structure of the solid-liquid interface, the growth behavior, and the resulting surface morphology. Whereas direct studies of the atomic-scale interface during growth with scanning probe techniques are strongly hampered by a limited time resolution as well as mass transport limitations (*e.g.*, shielding by the scanning tip), these problems may be overcome by the use of surface x-ray diffraction. As demonstrated in previous publications of our group [11,31-34], *in situ* surface x-ray diffraction (SXRD) in transmission geometry provides a powerful tool for the direct study of growth processes at the solid-liquid interface. Not only atomic-scale investigations of the in-plane surface structure are possible, but also temporal changes of the surface morphology during crystal growth are accessible with a time resolution down to 5 ms [35]. In addition to the influence of chloride on the growth behavior of homoepitaxially deposited Cu on Cu(001), we will demonstrate that also detailed information on the lateral in-plane structure during the growth process may be obtained by this technique.

2. Experimental Methods

The *in situ* SXRD experiments were carried out using a hanging meniscus x-ray transmission cell [31]. In this cell geometry, whose principle resembles commonly used cells for single crystal electrochemical measurements, the x-ray beam passes through an almost cylindrical free standing meniscus (~50 µl), which is established between the sample surface and a glass capillary. Hence, the scattered signal only stems from the investigated sample/electrolyte interface and a smoothly varying background is given by the liquid structure factor. For photon energies > 20 keV the transmissivity is > 75 %. A thin tube inside the glass capillary allows to adjust the meniscus size and to exchange the electrolyte via a remote-controlled pump system.

The electrochemical cell setup is a standard three electrode configuration. The counter electrode consists of a platinum sheet. The Ag/AgCl (3 M KCl) reference electrode, to which all mentioned potentials are referred to, is connected via an inner tube, which serves as a Luggin-capillary and ends 4 mm in front of the sample surface. This cell setup is well suited for the experiments reported here: Previous electrodeposition experiments on gold single crystal electrodes showed that the minimized cell resistivity and the nearly unrestricted mass transport through the cell due to the relatively large electrolyte volume allow combining *in situ* SXRD studies of rapidly changing systems with high quality electrochemical measurements [32-36]. A multi-functional potentiostat / galvanostat (CompactStat, Ivium Technologies, Eindhoven) was employed to control the electrode potential and the electrochemical current and apply defined sequences of potential steps.

As working electrode a hat shaped Cu(001) single crystal (Mateck, 99.999 %) with surface diameter of 6 mm was used. Prior to each experiment, the copper crystal was electropolished in 70 % orthophosphoric acid at an electrode potential of 1.8 V for at least three times 10 s. Subsequently, the crystal was rinsed with highly purified water (Milli-Q, 18.2 MΩ), covered by a droplet of water, and inserted into the electrochemical cell. In order to reduce the oxygen concentration in the electrochemical cell and in the electrolyte, the meniscus was kept in a flowing argon atmosphere (Ar 5.0, Air Products) during the experiment.

Sample alignment on the 6-circle diffractometer [37] was done at a potential of -0.20 V. From the alignment of two reflections in reciprocal space, a mean sample miscut of < 0.05° and a crystalline mosaicity of < 0.025° was estimated. The electrolytes were prepared from Milli-Q water, ultrapure $HClO_4$ (Romil UpA, 65-71 %), HCl (Merck Suprapur, 30 %), and $Cu(ClO_4)_2$ (Alfa Aesar, 99.999 %).

The x-ray scattering experiments were performed at the ID32 beamline of the European Synchrotron Radiation Facility (ESRF) using a photon energy of 22.5 keV and a grazing incidence angle of 0.437°. The pre-sample slits were 0.3 and 0.025 mm in horizontal and vertical directions, respectively, giving rise to an illuminated surface area of approximately 1 mm^2. A one-dimensional detector (Dectris Mythen 1K [36,38,39]), triggered by the potentiostat to precisely synchronize the electrochemical and the diffraction data, was employed with the detector pixel axis aligned in parallel to the sample surface. As reported recently in ref. [36], the use of this detector system allows to record the diffracted signal with an acquisition frequency of more than 200 Hz. From the cross sectional peak profiles, transients of the integrated peak intensity, peak position and peak width are obtained. The standard surface coordinates of the Cu(001) surface ($a_1 = a_2 = a_3 = 3.615$ Å, $\alpha = \beta = \gamma = 90°$) were chosen with the a_3-axis along the surface normal. The momentum transfer vector is then defined by $\vec{Q} = H \cdot \vec{b}_1 + K \cdot \vec{b}_2 + L \cdot \vec{b}_3$ with $\vec{a}_i \cdot \vec{b}_i = 2\pi\delta_{ij}$. *H, K, L* are the appropriate Miller diffraction indices.

3. Results and Discussion

3.1 Cu-induced Surface Smoothing

Prior to the deposition experiments, the Cu(001) sample was characterized in Cu-free 0.1 M $HClO_4$ + 1 mM HCl electrolyte. In figure 1 (solid line) a cyclic voltammogram in this electrolyte is shown, recorded at the beamline directly after sample preparation with the sample mounted on the diffractometer. Due to the reduction of residual oxygen in the electrolyte, the current density exhibits a potential dependent offset for potentials < -0.30 V. Cl adsorption and desorption manifests in form of two broad peaks between -0.36 V and -0.60 V, labeled as A_1 and C_1, respectively. Residual c(2×2) ordering exists down to potentials close to the onset of hydrogen evolution and only completely disappears at potentials negative of the peak C_2 in the cyclic voltammogram (at -0.57 V) [11]. This is confirmed by potential-dependent SXRD measurements at the (1,0,0.1) superstructure rod, which is solely dependent on the degree of c(2×2) order of the Cl adlayer (figure 1, dashed line). These data are in good agreement with previous studies of this system [11].

Subsequently, the solution was exchanged at -0.60 V during the diffraction studies by Cu-containing 1 mM $Cu(ClO_4)_2$-containing electrolyte (exchange rate 5 µl/s). Figure 2 (solid

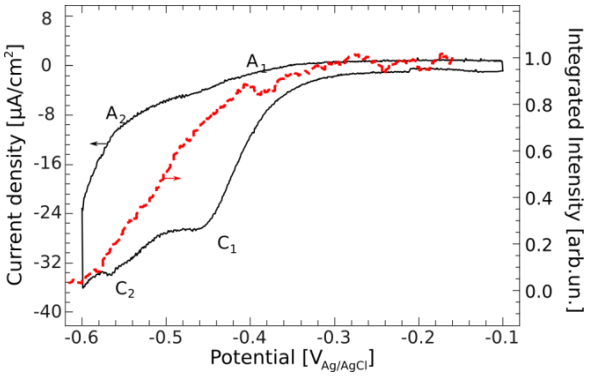

Fig. 1: Cyclic voltammogram (dE/dt = 20mV/s) of Cu(001) in 0.1 M $HClO_4$ + 1 mM HCl (solid line) as well as potential-dependent intensity of the Cl superstructure rod at (1,0,0.1) (dashed line).

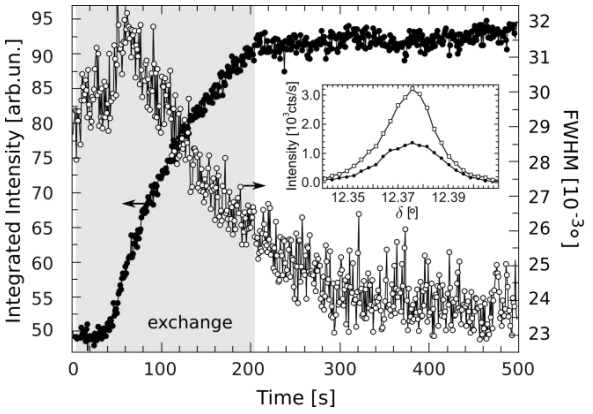

Fig. 2: Integrated intensity and FWHM at (1,1,0.5) during an electrolyte exchange at -0.60 V from 0.1 M $HClO_4$ + 1 mM HCl to 0.1 M $HClO_4$ + 1 mM HCl + 1 mM $Cu(ClO_4)_2$ (5 µl/s exchange rate). Parallel to the exchange (indicated by shaded area) the intensity (solid circles) increases and the FWHM (open circles) decreases, indicating surface smoothing. The inset shows two 1D detector frames, recorded at t=0 s (solid circles) and t=500 s (open squares).

circles) shows the time-dependent integrated intensity at (1,1,0.5) measured during the exchange. Approximately 20 seconds after initiating the electrolyte exchange – the time needed to pump the fresh electrolyte through the cell to the sample surface – the intensity increases steeply and flattens slightly with time. This increase can be also seen directly by comparing the two frames recorded at the beginning (0 s) and at the end (500s) of the transient (figure 2, inset), in which the peak remains at the same position (see below) but strongly increases in height. Since the surface is unrelaxed at -0.60 V [11] and the amount of adsorbed chloride is low, the scattered intensity at (1,1,0.5) is dominated by the roughness of the (1x1) bulk terminated crystal. Hence, the intensity increase indicates smoothing of the surface under deposition conditions at -0.60 V. From the absence of layering oscillations (see below) we conclude that the preferred growth mode at -0.60 V is step-flow growth.

180 seconds after its initiation, the exchange was stopped and the increase in intensity immediately ceases almost completely with only a marginal slope remaining. Apparently, the smoothing effect during electrolyte flow is strongly enhanced as compared to deposition under steady state conditions of the electrolyte. A similar surface smoothing, manifesting as an increase in intensity at (1,1,0.1), was also observed after stepping the potential back to -0.60 V from more positive values, where the surface roughens with time (see below). Also, in that case the effect is accelerated during electrolyte flow. We attribute the rapid recovery of the intensity to the high Cu surface step mobility in this potential regime [10], allowing for rapid smoothing of the rough surface even in the presence of deposition. This behavior resembles the smoothing effect found for Au(001) surfaces in $HAuCl_4$ at positive electrode potentials where adsorbed chloride ions enhance the surface mobility [32,40].

Further indication for surface smoothing is provided by the time-dependent full width at half maximum (FWHM) of the (1,1,0.5) reflection during exchange (open circles), shown in figure 2. The steep decrease, which continues even after stopping the exchange, indicates an increase in the average terrace size, underlining the smoothing effect of growth at -0.60 V. Assuming a Gaussian line shape of the peak a lower limit for the corresponding terrace size can be estimated via $\xi \sim 2\pi/\Delta Q = \lambda/(\cos(\delta/2) \cdot \mathrm{FWHM})$ with λ being the wave length and δ the in-plane scattering angle of the peak. From the final value FWHM = $2.4 \cdot 10^{-2}$ ° we obtain an average domain size larger than 1320 Å, indicating a very high surface quality. The latter seems to be a prerequisite for the smoothing observed at -0.60 V as well as the observation of growth oscillations discussed in the following.

3.2 Growth Behavior Studies

Direct *in situ* studies of the kinetic growth behavior during homoepitaxial electrodeposition on Cu(001) were carried out by SXRD in transmission geometry, using the method previously employed by our group [31-34]. Similar to diffraction studies of molecular beam epitaxy (MBE) under UHV conditions by SXRD or reflected high energy electron diffraction (RHEED) [22,41], the scattered intensity is monitored at selected reciprocal space positions as a function of time while depositing on the electrode surface. In these measurements the kinetic growth mode is inferred from characteristic changes in the scattered intensity close to the anti-Bragg position during growth: For 3D multilayer growth, the scattered intensity decays to low values, usually background level, with deposited amount due to the increasing surface roughness. Layer-by-layer growth manifests in characteristic growth oscillations in the intensity transient, corresponding to the successive growth of single monolayers. In case of step-flow growth, the terraces grow simultaneously, hence the overall surface morphology does not change with time, yielding a scattering signal at a constant high level. In addition to these well established categories a novel growth behavior was recently suggested, where several open layers (typically 2 to 3) grow simultaneously, but the roughness does not diverge as in true 3D growth [42]. Also in this smooth multilayer growth intensity oscillations can be observed. However, the oscillation amplitude decays with increasing amount of deposited material, until a steady state saturation value is reached, which is lower than the initial intensity.

In this work the growth of Cu(001) in 1 and 5 mM $Cu(ClO_4)_2$-containing solution was investigated by *in situ* SXRD. The measurements were performed close to the anti-Bragg condition (1,1,0.1) in order to optimize surface sensitivity and the scattered intensity [43]. The intensity at this reciprocal space position is determined by the occupation of (1×1) surface lattice sites and therefore sensitive to the adsorption of Cl adsorbates and Cu adatoms as well as surface roughness [11]. In the experiments the following procedure was employed: First, the potential was kept

for 5 minutes at -0.60 V, where the surface rapidly smoothens (see 3.1) in order to recover the initial Cu surface quality. Due to the slowly depleting Cu concentration in the small meniscus volume during the deposition, an exchange with 100 µl of fresh $Cu(ClO_4)_2$-containing electrolyte was initiated at this potential to replenish the Cu ion concentration. Directly after the exchange, the x-ray measurement was started. After 10.0 s at -0.60 V, a potential step to a more positive value E_{end} was initiated, at which the potential was kept for 60 s in 1 mM $Cu(ClO_4)_2$ and for 15 s in 5 mM $Cu(ClO_4)_2$. After the reverse potential step back to -0.60 V, the x-ray intensity was recorded for further 50 s (1 mM $Cu(ClO_4)_2$) or 15 s (5 mM $Cu(ClO_4)_2$), respectively, before the x-ray measurement was stopped.

Examples of recorded transients I(t)/I(0), showing the integrated background-corrected scattered intensity at (1,1,0.1) during these potential steps, are presented in figure 3a and 3b for the electrolytes containing 1 and 5 mM $Cu(ClO_4)_2$, respectively. A characteristic behavior is observed which will be exemplarily discussed for the transient to E_{end} = -0.50 V (figure 4a). Directly after the potential step, all transients exhibit an initial, fast decrease within 0.1 s (indicated as $I_A \rightarrow I_B$ in figure 4a), which is attributed to the increase in chloride surface coverage due to Cl adsorption (see below). The subsequent intensity changes at E_{end} (between I_B and I_C in figure 4a) are solely related to the growth process. Layer-by-layer growth oscillations are observable for potentials in the range from -0.55 to -0.15 V in both electrolytes. However, in the higher concentrated solution, where the deposition rate is higher, the signal-to-noise ratio decreases with increasing potential, making it harder to identify the layering oscillations, especially for the potentials of -0.20 and -0.15 V.
After stepping the potential back to -0.60 V, the integrated intensity increases immediately within 0.1 s, indicated as $I_C \rightarrow I_D$ in figure 4a, due to the desorption of chloride (see below). I_D is smaller than the initial intensity I_A due to surface roughening at potentials positive of -0.60 V, but usually recoveres rapidly as indicated by the rather quick, steady increase in the intensity transient (within about 10-30 s in 1 mM and 5-10 s in 5 mM $Cu(ClO_4)_2$-containing electrolyte).

In the potential regime, where growth oscillations are found, the oscillation amplitude decays usually within the first 3 periods. In analogy to previous scattering studies of homoepitaxial growth on (001)-oriented fcc-metal substrates [22,32,41,44], the damping is attributed to surface roughening due to non-ideal layer-by-layer growth. Furthermore, it may be caused by a loss of the phase relationship of incoherently superposed oscillations from different parts of the illuminated surface area (caused by small variations in the local deposition rates in the stagnant solution). As commonly done in MBE studies [44], we will classify the growth behavior as layer-by-layer growth if at least one complete oscillation period can be observed.

The oscillation period Δt is, within about ±4%, independent of the applied potential, as expected for diffusion limited growth. The small deviations are probably related to slight variations in the approach of steady-state hydrodynamic conditions after the electrolyte exchange prior to each transient. For 1 mM Cu ion concentration an average value Δt = 7.6 s is deduced from the first oscillation period, whereas for 5 mM ion concentration a value Δt = 1.6 s is found. These deposition times per monolayer are equivalent to growth rates of 7.9 and 37.5 ML/min, respectively, and agree within the experimental errors with the deposition rates obtained from the electrochemical current density recorded in parallel as well as the rates estimated for diffusion-limited deposition (assuming a diffusion constant $D = 10^{-5}\ cm^2/s$ and a Nernst diffusion layer with thickness $\delta_N = 3 \cdot 10^{-2}\ cm$).

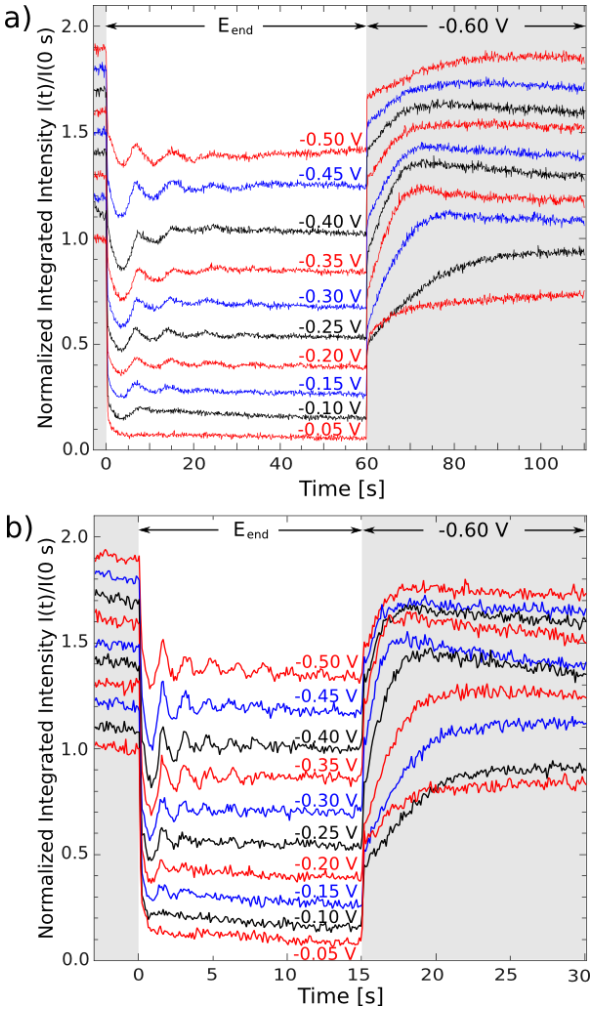

Fig. 3: Background-corrected integrated x-ray intensity at (1,1,0.1) as a function of time during Cu deposition on Cu(001) at different potentials in 0.1 M $HClO_4$ + 1 mM HCl containing **(a)** 1 mM $Cu(ClO_4)_2$ and **(b)** 5 mM $Cu(ClO_4)_2$. Both data sets show a transition from layer-by-layer growth, indicated by growth oscillations, to 3D growth with increasing potential. In the experiments the potential was stepped from -0.60 V (shaded areas) to a potential E_{end} and then back to -0.60 V. The curves are normalized to the initial intensity before the potential step and shifted with respect to each other by an offset of 0.1.

Layering oscillations are observed for potentials < -0.15 V. However, the oscillations are less pronounced with increasing potential, *i.e.,* their amplitude decreases. As argued before, this decrease of the oscillation amplitude reveals a deviation from ideal layer-by-layer to smooth multilayer and 3D growth with increasing potential. We will show in the following, that this finding is supported by (i) inspecting the ratio I_C/I_B, indicative for roughness evolution during growth and (ii) the detailed shape of the transients.

Conclusions on the extent of roughening during the growth process at each potential may be drawn from a comparison of the saturation intensity I_C obtained after prolonged growth with the initial intensity I_B found at E_{end} after adsorption of Cl. The ratio I_C/I_B (figure 4b) is a direct measure of the growth-induced decay in the average intensity due to increasing surface roughness [32]. For the potential range from -0.50 V to -0.35 V, the ratio stays at

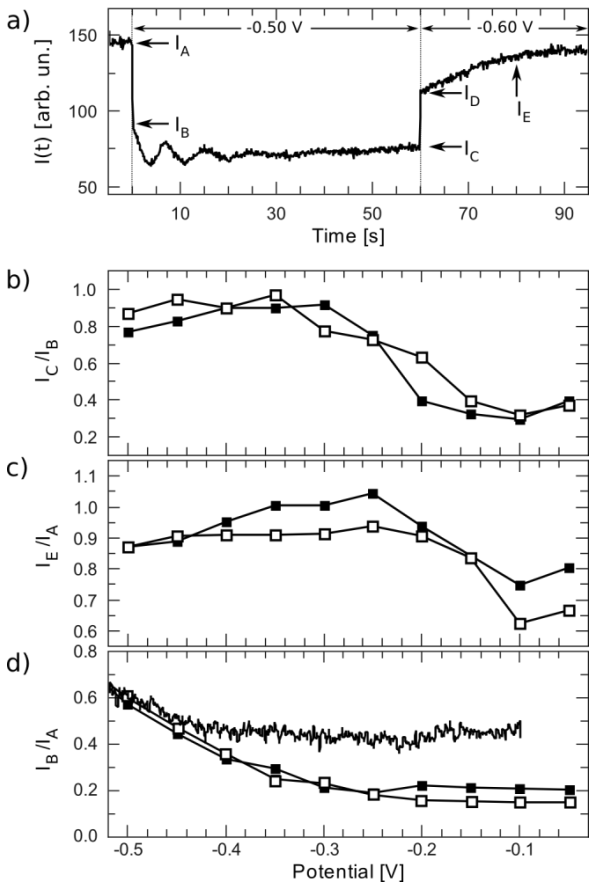

Fig. 4: (a) Example of an intensity transient taken from fig. 3. The labels I_A to I_E denote the intensity values at characteristic stages of the experiment (*cf.* text). Intensity ratios **(b)** I_C/I_B **(c)**, I_E/I_A, and **(d)** I_B/I_A obtained as a function of potential in 0.1 M $HClO_4$ + 1 mM HCl containing 1 (open squares) and 5 mM (filled squares) $(CuClO_4)_2$-containing electrolyte. For comparison, the potential-dependent intensity measured in Cu-free electrolyte (solid line) is included in (**d**).

a rather constant, high value of approximately 0.9. Hence, no substantial roughening of the surface occurs, indicating a rather ideal layer-by-layer growth. In contrast, at potentials > -0.35 V the ratio decreases significantly at more positive potentials, down to a value of ~ 40% positive of -0.20 V. This decrease clearly indicates a rougher surface morphology and thus a transition from (ideal) layer-by-layer to smooth multilayer [35] or 3D island growth towards more positive potentials.

Equivalent evidence for a potential-dependent transition from layer-by-layer to smooth multilayer or 3D growth is found by comparing the intensities measured at -0.60 V before and after growth at the potential E_{end} ,*i.e.*, the ratio I_E/I_A (figure 4c). The I_E values were obtained 20 s (1 mM $Cu(ClO_4)_2$) or 5 s (5 mM $Cu(ClO_4)_2$) after the step back to -0.60 V and correspond to the saturation value after initial recovery of the surface. For steps to potentials < -0.20 V I_E/I_A is close to 1, that is, the surface completely recovers within the time required to deposit 1-3 ML. In contrast, at more positive potentials, especially at -0.10 and -0.05 V, I_E/I_A becomes noticeably smaller, suggesting that the (3D) Cu deposition in this potential regime induces a more permanent surface roughness that is only incompletely reduced by the surface smoothing at -0.60 V (in fact, also in these cases the original intensity can be regained almost completely by a second, much slower smoothing process, occuring during the following 5 min. and the subsequent electrolyte exchange). Although the potential dependence of I_E/I_A is qualitatively similar to that of I_C/I_B, the decrease occurs at both copper concentrations at slightly more positive potentials for I_E/I_A. Consequently, despite a substantial surface roughening during growth at potentials between -0.30 and -0.20 V, the surface quality still quickly recovers under step-flow conditions. This can be explained by a smooth multilayer growth behavior in this potential regime, which also is supported by the observation of growth oscillations (see figure 3). In contrast, the more pronounced roughening at more positive potentials is attributed to a 3D growth mechanism, in accordance with the absence of such oscillations.

The above conclusions also manifest in the overall time-dependent evolution of the average intensities of the transients in figure 3, obtained by averaging I(t)/I(0) over a full oscillation period, *i.e.*, by removing the oscillatory component of the curves. Since the effects are more pronounced in the lower concentrated electrolyte, the discussion will focus on the transients shown in figure 3a. For the potentials from -0.50 V to -0.30 V, the average intensity exhibits over the first 30 s a constant value (*e.g.* -0.50 V) or increases slightly with deposition time (*e.g.* -0.40 V) until the intensity is close to the initial value I_B (see above). This indicates smooth growth at these potentials, where the layer-by-layer mechanism proceeds rather ideal, in agreement with the aforementioned conclusions. At more positive potentials (-0.25 to -0.20 V), this curve exhibits a constant lower value. An initially induced surface roughness due to the restructuring after the potential step is not compensated any more, at least not on the time scale of the performed experiment. Thus, the layer-by-layer mechanism tends to rougher growth, but the roughness remains at a constant finite value, indicating smooth multilayer growth. At the most positive potentials, -0.20 V to -0.05 V, a negative slope of the curve clearly indicates the gradual increase of surface roughness due to 3D growth.

Similar growth experiments were also intended with higher concentrated solution containing 20 mM $Cu(ClO_4)_2$. In this case the electrolyte exchange, performed at -0.60 V, resulted in an instantaneous decrease of the intensity to the background value, *i.e.*, the (1,1,0.1) peak completely disappeared. This indicates substantial roughening of the surface due to 3D growth during the exchange process, when the diffusion-limited current is particular high. Since the surface quality did not recover after this exchange, further experiments at this concentration were not attempted.

Under diffusion-limited conditions, as employed in these studies, the adatom flux is independent of the applied electrode potential. The observed potential-dependence of the growth behavior therefore has to be related to potential-dependent changes of the surface transport processes. The transitions from step-flow to layer-by-layer and then to 3D island growth indicate a decreasing Cu surface mobility with increasing potential. This behavior is clearly correlated with the potential-dependent structure of the chloride adlayer.

According to previous studies [11] in Cu-free electrolyte, the coverage and structural order of adsorbed Cl is potential dependent. Measurements during potential cycles in Cu-free solution (figure 4d, line) show that these variations with potential are highly reversible, *i.e.*, that the scattered intensity is a well-defined function of potential. Specifically, with increasing potential, the Cl coverage on the surface increases, leading to a decrease in intensity at (1,1,0.1) (see figure 1). The same trend is observed in Cu-containing electrolyte. Here, the intensity I_B after Cl adsorption, normalized by the initial intensity I_A before the

potential step (figure 4d, solid and open symbols), exhibits the same qualitative behavior. However, deviations from the results obtained in Cu-free electrolyte are observable for potentials >-0.45 V, where I_B/I_A is significantly lower. We assign this behavior to the additional effect of increased surface roughness after the potential step (see also discussion below).

At -0.60 V, chloride is adsorbed on the sample surface in form of a mobile adlayer with a Cl coverage in the range of 0.15 ML [11]. Under these conditions, the surface diffusion of deposited Cu atoms is apparently so high that all adatoms reach step edges, resulting in the observed step-flow growth. Positive of -0.57 V, the c(2×2) phase starts to develop on the surface. With increasing potential, the coverage of adsorbed Cl and the surface fraction of ordered areas increase, reaching saturation at approximately -0.30 V. The observed layer-by-layer growth in this intermediate potential regime suggests that the surface mobility of Cu is substantially lower in the presence of the partially c(2×2)-ordered Cl adlayer, but (under the employed deposition conditions) still sufficiently high to allow coalescence of the Cu adatom islands before deposition of the next layer commences. Once the c(2×2) adlayer is fully developed in the saturation regime above -0.30 V, the copper surface mobility is even more reduced, resulting in Cu nucleation on top of existing Cu islands and the onset of 3D surface growth. These trends in surface mobility are in accordance with previous STM observations by Vogt et al. [10].

3.3 Cl Adlayer Structure during Cu Growth

In addition to the measurements performed at (1,1,0.1), analogous studies were carried out at the position of the c(2×2) Cl superstructure rod in order to investigate the interdependency of the growth process and the ordering behavior of the c(2×2) Cl adlayer. Also here the intensity measurements were performed under grazing incidence conditions, corresponding to a reciprocal space position of (1,0,0.1).

In Cu-free electrolytes, our earlier studies revealed that steady-state intensities are typically obtained faster than 0.1 s upon potential steps [11], indicating a quick ordering/disordering process of the c(2×2). In 1 mM Cu-containing electrolyte, also an almost instantaneous increase in intensity (within < 0.1 s) from 0 at -0.60 V to an initial value > 0.5 of the long-term saturation value is observed. However, instead of remaining at a constant value the subsequent intensity transient exhibits a complex time-dependence, specifically a decrease for a few seconds and a subsequent increase to a maximum value.

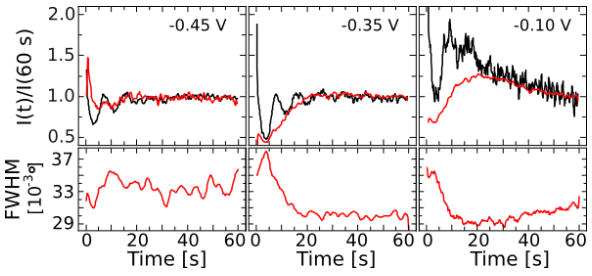

Fig. 5: Time-dependent integrated intensity (top panel, red line), and as FWHM (bottom panel) of the c(2×2) superstructure rod at (1,0,0.1) after potential steps from -0.60 V to the indicated potentials E_{end} in 1 mM $Cu(ClO_4)_2$-containing electrolyte. The black curve shows the corresponding intensity at (1,1,0.1). The intensity values were normalized to the intensity at 60 s for better comparability.

Figure 5 shows examples of the time-dependent integrated intensity (top panel, red line) as well as the FWHM (bottom panel, red) of the superstructure rod at (1,0,0.1) upon potential steps from -0.60 V to -0.45, -0.35 and -0.10 V in 1 mM $Cu(ClO_4)_2$-containing electrolyte. For comparison, the corresponding intensity curves at (1,1,0.1) from figure 3a are shown as well (black lines). All transients are normalized to the intensity at 60 s in order to ensure a better comparability (note that the absolute peak intensities on the partial c(2×2)-covered surface at -0.45 V are significantly lower than those at the more positive potentials, resulting in a more noisy signal).

We first discuss the behavior at -0.45 V, where the intensity at (1,1,0.1) shows layer-by-layer growth oscillations over ~30 s. During the growth of the first half monolayer (~5 s) after the potential step, the intensity measured at the c(2×2) superstructure rod decreases, but slightly increases again during the growth of the subsequent layers. Superimposed on this rise in signal seem to be weak oscillations, which are in phase with the oscillations at (1,1,0.1). At the time when the oscillations at (1,1,0.1) fade completely a constant saturation value is reached. The FWHM of the (1,0,0.1) Cl peak shows an approximately constant value throughout the transient.

At -0.35 V, where the transient at (1,1,0.1) exhibits similar growth oscillations, the intensity at (1,0,0.1) first slightly decreases during the first ~3 s and then substantially increases with time until it reaches a constant value of about twice the intensity of the initial value after the potential step. Again the intensity saturates approximately in parallel to the fading of the oscillations at (1,1,0.1). However, in contrast to the behavior at -0.45 V the time dependent transient of the FWHM of the c(2×2) superstructure rod at (1,0,0.1) exhibits, apart from an initial increase, a substantial decrease from 0.037° (>850 Å) to 0.030° (>1050 Å) in parallel to the intensity increase. Once the intensity reaches its maximum, the FWHM stays at a constant, low value. In view of the square symmetry of the Cu substrate, not only an radial broadening of the diffraction peak, manifesting in the FWHM, but also a similar broadening along the azimuthal direction in reciprocal space is expected, which is not accounted for by the integration of the 1D detector scans. The latter can partially explain the parallel changes in intensity and FWHM. Assuming an isotropic broadening of the superstructure rods, an estimate for the total integrated intensity, which is a measure of the degree of c(2×2) ordering in the Cl adlayer, can be obtained by multiplying I(t) with the FWHM. Applying this estimation to the transient at -0.35 V, the product I(t)·FWHM still increases by ~60 % between 3 and 20 s, suggesting that not only the c(2×2) domain size, but also the overall amount of c(2×2) order increases over this time period.

At the most positive potentials (-0.10 V), where the transient at (1,1,0.1) indicates predominant 3D growth, a clearly different behavior is found. Similar to the observations at -0.35 V, the intensity transient of the c(2×2) superstructure rod at (1,0,0.1) exhibits an increase in intensity to approximately the double of the initial value within the first ~20 s. However, after this increase, a continuous decay in intensity is observed, resembling the decrease at (1,1,0.1) due to the ongoing surface roughening after growth of the second layer. In parallel the FWHM of the peak at (1,0,0.1) slightly increases during the last 40 seconds of the scan. The relative changes of the FWHM over the latter time period are similar to the reciprocal changes in intensity, *i.e.*, the total in-plane intensity of the rod (estimated via I(t)·FWHM under the same assumptions as before) remains approximately constant. Hence, the behavior at times >20 s can be simply explained by the

shrinking terraces size, resulting from the roughening of the surface in the 3D growth regime.

In all three cases, the observed intensity transients at the Cl superstructure rod, although not exhibiting clear oscillations, resemble the average temporal evolution of those obtained at (1,1,0.1). The FWHM transients seem to be consistent with the corresponding integrated intensity transients (this is most obvious for the potentials -0.35 and -0.10 V). That is, the initial decrease during growth of the first half monolayer occurs in parallel to an increase in the FWHM, whereas the subsequent intensity increase is accompanied by a decrease in the FWHM. These findings are interpreted as changes in the size of coherently scattering domains of the ordered c(2×2) Cl adlayer, which depend on the detailed shape of the surface during the growth process.

These observations can be rationalized by the following model, which takes the mutual interactions of Cu adatoms and Cl adsorbates and their influence on the surface mobility of these surface species into account. Evidence for such interactions is also found in previous studies of Cu(001) in Cl-containing solution, in particular in the pronounced tendency to step faceting along the [100] directions [10,12-14]. Under the conditions of our experiments, the flux of the deposited species, *i.e.*, the rate by which Cu adatoms are formed on the the surface, is determined solely by diffusion-limited transport in the electrolyte and hence independent of time and potential. At the initial potential of -0.60 V the surface is covered by a low density, disordered Cl adlayer that permits a high surface mobility of Cu adatoms. Cu adatoms are therefore rapidly transported to existing step edges, resulting in a low adatom density on the terraces. Consequently, the nucleation probability of Cu monolayer islands is low and the growth proceeds via step flow.

The potential step to values ≥-0.50 V causes a rapid increase in the Cl surface coverage and the (partial) formation of the c(2×2) phase on the surface. This, on the one hand, leads to a substantial reduced Cu surface mobility. As a result, the Cu adatom density on the terraces rapidly rises until the nucleation threshold is reached and formation of Cu monolayer islands commences. In the regime where the surface is fully covered by the c(2×2) adlayer phase the mobility is apparently sufficiently low to promote nucleation on existing islands, suggesting that not only surface diffusion on terraces, but also interlayer transport is affected.

On the other hand, the presence of Cu adatoms *vice versa* also seems to severely affect the Cl surface dynamics, resulting in kinetic limitations of the Cl adlayer ordering. These are particularly noticeable in the potential regime ≥-0.45 V where the surface is (almost) fully covered by the c(2×2) adlayer phase. Here the total in-plane intensity (I(t)·FWHM) at (1,0,0.1) reaches saturation only after ~20 s, *i.e.*, on more than two orders of magnitude longer times scales as in Cu-free solution, where ordering occurs within <0.1 s. According to these observations the presence of Cu adatoms under growth inhibits the disorder-order phase transition. Support for this also comes from the initially high intensity and low FWHM after the potential step, when the Cu adatom concentration still is close to the (much lower) equilibrium value found at -0.60 V. Parallel to the increase in Cu adatom concentration within the first seconds at E_{end} the intensity drops, illustrating directly the adverse effects of Cu adatoms on the Cl ordering dynamics. At lower potentials, where the surface is only partially covered by the c(2×2) phase these mutual inhibitions of Cu adatom transport and Cl ordering are obviously less severe.

3.4 Oscillatory In-Plane Lattice Spacing

Further information can be obtained by a detailed analysis of the (1,1,0.1) peak shape under growth conditions. In figure 6a, the intensity I(t, δ) as a function of time and scattering angle δ, obtained from the 1D frames recorded during the first 30 s after a potential step to -0.50 V in 1 mM $Cu(ClO_4)_2$-containing electrolyte, is shown as a color map. In accordance with figure 3a, layer-by-layer growth oscillations in the intensity are clearly observable. Whereas the intensity distribution flank at higher scattering angles remains at a constant value, the flank at lower scattering angles exhibits a time-dependent structure. Hence, in addition to the amplitude, the width and the average position of the intensity distribution changes with time.

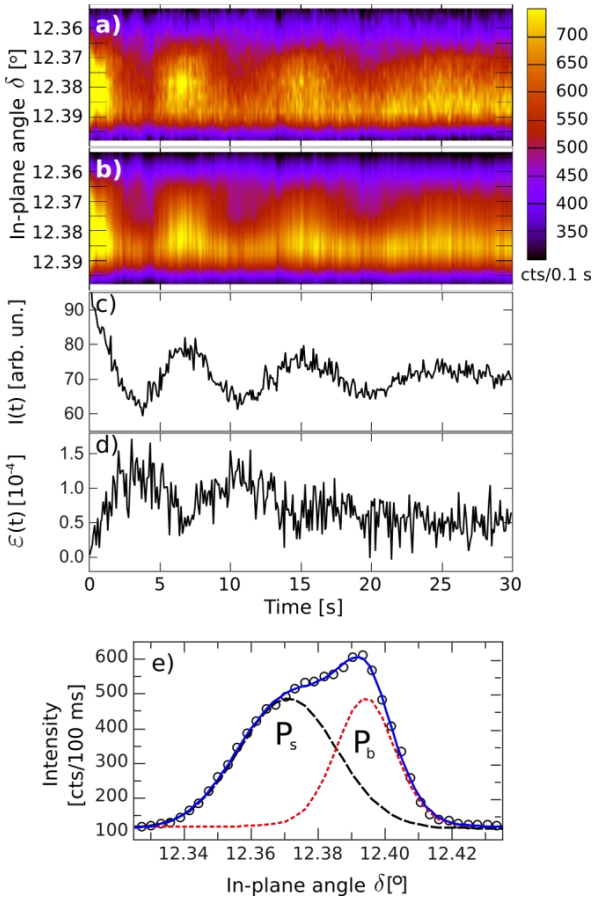

Fig. 6: (a) Intensity map of the 1D frames at (1,1,0.1) as a function of time, obtained after a potential step at t = 0 s to -0.50 V in 1 mM $Cu(ClO_4)_2$-containing electrolyte, and **(b)** corresponding best fit by the model described in the text. **(c)** Integrated intensity and **(d)** strain, determined from the fit results. **(e)** Peak profile at (1,1,0.1) obtained by averaging the frames between 2.3 and 5 s. The asymmetry suggests the existence of two peaks at slightly different positions, *i.e.,* different in-plane lattice spacings.

The latter effect was analyzed by determining the time-dependence of the averaged peak position $\delta_{av}(t)$ during the growth process. To obtain $\delta_{av}(t)$, we first fitted the intensity in each 1D detector frame by a sum of two pseudo-Voigt functions (indexed with 's' and 'b', respectively) and a linear background. The choice of this fit function was motivated by the observation of a peak splitting in the raw data, manifesting in a pronounced

shoulder (figure 6e). Within this model, both peak amplitudes (I_s, I_b), the background, and the position δ_s and full width at half maximum ($FWHM_s$) of the peak P_s at lower scattering angles were free fitting parameters. The position of the peak P_b at higher scattering angles was kept constant at $\delta_b = 12.389°$ for all frames. Systematic studies showed that at this δ_b value the χ^2 of the fits exhibit a clear minimum. In addition, also the width of P_b could be set to a constant value ($FWHM_b = 2.63 \cdot 10^{-2}$ °) without impairing the fit quality and the obtained result. All curves discussed below correspond to fit results based on the aforementioned constraints and yielded a χ^2 that was approximately independent of time, a behavior, which could not be achieved with a different choice of parameter settings. The intensity distribution corresponding to the best fit result for the data shown in figure 6a is presented in figure 6b. Obviously, all distinctive features, the oscillations as well as the frayed flank at lower scattering angles, are well reproduced.

From these results, we calculated the averaged peak position $\delta_{av}(t)$ as the first standardized moment (weighted mean value) of the in-plane angle dependent intensity distribution via $\delta_{av} = (I_s \cdot \delta_s + I_b \cdot \delta_b)/(I_s + I_b)$. In figure 6c and 6d, the total integrated intensity and the corresponding resulting strain, defined as $\varepsilon(t) = (\delta_{av}(t) - \delta_{av}(0\ s))/\delta_{av}(0\ s)$, are shown, respectively. Here we have utilized the fact that the peak position $\delta_{av}(0\ s)$ at -0.60 V is identical to the peak position found in Cu-free solution (see 3.1), and hence should not include deposition-induced strain (see also discussion below). Over the entire transient a positive strain, corresponding to an expansion of the in-plane Cu lattice, in the range of 10^{-4} is found. Clearly, an anti-phase shift of the strain relative to the integrated intensity can be observed in the transient, *i.e.,* the averaged strain increases for fractional surface coverages and has a local minimum when the layer is completed and the surface roughness is particularly low.

These findings strongly resemble observations by Fassbender *et al.* for Cu homoepitaxial deposition on clean Cu(001) surfaces under UHV conditions [29], measured with reflection high energy electron diffraction (RHEED). Also in this work the authors observe an oscillating in-plane lattice spacing of the topmost layer as a function of deposited Cu coverage, which exhibited an anti-phase correlation between strain and intensity. Based on these observations they suggested periodic expansions of the topmost layer for fractional coverages. This effect, first discovered and quantitatively explained by Massies and Grandjean [45] for $In_xGa_{1-x}As$ grown on GaAs, has been reported for diverse heteroepitaxial as well as homoepitaxial systems, *e.g.*, Co/Cu, Cu/Cu, FeNi, V/Fe, Mn/Fe, and CdTe [29,46-52]. Theoretical calculations and descriptions were given by Kern and Müller [53-55]. According to Massies and Grandjean, the oscillatory expansion of the in-plane lattice spacing can be explained by considering a nontetragonal elastic distortion of strained edges of deposited islands [45]. This expitaxial strain is assumed to result from a reduced coordination number of the atoms in the island edges. Specifically, the strain is maximal for half coverages. In addition, Lysenko *et al.* and Stepanyuk *et al.* confirmed by model calculations that an island size dependent mesoscopic mismatch in homoepitaxially grown deposits exists [56,57]. In detail, they demonstrated that vertical strain relaxations at the edges of single or double layer square Cu islands on both Cu(111) and Cu(001) lead to a strongly inhomogenous stress and strain distribution (strain field) both in the islands and the substrate, which may also cause in-plane lattice spacing variations. These strain fields typically decay towards the island center.

However, it should be noted that the extent of the strain effects (10^{-4}) observed in our study is about an order of magnitude smaller than reported by Fassbender *et al.* in ref. [29]. This may be caused by the different environment as well as by the different experimental methods employed by Fassbender *et al.* and by us: First, the c(2×2) chloride adlayer, which is present under electrochemical conditions at the potential studied here, is known to strongly influence the surface morphology, in particular inducing step faceting along the [100] directions[10,18-20]. This modification of the step structure may well affect the associated strain fields. Second, although RHEED and SXRD are both very sensitive to the arrangement of atomic layers in vicinity of the surface, the penetration depth of x-rays is much larger than for high energy electrons, which essentially are restricted to the first 1-2 surface layers. Therefore, in our study an effective strain is probed, which is much smaller than the strain effects determined by RHEED experiments.

Whereas Fassbender *et al.* restricted their analysis to the peak position and intensity, we discuss additionally the detailed peak shape of the time-dependent intensity distribution (fig. 6e). This provides a more comprehensive view, which allows a more detailed analysis of the observed surface effects.

In particular, the effective strain should manifest in two separated peaks at different diffraction angles. The existence of such two peaks, or at least an asymmetry in the peak shape, was also subject of a controversial discussion of RHEED observations by Müller *et al.*, where a 1% contraction of the topmost layer of Cu(001) in UHV due to tensile stress in the surface was reported [58]. In two independent comments, Baddorf *et al.* and Robinson *et al.* [59,60] stated that such an effect should be clearly observable using SXRD, specifically in a second, displaced diffraction peak or an asymmetry of the main diffraction peak. In a later low-energy electron diffraction study, Ovsyanko et al. found evidence for such a displaced diffraction peak, which they attributed to the formation of one-dimensional nanogrooves, induced by ion-bombardment, which involve the creation of steps that enable the observed 1% reconstruction. Similar evidence for the occurrence of displaced diffraction peaks was reported for the homoexpitaxial growth and sputtering of CdTe [50,51], although no detailed analysis of the time-dependence of these two peaks was performed.

In the following we interpret the time-dependent behavior of the peak shape within the two peak model employed in our fits, where we assign each peak to a distinct phase with a different in-plane lattice spacing and a defined surface coverage. Concretely, peak P_s corresponds to a phase consisting of the strained areas, which are located in the vicinity of steps, adatoms (see below), and other suface defects and have a defined width that corresponds to the effective extension of the local strain field. All remaining surface areas are assumed to be unstrained and contribute to peak P_b, which is constant in position. This simplified description neglects the gradual change in lattice spacing with increasing distance from the steps or adatoms, expected in reality [61]. However, a more sophisticated treatment would require data with significantly improved counting statistics, which cannot be obtained in these fast SXRD measurements. Our simplified model should capture the essential origin for the presence of two diffraction peaks with varying intensity and (in the case of P_s) position. Other explanations, e.g. the presence of two domains tilted with respect to each other or other macroscopic sample inhomogeneities [62], could not account for the observed time dependent behavior and therefore can be ruled out.

The variation in the fit parameters as a function of time at E_{end} is shown in figure 7 for the data presented in figure 6 as well as two other experiments, illustrating the behavior at different

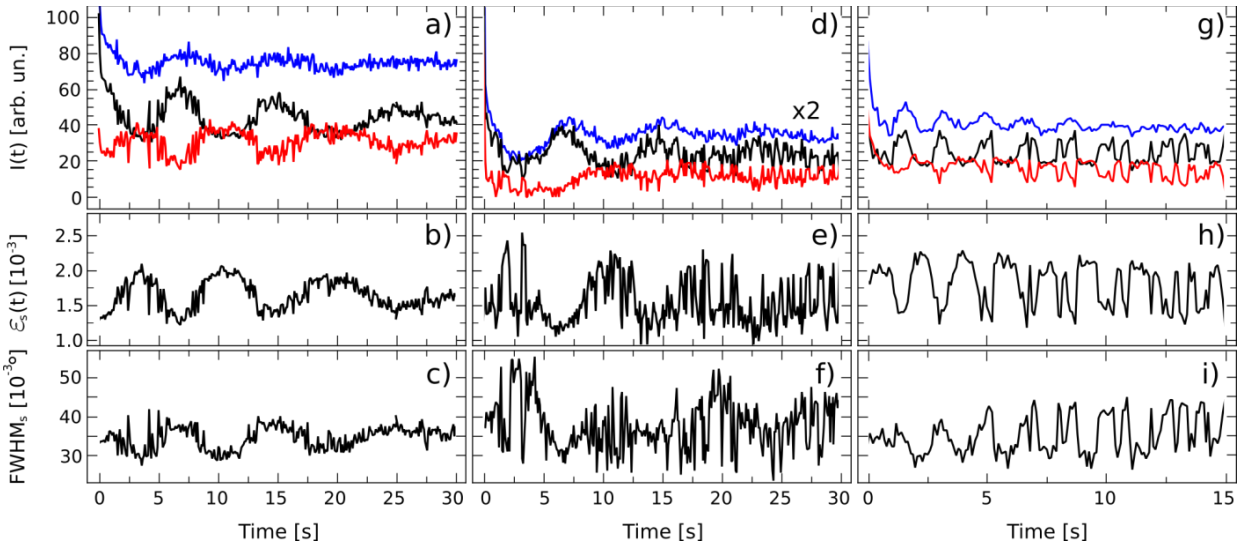

Fig. 7: Time-dependence of the obtained fit parameters for the experimental data after potential steps (at t 0 0 s) to -0.50 V (a-c) and -0.20 V (d-f) in 1 mM $Cu(ClO_4)_2$-containing electrolyte and to -0.50 V in 5 mM $Cu(ClO_4)_2$-containing electrolyte. **(a,d,g)** Integrated intensity of strain peak P_s (black), bulk peak P_b (red) and the sum of both peaks (blue). **(b,e,h)** Strain ε_S, obtained from the in-plane lattice spacing d_s of the strain peak. **(c,f,i)** FWHM of the strain peak.

potential (E_{end} = -0.20 V) or different Cu-concentration (5 mM $Cu(ClO_4)_2$-containing electrolyte). In all three cases, oscillations in the integrated intensities of both peak P_s and peak P_b are found, which are anti-phase shifted with respect to each other (figure 7a,d,g). The total integrated intensity (blue curve) oscillates in phase with the intensity of the strain peak P_s (black), but with a reduced amplitude due to the anti-phase shifted contribution of the bulk peak P_b (red). Consequently, the observed oscillations in figure 3 can be primarily attributed to the strained peak.

The position δ_b of the fixed peak P_b is at larger values than that of the initial (average) peak position in Cu-free solution, suggesting that the presence of steps on the original surface prior to Cu growth already induces noticeable strain. It therefore seems reasonable to assume that δ_b corresponds to the true bulk value and to calculate the strain ε_s in the strained areas from the relative separation of peak P_s from P_b via $\varepsilon_s(t) = (\delta_s - \delta_b)/\delta_b$ (figure 7b,e,h). We explicitly note that this procedure differs from that employed in our previous determination of the average strain ε (figure 6d) as well as in the work of Fassbender *et al.* [29]. Specifically, the resulting values are significantly larger.

Also $\varepsilon_s(t)$ exhibits oscillations, which are anti-phase shifted with respect to the oscillations in intensity of the peak P_s of the strained phase (figure 7a,d,g). Furthermore, oscillations are also observed in the width of peak P_s ($FWHM_s$), however, those do not have a well-defined phase shift with respect to the corresponding intensity curves. Whereas for the potential steps to -0.50 V an in-phase oscillation with the corresponding integrated intensity of P_s is found at both concentrations (figure 7c,i), a phase shift of π is found for the potential step to -0.20 V (figure 7f). It should be noted that also in other experiments with potential steps into the range -0.50 to -0.20 V (not shown) the intensity and strain ε_s exhibit the same time-dependent behavior, whereas the $FWHM_s$ seems to continuously change from approximately in-phase (-0.50 V) to largely out-of-phase (-0.20 V) with increasing potential.

The observation of the out-of-phase correlation of strain and intensity (fig. 7a/b), where the strain increases while the scattered intensity from the strained parts of the surface decreases, remains incomprehensible in a model based solely on strain contributions by step edges of islands and terraces. Hence, we propose to extent the model by Massies and Grandjean [45] by additionally taking strain contributions from other surface defects into account, in particular from deformations induced by adsorbed metal adatoms. The latter effect has been subject of many experimental and theoretical studies, which largely focused on the resulting surface stress [61,63-72]. According to these studies, the presence of low sub-monolayer coverages of undercoordinated adatoms at the substrate surface results in force-dipols which act on small regions of the surface and thus cause surface stress. Typically, the induced surface lattice displacements decay with the inverse square of the distance from the adsorption site. Moreover, calculations as well as *in situ* stress measurements during expitaxial growth of metal films revealed that the adatom induced surface stress has significant impact on the growth mechanisms and defect formation during crystal growth [64,71-75].

Taking this effect into account, the observed strain in our measurements includes contributions from the step edges of islands and terraces as well as from isolated adatoms present on the surface during deposition. Each of these defects will induce a strain field of characteristic extension in its vicinity. The magnitude of the strain associated with a single adatom will be considerably smaller than that originating from a step. However, the adatoms are rather uniformly distributed over the terraces of the substrate and hence capable of influencing a much larger surface fraction than the steps, whose average separation is determined by the average island searation, i.e., the nucleation density, or (in the case of step flow growth) the sample miscut. (The chloride coadsorbate is ignored, since it should not affect the time-dependence of the stress evolution after equilibrium coverage is reached within the first 0.1 s after the potential step).

Based on these considerations we propose the following microscopic scenario to tentatively explain the observed time-dependent behavior (illustrated schematically in figure 8). At -0.60 V growth proceeds via step flow and the step density on the surface is low. After the change to a more positive potential

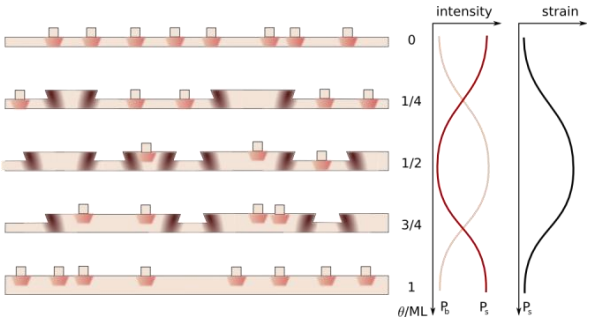

Fig. 8: Schematic model for microscopic mechanisms, underlyingthe observed time-dependence of the integrated intensities and strain. The adatoms are assumed to induce a small (red) and step edges a more pronounced (dark red) strain field.

the step density initially is unchanged, but the adatom density on the terraces rapidly increases due to the slower rate of surface transport to existing steps. As a result, the coverage of strained areas and consequently the intensity of peak P_s is large, but dominated by the contribution of the adatoms, which produce a low average strain ε_s (figure 8, θ = 0 ML). With increasing deposition time, nucleation and growth of monolayer islands on the surface commences. The steps of these islands act as sinks for Cu adatoms and the adatom density decreases, reaching a minimum at ~0.5 ML coverage of the topmost Cu layer, where the step density is maximal and the average distance an adatom has to travel before arriving at a step is minimal. The contribution of the steps to ε_s is now much larger, resulting in a larger strain value. However, since the overall step density is still relatively low (as indicated by the rather small peak widths), the total coverage of the strained areas and hence the intensity of P_s decreases in parallel with the decrease in adatom density (figure 8, θ = ½ ML). With ongoing deposition, the islands grow and the adatom density on the topmost layer increases again (figure 8, θ = ¾ ML) until the islands finally coalesce. This results in decreasing averaged strain and increasing intensity of P_s. This cycle repeats in the deposition of the subsequent layers, leading to the observed oscillatory behavior. The coverage of the remaining unstrained areas and the associated intensity of peak P_b obviously will show similar oscillations, which will exhibit a minimum when the coverage of strained areas is maximal and *vice versa*.

This model provides a reasonable explaination of the observed time-dependent behavior of intensity and strain. However, the time-dependence of the FWHM of the strain peak remains an open question. This is mainly related to the fact that the physical interpretation of the FWHM strongly depends on the underlying physical model. In view of the simplicity of our model, which neglects the existence of gradual changes between strained and unstrained surface areas, an interpretation was not attempted.

4. Conclusion

The *in situ* surface x-ray scattering studies of Cu(001) homoepitaxial electrodeposition in chloride-containing electrolyte presented here provide detailed insight into the underlying atomic-scale processes. With the time resolution of 0.1 s, made possible by the use of a fast one-dimensional detector system, the growth behavior could be observed at much higher deposition rates than in previous microscopic studies, specifically at ~7.6 and ~38.0 ML/min in 1 mM and 5 mM $Cu(ClO_4)_2$-containing electrolytes, respectively.

Our results indicate a pronounced mutual interaction of the Cl adlayer order and Cu growth. On the one hand, the presence of the c(2×2) Cl adlayer substantially influences the growth behavior and the resulting surface roughness, an effect we attributed to a reduction in the Cu surface mobility in the presence of this phase. Whereas at -0.60 V, where the adlayer is disordered, the data suggest step flow growth, oscillations in the potential regime of the (partially) c(2×2) ordered Cl adlayer indicating layer-by-layer growth were observed. In the potential range of the fully c(2×2) covered surface smooth multilayer growth and – at the most positive potentials – 3D growth is found. On the other hand, the kinetics of the c(2×2) adlayer ordering is orders of magnitude slower during Cu deposition than in Cu-free solution. Apparently, the presence of a high surface density of Cu adatoms on the substrate terraces substantially affect the order-disorder transition.Furthermore, from a detailed analysis of the anti-Bragg peak shape during growth, an oscillatory average strain in the surface layer is deduced, similar to findings by Fassbender *et al.* for the homoepitaxial growth of Cu(001) in UHV [29].

Our study demonstrates the possibility to obtain atomic-scale information on the surface structure of Cu electrodes *in situ* during electrochemical growth at moderately high growth rates. In order to further approach the conditions employed in technological plating process, such studies have to be performed at even higher deposition rates and in electrolytes of more complex composition. In particular, in industry organic additives, acting as levelers or brighteners, are commonly added to the plating bath. Fundamentally clarifying the influence of such additives on the crystal growth will be an important objective of future studies by this method.

Acknowledgements

We gratefully acknowledge the European Synchrotron Radiation Facility for providing synchrotron radiation facilities and the ID32 beamline staff for technical support, especially P. Rajput and L. André. We further thank the Deutsche Forschungsgemeinschaft for financial support via MA 1618/13-3.

REFERENCES

[1] P. C. Andricacos, C. Uzoh, J. O. Dukovic, J. Horkans, H. Deligianni, *IBM J. Res. Dev.* **42**, 567 (1998)
[2] D. Edelstein, J. Heidenreich, R. Goldblatt, W. Cote, C. Uzoh, N. Lustig, P. Roper, T. McDevitt, W. Motsiff, A. Simon, J. Dukovic, R. Wachnik, H. Rathore, R. Schulz, L. Su, S. Luce, J. Slattery, *Technical Digest, IEEE International Electron Devices Meeting* 1997, 773
[3] M. Datta, Electrodeposition, In Advanced Nanoscale ULSI Interconnects, Y. Shacham-Diamon, T. Osaka, M. Datta, T. Ohba (eds.), Springer 2009
[4] R. Rosenberg, D. C. Edelstein, C.-K. Hu, K. P. Rodbell, *Annu. Rev. Mater. Sci.* **30**, 229 (2000)
[5] T. P. Moffat, J. E. Bonewich, W. H. Huber, A. Stanishevsky, D. R. Kelly, G. R. Stafford, D. Josell, *J. Electrochem. Soc.* **147**, 4524 (2000)
[6] N. Ibl, In Comprehensive Treatise of Electrochemistry. J., E. Yeager, J. O'M. Bockris, B. Conway (eds.), Plenum Press, New York 6(1), 133, 239, (1982)
[7] J. W. Dini, In Modern Electroplating, M. Schlesinger, M. Paunovic (eds.), 4th edition, Wiley Interscience, New York, 61 (2000)
[8] R. Winnad, *Electrochim. Acta.* **39**, 1091 (1994)
[9] V. S. Donepudi, R. Venkatachalapathy, P. O. Ozemoyah, C. S. Johnson, J. Prakash, *Electrochem. Solid-State Lett.* **4**, C, 13 (2001)
[10] M.R. Vogt, A. Lachenwitzer, O.M. Magnussen, R.J. Behm, *Surf. Sci.* **399,** 49 (1998)
[11] Y. Gründer, D. Kaminski, F. Golks, K. Krug, J. Stettner, O. M. Magnussen, A. Franke, J. Stremme, E. Pehlke, *Phys. Rev. B* **81**, 174114 (2010)
[12] D.W. Suggs, A. J. Bard, *J. Phys. Chem.* **99,** 8349 (1995)
[13] T.P. Moffat, *Mater. Res. Soc. Symp. Proc.* **404**, 3 (1996)
[14] T.P. Moffat, *Mater. Res. Soc. Symp. Proc.* **451**, 75 (1997)
[15] W. Polewska, R. J. Behm, O. M. Magnussen, *Electrochim. Acta* **48,** 2915 (2003)
[16] O. M. Magnussen, L. Zitzler, B. Gleich, M. R. Vogt, R. J. Behm, *Electrochim. Acta* **46**, 3725 (2001)

[17] B. Ocko, I. Robinson, M. Weinert, R. Randler, D. Kolb, *Phys. Rev. Lett.* **83**, 780 (1999)
[18] Q. Wu, D. Barkey, *J. Electrochem. Soc.* **144**, L261 (1997)
[19] Q. Wu, D. Barkey, *J. Electrochem. Soc.* **147**, 1038-1045 (2000)
[20] Q. Wu, D. Barkey, *J. Electrochem. Soc.* **150**, C533-C537 (2003)
[21] S. Huo, W. Schwarzacher, *Phys. Rev. Lett.* **86**, 256 (2001)
[22] G. Rosenfeld, B. Poelsema, G. Comsa, in: D.A. King, D.P. Woodruff (Eds.), Growth and Properties of Ultrathin Epitaxial Layers, vol. 8, Elsevier Science B.V., Amsterdam, 1999, p. 66.
[23] J. F. Wendelken, A. K. Swan, W.-W. Pai, and J.-K. Zuo, in *Morphological Organization in Epitaxial Growth and Removal*, chapter *Morphology and Energy Barriers in Homoepitaxial Growth and Coarsening: A Case Study for Cu(100)*, pages 320–348, World Scientific Publishing, 1998.
[24] F. Rabbering, H. Wormeester, F. Everts, and B. Poelsema, Phys. Rev. B **79**, 075402 (2009).
[25] J. J. de Miguel, A. Sanchez, A. Cebollada, J. M. Gallego, J. Ferron, S. Ferrer, *Surf. Sci.* **189/190**, 1062 (1987)
[26] J.-K. Zou, J. F. Wendelken, H. Dürr, C.-L. Liu, *Phys. Rev. Lett.* **72**, 3064 (1994)
[27] C. Lee, G. T. Barkema, M. Breeman, A. Pasquarello, R. Car, *Surf. Sci. Lett.* **306**, L575 (1994)
[28] J. C. Girard, Y. Samson, S. Gauthier, S. Roussel, and J. Klein, Surf. Sci. **302**, 73 (1994)
[29] J. Fassbender, U. May, B. Schirmer, R. M. Jungblut, B. Hillebrands, G. Güntherodt, *Phys. Rev. Lett.* **75**, 4476 (1995)
[30] J. De la Figuera, J. E. Prieto, C. Ocal, and R. Miranda, Solid State Commun. **89**, 815 (1994).
[31] O. M. Magnussen, K. Krug, A. H. Ayyad, J. Stettner, *J. Electrochim. Acta* **53**, 3449-3458 (2008)
[32] K. Krug, J. Stettner, O. M. Magnussen, *Phys. Rev. Lett.* **96**, 246101-24614 (2006)
[33] D. Kaminski, K. Krug, F. Golks, J. Stettner, O. M. Magnussen, *J. Phys. Chem. C* **111**, 17067-17071 (2007)
[34] A. H. Ayyad, J. Stettner, O. M. Magnussen, *Phys. Rev. Lett.* **94**, 066106-066109 (**2005)**
[35] K. Krug, D. Kaminski, F. Golks, J. Stettner, O. M. Magnussen, *J. Phys. Chem. C* **114**, 18634 (2010)
[36] F. Golks, K. Krug, Y. Gründer, J. Zegenhagen, J. Stettner, O. M. Magnussen, J. Am. Chem. Soc. **133**, 3772 (2011)
[37] M. Lohmeier, E. Vlieg, *J. Appl. Cryst.* **26**, 706-716 (1993)
[38] B. Schmitt, C. Brönnimann, E. F. Eikenberry, F. Gonzo, C. Hörmann, R. Horisberger, B. Patterson, *Nucl. Instrum. Meth. A* **501**, 267-272 (2003)
[39] A. Bergamaschi, A. Cervellino, R. Dinapoli, F. Gozzo, B. Henrich, I. Johnson, P. Kraft, A. Mozzanica, B. Schmitt, X. Shi, *J. Synchr. Rad.* **17**, 653 (2010)
[40] K. Krug, Dissertation, University Kiel (2009)
[41] M. V. R. Murty, T. Curcic, A. Judy, B. H. Cooper, A. R. Woll, J. D. Brock, S. Kycia, R. L. Headrick, *Phys. Rev. B* **60,** 16956 (1999)
[42] V. I. Trofimov and V. G. Mokerov, *Mater. Sci. Eng. B* **89**, 420 (2002).
[43] E. Vlieg, A. W. Denier van der Gon, J. F. van der Veen, J. E Macdonald, C. Norris, *Phys. Rev. Lett.* **61**, 2241 (1988)
[44] M. V. RamanaMurty,T. Curcic, A. Judy, B. H. Cooper, A. Woll, J. D. Brock, S. Kycia, R. L. Headrick, *Phys. Rev. B* **60**, 16956 (1999)
[45] J. Massies, N. Grandjean, *Phys. Rev. Lett.* **71**, 1411 (1993)
[46] J.J. de Miguel, A. Cebollada, J. M. Gallego, R. Miranda, C. M. Schneider, P. Schuster, J. Kirschner, *J. Magn. Magn. Mater.* **93**, 1 (1991)
[47] F. O. Schumann, S. Z. Wu, R. F. Willis, *J. Appl. Phys*. **81**, 3898 (1997)
[48] P. Bencok, S. Andrieu, P. Arcade, C. Richter, V. Ilakovac, O. Heckmann, M. Vesely, K. Hricovini, *Surf. Sci.* **402-404**, 327 (1998)
[49] S. Andrieu, M. Finazzi, P. Bauer, H. Fischer, P. Lefèvre, A. Traverse, K. Hricovini, G. Krill, M. Piecuch, *Phys. Rev. B* **57**, 1985 (1998)
[50] J. M. Hartmann, A. Arnoult, L. Carbonell, V. H. Etgens, S. Tatarenko, *Phys. Rev. B* **57**, 15372 (1998)
[51] V. H. Etgens, E. M. Ribeiro-Teixeira, P. M. Mors, M. B. Veron, S. Tatarenko, M. Sauvage-Simkin, J. Alvarez, S. Ferrer, *Europhys. Lett.* **36**, 271 (1996)
[52] P. Turban, L. Hennet, S. Andrieu, *Surf. Sci.* **446**, 241 (2000)
[53] R. Kern, P. Müller, *Surf. Sci.* **392**, 103 (1997)
[54] P. Müller, *Eur. Phys. J. Appl. Phys.* **43**, 271–276 (2008)
[55] P. Müller, P. Turban, L. Lapena, S. Andrieu, *Surf.Sci.* **448**, 52 (2001)
[56] O. V. Lysenko, V. S. Stepanyuk, W. Hergert, J. Kirschner, *Phys. Rev. Lett.* **89**, 126102 (2002)
[57] V. S. Stepanyuk, D. V. Tsivlin, D. Sander, W. Hergert, J. Kirschner, Thin Solid Films **428**, 1-5 (2003)
[58] S. Müller, A. Kinne, M. Kottcke, R. Metzler, P. Bayer, L. Hammer, K. Heinz, *Phys. Rev. Lett.* **75**, 2862 (1995).
[59] A. P. Baddorf, A. K. Swan, J. F. Wendelken, preceding comment, *Phys. Rev. Lett.* **76**, 3658 (1996)
[60] I. K. Robinson, W. Moritz, F. Jona, M. A. Van Hove, preceding comment, *Phys. Rev. Lett.* **76**, 3659 (1996)
[61] K. H. Lau, W. Kohn, Surf. Sci. **65**, 607-618 (1977)
[62] S. K. Sinha, M. K. Sanyal, S. K. Satija, C. F. Majkrzak, D. A. Neumann, H. Homma, S. Szpala, A. Gibaud, H. Morkoc, Physica B **198**, 72 (1994)
[63] W. Haiss, R. J. Nichols, J. K. Sass, K. P. Charle, J. Electroanal. Chem. **452**, 199-202 (1998)
[64] C. Friesen, C. V. Thompson, Phys. Rev. Lett. **93**, 056104 (2004)
[65] R. V. Kukta, D. Kouris, K. Sieradzki, J. Mech. Phys. Sol. **51**, 1243-1266 (2003)
[66] L. E. Shilkrot, D. J. Srolovitz, Phys. Rev. B **53**, 11120 (1996)
[67] A. Peralta, D. Kouris, J. Knap, K. Sieradzki, J. Mech. Phys. Solids **46**, 1557-1579 (1998)
[68] K. H. Lau, Solid State Commun. **28**, 757-762 (1978)
[69] L. H. He, J. Mech. Phys. Sol. **58**, 1195-1211 (2010)
[70] C. Lee, G. T. Barkema, M. Breeman, A. Pasquarello, R. Car, Surf. Sci. Lett. **306**, L575-L578 (1994)
[71] R. C. Cammarata, T. M. Trimble, D. J. Srolovitz, J. Mater. Res. **15**, 2468 (2000)
[72] C. Friesen, S. C. Seel, C. V. Thompson, J. Appl. Phys. **95**, 1011 (2004)
[73] D. Sander, S. Ouazi, V. S. Stepanyuk, V. S. Stepanyuk, D. I. Bazhanov, J. Kirschner, Surf. Sci. **512**, 281 (2002)
[74] W. Xiao, P. A. Greaney, D. C. Chrzan, Phys. Rev. Lett. **90**, 156102 (2003)
[75] M. C. Bartelt, J. W. Evans, Phys. Rev. B **46**, 12675 (1992)

7 Homoepitaxial Growth of Cu(001) in PEG/Chloride-Containing Electrolyte

In the late 1990s, copper replaced aluminum as a silicon chip interconnect material for the fabrication of ultra-large scale integrated (ULSI) microchips [7, 8]. Since then, the 'damascene copper electroplating' process rose to the predominant technology for the fabrication of interconnects which are used in modern microelectronic devices [4, 7, 291]. As well, the interest in copper electrodeposition was renewed and the amount of studies concentrating on copper deposition increased enormously.

As described in the introduction, the success of this technique results from its ability of filling trenches and vias with dimensions $< 100\,\mathrm{nm}$ void- and seam-free by utilizing superconformal growth achieved by organic additives [7]. The introduction of additives with proper concentrations leads to differential electrodeposition, *i.e.*, with an increased deposition rate in the features as compared to the planar surface. This plating behavior, which is widely known as 'superfilling' or 'superconformal deposition' [13], was described in section 1.4.5.

In the last decade, much effort was made in order to understand the role of these additives in the copper electrodeposition process under superfilling conditions [9,13,92,95,97–99,105, 216,217,292–299]. Especially the simplification of the electrolyte additive systems to three (accelerator, inhibitor, leveler) or even two components (accelerator, inhibitor) [300, 301] have proven that even rather simple electrolytes containing chloride, a polyether and a sulfur-based organic molecule can achieve superconformal filling behavior [9, 15–18, 99]. Consequently, detailed studies of the influence and action of each of these additives became much simpler.

Today, the most commonly used and most widely discussed additive system[1] consists of polyethylene glycol (PEG), chloride ions and a sulfonate-terminated thiol, *e.g.*, bis-3-sodiumsulfopropyl disulfide (SPS) [9–11]. Studies by electrochemical methods, spectroscopic techniques, and ex-situ electron microscopy [7, 9, 12–14] revealed an integral picture in which the polyether in combination with chloride ions forms an overlayer on the copper surface that substantially inhibits the electrodeposition reaction ('inhibiting phase'). In contrast, the organosulfur compound disrupts the inhibiting film and consequently accelerates the deposition reaction ('accelerating phase'). The competition for available surface area of these two phases results, in combination with effects of transport, reaction kinetics, and sample geometry, in the observed superconformal filling.

In detail, the investigation of the PEG/chloride additive system, which exhibits a distinctly different filling behavior as observed for SPS-containing electrolytes [305, 306], is indispensable to fully understand the three-component system. As discussed in chapter 5, chloride ions are known to form ordered adlayers on low-index copper single crystal surfaces at potentials which are relevant for the plating process [25, 83, 210]. The addi-

[1] Attempts to explore other additive systems have been reported [9, 10, 102, 215, 295, 302–304].

tion of the polyether PEG (typical molar weight between 2000 and 6000 g) leads to the fast formation of an overlayer on the surface that substantially inhibits the electrodeposition reaction [9, 13, 92, 97–99, 216, 217, 292, 296–299] as compared to the PEG-free electrolyte [10, 98–102, 216]. Measurements with varying molecular weights of PEG revealed that molecules with at least more than 10 monomer units are needed to significantly inhibit the deposition reaction [297]. Ellipsometric studies by Walker *et al.* determined the relative change in film thickness upon adsorption of PEG to be potential-independent and of approximately 6 Å [217]. The adsorption of PEG and thus the inhibiting effect is strongly correlated with the presence of the chloride ions, as the chloride seems to act as the bridging ligand between PEG and the electrode surface [215]. Thus, in literature often the term 'PEG-Cl-complex' is used. However, the characteristic nature of the binding force of PEG in presence of the chloride layer is still unresolved and remains a controversial issue. Based on surface-enhanced Raman spectroscopy measurements, Feng *et al.* [298] proposed the formation of a PEG-Cu-Cl complex, in which the Cu^+ ion causes the binding to the chloride covered surface. However, similar adsorption of PEG was also observed on other surfaces in chemically distinct systems [217, 307]. Consequently, other explanations, which do not involve the presence of Cu^{2+} or Cu^+ in the electrolyte, were considered [217, 308]. For instance, Chai *et al.* proposed a model in which electrostatic interactions between adsorbed chloride with positively charged PEG are the reason for the binding of PEG on these surfaces [307].

A number of observations led to diverse hypotheses on how the PEG-Cl-film exactly influences the deposition reaction and thus the growth of the deposit on the crystal surface [296, 297, 309]. These include, amongst others, the formation of various polyether-Cu^+-Cl^- compounds, *e.g.*, helically wound PEG polyethers around a CuCl core [309], which are supposed to be responsible for the inhibitory effect. According to Walker and coworkers, the PEG-chloride film does not significantly block outer-sphere electron-transfer reactions [217]. However, as discussed in chapter 6, chloride in the electrolyte catalytically affects the rate determining step in the electrodeposition reaction (6.1) [197, 198], *i.e.*, the transition of Cu^{2+} to Cu^+ ions, which is related with an inner-sphere chloride bridging mechanism. Consequently, they propose that PEG adsorption on the copper surface may influence this rate-determining reaction by limiting the approach of Cu^{2+} ions to the catalytic chloride adlayer [196].

Upon addition of a sufonate-terminated thiol, *e.g.* SPS, the inhibiting effect associated with the PEG-chloride phase is disrupted and the rate of the deposition reaction increases towards the value of the unhibited copper deposition reaction [9–11]. Specifically, the thiol/disulfide functional group of the SPS molecules allows to disrupt the PEG-chloride film by coupling to the surface, whereas the sulfonate group prevents re-adsorption of PEG [9, 99]. Thus, surface sites which are not covered by the inhibiting phase become available, allowing for uninhibited copper deposition proceeding according to the overall reaction. Detailed studies by electroanalytical kinetic measurements in combination with superfilling experiments revealed that acceleration of the deposition reaction occurs already at very low coverages of SPS [9–11, 99, 103, 104, 310]. Typically, the concentration of SPS added to plating baths is a factor of 1000 to 20 times more diluted than the chloride concentration [311].

The superfilling behavior in electroplating systems containing aforementioned additives can be explained by the curvature enhanced adsorbate coverage (CEAC) model proposed by Moffat and coworkers [9, 10], in which the accumulation of the more strongly bound accelerator compound during area reduction on advancing concave sections accounts for the increased deposition rate at the bottom of trenches [9, 14]. This model was described in section 1.4.5.

Nevertheless, despite those numerous studies of Cu superconformal electrodeposition, the precise influence of the additives on the elementary steps of the deposition reaction, specifically on the atomic-scale processes, is largely not understood. This is mainly related to the lack of direct *in situ* atomic-scale studies of copper deposition under superfilling conditions by structure-sensitive methods, *e.g.*, scanning probe or surface diffraction methods. Previous *in situ* STM studies of the influence of additives on copper electrodeposition focused mainly on heteroepitaxial electrodeposition on gold or platinum single crystal electrodes from electrolytes containing a single organic additive [312–316]. In detail, Nichols *et al.* reported a substantially increased copper nucleation density in the presence of additives (derivatives of tris-aminophenyl and benzothiazolium (BT)) for the electrodeposition of copper from sulphuric and perchloric acid electrolytes [312]. Petri *et al.* observed a strong inhibitory effect of the coadsorbed PEG-chloride-film on copper bulk deposition on Au(111) [316]. The homoepitaxial deposition of copper on Cu(111) under the influence of different additives (excluding PEG), in addition to heteroepitaxial deposition on Au(111), has been investigated by Täubert and coworkers [313, 314]. However, such *in situ* high resolution scanning probe studies on the copper surface are usually strongly hampered by the presence of the non-conductive polymeric film (displacement of the PEG molecules by the tip).

In contrast, *in situ* SXRD studies are not limited by this drawback and can be performed in electrolytes of almost arbitrary composition. With the *in situ* SXRD studies of the homoepitaxial growth of Cu(001) in PEG-Cl-containing electrolyte, we contribute to the fundamental understanding of the precise influence of the PEG-chloride-film on the atomic-scale processes occurring during copper electrodeposition in electrolytes used in ULSI plating. Specifically, the experiments provide insight into the influence of the PEG-Cl-phase on the copper nucleation and growth mechanisms in superconformal deposition, which is indispensable in order to fully understand more complex two- and three-component systems.

In situ Surface X-Ray Diffraction Studies of the Influence of the PEG-Cl-Complex on Homoepitaxial Electrodeposition on Cu(001)

F. Golks[1,2], Y. Gründer[1,†], A. Drünkler[1], J. Roy[2], J. Stettner[1], J. Zegenhagen[2], O. M. Magnussen[1]

[1]*Institut für Experimentelle und Angewandte Physik, Universität Kiel, Leibnizstraße 19, 24098, Kiel, Germany*
[2]*European Synchrotron Radiation Facility, 6 Rue Jules Horowitz, 38000 Grenoble, France*

The adsorption of polytheylene glycol on Cu(001) in chloride-containing electrolyte was investigated by *in situ* surface x-ray diffraction, unambiguously verifying the existence of the ordered c(2×2) chloride adlayer structure in presence of the polymer. Potential-dependent measurements at selected positions in reciprocal space suggest the stabilization of the partially ordered chloride adlayer over a wider potential regime as compared to the situation in the PEG-free electrolyte. Crystal truncation and superstructure rod measurements reveal that the polymer interacts more strongly with the partially c(2×2) Cl covered surface than with the surface covered by a complete c(2×2) adlayer. Characteristic Debye-Waller-like out-of-plane disorder of the Cl atoms as well as Cu atoms in the second subsurface layer is induced. Furthermore, the influence of the PEG-Cl-complex on homoepitaxial growth is presented, revealing the occurrence of layer-by-layer growth oscillations for potentials up to -0.35 V with a significantly reduced deposition rate as compared to previously reported measurements in PEG-free electrolyte.

1. Introduction

With the ability to fill high-aspect ratio trenches and vias with widths < 100 nm void- and seam-free, the 'copper damascene process' rose to the predominant technology for the fabrication of interconnects of ultra large scale integrated (ULSI) microchips [1]. In this process, the competition of two additive-derived phases for available surface area, specifically a deposition inhibiting and an accelerating phase, is known to effect the observed bottom-up filling mechanism in these trenches, known as 'superfilling' or 'superconformal deposition' [2]. This behavior can be explained by the curvature enhanced adsorbate coverage (CEAC) model proposed by Moffat and coworkers [3,4]. Accordingly, during area reduction on advancing concave sections, the more strongly bound accelerator compound is accumulated, accounting for the increased deposition rate at the bottom of trenches [3,5]. Today's most commonly used and most widely discussed additive system consists of chloride ions, polyethylene glycol (PEG, typical molar weight between 2000 and 6000 g), and a sulfonate-terminated thiol.

Studies by electrochemical methods, spectroscopic techniques, and ex-situ electron microscopy [1-3,5,6] revealed an integral macroscopic picture of the complex interplay of the different components during electrodeposition in such plating baths. In absence of PEG, chloride ions form ordered monolayers on the low-index copper surfaces at potentials which are relevant for the plating process [7,8]. Ellipsometric studies by Walker *et al.* revealed a fast incremental change in the film thickness on top of the copper substrate by 6 Å upon addition of PEG to the chloride-containing electrolyte [9]. The as-formed Cl-PEG film is known to induce substantial inhibition of the electrodeposition reaction (*e.g.* [2,3,10]) as compared to the PEG-free electrolyte [4,10]. As the increase in the film thickness is independent from the order of addition of PEG and Cl to the solution, Walker *et al.* conclude the formation of similar film structures in both cases. These studies additionally reveal that the adsorption of PEG on the surface is correlated with the presence of chloride ions as only comparatively little adsorption of the polymer occurs in absence of Cl ions in the electrolyte. Basing on laser Raman spectroscopy, Healey *et al.* suggested that the chloride ions act as the bridging ligand between PEG and the electrode surface [11]. However, the characteristic nature of the binding force of the PEG film on the chloride layer is still unresolved and remains a controversial issue [12-15]. The existence of the ordered c(2×2) Cl adlayer structure in presence of the PEG film was commonly supposed, justified by the strong similarity of cyclic voltammograms obtained both in PEG-containing and PEG-free electrolytes, more precisely, by the occurrence of peaks indicative for chloride adlayer phase transitions [16]. In contrast, the thiol/disulfide functional group of the organosulfur compound disrupts the inhibiting film, leading to an acceleration of the deposition reaction [3,4,17,18].

Despite the spurred interest in copper electrodeposition accompanied by manifold research, precise information on the atomic-scale structure and on the influence of the additives on the elementary steps of the deposition reaction are largely lacking. Previous *in situ* STM studies of the influence of additives on copper electrodeposition focused mainly on heteroepitaxial electrodeposition on gold or platinum single crystal electrodes from electrolytes containing a single organic additive [19-23]. In addition to heteroepitaxial deposition on Au(111), homoepitaxial deposition of copper under the influence of different additives, excluding PEG, has been investigated by Täubert and coworkers [20,21]. However, such *in situ* high resolution scanning probe studies of the copper surface are usually strongly hampered by the presence of the inhibiting polymeric film. In addition, *in situ* growth studies under realistic reaction conditions by scanning probe techniques are limited both by low time resolution and shielding effects of the scanning tip on the electrochemical processes of interest [24].

In contrast, time-resolved *in situ* surface x-ray diffraction (SXRD) studies are not limited by these drawbacks. Recent studies of the homoepitaxial deposition and dissolution of fcc(001) metal single crystal electrodes proved the excellent applicability of this technique to growth studies in electrochemical environment [25-31]. Specifically, it was shown that by recording time-dependent intensity transients at or close to the anti-Bragg out-of-phase condition for scattering from consecutive layers, characteristic changes in the scattered intensity during growth allow to distinguish the kinetic growth behavior, namely 3D, layer-by-layer and step-flow growth.

The present study is a continuation of our fundamental investigations of the Cu(001)/Cl system reported recently. In particular, the potential-dependent chloride adlayer structure, copper homoepitaxial electrodeposition as well as the influence of the Cl adlayer on it were studied in detail for Cu(001) single crystal electrodes [31,32]. In the following, we will provide new insight into the influence of PEG on the chloride adlayer

† *Current address: School of Chemistry, University of Manchester, Oxford Road, Manchester, M13 9PL, UK*

formation kinetics and of the resulting Cl-PEG-complex on the atomic-scale electrodeposition process on the Cu(001) electrode surface.

2. Experimental Methods

For the *in situ* SXRD experiments presented here a hanging meniscus x-ray transmission cell described in ref. [25] was employed. Via a remote-controlled pump system, the electrolyte can be exchanged during the measurements. The applicability of this cell geometry to high quality *in situ* x-ray studies of electrochemical deposition was reported in ref. [25-27,31]. A multifunctional potentiostat (CompactStat, Ivium Technologies), in combination with a Ag/AgCl (3 M KCl) reference electrode ensured reliable control of electrode potential and electrochemical current.

As samples, hat shaped Cu(001) single crystals (Mateck, 99.999 %) with a 4-6 mm surface diameter were employed. Electropolishing in 70 % orthophosphoric acid at an electrode potential of 1.8 V for at least three times 10 s and subsequent rinsing with highly purified water (Milli-Q, 18.2 MΩ) ensured smooth surfaces with high purity. In order to avoid contaminations from air, the meniscus as well as the electrolytes were kept in a flowing argon atmosphere (Ar 5.0, Air Products). The electrolytes were prepared from Milli-Q water, ultrapure $HClO_4$ (Romil UpA, 65-71 %), HCl (Merck Suprapur, 30 %), $Cu(ClO_4)_2$ (Alfa Aesar, 99.999 %) and polyethylene glycol (Merck, > 95 %, 3000 g/Mol).

The SXRD experiments were performed at the ID32 beamline at the European Synchrotron Radiation Facility (ESRF) using a photon energy of 22.5 keV and a grazing incidence angle of 0.437°. Presample slits of 0.3 and 0.025 - 0.04 mm in horizontal and vertical directions, respectively, ensured enough counting statistics. A NaI point detector (Cyberstar) was employed for recording the potential-dependent scattered intensity in parallel to potential cycles (see below). For the measurements of crystal truncation rods as well as in the growth studies, a one-dimensional detector (Dectris Mythen 1K) was used with the pixel array aligned in parallel to the sample surface. As reported recently [30,31], the detector system is well suited for growth studies as it features fast data acquisition rates while simultaneously recording the entire peak cross-section, from which the integrated peak intensity, peak position and peak width are obtained. Moreover, the comparatively fast data acquisition allows reducing the mean irradiation time in crystal truncation rod (CTR) measurements to about 45 s per rod, which is a factor of 10 times shorter as compared to measurements employing the point detector. This is of great importance, since by limiting the radiation impinging on the sample surface, radiolytic effects can be diminished or even entirely avoided [33]. During all performed experiments, the extent of beam effects was estimated by performing 'sample scans' before and after each measurement, in which the scattered intensity at a fixed reciprocal space position is monitored while moving the sample surface perpendicularly with respect to the incoming beam, i.e. changing the position of the beam on the sample surface. Consequently, radiolytic effects could, if occurred, clearly be identified afterwards by a local intensity decrease at the position where the beam irradiated during the measurement.

The standard surface coordinates of the Cu(001) surface ($a_1 = a_2 = a_3 = 3.615$ Å, $\alpha = \beta = \gamma = 90°$) were employed with the a_3-axis pointing along the surface normal.

3. Results and Discussion

Prior to the studies in PEG-containing electrolyte, the electrochemical behavior of the Cu(001) sample surface was characterized in 0.1 M $HClO_4$ + 1 mM HCl by cyclic voltammetry (fig. 1 black). In accordance with our recent study of the chloride adlayer on Cu(001) in 10 mM HCl [32], the potential-dependent Cl adsorption and desorption manifests in form of broad waves between approx. -0.30 V and the onset of hydrogen evolution (the center of the cathodic wave is observable at -0.43 V). The phase transition from the c(2×2) ordered to a disordered Cl adlayer and vice versa occurs close to the onset of hydrogen evolution (~ -0.55 V).

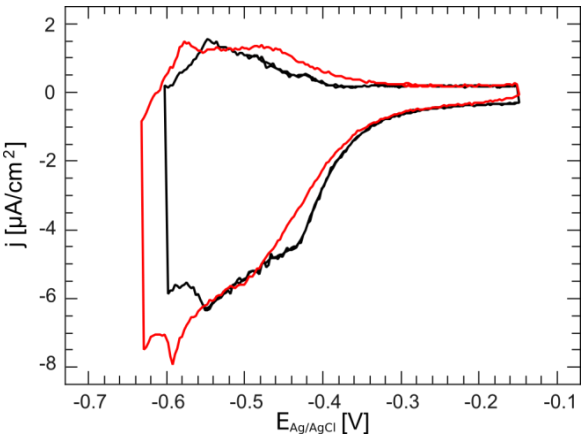

Fig. 1: Cyclic voltammogram of Cu(001) in 0.1 M $HClO_4$ + 1 mM HCl (black) and 0.1 M $HClO_4$ + 1 mM HCl + 0.1 mM PEG (red) at a scan rate of dE/dt = 20 mV/s.

After addition of 0.1 mM PEG to the electrolyte, the polymer adsorbs at the surface, resulting in a substantially changed cyclic voltammogram (fig. 1, red). In detail, the waves indicative for the adsorption/desorption processes broaden and slightly shift to more negative potential values by ~50 mV. Equally, the peaks indicating the transition from the (partially) ordered c(2×2) to the completely disordered Cl adlayer shift to more negative potential values by about 30 and 40 mV, respectively. This general shift to more negative potentials was recently interpreted by Moffat *et al.* as a stabilization of the chloride adlayer as the potential range of the existence of the adlayer is widened [16].

The phase transition behavior in 0.1 M $HClO_4$ + 1 mM HCl electrolyte was additionally investigated by SXRD measurements at selected positions in reciprocal space. Specifically, the potential-dependent scattered intensity at (1,0,0.1) and (2,0,1), *i.e.*, at the c(2×2) superstructure rod and at a substrate CTR, was recorded in parallel to potential cycles (fig. 2, black, dE/dt = 20 mV/s). Whereas the intensity measured at the former position is proportional to the degree of order of the c(2×2) Cl adlayer, data recorded at the anti-Bragg position (2,0,1) is primarily sensitive to the coverage of all Cu-hollow sites occupied with Cl atoms, independent of the degree of order [32,34]. The intensity decrease with increasing potential at (2,0,1) is related to successive chloride adsorption (fig. 2b), whereas the intensity increase at (1,0,0.1) from zero at the negative potential limit to a saturation value at potentials positive of about -0.40 V indicates the increase in the degree of c(2×2) ordering of the Cl adlayer (fig. 2a). These observations are in accordance with our recent study [32].

Upon exchange to PEG-containing electrolyte at -0.20 V, the chloride adlayer remains ordered in the c(2×2) structure as directly verified by successive transverse scans at (1,0,0.1) during and after the exchange. The potential-dependence of the scattered intensity notably changes with respect to measurements in PEG-free solution, as shown in fig. 2 (red). In detail, at the (1,0,0.1) superstructure rod position (fig. 2a), the intensity starts decreasing with a lower, constant slope at slightly more positive potentials as compared to the PEG-free electrolyte. Moreover, the intensity does not vanish for potentials down to -0.70 V. As in case of the

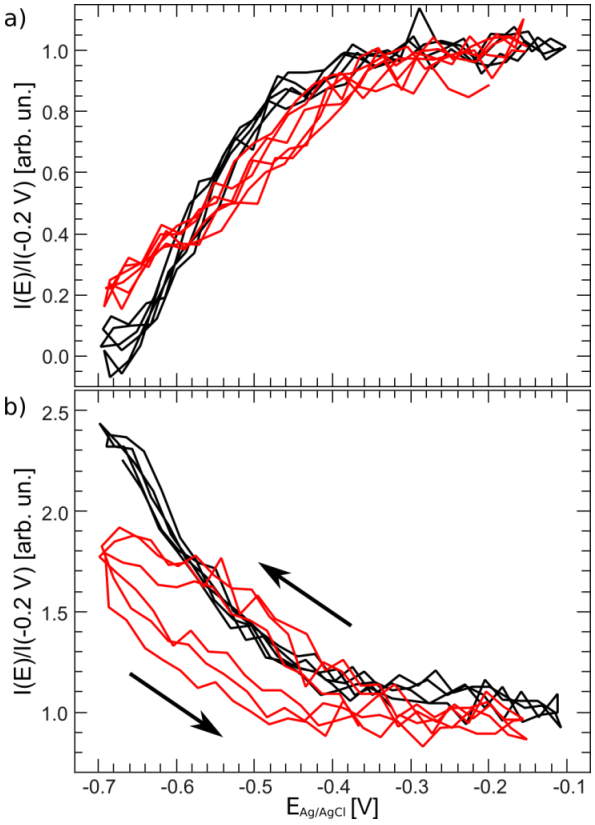

Fig. 2: Potential-dependent scattered intensity (dE/dt = 20 mV/s) of the Cu(001) single crystal surface in 0.1 M $HClO_4$ + 1 mM HCl (black) and 0.1 M $HClO_4$ + 1 mM HCl + 0.1 mM PEG (red) at **(a)** the Cl superstructure rod (1,0,0.1) and **(b)** the substrate's crystal truncation rod (2,0,1). All curves are normalized to the starting intensity, respectively.

PEG-free electrolyte, the potential-dependence of the scattered intensity at (1,0,0.1) was found to be reversible in our experiments, *i.e.*, both cathodic and anodic potential sweeps exhibit the same potential dependence. The reversibility of the intensity curves over several potential cycles allows to safely exclude radiolytic effects.

More drastic changes are observed in the potential-dependence of the scattered intensity at the (2,0,1) anti-Bragg condition (fig. 2b). From -0.10 to -0.57 V, the intensity increase during the cathodic potential sweep follows the curve measured in the PEG-free electrolyte. For more negative potentials, a deviation to comparably lower intensity values is observed, yielding a maximum intensity at the negative potential limit which is substantially lower as compared to the results obtained for the PEG-free electrolyte. The intensity measured in the anodic sweep, in contrast, decreases initially faster (for -0.70 V < E < -0.45 V), and then remains at a rather constant intensity value for more positive potentials, resulting in a hysteresis in the potential range between -0.70 and -0.30 V.

The reported x-ray data provide first unambiguous verification of the existence of the c(2×2) Cl adlayer in presence of PEG by *in situ* structure sensitive SXRD measurements. Specifically, the measurements performed at (1,0,0.1) reveal that the phase transition from the entirely ordered to the disordered Cl adlayer is extended to more negative and slightly more positive potentials, marginally limiting the existence of the entirely ordered c(2×2) structure to a narrower potential regime. Whereas without PEG, no c(2×2) order is found for potentials more negative than -0.65 V, in presence of PEG residual ordering exists at least down to -0.70 V, *i.e.*, clearly into the hydrogen evolution regime. These findings generally coincide with the common shift of the peaks indicative for the c(2×2) ↔ (1x1) transition as well as for the adsorption/desorption in the cyclic voltammogram to more negative potential values.

The presence of the residual chloride at the surface at -0.70 V is responsible for the comparably lower scattered intensity at the anti-Bragg (2,0,1) condition, supporting the stabilization effect of the (partially ordered) Cl adlayer in presence of PEG as supposed from the cyclic voltammogram [16]. However, the reason for the occurrence of the hysteresis still remains unsolved on the base of our limited set of data, which does not allow for a quantitative analysis of the complex interplay of different effects contributing to the scattered intensity at (2,0,1).

Further studies concentrated on the influence of the PEG adlayer on the interface structure. CTR measurements were performed before and after the exchange to PEG-containing electrolyte on the same sample. The (0,0,L), (1,1,L), (2,0,L) CTRs as well as the (1,0,L) superstructure rod were measured both at -0.20 V, in presence of the fully developed c(2×2) superstructure (fig. 3a), and at -0.55 V, where only a low c(2×2) coverage is existing (fig. 3b). The peak cross sections were taken at equidistant reciprocal space positions along the rods. For all peak profiles, the background intensity was determined and subtracted prior to integration. The error bars indicate the incertitude of the integrated intensity values.

Due to a negligible scattering contribution of PEG, the x-ray data yield no direct structural information about the polymer layer. However, the shape of the CTRs is determined by the atomic near-interface structure, specifically the arrangement of Cl and Cu atoms (relaxations, corrugation) and roughness, and thus may reveal information about the influence of PEG on the interface structure. As visible in fig. 3a, the L-dependent integrated intensity of all measured rods in absence and presence of PEG at -0.20 V is almost identical. In contrast, the CTRs measured at E = -0.55 V (fig. 3b) exhibit differences for the (0,0,L), (1,1,L), and (1,0,L) rods. In detail, the integrated intensities at (0,0,2.1) and (1,1,1.2), *i.e.*, close to the anti-Bragg conditions of the CTRs, respectively, are slightly higher in presence of PEG as compared to the PEG-free case. However, the position of the minimia and the shape of the CTRs in their vicinity are identical before and after the exchange. The most pronounced difference is observed in the L-dependence of the superstructure rod (1,0,L). Starting with the same integrated intensity at L = 0.1, a much faster signal decay with increasing L can be seen in the data obtained for the PEG-containing electrolyte. The superstructure rods measured at -0.20 V (with and without PEG) as well as the superstructure rod measured at -0.55 V in the PEG-free electrolyte exhibit a slight oscillation of the L-dependent intensity, in accordance with the discussion in ref. [32].

The marginal differences between the CTRs obtained in PEG-containing and PEG-free electrolyte at -0.20 V suggest that only a weak influence of the polymer film is exerted on the interface structure at this potential where the c(2×2) is entirely covering the surface. In detail, the CTR and superstructure rod shapes, with respect to minimia and the symmetry in vicinity of these minima, are identical, thus excluding significant rearrangement of the topmost atomic layers. Consequently, we expect the binding lengths, both within the chloride adlayer and the subsurface layers, to be essentially unaffected by the presence of PEG within precision of our data. The presence of intensity oscillations in the (1,0,L) superstructure rod support these conclusions. As discussed in our recent study [32], these oscillations are caused by an interference effect between the waves scattered at the chloride adlayer and the second subsurface copper layer, exhibiting exactly the same lateral periodicity as the superstructure. DFT calculations revealed that the corrugation of the second copper layer is a direct consequence of the presence of the chloride

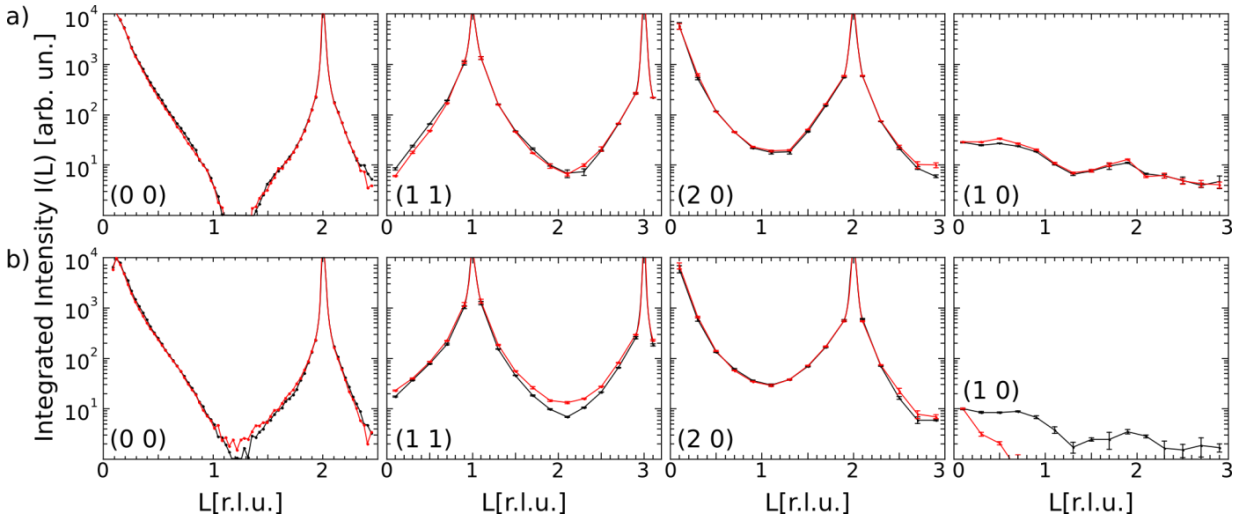

Fig. 3: Integrated intensity I(L) for crystal truncation rods and the lowest-order c(2×2) superstructure rod measured for Cu(001) in 0.1 M $HClO_4$ + 1 mM HCl (black) and after exchange to 0.1 M $HClO_4$ + 1 mM HCl + 0.1 mM PEG (red) at **(a)** -0.20 V and **(b)** -0.55 V.

adlayer [32]. Thus, the presence of PEG at the surface is not notably changing the electrostatic conditions at the interface at -0.20 V.

At -0.55 V, the substantially faster intensity decay at (1,0,L) with increasing L-values in presence of PEG suggests a modified characteristic of the c(2×2) ordered Cl adlayer as well as of the second subsurface Cu layer, which may be explained by an enhanced out-of-plane Debye-Waller factor of the Cl and Cu atoms, respectively. This effect may also explain the slight intensity increase close to the minima of the CTRs upon adsorption of PEG.

Based on our CTR data (fig. 3) and potential-dependent measurements (fig. 2) we assume that the mode and extent of interaction of PEG with the chloride adlayer is strongly correlated to the degree of order of the latter. As can be seen in the differences of the measured superstructure rods at both potentials, respectively, the interaction of PEG seems to be significantly stronger in presence of the partially than the entirely developed c(2×2) Cl adlayer.

Growth mode studies were carried out for Cu(001) in 0.1 M $HClO_4$ + 1 mM HCl + 1 mM $Cu(ClO_4)_2$ + 0.1 mM PEG electrolyte. As known from previous studies of homoepitaxial growth on fcc(001) metal surfaces, the three growth modes 3D, layer-by-layer, and step-flow growth yield a characteristic time-dependence of the scattered intensity measured at the anti-Bragg out-of-phase condition for scattering from consecutive layers [25-27,31]. In detail, 3D growth leads to a continuously decaying signal with deposited amount due to increasing surface roughness. Layer-by-layer growth manifests in characteristic growth oscillations in the intensity transient, reflecting the successive growth of single monolayers. In case of step-flow growth, simultaneous growth of all terraces yields a time-independent scattering signal at a constant high level, as the overall surface morphology does not change.

The scattered intensity was recorded at (1,1,0.1), applying the same procedure as recently reported in ref. [31]. After replenishing the Cu concentration in the meniscus by an exchange with 100 µl of fresh $Cu(ClO_4)_2$-containing electrolyte, the x-ray measurement was started. During the first 10 seconds, the potential was kept at -0.55 V, before a potential step to a more positive potential E was initiated. The latter lasted for 120 s and 20 s after the reverse potential step to -0.55 V, the x-ray intensity measurement was stopped. In-between the potential step experiments, the potential was kept at -0.55 V. Potential step experiments were performed for the potential E ranging from -0.55 to -0.25 V.

The time-dependent, background-corrected integrated intensity of these transients is shown in fig. 4a. Already before the potential step is performed, *i.e.*, within the first 10 seconds, a substantial decrease in the scattered intensity is observable in all transients, which we attribute to a residual influence of the electrolyte exchange before the experiment. The potential step to more positive potentials at 0 s leads to a quick drop (< 0.2 s) in the intensity transient, which is attributed to fast adsorption of Cl. Upon the potential step, the decrease continues for approximately 7-10 s before a minimal value is reached and the intensity starts increasing again. In the subsequent period until 120 s, oscillations are observable for the potentials $-0.55 \leq E \leq -0.35$ V, however, in case of the potentials -0.40 and -0.35 V, the oscillations are hard to identify as the amplitude is very low. These oscillations are identified as layer-by-layer growth oscillations. Except for the transient recorded at -0.55 V, the oscillations fade within 2-5 periods, due to non-ideal layer-by-layer growth [26,35] as well as a loss of the phase relationship of incoherently superposed oscillations from different parts of the illuminated surface area. The oscillation periods vary between the shown scans and even for transients measured again under the same conditions for the same potential by approximately ±8 % (not shown).

Compared to our growth behavior studies in PEG-free electrolyte, the oscillation period is significantly longer by a factor of approximately 3, in accordance with the electrochemical current measured in parallel. Thus, the inhibiting effect of PEG in combination with Cl during copper electrodeposition is directly observable in our atomic-scale growth study. The occurrence of layer-by-layer growth oscillations is limited to a narrower potential regime, ranging from -0.55 V to -0.35 V, whereas in PEG-free electrolyte oscillations were observed up to -0.15 V. It seems that the transition tendency towards 3D growth is shifted to more negative potentials for PEG-containinig electrolyte. However, for a quantitative analysis of the observed growth behavior transition an extended set of data is required. Furthermore, during the growth experiments indications for beam influence effects were observed and could not be completely avoided, strongly hampering precise conclusions. In detail, we found evidence that the ordered c(2×2) Cl adlayer was affected by

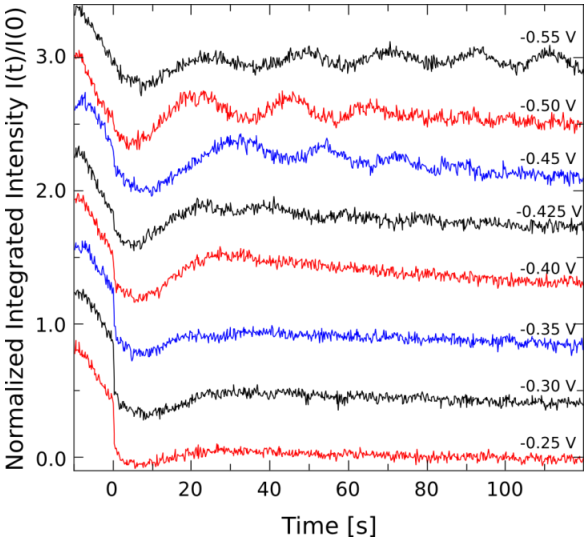

Fig. 4: Background-corrected integrated x-ray intensity at (1,1,0.1) as a function of deposition time for deposition on Cu(001) at different potentials in 0.1 M $HClO_4$ + 1 mM HCl + 0.1 mM PEG + 1 mM $Cu(ClO_4)_2$. With increasing potential, a transition from layer-by-layer to 3D growth is observable. All data shown is raw data from a numerical integration of the peak cross-section. The curves are shifted with respect to each other to ensure visibility.

irradiation at potentials more negative than -0.35 V. However, within the waiting time between two potential step experiments (5 min), reproducible surface conditions could be achieved, as verified by the comeback of the intensity both at (1,1,0.1) and (1,0,0.1). Consequently, the Cu surface structure and the c(2×2) Cl adlayer recovered reproducibly.

4. Conclusions

The present work was carried out as continuation of our investigations of the Cu(001)/Cl system reported recently [31,32]. In particular, we presented combined electrochemical and *in situ* SXRD studies of the influence of PEG on the Cu(001) single crystal surface structure in chloride-containing electrolyte. Our x-ray data revealed a first unambiguous verification of the existence of the ordered c(2×2) chloride adlayer structure in presence of the polymer, as was previously assumed from electrochemical data. The phase transition from the ordered c(2×2) to the disordered Cl adlayer was found to be spread over a wider potential regime as compared to our results in the PEG-free electrolyte, thus stabilizing the (partially) ordered chloride adlayer into the potential regime where significant hydrogen evolution occurs. CTR measurements in absence and presence of PEG revealed that the polymer interacts more strongly with the partially c(2×2) Cl covered surface than with the entirely covered surface. The degree of order of the Cl atoms as well as Cu atoms in the second subsurface layer, which exhibit the same c(2×2) order, is influenced, in detail by an enhancement of the vertical statistical displacements. In direct growth behavior studies we observed the occurrence of layer-by-layer growth oscillations over a wide potential regime up to -0.35 V. The deposition rate is reduced by a factor of ~3 as compared the previously reported measurements in PEG-free electrolyte, clearly supporting the inhibiting effect of the PEG-Cl-complex on the deposition reaction.

Acknowledgements

We gratefully acknowledge the European Synchrotron Radiation Source for providing synchrotron radiation facilities and the ID32 beamline staff for technical support. We further thank the Deutsche Forschungsgemeinschaft for financial support via MA 1618/13-3.

REFERENCES

[1] P. C. Andricacos, C. Uzoh, J. O. Dukovic, J. Horkans, H. Deligianni, Electrochem. Microfab. 42 (1998)
[2] P. M. Vereecken, R. A. Binstead, H. Deligianni, P. C. Andricacos, IBM J. Res. & Dev. 49, 3 (2005)
[3] T. P. Moffat, D. Wheeler, M. D. Edelstein, D. Josell, IBM J. Res. & Dev. 49, 19 (2005).
[4] T. P. Moffat, D. Wheeler, D. Josell, in Superconformal Film Growth: Advances in Electrochemical Science and Engineering, page 109, Wiley-VCH, 2008.
[5] D. Josell, D. Wheeler, W. H. Huber, T. P. Moffat, Phys. Rev. Lett. 87, 16102 (2001).
[6] J. L. P. Vanysek, M. Alodan, O. M. Magnussen, editors, in Electrochemical Science and Technology of Copper, Proceedings of the Electrochemical Society, Vol. 2000-30, Electrochmical Society, Pennington, 2003.
[7] O. M. Magnussen, Chem. Rev 102, 679 (2002).
[8] T. P. Moffat, in Electrochemical Processing in ULSI Fabrication and Semiconductor/Metal Deposition 2, page 41, Electrochemical Society Proceedings Series, Pennington, 1999.
[9] M. L. Walker, L. J. Richter, T. P. Moffat, J. Electrochem. Soc. 152, C403 (2005).
[10] J. J. Kelly, A. C. West, J. Electrochem. Soc. 145, 3477 (1998).
[11] J. P. Healy, D. Pletcher, M. Goodenough, J. Electroanal. Chem. 338, 155 (1992).
[12] Z. V. Feng, X. Li, A. A. Gewirth, J. Phys. Chem. B 107, 9415 (2003).
[13] M. L. Walker, L. J. Richter, T. P. Moffat, J. Electrochem. Soc. 152, C403 (2005).
[14] L. Chai, R. Goldberg, N. Kampf, J. Klein, Langmuir 24, 1570 (2008).
[15] K. Doblhofer, S. Wasle, D. M. Soares, K. G. Weil, G. Ertl, J. Electrochem. Soc. 150, C657 (2003).
[16] T. P. Moffat, L. Y. Ou Yang, J. Electrochem. Soc. 157, D228 (2010).
[17] M. J. Willey, A. C. West, J. Electrochem. Soc. 154, D156 (2007).
[18] W. P. Dow, M.-Y. Yen, Electrochem. Solid-State Lett. 8, C161 (2005).
[19] R. J. Nichols, C. E. Bach, H. Meyer, Ber. Bunsenges. Phys. Chem. 97, 1012 (1993).
[20] C. E. Täubert, Influence of Different Additives on the Copper Electroplating onto Au(111) and Cu(111) Substrates, PhD thesis, Universität Ulm, 2006.
[21] C. E. Täubert, D. M. Kolb, U. Memmert, H. Meyer, J. Electrochem. Soc. 154, 293 (2007).
[22] M. Wünsche, R. J. Nichols, R. Schumacher, W. Beckmann, H. Meyer, Electrochim. Acta 38, 647 (1993).
[23] M. Petri, D. M. Kolb, U. Memmert, H. Meyer, J. Electrochem. Soc. 151, C793 (2004).
[24] J. Divisek, B. Steffen, U. Stimming, W. Schmickler, J. Electroanal. Chem. 440, 169 (1997).
[25] O. M. Magnussen, K. Krug, A. H. Ayyad, J. Stettner, J. Electrochim. Acta 53, 3449-3458 (2008)
[26] K. Krug, J. Stettner, O. M. Magnussen, Phys. Rev. Lett. 96, 246101 (2006)
[27] D. Kaminski, K. Krug, F. Golks, J. Stettner, O. M. Magnussen, J. Phys. Chem. C 111, 17067-17071 (2007)
[28] A. H. Ayyad, J. Stettner, O. M. Magnussen, Phys. Rev. Lett. 94, 66106 (2005)
[29] K. Krug, D. Kaminski, F. Golks, J. Stettner, O. M. Magnussen, J. Phys. Chem. C 114, 18634 (2010)
[30] F. Golks, K. Krug, Y. Gründer, J. Zegenhagen, J. Stettner, O. M. Magnussen, J. Am. Chem. Soc. 133, 3772 (2011)
[31] F. Golks, J. Stettner, Y. Gründer, K. Krug, J. Zegenhagen, O. M. Magnussen, to be published
[32] Y. Gründer, D. Kaminski, F. Golks, K. Krug, J. Stettner, O. M. Magnussen, A. Franke, J. Stremme, E. Pehlke, Phys. Rev. B 81, 174114 (2010)
[33] J. M. Holton, J. Synchrotron Rad. 16, 133–142 (2009).
[34] J. X. Wang, T. Wandlowski, B. M. Ocko, in Proceedings of the Symposium on the Electrochemical Double Layer, edited by C. Korzeniewski, B. E. Conway, The Electrochemical Society, Pennington, NJ, 1997, p. 293.
[35] G. Rosenfeld, B. Poelsema, G. Comsa, in: D.A. King, D.P. Woodruff (Eds.), Growth and Properties of Ultrathin Epitaxial Layers, vol. 8, Elsevier Science B.V., Amsterdam, 1999, p. 66.

8 Summary

With the ability to fill high-aspect ratio trenches and vias with widths < 100 nm void- and seam-free, the copper damascene process rose to the predominant technology for the fabrication of interconnects of modern ultra-large scale integrated microchips. Fundamental atomic-scale studies of copper electrodeposition, which aimed at deepening the understanding of homoepitaxial growth in electrochemical environment, especially of the processes occurring under the employed superconformal growth conditions, were reported in this work. The surface structure and morphology of Cu(001) and Cu(111) electrodes in chloride-containing electrolyte was investigated by *in situ* surface x-ray diffraction (SXRD). Specifically, the high surface sensitivity of the SXRD technique allowed to investigate potential induced structural changes in the chloride adlayer as well as on the underlying substrate with unsurpassed precision. Furthermore, homoepitaxial electrodeposition of copper on Cu(001) single crystal electrodes in absence and presence of the organic additive polyethylene glycol (PEG) was studied. This molecule, a frequently added component in modern industrial plating baths, serves as inhibitor for the deposition reaction and is indispensable for the realisation of superconformal growth. Operating under diffusion-limited, realistic deposition conditions, the growth behavior was studied in dependence of the electrode potential for two different deposition rates (*i.e.*, copper ion concentrations). Manifold results allowed to deepen the understanding of the complex relationship between the atomic-scale structure of the solid-liquid interface, the growth behavior and the resulting surface morphology.

Substantial progress in time resolution of the SXRD experiments was achieved by the implementation of a fast one-dimensional x-ray detector into the existing diffractometer setup. For the first time, *in situ* SXRD studies of growth and etching processes at the solid-liquid interface become possible at technologically relevant rates, *i.e.*, at rates involving more than 10 monolayers per second. Besides the importance for the presented *in situ* investigation of electrodeposition processes in the scope of the damascene process, the new setup may facilitate future time-resolved SXRD studies of all kind of surface processes. The potential of gaining directly detailed structural information on the growth interface during realistic reaction conditions may help to provide fundamental insight into electrochemical processes, *e.g.*, related to catalytic reactions, electrodeposition and electrodissolution. In addition, the applicability of modern growth theories to electrochemical deposition and dissolution processes at high rates may be examined. Concretely, the potential of the new developed SXRD setup was tested in a preparatory experiment using the electrochemical dissolution of Au(001) in chloride-containing solution as an example. The substantial progress in the time resolution allowed to directly follow the atomic-scale etching processes at the solid-liquid interface with a data acquisition rate of down to five milliseconds, revealing that even at dissolution rates of more than 20 monolayers per second, gold etching proceeds in a layer-by-layer mechanism. Moreover, these studies revealed that *in situ* mea-

surements employing deposition or dissolution rates of up to 100 monolayers per second are in principle feasible.

Due to its importance for the copper electrodeposition process, the atomic-scale structure of the electrochemical interfaces between the low index copper electrode surfaces Cu(001) and Cu(111) and chloride-containing electrolyte, respectively, has been investigated by combined SXRD and electrochemical measurements and was discussed with respect to modern theories (density functional theory (DFT) and halide adlayer theories, respectively). Specifically, in case of chloride adsorbed on Cu(001), the presence of the c(2×2) superstructure inducs a corrugation of the second subsurface copper layer. In comparison with a recent SXRD study of the Cu(001)-Cl-system in UHV, the presence of the electrolyte leads to a reversal in the buckling of this layer. DFT calculations by A. Franke, J. Stremme, and E. Pehlke reproduced this behavior by accounting for the outer part of the electrochemical double layer. Additional experiments, focusing on the potential dependence of the halide adlayer on Cu(001), revealed that the c(2×2) structure persists down to potentials close to the onset of hydrogen evolution, however, with decreasing potential the degree of order of the chloride adlayer decreases. Even at potentials as negative as -0.7 V, disordered chloride remains at the surface. The presented study of the surface morphology of Cu(111) in chloride-containing electrolyte revealed a two-dimensional incommensurate chloride adlayer with a rotated hexagonal structure. The highly precise determination allowed to solve the discrepancy of different proposed adlayer structures, which were observed in previous *in situ* STM studies. The potential-dependent rotation and compressibility of the adlayer structure was discussed on the basis of modern adlayer theories. Surprisingly, a closer similarity to under-potentially deposited metal adlayers than to other halide adlayers on different metals was found. The structural data obtained in both studies provides deeper insight into the interaction of chloride with copper electrode surfaces, which is highly relevant to fundamental questions related to copper electrodeposition and corrosion. Consequently, these studies served as a basis for the subsequent electrodeposition studies on the Cu(001) surface. Nevertheless, detailed surface crystallographic studies as presented here also provide experimental data that can be directly compared to calculations and models within modern theories and thus contribute to testing and guidance of the development of more precise *ab initio* theories for the description of electrochemical phase boundaries.

Detailed *in situ* growth behavior studies during the homoepitaxial electrodeposition on Cu(001) in simple chloride-containing electrolyte were performed by employing simultaneous SXRD and electrochemical measurements. Time-dependent changes in the scattered x-ray signal were recorded with the one-dimensional detector system at selected reciprocal space positions as a function of the electrode potential. This allowed to monitor the atomic-scale deposition processes under diffusion-limited, realistic growth conditions at large deposition overpotentials with a time resolution of 0.1 s. For deposition rates of ~ 7.6 and ~ 38.0 ML/min, transitions from step-flow to layer-by-layer to multilayer growth were observed with increasing potential, with layer-by-layer growth being the dominating growth mechanism. The interesting potential dependence of the occurring growth behavior can be explained by a substantially decreasing surface diffusion of the copper adatoms induced by the developing degree of order of the chloride adlayer with increasing potential. The presence of copper adatoms during growth *vice versa* is found to affect the chloride surface dynamics, resulting in a pronounced kinetic inhibition of the chloride adlayer ordering

process. In contrast to observations in copper-free electrolyte, the ordering process occurs on time-scales which are by about two orders of magnitude longer. Furthermore, from a detailed analysis of the peak shape measured with the one-dimensional detector during layer-by-layer growth, a time-dependent oscillatory average strain in the surface layer is deduced, similar to earlier findings for heteroepitaxial as well as homoepitaxial growth, *e.g.*, for Cu(001) homoepitaxy in UHV [317]. However, beyond the models which have been proposed for the explanation of these in-plane lattice spacing oscillations, the detailed analysis of our measurements allowed to derive a more comprehensive model, which, in addition to relaxations in island edges, also accounts for surface strain induced by the presence of copper adatoms at the surface. In total, these observations reflect the particular importance of the solid surface structure and of the influence of the halide adlayer on the growth process.

In continuation of these fundamental studies with respect to additive-containing electrolytes, the homoepitaxial growth of Cu(001) in electrolyte containing chloride and the inhibitor polyethylene glycol was investigated by combined electrochemical methods and *in situ* SXRD. For the first time, direct verification of the existence of the ordered c(2×2) chloride adlayer structure in the presence of the polymer was provided. The phase transition from the ordered to the disordered chloride adlayer was found to be spread over a wider potential regime as compared to the observations in the PEG-free electrolyte, indicating the stabilization of the ordered chloride adlayer phase. Crystal truncation rod measurements in absence and presence of PEG revealed that the polymer interacts more strongly with the partially c(2×2) covered surface, inducing changed characteristics in the degree of order of the chloride atoms (out-of-plane vibration). In direct growth behavior studies the occurrence of layer-by-layer growth oscillations was observed over a wide potential regime with a transition to multilayer growth with increasing potential. The deposition rate is reduced by a factor of ~ 3 as compared to the measurements in PEG-free electrolyte, thus clearly supporting the inhibiting effect of the PEG-Cl-complex on the deposition reaction. This deceleration effect during copper electrodeposition, induced by the inhibitor PEG, was observed for the first time with atomic-scale structure sensitive methods.

To conclude, the presented studies mark an important progress in the investigation of copper electrodeposition in electrolytes containing additives used in ULSI plating. For the first time, atomic-scale structural data as well as highly time-resolved data during the growth process were obtained by *in situ* SXRD, allowing to contribute to a fundamental mechanistic understanding of the processes occurring during the early stages of growth in such electrolytes.

Further studies in continuation of the present work may concentrate on the investigation of the important role of the additives SPS or MPSA in the deposition processes, employing in a similar way high-resolution *in situ* SXRD and electrochemical techniques. The investigation of copper homoepitaxial electrodeposition in electrolytes containing the same species as used in baths exhibiting 'superfilling' conditions, *i.e.*, the combination of chloride, PEG and SPS or MPSA, would be desirable in order to deepen the fundamental mechanistic understanding of the influence of these additives on copper electrodeposition employed for the formation of ULSI microchips. The provided basic knowledge will be of great importance for the further development of plating bath formulations, with the intention to further reduce the dimensions of today's mass-produced microchips in the future.

In addition, the current setup may be extended by employing a two-dimensional detector in order to determine the mesoscopic in-plane structure of the Cu(001) growth front in these electrolytes in more detail. Amongst others, adatom surface diffusion during 2D growth and kinetic roughening during the initial stages of 3D growth may be addressed with these grazing incidence small angle x-ray scattering experiments (GISAXS), in terms of deepen the understanding of the atomic-scale kinetics during the initial stages of electrodeposition. Such studies may reveal the saturation island density as well as the diffusion constant in dependence of the applied electrode potential. Moreover, detailed studies of the kinetic scaling behavior may shed light on the dependence of the rms-roughness on deposition time. Similar AFM studies on the micrometer scale revealed anomalous or normal scaling behavior, depending on the electrolyte composition [284]. With GISAXS measurements, atomic-scale data is obtained, thus allowing to examine the origin of the latter findings.

A Appendices

A.1 Technical Details: ID32 Beamline, X-Ray Optics, Mythen 1K

The most important design parameters of the ID32 beamline, its source and optical elements, as well as of the Mythen 1K detector are summarized in table A.1. Data are taken from ref. [133, 139] and represent the status at the time of the experiments (2008 - 2010). Further detailed information on the detector is given in ref. [138, 140].

X-Ray Source Summary			
	1^{st} undulator	2^{nd} undulator	3^{rd} undulator
magnet period	35 mm	35 mm	42 mm
K_{max}	2.3957	2.3246	3.2025
B_{max}	2.08 T	2.01 T	1.95 T
total power at 200 mA	1.8 kW	1.8 kW	3.2 kW
max. power density at 30 m	90 Wmm^{-2}	90 Wmm^{-2}	90 Wmm^{-2}
source size	0.900×0.02 mm^2 (horizontal $\times$ vertical) FWHM		
beam divergence at 10 keV	0.030×0.020 $mrad^2$ (horizontal $\times$ vertical) FWHM		
peak flux at 25 m at 200 mA	$7 \cdot 10^{14}$ photons s^{-1} mm^{-2}, 0.1% bandwidth		
energy range	$E_{min} = 1.4$ keV, $E_{max} = 30$ keV		

X-Ray Optics Summary	
at 30 m from source	Si(111) monochromator with two crystals, LN_2 cooled
at 41 m from source	450 mm long mirror, SiO_2, Ni, Pd coatings fixed angle of $\sim 0.1°$
beam size at sample (H $\times$ V)	0.3×0.04 mm^2 focused at E = 22.5 keV
energy resolution $\Delta E/E$	$\leq 10^{-4}$
flux at sample (focused beam)	$1.5 \cdot 10^{11}$ photons s^{-1} at E = 22.5 keV, hg = 0.25 mm, vg = 0.01 mm, slvg = slhg = 0.5 mm, I_{ring} = 200 mA

Mythen 1K Detector	
Sensor type	linear array of 1280 reverse biased silicon diodes
Sensitive area	1280 strips of (50 ± 3) µm $\times$ 8 mm $\rightarrow$ 64×8 mm^2
Energy range	5 - 30 keV
Maximum counting rate	$2 \cdot 10^5$ counts s^{-1} $strip^{-1}$
Readout time	0.3 ms
Frame rate & dynamic range	24 bit: 25 Hz, 16/8 bit: 300 Hz, 4 bit: 600 Hz
Detector dimensions	(WHD) $74 \times 100 \times 25$ mm^3, 280 g
$d_{sample\text{-}detector}$	1000 mm
mounting angle to NaI	$\Delta\gamma \approx 19.3°$, $\Delta\delta \approx 0.02°$ (*cf.* section A.3.2)

Table A.1: Technical details of the ID32 x-ray source, beamline optics and the Mythen 1K detector.

A.2 Macros for the Implementation of the Mythen 1K into SPEC

In order to record a full set of crystal truncation rods automatically and thus within the shortest time possible, the Mythen detector has to be synchronized with the diffractometer motor movements. Specifically, single detector frames have to be taken in-between navigating to different reciprocal space positions along the CTR. Since, at the time when the experiments were carried out, no direct implementation of the Mythen detector into the SPEC diffractometer software existed, a workaround was developed. Data obtained by employing this method are presented in chapter 7.

Figure A.1 sketches the given situation at ID32 (June 2010):

ID32ctrl: The ID32ctrl computer allows to control the entire diffractometer (and beamline) via a SPEC session. Every motor movement has to be launched within this session, either manually (single command) or using a macro.

Mythen control computer: The Mythen control computer communicates with the Mythen 1K detector using the Mythen graphical user interface (MythenGUI) or a command-line tool. The latter may be launched within a secure shell session from the ID32ctrl computer.

Mythen 1K: The Mythen 1K detector receives commands only from the Mythen control computer and sends the recorded data back for storage.

ESRF Network: All three components, the diffractometer system and secondary equipment (printers, server, etc.) are connected via the ESRF network, allowing communication among them.

Icepap Interface: The interface allows communication with the diffractometer motors.

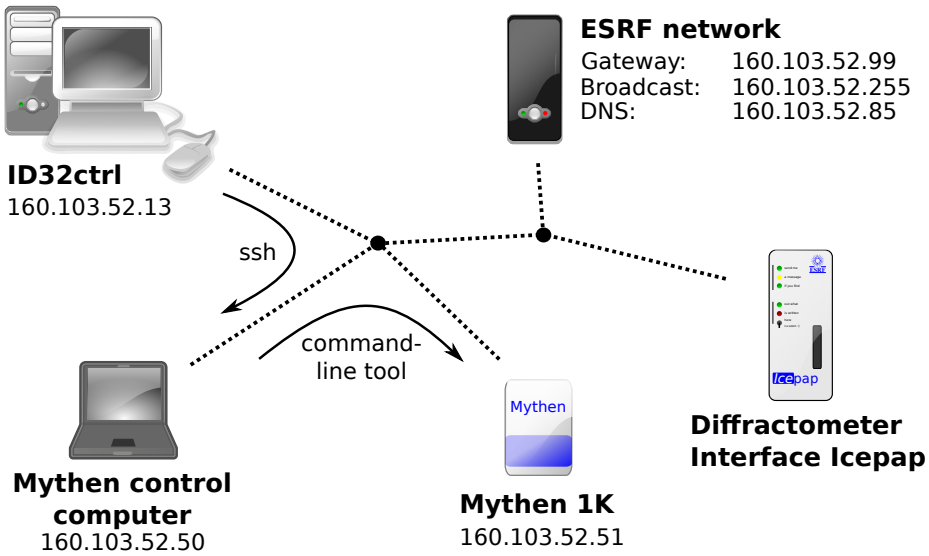

Figure A.1: Schematic illustration of the ID32 computer network. By establishing a secure shell connection (ssh) from ID32ctrl to the Mythen control computer, the command-line tool is started for the communication with the Mythen 1K detector.

The following SPEC commands are available, defined in the file 'mythenmacros.mac', which is listed below in listing A.1.

tomyt: Command to change the diffractometer mode from the NaI point detector to the Mythen 1K. The diffractometer moves the gam/del motors by the angles defined in the macro (has to be defined at the end of the alignment procedure, *cf.* section 3.1.3).

tonai: Command to change the diffractometer mode from the Mythen 1K to the NaI point detector. The diffractometer moves the gam/del motors by the angles defined in the macro (has to be defined at the end of the alignment procedure, *cf.* section 3.1.3).

ctr1d: Command for measuring an entire crystal truncation rod. The command syntax is 'ctr1d $H_{low\ L}$ $K_{low\ L}$ $L_{low\ L}$ $H_{high\ L}$ $K_{high\ L}$ $L_{high\ L}$ L_{start} L_{end} L_{step} time/s filename'. The raw data of single frames measured at different L-values is stored in single files, additionally, the diffractometer motor positions are saved for further data analysis (calculation of correction factors).

timescan1d: Command for recording a time scan with the Mythen 1K detector. The command syntax is 'timescan1d acquisition_time/ms duration/s filename'.

Listing A.1: Source code of the macros used for the implementation of the Mythen 1K into SPEC.

```
# Quick implementation of Mythen 1K to Spec (no data import in spec)
# F. Golks  06/03/2010
# last change:  01/05/2010

##########################################################
# please DON'T modify the original macros (use a local copy)  #
# remark: time values are given in s!                         #
##########################################################

# initializing detector mode: 0 represents NaI, 1 represents Mythen
mythenactive = 0


def tomyt'{
  # change from NaI to Mythen detector

   if(mythenactive == 1){
     if(yesno("Warning: Diffractometer already in Mythen mode! Continue?",0) != 1)
       {exit}
     }

   local gam_old gam_new del_old del_new
   gam_old = A[gam]
   gam_new = gam_old - 19.21
   del_old = A[del]
   del_new = del_old + 0.30

   printf("\nChanging from NaI to Mythen (set gam from %.4f to %.4f, del from %.4f
     to %.4f)\n", gam_old, gam_new, del_old, del_new)

   set gam gam_new
   set del del_new
   umv gam gam_old
   umv del del_old
}'
```

```
36
37
38  def tonai'{
39    # change from Mythen to NaI detector
40
41    if(mythenactive == 0){
42      if(yesno("Warning: Diffractometer already in NaI mode! Continue?",0) != 1)
43        {exit}
44      }
45
46    local gam_old gam_new del_old del_new
47    gam_old = A[gam]
48    gam_new = gam_old + 19.21
49    del_old = A[del]
50    del_new = del_old - 0.30
51
52    printf("\nChanging from Mythen to NaI (set gam from %.4f to %.4f, del from %.4f
53      to %.4f)\n", gam_old, gam_new, del_old, del_new)
54
55    set gam gam_new
56    set del del_new
57    umv gam gam_old
58    umv del del_old
59  }'
60
61
62  def getmaxint'{
63    # get intensity value from Mythen ping
64    tmp = sprintf("ssh mythen@160.103.52.50 /home/mythen/MythenSoft/bin/text_client
65      160.103.52.51 -time 0.1 -frames 1 -start -fname /home/mythen/MythenSoft/module
66      /SN026/data/tmp.raw")
67    unix(tmp)
68    unix("ssh mythen@160.103.52.50 python /home/mythen/programs/getmax.py",
69      filtervalue)
70  }'
71
72
73  def ctr1d'{
74    # CTR macro for mythen detector
75    # adapted from O. Robach (14/11/2001)
76
77    setfilter 15
78    filtervalue = 13000
79    i = $#
80    if (i < 11){print \
81        "Record full CTR with Mythen detector
82         syntax : ctr1d <H0> <K0> <L0> <H1> <K1> <L1> <L_start> <L_end> <L_step>
83             <time [s]> <filename>
84         WARNING :
85          - enter the L_step, not the number of intervals
86          - L_end needs to be larger than L_start
87
88         What the CTR command does :
89         it measures an aligned CTR in Mythen 1K detector frames,
90           automatically adjusting with L, safing in name_...
91
92         What needs to be done before using the CTR command :
93          - align theta and delta on a point at LOW L=l0 on the CTR to be measured.
94          - Do a wh and note the aligned values h0, l0, l0
95          - align theta and delta on a point at HIGH L=l1 on the CTR to be measured.
96          - Do a wh and note the aligned values h1, l1, l1
97          - Then use h0, k0, l0, h1, k1, l1 as input for the CTR command"
98      exit}
99
100   if ($9 > $10){
101     print "L_end should be larger than L_start"
102     exit
103     }
```

```
104
105   local valH0
106   local valK0
107   local valL0
108   local valH1
109   local valK1
110   local valL1
111   local valstart
112   local valend
113   local valstep
114   local timeormon
115   local indexd
116
117   local valH
118   local valK
119   local valL
120   local r
121
122   valH0       = $1
123   valK0       = $2
124   valL0       = $3
125   valH1       = $4
126   valK1       = $5
127   valL1       = $6
128   valstart    = $7
129   valend      = $8
130   valstep     = $9
131   timeormon   = $10
132   filename    = "$11"
133
134   if (valstep < 0.0) valstep=-valstep
135   valL=valstart
136   indexd = 0
137   while (valL<=valend+0.00001) {
138     indexd +=1
139
140     r = (valL-valL0)/(valL1-valL0)
141     valH = valH0 + r *(valH1-valH0)
142     valK = valK0 + r *(valK1-valK0)
143
144     p "*************************************"
145     p "h k l = " valH " " valK " " valL
146     p "*************************************"
147     ubr valH valK valL
148     wh
149
150     # filter control: 100 ms testping with filter 15, then removing step-by-step
151       filters according to measured response
152
153     setfilter 9
154     getmaxint
155     if (filtervalue >= 1250                        ){setfilter 9}
156     if (filtervalue >=  192 && filtervalue <= 1249){setfilter 8}
157     if (filtervalue >=   50 && filtervalue <=  191){setfilter 7}
158     if (                       filtervalue <=   30){
159       setfilter 4
160       getmaxint
161       if (filtervalue >= 1250                        ){setfilter 4}
162       if (filtervalue >=  192 && filtervalue <= 1249){setfilter 3}
163       if (filtervalue >=   50 && filtervalue <=  191){setfilter 2}
164       if (filtervalue <= 30){
165         setfilter 0
166         getmaxint
167         if (filtervalue <= 300){timeormon = 2}
168         if (filtervalue <= 200){timeormon = 3}
169         }
170       }
171
```

```
172       tmp = sprintf("ssh mythen@160.103.52.50 /home/mythen/MythenSoft/bin/
173         text_client 160.103.52.51 -time %s -frames 1 -start -fname /home/mythen/
174         MythenSoft/module/SN026/data/%s_%i.raw", timeormon, filename, indexd)
175       unix(tmp)
176       setfilter 15
177       tmp1 = sprintf("Index = %s, Gam = %s, del = %s, chi = %s, phi = %s",indexd,
178         A[gam],A[del],A[chi],A[phi])
179       tmp = sprintf(" echo %s >> /mntdirect/_data_visitor/si2074/id32/%s_info",tmp1,
180         filename)
181       unix(tmp)
182
183       valL=valL+valstep
184     }
185   }'
186
187   def timescan1d'{
188     # macro for launching a Mythen timescan
189
190     i = $#
191     if (i < 3){print \
192         "Record timescan with Mythen detector
193          syntax : timescan1d <acquisition time [ms]> <length [s]> <rootname>"
194       exit}
195
196     local rate
197     local length
198     rate     = $1/1000
199     length   = $2
200     number   = length/rate
201     filename = "$3"
202
203
204     tmp = sprintf("ssh mythen@160.103.52.50 /home/mythen/MythenSoft/bin/
205       text_client 160.103.52.51 -time %s -frames %s -start -fname /home/mythen/
206       MythenSoft/module/SN026/data/%s.raw", rate, number, filename)
207     unix(tmp)
208   }'
```

A.3 The Mythen 1K in Reciprocal Space

A.3.1 Six-Circle Diffractometer Calculations

In this section, the precise calculation of the reciprocal space $\vec{q}$ vectors for each pixel stripe of the Mythen 1K is sketched. A relation, linking the reciprocal space and the laboratory frame of reference, is indispensable. Mathematically expressed, this orientation in reciprocal space is based on an 'orientation matrix' **UB**, which has to be calculated after specifying the crystal lattice parameters, which define the matrix **B**, and two reflections OR0 and OR1, from which the matrix **U** can be inferred. Detailed angle calculations for the six-circle diffractometer, as they will be briefly sketched here, were carried out by Lohmeier and Vlieg and are described in ref. [135].

According to equation (2.1)[1], the scattering vector in reciprocal space is defined, with respect to the (not necessarily) crystalline coordinate system, by

$$\vec{q}_{\mathrm{rs}} = H \cdot \vec{a}_1^* + K \cdot \vec{a}_2^* + L \cdot \vec{a}_3^* \,, \tag{A.1}$$

with the three reciprocal lattice vectors $\vec{a}_i^*$. Real space and reciprocal space lattice vectors are related via $\vec{a}_i \cdot \vec{a}_j^* = 2\pi\delta_{ij}$. α_i and β_i, $i = (1, 2, 3)$, denote the real and reciprocal space angles between the vectors.

The used diffractometer with its six circles was introduced in section 3.1.2. The Cartesian laboratory frame of reference consists of the three $\vec{x}$, $\vec{y}$, and $\vec{z}$ axes shown in figure A.2a. The z-axis is perpendicular to the laboratory floor and the xy-plane lies in the floor, with the positive y-axis pointing along the direction of the incoming x-ray beam (the x-ray beam is assumed to be parallel to the floor). The diffractometer is used in the 'z-axis mode', in which the sample circles χ and φ are used to fix the sample surface normal in coincidence with the diffractometer ϑ axis.
The scattering vector may be evaluated with respect to this Cartesian laboratory frame, yielding $\vec{q}_{\mathrm{lab}}$, which is defined by the angular settings of the diffractometer as well as by the chosen energy of the x-ray beam. However, it is more convenient to refer the vector to the axes of a Cartesian coordinate system, which is tilted by the angle of incidence α (so-called α-frame). Both coordinate systems are linked by a rotation matrix **A**,

$$\vec{q}_\alpha = \begin{pmatrix} q_{\alpha,x} \\ q_{\alpha,y} \\ q_{\alpha,z} \end{pmatrix} = \boldsymbol{A}^{-1}\, \vec{q}_{\mathrm{lab}} = \begin{pmatrix} 1 & 0 & 0 \\ 0 & \cos\alpha & -\sin\alpha \\ 0 & \sin\alpha & \cos\alpha \end{pmatrix}^{-1} \vec{q}_{\mathrm{lab}} \,. \tag{A.2}$$

From figure A.2b, which shows the scattering geometry in the α-frame, the following relation can be deduced:

$$\vec{q}_\alpha = \vec{k}_f - \vec{k}_i = k_0 \cdot \begin{pmatrix} -\sin\delta \cdot \cos\gamma \\ \cos\delta \cdot \cos\gamma - \cos\alpha \\ \sin\gamma + \sin\alpha \end{pmatrix} , \tag{A.3}$$

with $k_0 = 2\pi/\lambda$.

[1] for clarity reasons, the scattering vector as given in the reciprocal space frame with respect to the crystalline coordinate system will be denoted by $\vec{q}_{\mathrm{rs}}$

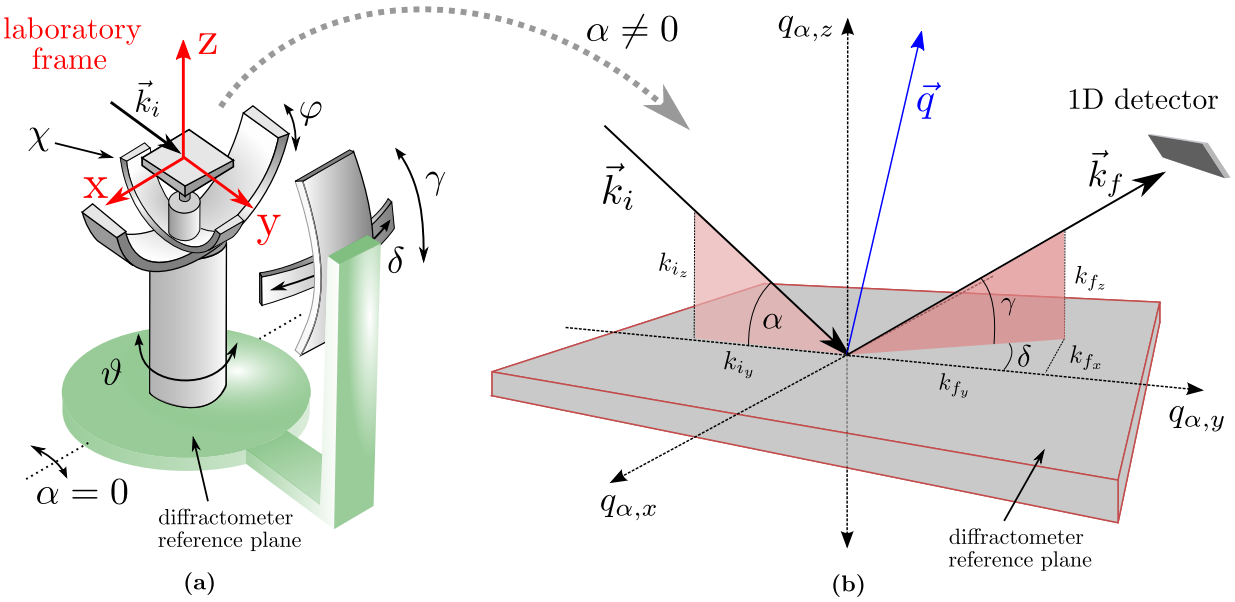

Figure A.2: Illustration of the frames of reference used for the six-circle diffractometer calculations. **(a)** Schematic drawing of the six-circle diffractometer with all circles set to zero. In red, the Cartesian laboratory frame of reference is drawn in. The z-axis is chosen to be perpendicular to the floor (parallel to the ϑ-axis for $\alpha = 0$) and the positive y-axis points along the direction of the x-ray beam. **(b)** Scattering geometry with respect to the α-frame of reference, used for the derivation of equation (A.3). With the constraint of $\chi = \varphi = 0$, the diffractometer reference plane corresponds to the sample plate.

The transformation into the reciprocal space coordinates $\vec{q}_{\mathrm{rs}}$ or vice versa is calculated according to the matrix equation

$$\begin{aligned} \vec{q}_{\mathrm{rs}}(H,K,L) &= (\mathbf{UB})^{-1}\ \mathbf{\Phi}^{-1}\ \mathbf{X}^{-1}\ \mathbf{\Theta}^{-1}\ \vec{q}_{\alpha}(\alpha,\delta,\gamma,k_0) \\ &= (\mathbf{UB})^{-1}\ \vec{q}_{\varphi}(\alpha,\delta,\gamma,\vartheta,\chi,\varphi,k_0)\,. \end{aligned} \tag{A.4}$$

Therein, $\vec{q}_{\alpha}$ is successively converted into the Cartesian coordinate frames belonging to the three diffractometer axes ϑ, χ and φ by successive application of rotation matrices about the corresponding angles, respectively. According to the six-circle diffractometer geometry depicted in figure A.2a, these matrices are given by

$$\mathbf{\Theta} = \begin{pmatrix} \cos\vartheta & \sin\vartheta & 0 \\ -\sin\vartheta & \cos\vartheta & 0 \\ 0 & 0 & 1 \end{pmatrix} \quad \mathbf{X} = \begin{pmatrix} \cos\chi & 0 & \sin\chi \\ 0 & 1 & 0 \\ -\sin\chi & 0 & \cos\chi \end{pmatrix} \quad \mathbf{\Phi} = \begin{pmatrix} \cos\varphi & \sin\varphi & 0 \\ -\sin\varphi & \cos\varphi & 0 \\ 0 & 0 & 1 \end{pmatrix}. \tag{A.5}$$

Subsequently, the multiplication with the inverse orientation matrix $(\mathbf{UB})^{-1}$ establishes the orientational relationship, *i.e.*, the coordinate transformation from the diffractometer φ-reference system, in which the scattering vector is denoted as $\vec{q}_{\varphi}$, into the crystalline Cartesian coordinate system of the reciprocal space, in which the scattering vector is then denoted as $\vec{q}_{\mathrm{rs}}$. Specifically, the matrix $\mathbf{B}$ converts a given vector from the crystal lattice frame, which might even be triclinic, into a Cartesian coordinate frame[2] or vice versa.

[2]The reciprocal Cartesian coordinate frame is defined with $\vec{e}_1$ parallel to $\vec{a}_1^*$, $\vec{e}_2$ in the plane of $\vec{a}_2^*$ and $\vec{a}_3^*$ and $\vec{e}_3$ perpendicular to that plane ($|\vec{e}_i| = 1$).

Specifically, **B** only depends on the crystal lattice parameters and has been calculated by Busing and Levy [318]

$$\mathbf{B} = \begin{pmatrix} \vec{a}_1^* & \vec{a}_2^* \cdot \cos\beta_3 & \vec{a}_3^* \cdot \cos\beta_2 \\ 0 & \vec{a}_2^* \cdot \sin\beta_3 & -\vec{a}_3^* \cdot \sin\beta_2 \cos\alpha_1 \\ 0 & 0 & 2\pi/|\vec{a}_3| \end{pmatrix} . \tag{A.6}$$

The elements of **U** are defined by the sample alignment and thus have to be calculated for every aligned crystal. The fundamental equation underlying the computation is given by:

$$\vec{q}_\varphi = \mathbf{UB} \cdot \vec{q}_{\mathrm{rs}} = \mathbf{\Phi}^{-1}\ \mathbf{X}^{-1}\ \mathbf{\Theta}^{-1} \cdot \vec{q}_\alpha(\alpha, \delta, \gamma, k_0) . \tag{A.7}$$

Starting with the reciprocal lattice vectors (Miller indices) of the two aligned Bragg reflections OR0 and OR1, an orthonormal matrix $\mathbf{Q}_{\mathrm{rs}}$ is generated (the third vector is calculated using the cross product). In addition, a second orthonormal matrix $\mathbf{Q}_\varphi$ of momentum transfer vectors, given with respect to the diffractometer φ-frame. For this purpose, the two sets of appropriate angular motor positions (eq. (A.3)) and the inverse rotation matrices (eq. (A.5)) are needed according to equation (A.7). Finally, **U** is calculated from these matrices with

$$\mathbf{U} = \mathbf{Q}_\varphi \cdot \mathbf{Q}_{\mathrm{rs}}^{-1} . \tag{A.8}$$

B has been omitted as $\mathbf{Q}_{\mathrm{rs}}$ and $\mathbf{Q}_\varphi$ are orthonormal.

Calculation of the Crystal Miscut

As mentioned before, the diffractometer is used in the z-axis mode, in which the two angles χ and φ are kept constant in order to fix the orientation of the optical (or averaged physical) surface normal in coincidence with the ϑ-circle axis, *i.e.*, the angle of incidence fixed with respect to the crystal surface.

The crystal miscut is then calculated as angle between the (optical) surface normal, $\vec{q}_{\mathrm{rs}}^{\perp}$, and the reciprocal unit cell direction $\vec{a}_3^*$, which is assumed to point in the direction of the ideal surface normal without miscut:

$$\mu = \arccos\left(\frac{\vec{q}_{\mathrm{rs}}^{\perp} \cdot \vec{a}_3^*}{|\vec{q}_{\mathrm{rs}}^{\perp}| \cdot |\vec{a}_3^*|} \right) . \tag{A.9}$$

$\vec{q}_{\mathrm{rs}}^{\perp}$ is related to $\vec{q}_\varphi^{\perp}$ according to equation (A.4) and thus can be calculated from φ and χ:

$$\vec{q}_{\mathrm{rs}}^{\perp} = (\mathbf{UB})^{-1} \cdot \vec{q}_\varphi^{\perp} = \mathbf{B}^{-1}\ \mathbf{U}^{-1} \cdot \begin{pmatrix} -\cos\varphi \cdot \sin\chi \\ -\sin\varphi \cdot \sin\chi \\ \cos\chi \end{pmatrix} . \tag{A.10}$$

However, a precise determination of the crystal miscut is difficult if the sample alignment is not performed pedantically. Moreover, choosing reflections with rather low L values limits the accuracy of the alignment and with it the accuracy of the determined miscut angle.

Calculation of the (H, K, L) Coordinates of the Mythen 1K Detector Pixels

The (H, K, L) coordinates of every Mythen detector pixel are calculated using equation (A.3) and (A.4) for varying angles of δ (and γ). An implementation of the calculation routines into the Python™ programming language is given in listing A.2.

In figure A.3, typical measurements performed with the Mythen 1K (red) and with the NaI point detector (black) are directly compared. These data were obtained for a Cu(001) sample at 22.5 keV at (1,1,0.5). In A.3a the scattered intensity in dependence of the in-plane angle δ is shown. The high density of measured points, as compared to a typical point detector scan ($\pm 0.2°$ with 30 points), can be clearly seen. An H-K-map of the calculated reciprocal space positions of each detector pixel in comparison to the measured H-K-positions of the corresponding NaI point detector scan illustrates the angular spread of the Mythen pixel array ($\sim \pm 1.83°$).

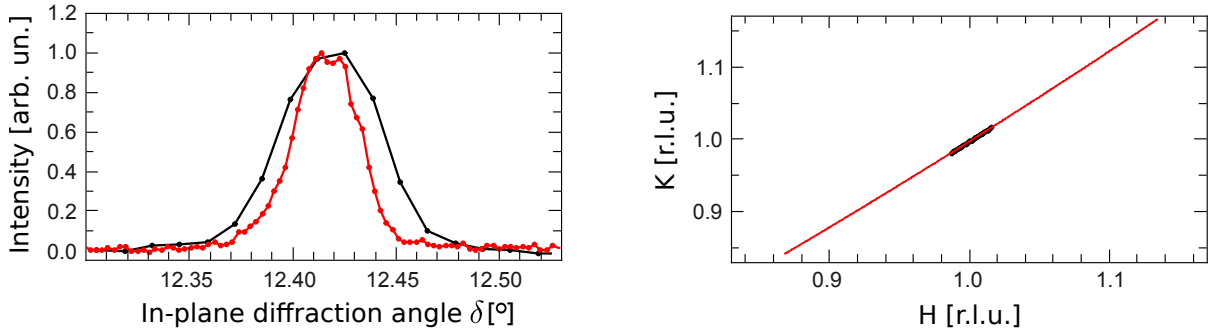

Figure A.3: Comparison of the in-plane cross-section at (1,1,0.5) of a Cu(001) sample at 22.5 keV measured with the NaI point detector (black) and the Mythen 1K (red). (a) The cross-section in dependence of the in-plane scattering angle δ. (b) H-K-map illustrating the angular range covered by the Mythen 1K ($\sim \pm 1.83°$) compared to a typical scan performed with the NaI point detector (typically $\pm 0.2°$).

Listing A.2: Implementation of the six-circle diffractometer calculations into the Python™ programming language. The purpose of the script is the calculation of the miscut angle μ of an aligned crystal and of the precise pixel positions of the Mythen 1K in reciprocal space. However, due to the universal formalism, it can be easily adapted for other calculations.

```
#! /usr/bin/python
# Script written by F. Golks for
#       - calculating miscut of an aligned crystal
#       - calculating the reciprocal space coordinates of the Mythen 1K pixels
# basing on E. Vlieg's six-circle calculations
# [M. Lohmeier and E. Vlieg, Journal of Applied Crystallography 26, 706 (1993)]
# 16/09/2010, University Kiel, ESRF Grenoble

from numpy import matrix, vdot, dot, arctan, sqrt, array, cross, zeros
from math import pi, cos, acos, sin, asin, atan
import sys


############ Definition of Variables/Constants ############

# General Settings (change if necessary)
energy        = 22500
mythen_range = 35   # defines number of channels for which HKL will be calculated

# Definition of Constants
h        = 6.62606876e-34
c        = 299792458
energy   = energy * 1.60217646e-19
lam      = h*c/energy
wave     = 2*pi/lam*1e-10
rad      = 360.0/2.0/pi

# set direct lattice (Copper crystal, change if necessary)
A1 = A2 = A3 = 3.615
A4 = A5 = A6 = 90.0/rad

# define dummy dictionaries
OR0 = {"h":0,"k":0,"l":0,"alpha":0,"delta":0,"gamma":0,"theta":0,"chi":0,"phi":0}
OR1 = {"h":0,"k":0,"l":0,"alpha":0,"delta":0,"gamma":0,"theta":0,"chi":0,"phi":0}


############## Definition of Functions ##############

def sqrt(a):
    return a*a

def veclength(v):
    return sqrt(v[0]*v[0]+v[1]*v[1]+v[2]*v[2])

def matrix_product(M, N):
  dum = aim = [[0,0,0],[0,0,0],[0,0,0]]
  for i in range(3):
    for j in range(3):
      dum[i][j] = N[i][j]
  for i in range(3):
    for j in range(3):
      aim[i][j] = 0.
      for k in range(3):
        aim[i][j] += M[i][k]*dum[k][j]
  return aim

def determinant(matrix):
  return (matrix[0][0]*(matrix[1][1]*matrix[2][2]-matrix[2][1]*matrix[1][2])
    + matrix[1][0]*(matrix[2][1]*matrix[0][2]-matrix[0][1]*matrix[2][2])
    + matrix[2][0]*(matrix[0][1]*matrix[1][2]-matrix[1][1]*matrix[0][2]))

def matrix_inversion(matrix):
```

```
63    det = determinant(matrix)
64    if abs(det) < 1e-5: return 0
65    m_inv = [[0,0,0],[0,0,0],[0,0,0]]
66    for i in range(0,3):
67      iplus1 = (i+1)%3
68      iplus2 = (i+2)%3
69      for j in range(0,3):
70        jplus1 = (j+1)%3;
71        jplus2 = (j+2)%3;
72        m_inv[j][i] = (matrix[iplus1][jplus1]*matrix[iplus2][jplus2]
73          - matrix[iplus2][jplus1]*matrix[iplus1][jplus2])/det
74    return m_inv
75
76  def transpose(matrix):
77    mtrans = [[0,0,0],[0,0,0],[0,0,0]]
78    for i in range(0,3):
79      for j in range(0,3):
80        mtrans[i][j] = matrix[j][i]
81    return mtrans
82
83  def create_rotation_matrix(angle, axis):
84    # Set up a matrix "m" for a rotation by "angle" around given "axis" (eq. A.5)
85    # Check whether the axis is allowed
86    if axis < 1 or axis > 3: return 0
87
88    # determine the proper indices for the matrix ("rechtshaendiges System")
89    axis -= 1
90    axis_plus1 = (axis+1)%3
91    axis_plus2 = (axis+2)%3
92    if axis_plus1 == 2:
93      axis_plus1 = 0
94      axis_plus2 = 2
95
96    # assign values to all matrix elements
97    m = [[0,0,0],[0,0,0],[0,0,0]]
98    m[axis][axis] = 1.
99    m[axis_plus1][axis] = 0.
100   m[axis_plus2][axis] = 0.
101   m[axis][axis_plus1] = 0.
102   m[axis_plus1][axis_plus1] = cos(angle)
103   m[axis_plus2][axis_plus1] = sin(angle)
104   m[axis][axis_plus2] = 0.
105   m[axis_plus1][axis_plus2] = -sin(angle)
106   m[axis_plus2][axis_plus2] = cos(angle)
107   return m, 1
108
109 def matrixtimesvector(matrix, b):
110   b_tmp = a = [0,0,0]
111   for i in range(0,3):
112     b_tmp[i] = b[i]
113   for i in range(0,3):
114     a[i] = 0.
115     c = 0
116     for j in range(0,3):
117       a[i] += matrix[i][j]*b_tmp[j]
118   return a
119
120 def q_comp(alpha, delta, gamma, theta, chi, phi, wave):
121   # Compute momentum transfer q in phi-axis frame from angular settings (eq. A.7):
122   #                -1      -1        -1
123   # q_phi = (PHI)    (CHI)    (theta)    q_alpha
124   # Note: q_phi is defined as UB*q_rs(hkl)
125
126   # get invers matrices
127   thetainv_mat, ret = create_rotation_matrix(theta, 3)
128   chiinv_mat, ret1  = create_rotation_matrix(chi, 2)
129   phiinv_mat, ret2  = create_rotation_matrix(phi, 3)
130
```

```
131   # Compute momentum transfer in alpha-axis coordinate frame according to eq. A.3
132   q     = [0,0,0]
133   q[0] = (sin(delta)*cos(gamma))*wave
134   q[1] = (cos(delta)*cos(gamma)-cos(alpha))*wave
135   q[2] = (sin(gamma)+sin(alpha))*wave
136
137   # Transform q to phi-axis frame
138   q     = matrixtimesvector(thetainv_mat,q)
139   q     = matrixtimesvector(chiinv_mat,q)
140   q     = matrixtimesvector(phiinv_mat,q)
141   return q
142
143 def U_comp():
144   # used variables:
145   # OR0, OR1: user defined rec. space vectors of the two alignment reflections
146   # r_matrix: containing rec. space vectors OR0, OR1 (in Cartesian crystal frame)
147   #   third vector is calculated using outer vector product
148   # q_matrix: calculated from diffractometer motor positions (in phi frame)
149   #   has 2 momentum transfer vectors as rows, 3rd is calculated as above
150   # B: B matrix calculated from crystal lattice specifications
151
152   # Compute OR0/OR1 reciprical space vectors in the Cartesian crystal frame
153   r_matrix       = [[0,0,0],[0,0,0],[0,0,0]]
154   r_matrix[0][0] = OR0["h"]
155   r_matrix[0][1] = OR0["k"]
156   r_matrix[0][2] = OR0["l"]
157   r_matrix[1][0] = OR1["h"]
158   r_matrix[1][1] = OR1["k"]
159   r_matrix[1][2] = OR1["l"]
160   r_matrix[0]    = matrixtimesvector(B, r_matrix[0])
161   r_matrix[1]    = matrixtimesvector(B, r_matrix[1])
162
163   # Compute momentum transfer in phi frame (k_0 = 1, will be normalized anyway)
164   q_matrix    = [[0,0,0],[0,0,0],[0,0,0]]
165   q_matrix[0] = q_comp(OR0["alpha"], OR0["delta"], OR0["gamma"], OR0["theta"],
166                        OR0["chi"], OR0["phi"], 1.)
167   q_matrix[1] = q_comp(OR1["alpha"], OR1["delta"], OR1["gamma"], OR1["theta"],
168                        OR1["chi"], OR1["phi"], 1.)
169
170   # Compute third reflection which is perpendicular to the first two
171   r_matrix[2] = cross(r_matrix[0],r_matrix[1])
172   q_matrix[2] = cross(q_matrix[0],q_matrix[1])
173
174   # Make second reflection perpendicular to first and third
175   r_matrix[1] = cross(r_matrix[2],r_matrix[0])
176   q_matrix[1] = cross(q_matrix[2],q_matrix[0])
177
178   # Normalize all vectors to unity
179   for i in range(0,3):
180     r_length = veclength(r_matrix[i])
181     q_length = veclength(q_matrix[i])
182     if (r_length < 1e-4 or q_length < 1e-4):
183       print "ERROR, invalid orientation reflection"
184     else:
185       for j in range(0,3):
186         r_matrix[i][j] /= r_length
187         q_matrix[i][j] /= q_length
188
189   # Transpose matrices (need three reflections as column vectors)
190   r_matrix = transpose(r_matrix)
191   q_matrix = transpose(q_matrix)
192
193   # Compute orientation matrix U
194   inv_r_matrix = matrix_inversion(r_matrix)
195   U = matrix_product(q_matrix,inv_r_matrix)
196   return U
197
198 def angles_to_hkl(alpha, delta, gamma, theta, chi, phi, wave):
```

```
199     # Compute r.l. Miller indices from angular set using eq. A.4:
200     #                          -1      -1      -1       -1
201     #  q_rs(h,k,l) = (UB)    (PHI)    (CHI)    (THETA)    q_alpha
202
203     q_alpha = q_rs = [0,0,0]
204
205     # Compute momentum transfer in alpha-axis coordinate frame
206     q_alpha[0] = (sin(delta)*cos(gamma))*wave
207     q_alpha[1] = (cos(delta)*cos(gamma)-cos(alpha))*wave
208     q_alpha[2] = (sin(gamma)+sin(alpha))*wave
209
210     # Create rotation matrices
211     theta_mat = create_rotation_matrix(theta, 3)
212     chi_mat   = create_rotation_matrix(chi, 2)
213     phi_mat   = create_rotation_matrix(phi, 3)
214     UB_inv    = matrix_inversion(UB)
215
216     # Transform qset to reciprocal lattice frame
217     q1    = matrixtimesvector(theta_mat,q_alpha)
218     q2    = matrixtimesvector(chi_mat,q1)
219     q3    = matrixtimesvector(phi_mat,q2)
220     q_rs  = matrixtimesvector(UB_inv,q3)
221     return q_rs
222
223
224 ##########################################################
225 #  Main Main Main Main Main Main Main Main Main Main Main  #
226 ##########################################################
227
228 # calculate reciprocal unit cell vectors and angles
229 volume  = A1*A2*A3*sqrt(1+2*cos(A4)*cos(A5)*cos(A6)-sqrt(cos(A4))-sqrt(cos(A5))
230             -sqrt(cos(A6)))
231 B1      = 2*pi*A2*A3*sin(A4)/volume
232 B2      = 2*pi*A1*A3*sin(A5)/volume
233 B3      = 2*pi*A1*A2*sin(A6)/volume
234 B4      = acos((cos(A5)*cos(A6)-cos(A4))/(sin(A5)*sin(A6)))
235 B5      = acos((cos(A4)*cos(A6)-cos(A5))/(sin(A4)*sin(A6)))
236 B6      = acos((cos(A4)*cos(A5)-cos(A6))/(sin(A4)*sin(A5)))
237
238 # compute matrix B according to equation A.6
239 B       = [[0,0,0],[0,0,0],[0,0,0]]
240 B[0][0] = B1
241 B[1][0] = B[2][0] = B[2][1] = 0.
242 B[0][1] = B2*cos(B6)
243 B[1][1] = B2*sin(B6)
244 B[0][2] = B3*cos(B5)
245 B[1][2] = -B3*sin(B5)*cos(A4)
246 B[2][2] = 2.0*pi/A3
247
248 # get user input for OR0, OR1, motor
249 print ("*******Input of General Settings:*******\n")
250 OR0["alpha"] = float(raw_input("Alpha: "))/rad
251 OR0["chi"]   = float(raw_input("Chi: "))/rad
252 OR0["phi"]   = float(raw_input("Phi: "))/rad
253
254 print ("****Orientation Matrix Reflection 1:****\n")
255 OR0["h"]     = float(raw_input("Miller index h: "))
256 OR0["k"]     = float(raw_input("Miller index k: "))
257 OR0["l"]     = float(raw_input("Miller index l: "))
258 OR0["delta"] = float(raw_input("Delta: "))/rad
259 OR0["gamma"] = float(raw_input("Gamma: "))/rad
260 OR0["theta"] = float(raw_input("Theta: "))/rad
261
262 print ("****Orientation Matrix Reflection 1:****\n")
263 OR1["h"]     = float(raw_input("Miller index h: "))
264 OR1["k"]     = float(raw_input("Miller index k: "))
265 OR1["l"]     = float(raw_input("Miller index l: "))
266 OR1["delta"] = float(raw_input("Delta: "))/rad
```

```
267 OR1["gamma"] = float(raw_input("Gamma: "))/rad
268 OR1["theta"] = float(raw_input("Theta: "))/rad
269 OR1["alpha"] = OR0["alpha"]
270 OR1["chi"]   = OR0["chi"]
271 OR1["phi"]   = OR0["phi"]
272 TAU          = -OR0["phi"]
273 SIGMA        = -OR0["chi"]
274
275 print ("****Position of Mythen Measurements:****\n")
276 my_del       = float(raw_input("Delta: "))/rad
277 my_th        = float(raw_input("Theta: "))/rad
278 my_chi       = float(raw_input("Chi: "))/rad
279 my_phi       = float(raw_input("Phi: "))/rad
280 my_alp       = float(raw_input("AlphaTheta: "))/rad
281 my_gam       = float(raw_input("Gamma: "))/rad
282
283 # calculate UB matrix
284 U        = U_comp()
285 UB       = matrix_product(U, B)
286 U_inv    = matrix_inversion(U)
287 B_inv    = matrix_inversion(B)
288
289 # calculate miscut as angle between surface normal and b_3 = [0,0,1]
290 s_phi    = [0,0,0]
291 b_3      = [0.0,0.0,1.0]
292 s_phi[0] = cos(TAU)*sin(SIGMA)
293 s_phi[1] = -sin(TAU)*sin(SIGMA)
294 s_phi[2] = cos(SIGMA)
295 s_cryst  = matrixtimesvector(U_inv, s_phi)
296 s_rs     = matrixtimesvector(B_inv, s_cryst)
297
298 miscut   = acos(vdot(s_rs,b_3)/(abs(veclength(s_rs))*abs(veclength(b_3))))
299 s_rs   = s_rs/veclength(s_rs)
300
301 print ("Surface normal is along [h,k,l] = [%f,%f,%f]" % (s_rs[0],s_rs[1],s_rs[2]))
302 print ("The miscut angle is %f degrees." % (miscut*rad))
303
304 # calculate Mythen HKL set from angle variation in delta
305 H_array = K_array = L_array = H_array2 = K_array2 = L_array2 = []
306 angle = angle2 = []
307
308 for i in range(mythen_range):
309   del_tmp = my_del + atan(i*0.05/1000)
310   angle.append(str(del_tmp*rad))
311   vec = angles_to_hkl(my_alp, del_tmp, my_gam, my_th, my_chi, my_phi, wave)
312   H_array.append(str(vec[0]))
313   K_array.append(str(vec[1]))
314   L_array.append(str(vec[2]))
315
316   del_tmp = my_del - atan((mythen_range - 1 - i)*0.05/1000)
317   angle2.append(str(del_tmp*rad))
318   vec = angles_to_hkl(my_alp, del_tmp, my_gam, my_th, my_chi, my_phi, wave)
319   H_array2.append(str(vec[0]))
320   K_array2.append(str(vec[1]))
321   L_array2.append(str(vec[2]))
322
323 H_det = H_array2[0:-1] + H_array
324 K_det = K_array2[0:-1] + K_array
325 L_det = L_array2[0:-1] + L_array
326 angle = angle2[0:-1] + angle
327
328 for i in range(len(H_det)):
329   print (angle[i] + " " + H_det[i] + " " + K_det[i] + " " + L_det[i])
```

A.3.2 Mythen 1K Alignment Procedure

As explained in section 3.1.3, the Mythen 1K detector is mounted below the existing point detector under an out-of-plane angle $\Delta\gamma$ (and an unavoidable small in-plane angle $\Delta\delta$), *cf.* figure 3.2a. The value of $\Delta\gamma$ is obtained by aligning the detector center (in the short direction) on the primary beam. As depicted in figure A.4a, this is done after removal of the detector and using a small detector slit (aperture 0.5 mm) and a wide guard slit. The center of the dectector, which is coincident with the center of the detector slit, is then found by measuring the intensity on the x-ray diode D3 in dependence of the angle γ. In the obtained peak maximum, the detector slit center and thus the detector center is well aligned with the direct beam. Afterwards, the detector slit is removed (in the experiments reported here no detector slit was employed) and the guard slit (2 mm aperture) is adjusted to be collinear with respect to the x-ray beam via the 'burned paper technique' (shown in A.4b). *I.e.*, the slit center is adjusted via vertical translation to the position of the direct beam, which is measured using a x-ray sensitive paper (black spot where beam irradiated).

The in-plane offset $\Delta\delta$ was determined by moving the motor del stepwise until the measured peak shape of the primary beam was centered to the center pixel (640) on the Mythen. Both offset values were subsequently inserted into the macro files introduced in section A.2.

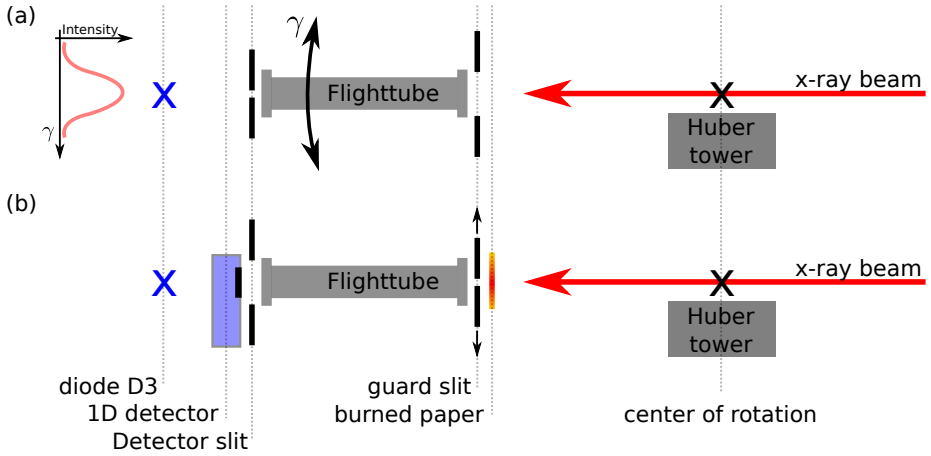

Figure A.4: Schematic illustration of the alignment procedure for the Mythen 1K.

A.3.3 Acceptance Angle Correction

As illustrated in the figure to the right, the Mythen 1K detector is not a segment of a sphere with a radius according to the length of the vector $\vec{r}_c$ from the sample to the detector center. Thus, the acceptance angle of the pixels is not uniform but decreases with increasing tangential distance x from the detector center. An estimation will show that the resulting difference in the recorded intensity is negligible in case of low intensities as they are usually recorded at anti-Bragg condition.

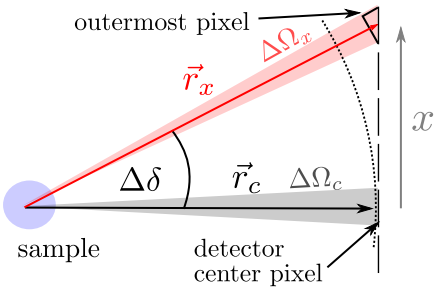

Therefore, the differential cross-section, *i.e.*, the normalization of the scattered intensity I on the incident flux (I_0/A_0) and the solid angle of the detector $(\Delta\Omega)$ is taken into account, defined by

$$\frac{\mathrm{d}\sigma}{\mathrm{d}\Omega} = \frac{1}{I_0/A_0} \cdot \frac{\mathrm{d}I}{\mathrm{d}\Omega} \overset{*}{\approx} \frac{\Delta I}{(I_0/A_0)\Delta\Omega}\,, \tag{A.11}$$

with the intensity and cross-section of the incident x-ray beam, I_0 and A_0, respectively [119]. In the step denoted with $*$, it is assumed that $\Delta\Omega$ is sufficiently small, leading to an approximately constant intensity within the solid angle $\Delta\Omega$. The acceptance angle of the center pixel with the area A_c is defined by

$$\Delta\Omega_c = \frac{\Delta A_c}{r_c^2}\,. \tag{A.12}$$

For an outer pixel in the distance x from the detector center, the sample-pixel distance is enlarged to $r_x = \sqrt{r_c^2 + x^2}$. Moreover, the surface normal of this pixel is tilted by the in-plane angle $\Delta\delta = \arccos(r_c/r_x)$ with respect to the position vector $\vec{r}_x$. The projection of the pixel surface area onto the sphere is given by $\Delta A_x = \Delta A_c \cos\Delta\delta$. Thus, the acceptance angle of the pixel can be calculated as

$$\Delta\Omega_x = \frac{\Delta A_x}{r_x^2} = \frac{\Delta A_c}{r_x^3} \cdot r_c\,. \tag{A.13}$$

The ratio of the two differential cross-sections allows to estimate the maximal error related to the varying acceptance angles by using the outermost pixel at $x = 3.2\,\mathrm{cm}$ and $r_c = 100\,\mathrm{cm}$:

$$\frac{\Delta\Omega_x}{\Delta\Omega_c} = \frac{\Delta A_c \cdot r_c}{r_x^3} \cdot \frac{r_c^2}{\Delta A_c} = \left(\frac{r_c}{r_x}\right)^3 = 0,99847\,. \tag{A.14}$$

This corresponds to an error of 0.153%. Consequently, this effect can safely be neglected as the statistical error $1/\sqrt{N}$ of every measurement is much higher in case of rather low counting statistics, more precisely for $N < 4 \cdot 10^5$ counts per second. As this is the case for all measurements performed at anti-Bragg throughout this work, equation (A.11) is, in a first approximation, fulfilled for all pixels of the detector and no correction factors have to be applied to the data reported in this thesis.

A.3.4 Polarization Correction

Similar to the angular acceptance, also the polarization of the x-ray beam changes from pixel to pixel and thus the measured intensity of each pixel has in principle to be corrected in dependence of the position given by α, δ and γ according to the polarization factor

$$P \approx P_{\text{hor.}} = 1 - \Big(\sin\alpha \cdot \cos\delta \cdot \cos\gamma + \cos\alpha \cdot \sin\gamma\Big)^2 \tag{A.15}$$

Using some typical angular values for α, δ and γ, in detail the set of angles corresponding to the (1,1,0.1) anti-Bragg condition of Cu(001) at the x-ray beam energy of 22.5 keV, the relative deviation of the polarization correction factor in the outermost pixels, ΔP, as compared to the correction factor for the center pixel, P_{center}, can be quickly estimated according to equation (A.15):

$$\begin{aligned} \frac{\Delta P}{P_{\text{center}}} &= \frac{\partial P}{\partial \delta} \cdot \Delta\delta \cdot \frac{1}{P_{\text{center}}} \\ &= \frac{2\cos\gamma\sin\alpha\sin\delta\ (\cos\gamma\cos\delta\sin\alpha + \cos\alpha\sin\gamma)}{1 - (\sin\alpha\cos\delta\cos\gamma + \cos\alpha\sin\gamma)^2} \cdot \Delta\delta \\ &\approx 1.57715 \cdot 10^{-6}\,. \end{aligned} \tag{A.16}$$

Therein, $\Delta\delta = 1.833°$ is the maximum angular spread between the center and the outermost pixel of the Mythen 1K. For the calculation, following values were used in equation (A.16): $\alpha = 0.437°$, $\gamma \approx 0.437°$, $\delta = 12.3757°$. Thus, the polarization correction factor can also safely be neglected for the measurements presented in this work.

A.4 The NaI Point Detector in Reciprocal Space

A.4.1 Correction Factors for the Integrated Intensity

In this section, the geometrical correction factors are discussed, which occur in the measurement of the integrated intensities of surface diffraction rods for the case of a six-circle diffractometer using the NaI point detector. A detailed derivation is given by E. Vlieg [130, 319]. All equations are valid for any incoming or outgoing angle of the x-ray beam, however, they are particularly important for large perpendicular momentum transfers, *i.e.*, at high L values. Once all correction factors are known, the structure factors may be calculated with a common scale factor from the set of CTR measurements.

Following the convention of motor names at ID32, the in-plane and out of-plane angles defined by incident and diffracted beam are called δ and γ, respectively. The angle of incidence with respect to the sample surface is called α. The angle of rotation about the surface normal is called ϑ (*cf.* figure 3.2b in section 3.1.2). By using the integrated intensity[3] for a structural analysis, influences caused by sample or beam inhomogeneities (*e.g.*, beam profile and divergence) are eliminated [111]. Therefore, an intensity peak profile is obtained by recording the diffracted intensity while rotating the crystal through the reflection condition as a function of ϑ (so-called rocking scan, *cf.* figure A.5a). If I_0 denotes the integrated intensity of the resulting, background subtracted intensity profile, the corrected integrated intensity I_c is given by

$$I_c = K \cdot L(\vartheta_{\mathrm{B}}) \cdot P(\vartheta_{\mathrm{B}}) \cdot G(\vartheta_{\mathrm{B}}) \cdot A(\vartheta_{\mathrm{B}}) \cdot I_0 \,. \tag{A.17}$$

Therein, ϑ_{B} is the Bragg angle of the reflection[4] and K is a constant, which, amongst others, accounts for adsorption. The subsequent factors will be discussed briefly.

Lorentz factor $L(\vartheta_{\mathrm{B}})$: The Lorentz correction factor is a geometrical correction of the integration volume, which converts I_0 as an angular dependent unit into a unit depending on reciprocal lattice units (r.l.u.):

$$L = \Big(\cos\alpha \cdot \cos\gamma \cdot \sin\delta \Big)^{-1} \tag{A.18}$$

Polarization factor $P(\vartheta_{\mathrm{B}})$: The polarization factor accounts for the horizontally polarized nature of the light emitted by the undulator (vertical polarization is negligible in case of synchrotron radiation [130]). The observed integrated intensity has to be corrected in dependence of the position of the detector, given by α, δ and γ:

$$P \approx P_{\mathrm{hor.}} = 1 - \Big(\sin\alpha \cdot \cos\delta \cdot \cos\gamma + \cos\alpha \cdot \sin\gamma \Big)^2 \tag{A.19}$$

Rod interception factor $G(\vartheta_{\mathrm{B}})$: Since in surface x-ray diffraction the diffraction occurs along crystal truncation rods in the surface normal direction, particular attention

[3] strictly speaking, the 3D peak volume has to be integrated

[4] and includes the set of angles α, δ and γ for the appropriate reflection

must be paid to the detector resolution in this direction. Specifically, for in-plane measurements with small γ, the ΔL acceptance of the detector in parallel to the CTR is solely determined by the detector slits. However, for measurements at higher L values, as shown in figure A.5b, the detector acceptance in L direction is determined by the out-of-plane angle γ and has to be corrected by:

$$G = \cos(\gamma) \tag{A.20}$$

Area correction $A(\vartheta_B)$: As shown in figure A.5c, the in-plane rotation δ of the detector defines the active part of the surface which is contributing to the measured intensity. Usually, *i.e.*, if the chosen energy is not too high and $|\vec{q}|$ not too small, the following correction factor can be applied:

$$A = \frac{1}{\sin(\delta)} \tag{A.21}$$

In case of squared samples or higher energies, the area contributing to the scattered intensity is defined by the sample shape and a more complex correction factor has to be used (not in this work).

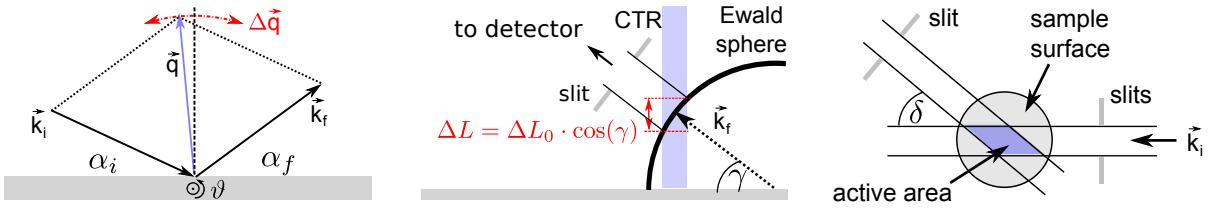

(a) Rocking scan **(b)** Rod interception **(c)** Area correction

Figure A.5: (a) Illustration of the rocking scan geometry in reciprocal space. (b) Schematic for deriving the rod interception factor. The cross-section of the rod 'seen' by the detector is proportional to $\cos\gamma$. (c) Area correction factor: In case the active sample area does not protrude the crystal surface, it can be calculated as the area of an parallelogram described by the widths of incident and diffracted beam (determined by the entrance and detector slits, respectively).

A.4.2 Instrumental Resolution employing the NaI Point Detector

The instrumental resolution of the NaI point detector in the out-of-plane direction, ΔL, in the radial in-plane direction, ΔR, as well as for a rocking scan, $\Delta\vartheta$, depends on the choice of the slit sizes s_{hg} and s_{vg} of the horizontal and vertical detector slits, respectively, as well as on the divergence of the x-ray beam. In the following, correction factors will be derived for a (001) terminated cubic crystal, neglecting the beam divergence, which is typically of the order of 30×20 µrad^2. The crystal lattice shall be defined in a right-handed surface coordinate system with two perpendicular vectors $\vec{a}_1$ and $\vec{a}_2$ lying in the surface plane and one vector $\vec{a}_3$ along the surface normal. The vectors $\vec{a}_1^*$, $\vec{a}_2^*$ and $\vec{a}_3^*$ denote the corresponding reciprocal unit cell vectors.

The scattering geometry is the same as used in the previous chapters, referred to the α-frame shown in figure A.2b and A.6a, and equation (2.1) is fulfilled. The scattering vector $\vec{q}$ is the sum of a component parallel to the surface, $\vec{q}_{\parallel}$, and a component perpendicular to the surface, $\vec{q}_{\perp}$ (*cf.* figure A.6a). The length $\vec{q}_{\parallel}$ can be determined from equation (A.3) as

$$|\vec{q}_{\parallel}| = \sqrt{\vec{q}_{\alpha,x}^{\,2} + \vec{q}_{\alpha,y}^{\,2}} \overset{\cos\alpha\approx 1}{=} k_0 \cdot \sqrt{\cos^2\gamma - 2\cos\delta\cos\gamma + 1}\,. \tag{A.22}$$

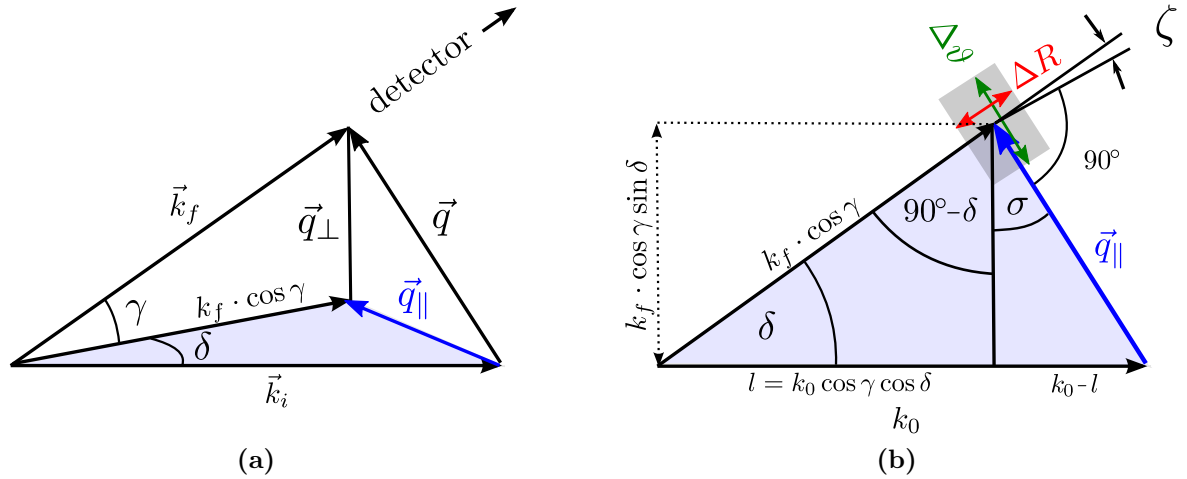

Figure A.6: Illustration of the scattering geometry in grazing incidence diffraction. (a) The scattering vector $\vec{q} = \vec{k}_f - \vec{k}_i$ can be split in a component parallel and perpendicular to the surface, labeled as $\vec{q}_{\parallel}$ and $\vec{q}_{\perp}$, respectively. The blue shaded triangle marks the plane spanned by the vectors $\vec{q}_{\parallel}$ and $\vec{k}_i$ (and not the sample surface). (b) Projection of the geometry shown in (a) into the plane spanned by the vectors $\vec{q}_{\parallel}$ and $\vec{k}_i$. The gray shaded rectangle illustrates the reciprocal space area seen by the detector.

Out-of-Plane Resolution

According to the rod interception correction factor (equation (A.20)), the out-of-plane resolution ΔL in reciprocal lattice units is given by

$$\Delta L = \Delta L_0 \cdot \cos\gamma = \Delta\gamma \cdot \frac{k_0}{|\vec{a}_3^*|} \cdot \cos\gamma \overset{*}{=} \frac{s_{\mathrm{vg}}[\mathrm{m}]}{1\ \mathrm{m}} \frac{2\pi}{\lambda} \frac{|\vec{a}_3|}{2\pi} \cdot \cos\gamma = \frac{s_{\mathrm{vg}}[\mathrm{m}]}{1\ \mathrm{m} \cdot \lambda} |\vec{a}_3| \cdot \cos\gamma. \tag{A.23}$$

Therein, ΔL_0 is the resolution in the L-direction for $\gamma \approx 0$, k_0 is the wave number and λ the wavelength of the used x-ray beam. The step marked with $*$ accounts for the angular resolution $\Delta\gamma$, which is defined by the vertical slit size at 1 meter distance to the sample: $\Delta\gamma = s_{\text{vg}}[\text{m}]/1\text{ m}$.

In-Plane Resolution

In figure A.6b, the projection of the exit wave vector $\vec{k}_f$ and the scattering vector $\vec{q}$ into the plane spanned by the vectors $\vec{q}_\parallel$ and $\vec{k}_i$ is shown. For the indicated angle $\zeta = 90 - (90 - \delta) - \sigma = \delta - \sigma$, a useful relation can be obtained:

$$\begin{aligned} |\vec{q}_\parallel| \cdot \cos\zeta &= |\vec{q}_\parallel| \cdot \cos(\delta - \sigma) \\ &= |\vec{q}_\parallel| \cdot (\cos\delta\cos\sigma + \sin\delta\sin\sigma) \\ &= \cos\delta \cdot |\vec{q}_\parallel| \cdot \cos\sigma + \sin\delta \cdot |\vec{q}_\parallel| \cdot \sin\alpha \\ &= \cos\delta \cdot k_0 \cdot \cos\gamma \cdot \sin\delta + \sin\delta \cdot k_0(1 - \cos\delta \cdot \cos\gamma) \\ &= k_0 \cdot \sin\delta\,. \end{aligned} \tag{A.24}$$

Furthermore, a gray rectangle in figure A.6b indicates the resolution function of in-plane scans, *i.e.*, the area $\Delta\vartheta \cdot \Delta R$ of the scattering plane as seen by the detector. $\Delta\vartheta$ and ΔR denote the resolution in the direction of a rocking and a radial scan, respectively, and can be determined as

$$\Delta\vartheta\ [^\circ] = \frac{\Delta\gamma \cdot k_0 \cdot \sin\gamma}{|\vec{q}_\parallel| \cdot \cos\zeta} \overset{(A.24)}{=} \frac{\Delta\gamma \cdot \sin\gamma}{\sin\delta} \overset{*}{=} \frac{s_{\text{vg}}[\text{m}]}{1\text{ m}} \cdot \frac{\sin\gamma}{\sin\delta} \tag{A.25}$$

$$\Delta R = \frac{\Delta\delta \cdot k_0}{|\vec{a}^*| \cdot \cos\zeta} \overset{(A.24)}{=} \frac{\Delta\delta \cdot |\vec{q}_\parallel|}{|\vec{a}^*| \cdot \sin\delta} \overset{*}{=} \frac{s_{\text{hg}}[\text{m}]}{1\text{ m}} \cdot \frac{|\vec{q}_\parallel|}{|\vec{a}^*| \cdot \sin\delta}\,. \tag{A.26}$$

Here again, in the step marked with $*$, $\Delta\gamma$ and $\Delta\delta$ were replaced by the relations $\Delta\gamma = s_{\text{vg}}[\text{m}]/1\text{ m}$ and $\Delta\delta = s_{\text{hg}}[\text{m}]/1\text{ m}$.

A.5 Statistics of Weighted Samples

The functions described below allow the computation of statistics for weighted samples and have been implemented in the software 'MDAPro' (*cf.* section 3.1.4). For the calculations, an array of samples x_i (channels) with associated weights w_i (measured intensity) are needed. Each sample x_i is considered as drawn from a Gaussian distribution with variance σ_i^2 [320, 321]. In chapter 4, this approach allowed to successfully calculate the position, standard deviation and skewness of a measured asymmetric peak profile, which could not be fitted using a single Gaussian or single pseudo-Voigt peak shape (compare discussion *ibidem*).

The weighted mean of a non-empty set of data x_i is calculated using the weights w_i according to

$$\overline{\mu} = \frac{\sum_i w_i \cdot x_i}{\sum_i w_i} \,. \tag{A.27}$$

The weighted sample variance of the dataset x_i with corresponding weights w_i is defined as the second standardized moment of the dataset,

$$\sigma = \sqrt{\frac{\sum_i w_i}{(\sum_i w_i)^2 - \sum_i w_i^2} \cdot \left| \sum_i w_i \cdot (x_i - \overline{\mu})^2 \right|} \,. \tag{A.28}$$

In probability theory and statistics, the asymmetry of a probability distribution of a random variable can be characterized by the skewness parameter. The following function computes the weighted skewness as the third standardized moment of the dataset x_i using the given values of the weighted mean $\overline{\mu}$ and weighted standard deviation σ:

$$\xi = \frac{\sum_i (w_i \cdot (x_i - \overline{\mu})^3 / \sigma^3)}{\sum_i w_i} \,. \tag{A.29}$$

The skewness value can be positive or negative. As illustrated qualitatively in figure A.7, a negative (positive) skew is characterized by a longer tail on the left (right) side of the probability density function. Thus, the bulk of values, including the median, lie to the right (left) of the mean. In case of a vanishing skewness value, an even but not necessarily symmetric distribution is implied.

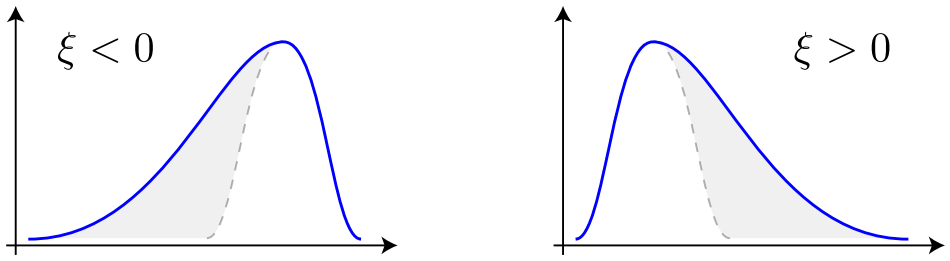

(a) Negative skew **(b)** Positive skew

Figure A.7: Illustration of positive and negative skew for the case of a Gaussian distribution.

B List of Acronyms

AES	Auger Electron Spectroscopy
AFM	Atomic Force Microscope
BTA	Benzotriazole
CD	Cyclic Diffractogram
CE	Counter Electrode
CEAC	Curvature Enhanced Accelerator Coverage (Model)
CMP	Chemical-Mechanical Polishing
CRL	Compound Refractive Lenses
CTR	Crystal Truncation Rod
CV	Cyclic Voltammogram
CVD	Chemical Vapour Deposition
DFT	Density Functional Theory
EAM	Embedded Atom Method
EQCM	Electrochemical Quartz Crystal Microbalance
ESB	Ehrlich-Schwoebel Barrier
ESRF	European Synchrotron Radiation Facility
fcc	face centered cubic
FWHM	Full Width Half Maximum
GID	Grazing Incidence Diffraction
GISAXS	Grazing Incidence Small Angle X-ray Scattering
HAS	Helium Atom Scattering
LEED	Low Energy Electron Diffraction
l.u.	lattice units
MBE	Molecular Beam Epitaxy
ML	Monolayer
MPSA	3-Mercapto-1-Propane Sulfonic Acid
NHE	Normal Hydrogen Electrode
OCP	Open Circuit Potential
OPD	Over-Potential Deposition
PCTFE	Poly-Chloro-Tri-Fluoro-Ethylene, KEL-F™
PEG	Poly-Ethylene-Glycol
PTFE	Poly-Tetra-Fluoro-Ethylene, Teflon™
RE	Reference Electrode
RHE	Reversible Hydrogen Electrode
RHEED	Reflection High Energy Electron Diffraction
r.l.	reciprocal lattice
r.l.u.	reciprocal lattice units
rms	root mean square
ROI	Range Of Interest
SCE	Saturated Calomel Electrode
SHE	Standard Hydrogen Electrode
SPA-LEED	Spot Profile Analyzing Low Energy Electron Diffraction
SPM	Scanning Probe Microscope
SPS	bis(sodiumsulfopropyl) disulfide
STM	Scanning Tunneling Microscope
SXRD	Surface X-Ray Diffraction
SXS	Surface X-ray Scattering
TDB	Terrace Diffusion Barrier
UHV	Ultra-High Vacuum
ULSI	Ultra-Large Scale Integrated
UPD	Under-Potential Deposition
WE	Working Electrode
XBPM	X-Ray Beam Position Monitor
XRD	X-Ray Diffraction
XRV	X-Ray Voltammetry

C Bibliography

[1] D. Landolt, J. Electrochem. Soc. **149**, 9 (2002).

[2] W. H. Safranek, *The Properties of Electrodeposited Metals and Alloys, 2nd ed.*, AESF Orlando, 1986.

[3] J. W. Dini, in *Modern Electroplating, Fourth Edition*, chapter Electrodeposition of Copper, pages 61–138, Electrochemical Society Series, 2000.

[4] Y. Shacham-Diamand, T. Osaka, M. Datta, and T. Ohba, *Advanced Nanoscale ULSI Interconnects: Fundamentals and Applications*, Springer, 2009.

[5] G. E. Moore, Electronics **38** (1965).

[6] P. Dixit and J. Miao, J. Electrochem. Soc. **153**, G552 (2006).

[7] P. C. Andricacos, C. Uzoh, J. O. Dukovic, J. Horkans, and H. Deligianni, Electrochem. Microfab. **42** (1998).

[8] P. C. Andricacos, Electrochem. Soc. Interf. **8**, 32 (1999).

[9] T. P. Moffat, D. Wheeler, M. D. Edelstein, and D. Josell, IBM J. Res. & Dev. **49**, 19 (2005).

[10] T. P. Moffat, D. Wheeler, and D. Josell, in *Superconformal Film Growth: Advances in Electrochemical Science and Engineering*, page 109, Wiley-VCH, 2008.

[11] M. J. Willey and A. C. West, J. Electrochem. Soc. **154**, D156 (2007).

[12] P. Vanysek, M. Alodan, J. Lipkowski, and O. M. Magnussen, editors, in *Electrochemical Science and Technology of Copper, Proceedings of the Electrochemical Society, Volume 2000-30*, Electrochemical Society, Pennington, 2003.

[13] P. M. Vereecken, R. A. Binstead, H. Deligianni, and P. C. Andricacos, IBM J. Res. & Dev. **49**, 3 (2005).

[14] D. Josell, D. Wheeler, W. H. Huber, and T. P. Moffat, Phys. Rev. Lett. **87**, 16102 (2001).

[15] D. Wheeler, D. Josell, and T. P. Moffat, J. Electrochem. Soc. **150**, C302 (2003).

[16] A. C. West, S. Mayer, and J. Reid, Electrochem. Solid-State Lett. **4**, C50 (2001).

[17] T. P. Moffat, D. Wheeler, W. H. Huber, and D. Josell, Electrochem. Solid-State Lett. **4**, C26 (2001).

[18] D. Josell, D. Wheeler, W. H. Huber, J. E. Bonevich, and T. P. Moffat, J. Electrochem. Soc. **148**, C767 (2001).

[19] G. Rosenfeld, B. Poelsema, and G. Comsa, in *The Chemical Physics of Solid Surfaces Volume 8: Growth and Properties of Ultrathin Epitaxial Layers*, chapter *Epitaxial Growth Modes far from Equilibrium*, pages 66–101, Elsevier Science, 1997.

[20] M. V. Ramana Murty, T. Curcic, A. Judy, B. H. Cooper, A. R. Woll, J. D. Brock, S. Kycia, and R. L. Headrick, Phys. Rev. B **60**, 16956 (1999).

[21] J. A. Venables, G. D. T. Spiller, and M. Hanbücken, Rep. Prog. Phys. **47**, 399 (1984).

[22] J. Divisek, B. Steffen, U. Stimming, and W. Schmickler, J. Electroanal. Chem. **440**, 169 (1997).

[23] O. Skylar, T. H. Treutler, N. Vlachopoulos, and G. Wittstock, Surf. Sci. **597**, 181 (2005).

[24] Z. Nagy and H. You, Electrochim. Acta **47**, 3037 (2002).

[25] O. M. Magnussen, Chem. Rev. **102**, 679 (2002).

[26] M. F. Toney and B. M. Ocko, Synchr. Rad. News **6**, 28 (1993).

[27] B. M. Ocko, O. M. Magnussen, J. X. Wang, and R. R. Adzic, in *Nanoscale Probes of the Solid/Liquid Interface*, page 103, Kluwer Academic Press, 1994.

[28] B. M. Ocko and J. Wang, in *Synchrotron Techniques in Interfacial Electrochemistry*, Kluwer Academic Press, 1994.

[29] B. M. Ocko, I. K. Robinson, M. Weinert, R. J. Randler, and D. M. Kolb, Phys. Rev. Lett. **83**, 780 (1999).

[30] D. M. Smilgies, R. Feidenhans'l, G. Scherb, D. M. Kolb, A. Kazimirov, and J. Zegenhagen, Surf. Sci. **367**, 40 (1996).

[31] Y. Gründer, F. U. Renner, T.-L. Lee, B. O. Fimland, and J. Zegenhagen, ESRF Highlights (2007).

[32] Z. Nagy, R. M. Yonco, C. A. Melendres, C. A. Yun, and V. A. Maroni, Electrochim. Acta **36**, 209 (1991).

[33] K. Tamura, B. M. Ocko, J. X. Wang, and R. R. Adžić, J. Phys. Chem. B **106**, 3896 (2002).

[34] A. H. Ayyad, J. Stettner, and O. M. Magnussen, Phys. Rev. Lett. **94**, 066106 (2005).

[35] G. Scherb, A. Kazimirov, and J. Zegenhagen, Rev. Sci. Instr. **69**, 512 (1998).

[36] K. Krug, J. Stettner, and O. M. Magnussen, Phys. Rev. Lett. **96**, 246101 (2006).

[37] D. Kaminski, K. Krug, F. Golks, J. Stettner, and O. M. Magnussen, J. Phys. Chem. C **111**, 17067 (2007).

[38] O. M. Magnussen, K. Krug, A. H. Ayyad, and J. Stettner, Electrochim. Acta **53**, 3449 (2008).

[39] K. Krug, D. Kaminski, F. Golks, J. Stettner, and O. M. Magnussen, J. Phys. Chem. C **114**, 18634 (2010).

[40] K. Krug, *In-situ Surface X-ray Diffraction Studies of Homoepitaxial Growth and Dissolution at Gold Single Crystal Electrodes*, PhD thesis, Universität Kiel, 2009.

[41] K. Krug, J. Stettner, and O. M. Magnussen, ESRF Highlights (2006).

[42] N. Sato, *Electrochemistry at Metal and Semiconductor Electrodes*, Elsevier Science, 1998.

[43] C. H. Hamann, A. Hamnett, and W. Vielstich, *Electrochemistry*, Wiley-VCH, 2007.

[44] W. Schmickler, *Grundlagen der Elektrochemie*, Springer, 1. edition, 2007.

[45] J. O. M. Bockris and A. K. N. Reddy, *Modern Electrochemistry*, Springer, 2000.

[46] J. O. M. Bockris, B. E. Conway, and E. Yeager, *Comprehensive Treatise of Electrochemistry*, volume 1, Plenum Press, New York, 1980.

[47] P. Zelenay and A. Wieckowski, *Electrochemical Interfaces*, Wiley-VCH, 1991.

[48] M. Paunovic and M. Schlesinger, *Fundamentals of Electrochemical Deposition*, Wiley & Sons, 2. edition, 2006.

[49] A. J. Bard and L. R. Faulkner, *Electrochemical Methods: Fundamentals and Applications*, Wiley & Sons, 2. edition, 2000.

[50] V. M. Schmidt, *Elektrochemische Verfahrenstechnik: Grundlagen, Reaktionstechnik, Prozessoptimierung*, Wiley-VCH, 2003.

[51] D. M. Kolb, Angew. Chem. **113**, 1198 (2001).

[52] D. M. Kolb, D. L. Rath, R. Wille, and W. N. Hansen, Ber. Bunsenges. Phys. Chem. **87**, 1108 (1983).

[53] R. Reeves, *Comprehensive Treatise of Electrochemistry*, volume 1, Plenum Press, New York, 1980.

[54] M. Habib, *Specific Adsorption of Anions*, Plenum Press, New York, 1980.

[55] J. A. V. Butler, Proc. Roy. Soc. A **112**, 129 (1926).

[56] E. A. Guggenheim, J. Phys. Chem. **33**, 842 (1929).

[57] J. Tafel, Z. Physik. Chem. **50**, 641 (1905).

[58] G. Prentice, *Electrochemical Engineering Principles*, Prentice Hall International Series, 1991.

[59] E. Sibert, F. Ozanam, F. Maroun, R. J. Behm, and O. M. Magnussen, Surf. Sci. **572**, 115 (2004).

[60] P. Wilkinson, Gold Bull. **19**, 75 (1986).

[61] G. Wulff, Z. Krist. Min. **34**, 449 (1901).

[62] M. Vollmer, *Kinetik der Phasenumwandlung*, Steinkopff-Verlag, 1939.

[63] H. Brune, Surf. Sci. Rep. **31**, 121 (1998).

[64] E. B. Budevski, V. Bostanov, and G. T. Staikov, Ann. Rev. Mater. Sci. **10**, 85 (1980).

[65] E. B. Budevski, G. T. Staikov, and W. J. Lorenz, *Electrochemical Phase Formation and Growth*, Wiley-VCH, 1996.

[66] W. Kossel, Nachr. Ges. Wiss. Göttingen Math. Phys. Kl. **135** (1927).

[67] I. N. Stranski, Z. Phys. Chem. **136**, 259 (1928).

[68] W. K. Burton, N. Cabrera, and F. C. Frank, Philos. Trans. Roy. Soc. London A **243**, 299 (1951).

[69] D. W. Bassett and P. R. Webber, Surf. Sci. **70**, 520 (1978).

[70] P. J. Feibelman, Phys. Rev. Lett. **65**, 729 (1990).

[71] G. L. Kellogg and P. J. Feibelman, Phys. Rev. Lett. **64**, 3143 (1990).

[72] T. T. Tsong and C. L. Chen, **355**, 328 (1992).

[73] G. Ehrlich and F. G. Hudda, J. Chem. Phys. **44**, 1039 (1966).

[74] R. L. Schwoebel and E. J. Shipsey, J. Appl. Phys. **37**, 3682 (1966).

[75] R. L. Schwoebel, J. Appl. Phys. **40**, 614 (1969).

[76] Y. He and E. Borguet, Faraday Discuss. **121**, 17 (2002).

[77] M. I. Haftel and M. Rosen, Phys. Rev. B **68**, 165402 (2003).

[78] E. Bauer, Z. Kristallogr. **110**, 372 (1958).

[79] F. Reif, *Fundamentals of Statistical and Thermal Physics*, McGraw-Hill, 1965.

[80] F. Reif and H. L. Scott, Am. J. Phys. **66**, 164 (1965).

[81] V. I. Trofimov and V. G. Mokerov, Mater. Sci. Eng. B **89**, 420 (2002).

[82] V. I. Trofimov and V. G. Mokerov, Thin Sol. Films **428**, 66 (2003).

[83] C. B. Ehlers, I. Villegas, and J. L. Stickney, J. Electroanal. Chem. **284**, 403 (1990).

[84] I. Villegas, C. B. Ehlers, and J. L. Stickney, J. Electrochem. Soc. **137**, 3143 (1990).

[85] M. R. Vogt, F. A. Möller, C. M. Schilz, O. M. Magnussen, and R. J. Behm, Surf. Sci. Lett. **367**, L33 (1996).

[86] M. R. Vogt, A. Lachenwitzer, O. M. Magnussen, and R. J. Behm, Surf. Sci. **399**, 49 (1998).

[87] A. Damjanovic, M. Paunovic, and J. O. Bockris, J. Electroanal. Chem. **9**, 93 (1965).

[88] A. Wu and D. P. Barkey, J. Electrochem. Soc. **150**, C533 (2003).

[89] T. C. Franklin, Surf. Coat. Techn. **30**, 415 (1987).

[90] W. U. Schmidt, R. C. Alkire, and A. A. Gewirth, J. Electrochem. Soc. **143**, 3122 (1996).

[91] L. Oniciu and L. Mureşan, J. Appl. Electrochem. **21**, 565 (1991).

[92] W. Dow, M. Y. Yen, W. B. Lin, and S. W. Ho, J. Electrochem. Soc. **152**, C769 (2005).

[93] J. J. Senkevich, C. J. Mitchell, G.-R. Yang, and T.-M. Lu, Colloid. Surf. A **221**, 29 (2003).

[94] J. J. Senkevich, F. Tang, D. Rogers, J. T. Drotar, C. Jezewski, W. A. Lanford, G.-C. Wang, and T.-M. Lu, Chem. Vapor Depos. **9**, 258 (2003).

[95] S. K. Kim, D. Josell, and T. P. Moffat, J. Electrochem. Soc. **153**, C616 (2006).

[96] M. Tan, C. Guymon, D. R. Wheeler, and J. N. Harb, J. Electrochem. Soc. **154**, D78 (2007).

[97] M. L. Walker, L. J. Richter, and T. P. Moffat, J. Electrochem. Soc. **153**, C557 (2006).

[98] J. J. Kelly and A. C. West, J. Electrochem. Soc. **145**, 3477 (1998).

[99] T. P. Moffat, D. Wheeler, and D. Josell, J. Electrochem. Soc. **151**, C262 (2004).

[100] M. E. H. Garrido and M. D. Pritzker, J. Electrochem. Soc. **156**, D36 (2009).

[101] M. E. H. Garrido and M. D. Pritzker, J. Electrochem. Soc. **156**, D175 (2009).

[102] H. M. Chen, S. J. Parulekar, and A. Zdunek, J. Electrochem. Soc. **155**, D341 (2008).

[103] W. P. Dow and M.-Y. Yen, Electrochem. Solid-State Lett. **8**, C161 (2005).

[104] W. P. Dow and M.-Y. Yen, J. Electrochem. Soc. **156**, D155 (2009).

[105] T. P. Moffat, D. Wheeler, S. K. Kim, and D. Josell, J. Electrochem. Soc. **153**, C127 (2006).

[106] L. G. Parratt, Phys. Rev. **95**, 359 (1954).

[107] J. Als-Nielsen, Physica A **140**, 376 (1986).

[108] H. Dosch, Phys. Rev. B **35**, 2137 (1987).

[109] S. K. Sinha, E. B. Sirota, S. Garoff, and H. B. Stanley, Phys. Rev. B **38**, 2297 (1988).

[110] I. K. Robinson, Phys. Rev. B **33**, 3830 (1986).

[111] R. Feidenhans'l, Surf. Sci. Rep. **10**, 105 (1989).

[112] P. Eisenberger and W. C. Marra, Phys. Rev. Lett. **46**, 1081 (1981).

[113] W. C. Marra, P. Eisenberger, and A. Cho, J. Appl. Phys. **50**, 6927 (1979).

[114] P. H. Fuoss and S. Brennan, Ann. Rev. Mater. Sci. **20**, 365 (1990).

[115] A. Guinier, *X-Ray Diffraction in Crystals, Imperfect Crystals and Amorphous Bodies*, Dover Publications, 1994.

[116] B. E. Warren, *X-Ray Diffraction*, Dover Publications, Inc., 1990.

[117] I. K. Robinson and D. J. Tweet, Rep. Prog. Phys. **55**, 599 (1992).

[118] I. K. Robinson, in *Handbook on Synchrotron Radiation Volume 3*, North Holland, 1991.

[119] J. Als-Nielsen and D. McMorrow, *Elements of Modern X-ray Physics*, Wiley & Sons, 1. edition, 2001.

[120] E. Vlieg, J. F. Van der Veen, S. J. Gurman, C. Norris, and J. E. Macdonald, Surf. Sci. **210**, 301 (1989).

[121] M. F. Toney and O. R. Melroy, in *Electrochemical Interfaces: Modern Techniques for In-Situ Interface Characterization*, Wiley & Sons, 1991.

[122] M. F. Toney, J. G. Gordon, and O. R. Melroy, SPIE Proc. **1550**, 140 (1991).

[123] J. D. Jackson, *Classical Electrodynamics*, Wiley & Sons, 1999.

[124] S. R. Andrews and R. A. Cowley, J. Phys. C **18**, 6247 (1985).

[125] F. Laves and W. Nieuwenkamp, Z. Kristallogr. (Abt. A) **273**, 279 (1935).

[126] M. von Laue, Akad. Verlagsges. Becker & Erler Leipzig (1941).

[127] M. von Laue, Akad. Verlagsges. Leipzig **355** (1948).

[128] M. von Laue and E. H. Wagner, Akad. Verlagsges. Frankfurt (1960).

[129] E. Vlieg, A. W. Denier van der Gon, and J. F. van der Veen, Phys. Rev. Lett. **61**, 2241 (1988).

[130] E. Vlieg, J. Appl. Cryst. **30**, 532 (1997).

[131] G. Renaud, Surf. Sci. Rep. **32**, 1 (1998).

[132] C. Kunz, J. Phys. Condens. Matter **13**, 7499 (2001).

[133] J. Zegenhagen, B. Detlefs, T.-L. Lee, S. Thiess, H. Isern, L. Petit, L. André, J. Roy, Y. Mi, and I. Joumard, J. Electron Spectrosc. Relat. Phenom. **178–179**, 258 (2010).

[134] Huber Diffraktionstechnik GmbH & Co. KG, 83253 Rimsting, Germany.

[135] M. Lohmeier and E. Vlieg, J. Appl. Cryst. **26**, 706 (1993).

[136] G. Swislow, CSS Certified Scientific Software, *SPEC X-Ray Diffraction Software and Documentation*, Cambridge, MA 02139, USA.

[137] Dectris Ltd., 5400 Baden, Switzerland.

[138] B. Schmitt, C. Brönnimann, E. F. Eikenberry, F. Gozzo, C. Hörmann, R. Horisberger, and B. Patterson, Nucl. Instrum. Meth. Phys. Res. A **501**, 267 (2003).

[139] Dectris Ltd., *Technical Documentation Mythen 1K*, 2009, 5400 Baden, Switzerland.

[140] A. Bergamaschi, A. Cervellino, R. Dinapoli, F. Gozzo, B. Henrich, I. Johnson, P. Kraft, A. Mozzanica, B. Schmitt, and X. Shi, J. Synchr. Rad. **17**, 653 (2010).

[141] G. Scherb, A. Kazimirov, and J. Zegenhagen, Rev. Sci. Instrum. **69**, 512 (1998).

[142] J. E. DeVilbiss, J. X. Wang, B. M. Ocko, K. Tamura, R. R. Adzic, I. A. Vartanyants, and I. K. Robinson, Electrochim. Acta **47**, 3057 (2002).

[143] S. Zheng, K. Krug, F. Golks, D. Kaminski, S. Morin, and O. M. Magnussen, J. Electroanal. Chem. **649**, 189 (2010).

[144] K. M. Robinson and W. O'Grady, Rev. Sci. Instrum. **64**, 1061 (1993).

[145] Ivium Technologies, 5612 AJ Eindhoven, The Netherlands.

[146] MaTecK - Material-Technologie & Kristalle GmbH, 52428 Jülich, Germany.

[147] J. Clavilier, J. Electroanal. Chem. **107**, 211 (1980).

[148] R. Sonnenfeld and P. K. Hansma, Science **232**, 211 (1986).

[149] X. G. Zhang and U. Stimming, J. Electroanal. Chem. **291**, 273 (1990).

[150] X. G. Zhang and U. Stimming, Corr. Sci. **30**, 951 (1990).

[151] B. J. Cruickshank, A. A. Gewirth, R. M. Rynders, and R. C. Alkire, J. Electrochem. Soc. **139**, 2829 (1992).

[152] B. J. Cruickshank, D. D. Sneddon, and A. A. Gewirth, Surf. Sci. **281**, 308 (1993).

[153] J. R. LaGraff and A. A. Gewirth, J. Phys. Chem. **99**, 10009 (1995).

[154] J. R. LaGraff and A. A. Gewirth, in *Nanoscale Probes of the Solid/Liquid Interface*, page 83, Kluwer Academic Press, 1995.

[155] A. A. Gewirth and B. K. Niece, Chem. Rev. **97**, 1129 (1997).

[156] D. W. Suggs and A. J. Bard, J. Am. Chem. Soc. **116**, 10725 (1994).

[157] N. Ikemiya, T. Kubo, and S. Hara, Surf. Sci. **323**, 81 (1995).

[158] T. P. Moffat, Mater. Res. Soc. Symp. Proc. **404**, 3 (1996).

[159] T. P. Moffat, Mater. Res. Soc. Symp. Proc. **451**, 75 (1997).

[160] H. S. O. Chan, K. H. Ho, L. Zhou, N. Luo, S. C. Ng, and S. F. Y. Li, Langmuir **12**, 2580 (1996).

[161] A. Lachenwitzer, M. R. Vogt, O. M. Magnussen, and R. J. Behm, Surf. Sci. **382**, 107 (1997).

[162] M. R. Vogt, W. Polewska, O. M. Magnussen, and R. J. Behm, J. Electrochem. Soc. **144**, L113 (1997).

[163] K. Itaya, Prog. Surf. Sci. **58**, 121 (1998).

[164] W. Polewska, M. R. Vogt, O. M. Magnussen, and R. J. Behm, J. Phys. Chem. B **103**, 10440 (1999).

[165] M. R. Vogt, *Corrosion and Corrosion Inhibition of Copper Electrodes in Hydrochloric and Sulfuric Acid Solution: An in-situ STM and in-situ FTIR Spectroscopy Study*, PhD thesis, Universität Ulm, 1998.

[166] O. M. Magnussen, M. R. Vogt, J. Scherer, and R. J. Behm, Appl. Phys. A **66**, 447 (1998).

[167] O. M. Magnussen and M. R. Vogt, Phys. Rev. Lett. **84**, 357 (2000).

[168] W. Polewska, R. J. Behm, and O. M. Magnussen, Electrochim. Acta **48**, 2915 (2003).

[169] L. Zitzler, B. Gleich, O. M. Magnussen, and R. J. Behm, Electrochem. Soc. Proc. **99-28**, 38 (2000).

[170] L. Zitzler, *Video-STM-Untersuchungen von Reaktionen an der Metall-Flüssigkeits-Grenzfläche*, Master's thesis, Universität Ulm, 2000.

[171] O. M. Magnussen, L. Zitzler, B. Gleich, M. R. Vogt, and R. J. Behm, Electrochim. Acta **46**, 3725 (2001).

[172] D. M. Kolb and J. Schneider, Surf. Sci. **162**, 764 (1985).

[173] B. Ocko, J. Wang, A. Davenport, and H. Isaacs, Phys. Rev. Lett. **65**, 1466 (1990).

[174] B. M. Ocko, G. Helgesen, B. Schardt, J. Wang, and A. Hamelin, Phys. Rev. Lett. **69**, 3350 (1992).

[175] I. M. Tidswell, N. M. Marković, C. A. Lucas, and P. N. Ross, Phys. Rev. B **47**, 16542 (1993).

[176] O. M. Magnussen, *In-Situ Rastertunnelmikroskop-Untersuchungen zu Rekonstruktion, Anionenadsorption und Unterpotentialabscheidung auf Goldelektroden*, PhD thesis, Universität Ulm, 1993.

[177] A. Cuesta and D. M. Kolb, Surf. Sci. **465**, 310 (2000).

[178] M. Labayen, C. Ramirez, W. Schattke, and O. M. Magnussen, Nature Materials **2**, 783 (2003).

[179] M. Labayen and O. M. Magnussen, Surf. Sci. **573**, 128 (2004).

[180] T. Heumann and H. Panesar, Z. Phys. Chem. **229**, 84 (1965).

[181] S. Ye, C. Ishibashi, K. Shimazu, and K. Uosaki, J. Electrochem. Soc. **145**, 1614 (1998).

[182] J. Gauer and G. Schmid, J. Electroanal. Chem. **279**, 1970 (1970).

[183] S. Ye, C. Ishibashi, and K. Uosaki, Langmuir **15**, 807 (1999).

[184] S. Ye, C. Ishibashi, and K. Uosaki, Electrochem. Soc. Proc. **PV-2000-35**, 133 (2001).

[185] Reprinted from Electrochemical Society Proceedings, p. PV-2000-35, 133 (2001), reproduced by permission of ECS – The Electrochemical Society.

[186] F. Golks, K. Krug, Y. Gründer, J. Zegenhagen, J. Stettner, and O. Magnussen, J. Am. Chem. Soc. **133**, 3772 (2011), http://pubs.acs.org/doi/abs/10.1021/ja1115748.

[187] H. Gerischer and C. W. Tobias, *Advances in Electrochemical Science and Engineering*, volume 3, Wiley-VCH, 1994.

[188] J. O. M. Bockris, B. E. Conway, E. Yeager, and R. E. White, *Electrochemical Materials Science*, volume 4, Plenum Press, New York, 1981.

[189] O. M. Magnussen, B. M. Ocko, R. R. Adzic, and J. Wang, Phys. Rev. B **51**, 5510 (1995).

[190] O. M. Magnussen, J. Wang, R. R. Adzic, and B. M. Ocko, J. Phys. Chem. **100**, 5500 (1996).

[191] B. M. Ocko, G. M. Watson, and J. Wang, J. Phys. Chem. **98**, 897 (1994).

[192] B. M. Ocko, O. M. Magnussen, R. R. Adzic, J. X. Wang, Z. Shi, and J. Lipkowski, J. Electroanal. Chem. **376**, 35 (1994).

[193] B. M. Ocko, O. M. Magnussen, J. X. Wang, R. R. Adic, and T. Wandlowski, Physica B **221**, 238 (1996).

[194] T. Wandlowski, J. X. Wang, O. M. Magnussen, and B. M. Ocko, J. Phys. Chem. **100**, 10277 (1996).

[195] A. Ignaczak and J. A. N. F. Gomes, J. Electroanal. Chem. **420**, 71 (1997).

[196] J. W. Halley, B. B. Smith, S. Walbran, L. A. Curtiss, R. O. Rigney, A. Sutjianto, N. C. Hung, R. M. Yonco, and Z. Nagy, J. Chem. Phys. **110**, 6538 (1999).

[197] Z. Nagy, J. P. Blaudeau, N. C. Hung, L. A. Curtiss, and D. J. Zurawski, J. Electrochem. Soc. **142**, L87 (1995).

[198] M. Yokoi, S. Konishi, and T. Hayashi, Denki Kagaku oyobi Kogyo Butsuri Kagaku **51**, 460 (1983).

[199] J. K. Sass and K. Bange, in *Electrochemical Surface Science*, page 54, American Chemical Society, Washington, 1988.

[200] J. K. Sass, D. Lackey, J. Schott, and B. Straehler, Surf. Sci. **247**, 239 (1991).

[201] J. Wang, B. M. Ocko, A. J. Davenport, and H. S. Isaacs, Phys. Rev. B **46**, 10321 (1992).

[202] C. A. Lucas, N. M. Markovic, and P. N. Ross, Phys. Rev. B **55**, 7964 (1997).

[203] S. Huemann, N. T. M. Hai, P. Broekmann, K. Wandelt, H. Zajonz, H. Dosch, and F. Renner, J. Phys. Chem. B **110**, 24955 (2006).

[204] M. Saracino, P. Broekmann, K. Gentz, M. Becker, H. Keller, F. Janetzko, T. Bredow, K. Wandelt, and H. Dosch, Phys. Rev. B **79**, 115448 (2009).

[205] O. Endo, M. Kiguchi, T. Yokoyama, M. Ito, and T. Ohta, J. Electroanal. Chem. **473**, 19 (1999).

[206] O. Endo, H. Kondoh, Y. Yonamoto, T. Yokoyama, and T. Ohta, Surf. Sci. **463**, 135 (2000).

[207] K. Doblhofer, S. Wasle, D. M. Soares, K. G. Weil, G. Weinberg, and G. Ertl, Z. Phys. Chem. **217**, 479 (2003).

[208] T. Kekesi and M. Isshiki, J. Appl. Electrochem. **27**, 982 (1997).

[209] M. Pourbaix, *Atlas d'Equilibres Electrochimiques à 25°C*, Gauthier-Villars, Paris, 1963.

[210] T. P. Moffat, in *STM Studies of Halide Adsorption on Cu(100), Cu(110) and Cu(111): Electrochemical Processing in ULSI Fabrication and Semiconductor/Metal Deposition 2*, page 41, Electrochemical Society Proceedings Series, Pennington, 1999.

[211] C. Stuhlmann, B. Wohlmann, Z. Park, M. Kruft, P. Broekmann, and K. Wandelt, in *Solid-liquid Interfaces, Macroscopic Phenomena-Microscopic Understanding, Topics in Applied Physics, volume 85*, chapter *Epitaxial Growth Modes far from Equilibrium*, pages 199–221, Springer, New York, 2002.

[212] J. Inukai, Y. Osawa, and K. Itaya, J. Phys. Chem. B **102**, 10034 (1998).

[213] L. J. Wan and K. Itaya, J. Electroanal. Chem. **473**, 10 (1999).

[214] W. H. Li, Y. Wang, J. H. Ye, and S. F. Y. Li, J. Phys. Chem. B **105**, 1829 (2001).

[215] J. P. Healy, D. Pletcher, and M. Goodenough, J. Electroanal. Chem. **338**, 155 (1992).

[216] K. R. Hebert, J. Electrochem. Soc. **152**, C283 (2005).

[217] M. L. Walker, L. J. Richter, and T. P. Moffat, J. Electrochem. Soc. **152**, C403 (2005).

[218] G. H. C. J. Wijts, *In-situ Surface X-Ray Diffraction during Electrochemical Studies on Cu(110)*, Master's thesis, University of Leiden, 2009.

[219] T. Wandlowski, J. X. Wang, and B. M. Ocko, J. Electroanal. Chem. **500**, 418 (2001).

[220] T. Kramar, D. Vogtenhuber, R. Podloucky, and A. Neckel, Electrochim. Acta **40**, 43 (1995).

[221] A. Migani, C. Sousa, and F. Illas, Surf. Sci. **574**, 297 (2005).

[222] A. Migani and F. Illas, J. Phys. Chem. B **110**, 11894 (2006).

[223] B. M. Ocko, J. X. Wang, and T. Wandlowski, Phys. Rev. Lett. **79**, 1511 (1997).

[224] D. Westphal and A. Goldmann, Solid State Commun. **35**, 437 (1980).

[225] D. Westphal, A. Goldmann, F. Jona, and P. M. Marcus, Solid State Commun. **44**, 685 (1982).

[226] K. N. Eltsov, A. N. Klimov, V. Y. Yurov, U. Bardi, M. Galeotti, V. M. Shevlyuga, and A. M. Prokhorov, JETP Lett. **62**, 444 (1995).

[227] M. Galeotti, B. Cortigiani, M. Torrini, U. Bardi, B. Andryushechkin, A. Klimov, and K. Eltsov, Surf. Sci. **349**, L164 (1996).

[228] M. Kiguchi, T. Yokoyama, S. Terada, M. Sakano, Y. Okamoto, T. Ohta, Y. Kitajima, and H. Kuroda, Phys. Rev. B **56**, 1561 (1997).

[229] C. Y. Nakakura, V. M. Phanse, and E. I. Altman, Surf. Sci. **370**, L149 (1997).

[230] C. Y. Nakakura, G. Zheng, and E. I. Altman, Surf. Sci. **401**, 173 (1998).

[231] D. W. Suggs and A. J. Bard, J. Phys. Chem. **99**, 8349 (1995).

[232] Reprinted from Surface Science 367, M. R. Vogt, F. A. Möller, C. M. Schilz, O. M. Magnussen, R. J. Behm, *Adsorbate-induced step faceting of Cu(100) electrodes in HCl*, p. L33, 1996, with permission from Elsevier.

[233] H. C. N. Tolentino, M. De Santis, Y. Gauthier, and V. Langlais, Surf. Sci. **601**, 2962 (2007).

[234] Y. Gründer, D. Kaminski, F. Golks, K. Krug, J. Stettner, O. M. Magnussen, A. Franke, J. Stremme, and E. Pehlke, Phys. Rev. B **81**, 174114 (2010).

[235] J. L. Stickney and C. B. Ehlers, J. Vac. Sci. Techn. A **7**, 1801 (1989).

[236] M. Kruft, B. Wohlmann, C. Stuhlmann, and K. Wandelt, Surf. Sci. **377**, 601 (1997).

[237] P. Broekmann, M. Wilms, M. Kruft, C. Stuhlmann, and K. Wandelt, J. Electroanal. Chem. **467**, 307 (1999).

[238] M. Wilms, P. Broekmann, M. Kruft, C. Stuhlmann, and K. Wandelt, Appl. Phys. A **66**, 473 (1998).

[239] W. Haiss, J. K. Sass, X. Gao, and M. J. Weaver, Surf. Sci. **274**, L593 (1992).

[240] X. Gao and M. J. Weaver, J. Am. Chem. Soc. **114**, 8544 (1992).

[241] A. D. Novaco and J. P. McTague, Bull. Am. Phys. Soc. **23**, 293 (1978).

[242] A. D. Novaco and J. P. McTague, Phys. Rev. B **20**, 2469 (1979).

[243] F. Grey and J. Bohr, Europhys. Lett. **18**, 717 (1992).

[244] F. Grey and J. Bohr, in *Phase Transitions in Surface Films 2*, pages 83–96, Plenum Press, New York, 1991.

[245] A. Zangwill, in *Evolution of Surface and Thin Film Microstructure*, Materials Research Society, Pittsburg, 1993.

[246] J. K. Zuo and J. F. Wendelken, Phys. Rev. Lett. **78**, 2791 (1997).

[247] J. C. Girard, Y. Samson, S. Gauthier, S. Roussel, and J. Klein, Surf. Sci. **302**, 73 (1994).

[248] E. Kopatzki, S. Günther, W. Nichtl-Pecher, and R. J. Behm, Surf. Sci. **284**, 154 (1993).

[249] J. A. Stroscio and D. T. Pierce, Phys. Rev. B **49**, 8522 (1994).

[250] J. A. Stroscio, D. T. Pierce, and R. A. Dragoset, Phys. Rev. Lett. **70**, 3615 (1993).

[251] J. M. Wen, S. L. Chang, J. W. Burnett, J. W. Evans, and P. A. Thiel, Phys. Rev. Lett. **73**, 2591 (1994).

[252] J. F. Wendelken, A. K. Swan, W.-W. Pai, and J.-K. Zuo, in *Morphological Organization in Epitaxial Growth and Removal*, chapter *Morphology and Energy Barriers in Homoepitaxial Growth and Coarsening: A Case Study for Cu(100)*, pages 320–348, World Scientific Publishing, 1998.

[253] F. Rabbering, H. Wormeester, F. Everts, and B. Poelsema, Phys. Rev. B **79**, 075402 (2009).

[254] J. J. de Miguel, A. Sánchez, A. Cebollada, J. M. Gallego, J. Ferrón, and S. Ferrer, Surf. Sci. **189**, 1062 (1987).

[255] J. K. Zuo and J. F. Wendelken, Phys. Rev. Lett. **70**, 1662 (1993).

[256] W. F. Egelhoff and I. Jacob, Phys. Rev. Lett. **62**, 921 (1989).

[257] H. J. Ernst, F. Fabre, and J. Lapujoulade, Surf. Sci. **275**, L682 (1992).

[258] C.-L. Liu, Int. J. Mod. Phys. **9**, 1 (1995).

[259] G. Boisvert and L. J. Lewis, Phys. Rev. B **56**, 7643 (1997).

[260] C. Lee, G. T. Barkema, M. Breeman, A. Pasquarello, and R. Car, Surf. Sci. **306**, L575 (1994).

[261] J. De la Figuera, J. E. Prieto, C. Ocal, and R. Miranda, Solid State Commun. **89**, 815 (1994).

[262] K. Morgenstern, G. Rosenfeld, B. Poelsema, and G. Comsa, Phys. Rev. Lett. **74**, 2058 (1995).

[263] W. W. Pai, A. K. Swan, Z. Zhang, and J. F. Wendelken, Phys. Rev. Lett. **79**, 3210 (1997).

[264] J. M. Wen, J. W. Evans, M. C. Bartelt, J. W. Burnett, and P. A. Thiel, Phys. Rev. Lett. **76**, 652 (1996).

[265] Reprinted from World Scientific Publishing, J. F. Wendelken, A. K. Swan, W.-W. Pai, J.-K. Zuo, *Morphology and Energy Barriers in Homoepitaxial Growth and Coarsening: A Case Study for Cu(100)*, in *Morphological Organization in Epitaxial Growth and Removal*, Z. Zhang, M. G. Lagally (eds.), p. 320. Copyright 1998, World Scientific Publishing.

[266] F. A. Möller, O. M. Magnussen, and R. J. Behm, Phys. Rev. Lett. **77**, 3165 (1996).

[267] F. A. Möller, O. M. Magnussen, and R. J. Behm, Phys. Rev. Lett. **77**, 5249 (1996).

[268] S. Morin, A. Lachenwitzer, O. M. Magnussen, and R. J. Behm, Phys. Rev. Lett. **83**, 5066 (1999).

[269] S. Strbac, O. M. Magnussen, and R. J. Behm, Phys. Rev. Lett. **83**, 3246 (1999).

[270] E. Sibert, F. Ozanam, F. Maroun, O. M. Magnussen, and R. J. Behm, Phys. Rev. Lett. **90**, 56102 (2003).

[271] T. Vitanov, A. Popov, and E. B. Budevski, J. Electrochem. Soc. **121**, 207 (1974).

[272] V. Bostanov, G. Staikov, and D. K. Roe, J. Electrochem. Soc. **122**, 1301 (1975).

[273] Reprinted figures with permission from K. Krug, J. Stettner, O. M. Magnussen, Physical Review Letters 96, p. 246101, 2006. Copyright 2006 by the American Physcial Society.

[274] M. Yokoi, S. Konishi, and T. Hayashi, Denki Kagaku oyobi Kogyo Butsuri Kagaku **51**, 310 (1983).

[275] U. Bertocci, Electrochim. Acta **11**, 1261 (1966).

[276] A. I. Molodov, G. N. Markosyan, and V. V. Losev, Electrochim. Acta **17**, 701 (1972).

[277] S. Krzewska, Electrochim. Acta **42**, 3531 (1997).

[278] A. Jardy, L. M. Legal, M. Keddam, and H. Takenouti, Electrochim. Acta **37**, 2195 (1992).

[279] F. K. Crunkwell, Electrochim. Acta **15**, 2707 (1992).

[280] O. E. Barcia, O. R. Mattos, N. Pébère, and B. Tribollet, J. Electrochem. Soc. **140**, 2825 (1993).

[281] H. P. Lee, K. Nobe, and A. J. Pearlstein, J. Electrochem. Soc. **132**, 1031 (1985).

[282] H. P. Lee and K. Nobe, J. Electrochem. Soc. **133**, 2035 (1986).

[283] F. R. van Dijk, H. J. W. Zandvliet, and B. Poelsema, J. Appl. Phys. **99**, 123506 (2006).

[284] S. Huo and W. Schwarzacher, Phys. Rev. Lett. **86**, 256 (2001).

[285] Reprinted from Electrochimica Acta 46, O. M. Magnussen, L. Zitzler, B. Gleich, M. R. Vogt, R. J. Behm, *Adsorbate-induced step faceting of Cu(100) electrodes in HCl*, p. 3725, 2001, with permission from Elsevier.

[286] W. Polewska, M. R. Vogt, O. M. Magnussen, and R. J. Behm, SPIE-Int. Soc. Opt. Eng. **4413**, 233 (2001).

[287] E. Kopatzki and R. J. Behm, Phys. Rev. Lett. **74**, 1399 (1995).

[288] E. Kopatzki and R. Behm, Surf. Sci. **245**, 255 (1991).

[289] J. Zegenhagen, T.-L. Lee, Y. Gründer, F. U. Renner, and B.-O. Fimland, Z. Physik. Chem. **221**, 1273 (2007).

[290] Y. Gründer, *X-Ray in-situ Study of Copper Electrodeposition on UHV Prepared GaAs(001) Surfaces*, PhD thesis, Technische Universität Berlin, 2008.

[291] *International Technology Roadmap for Semiconductors, ITRS*, 2007, http://www.itrs.net/Links/2007ITRS/2007_Chapters/2007_Interconnect.pdf.

[292] Y. Cao, P. Taephaisitphongse, R. Chalupa, and A. C. West, J. Electrochem. Soc. **148**, C466 (2001).

[293] M. Kang and A. A. Gewirth, J. Electrochem. Soc. **150**, C426 (2003).

[294] M. Hasegawa, Y. Negishi, T. Nakanishi, and T. Osaka, J. Electrochem. Soc. **152**, C221 (2005).

[295] T. P. Moffat, B. Baker, D. Wheeler, and D. Josell, Electrochem. Solid-State Lett. **6**, C59 (2003).

[296] D. Stoychev, Trans. Inst. Met. Finish. **76**, 73 (1998).

[297] M. Yokoi, S. Konishi, and T. Hayashi, Denki Kagaku oyobi Kogyo Butsuri Kagaku **52**, 218 (1984).

[298] Z. V. Feng, X. Li, and A. A. Gewirth, J. Phys. Chem. B **107**, 9415 (2003).

[299] K. R. Hebert, S. Adhikari, and J. E. Houser, J. Electrochem. Soc. **152**, C324 (2005).

[300] T. P. Moffat, J. E. Bonevich, W. H. Huber, A. Stanishevsky, D. R. Kelly, G. R. Stafford, and D. Josell, J. Electrochem. Soc. **147**, 4524 (2000).

[301] P. Taephaisitphongse, Y. Cao, and A. C. West, J. Electrochem. Soc. **148**, C492 (2001).

[302] J. W. Gallaway, M. J. Willey, and A. C. West, J. Electrochem. Soc. **156**, D146 (2009).

[303] J. Mendez, R. Akolkar, and U. Landau, J. Electrochem. Soc. **156**, D474 (2009).

[304] C. Gabrielli, P. Moçotéguy, H. Perrot, D. Nieto-Sanz, and A. Zdunek, Electrochim. Acta **51**, 1462 (2006).

[305] B. H. Wu, C. C. Wan, and Y. Y. Wang, J. Appl. Electrochem. **33**, 823 (2003).

[306] M. Hayase, M. Taketani, K. Aizawa, T. Hatsuzawa, and K. Hayabusa, Electrochem. Solid-State Lett. **5**, C98 (2002).

[307] L. Chai, R. Goldberg, N. Kampf, and J. Klein, Langmuir **24**, 1570 (2008).

[308] K. Doblhofer, S. Wasle, D. M. Soares, K. G. Weil, and G. Ertl, J. Electrochem. Soc. **150**, C657 (2003).

[309] M. R. H. Hill and G. T. Rogers, J. Electroanal. Chem. Interf. Electrochem. **86**, 179 (1978).

[310] T. P. Moffat, D. Wheeler, C. Witt, and D. Josell, Electrochem. Solid-State Lett. **5**, C110 (2002).

[311] T. P. Moffat and L. Y. Ou Yang, J. Electrochem. Soc. **157**, D228 (2010).

[312] R. J. Nichols, C. E. Bach, and H. Meyer, Ber. Bunsenges. Phys. Chem. **97**, 1012 (1993).

[313] C. E. Täubert, *Influence of Different Additives on the Copper Electroplating onto Au(111) and Cu(111) Substrates*, PhD thesis, Universität Ulm, 2006.

[314] C. E. Täubert, D. M. Kolb, U. Memmert, and H. Meyer, J. Electrochem. Soc. **154**, 293 (2007).

[315] M. Wünsche, R. J. Nichols, R. Schumacher, W. Beckmann, and H. Meyer, Electrochim. Acta **38**, 647 (1993).

[316] M. Petri, D. M. Kolb, U. Memmert, and H. Meyer, J. Electrochem. Soc. **151**, C793 (2004).

[317] J. Fassbender, U. May, B. Schirmer, R. M. Jungblut, B. Hillebrands, and G. Güntherodt, Phys. Rev. Lett. **75**, 4476 (1995).

[318] W. R. Busing and H. A. Levy, Acta Cryst. **22**, 457 (1967).

[319] E. Vlieg, *From Beam Time to Structure Factors*, 2002.

[320] P. R. Bevington and D. K. Robinson, *Data Reduction and Error Analysis for the Physical Sciences*, volume 336, McGraw-Hill, 1969.

[321] I. N. Bronstein, K. A. Semendjajew, G. Musiol, and H. Mühlig, *Taschenbuch der Mathematik*, Harri Deutsch Verlag, 2008.

Scientific Contributions

Publications

- ***In situ* Surface X-Ray Diffraction Studies of the Influence of the PEG-Cl-Complex on Homoepitaxial Electrodeposition on Cu(001)**
  F. Golks, Y. Gründer, A. Drünkler, J. Roy, J. Stettner, J. Zegenhagen, O. M. Magnussen
  to be submitted

- ***In situ* Surface X-Ray Diffraction Studies of Homoepitaxial Growth on Cu(001) From Aqueous Acidic Electrolyte**
  F. Golks, J. Stettner, Y. Gründer, K. Krug, J. Zegenhagen, O. M. Magnussen
  to be submitted

- **Structure and Electrocompression of Chloride Adlayers on Cu(111)**
  Y. Gründer, A. Drünkler, F. Golks, G. Wijts, J. Stettner, J. Zegenhagen, O. M. Magnussen
  submitted to Surf. Sci. (2011)

- **High-Speed *in situ* Surface X-ray Diffraction Studies of the Electrochemical Dissolution of Au(001)**
  F. Golks, K. Krug, Y. Gründer, J. Zegenhagen, J. Stettner, O. M. Magnussen
  J. Am. Chem. Soc. 133, 3772–3775 (2011)

- **Real-time surface x-ray scattering study of Au(111) electrochemical dissolution**
  K. Krug, D. Kaminski, F. Golks, J. Stettner, O. M. Magnussen
  J. Phys. Chem. C, 114, 18634–18644 (2010)

- **Study of Bi UPD structures on Au(100) using *in situ* surface x-ray scattering**
  S. H. Zheng, K. Krug, F. Golks, D. Kaminski, S. Morin, O. M. Magnussen
  J. Electroanal. Chem., 649, 189–197 (2010)

- **Reversal of chloride-induced Cu(001) subsurface buckling in electrochemical environment: An *in situ* surface x-ray diffraction and density functional theory study**
  Y. Gründer, D. Kaminski, F. Golks, K. Krug, J. Stettner, O. M. Magnussen, A. Franke, J. Stremme, E. Pehlke
  Phys. Rev. B 81, 174114 (2010)

- **Time-Dependent Diffraction Studies of Au(100) Electrode Surface During Deposition**
  D. Kaminski, K. Krug, F. Golks, J. Stettner, O. M. Magnussen
  J. Phys. Chem. C, 111, 17067–17071 (2007)

Poster Presentations

- ***In situ* surface x-ray diffraction studies of homoepitaxial growth on Cu(001) from aqueous electrolyte**
  F. Golks, Y. Gründer, J. Stettner, K. Krug, D. Kaminski, J. Zegenhagen, O. M. Magnussen
  ESRF Usermeeting
  Grenoble, February 2011

- ***In situ* surface x-ray diffraction studies of the adsorption of the Cl-PEG complex and of Cu electrodeposition on Cu(001)**
  F. Golks, Y. Gründer, J. Stettner, K. Krug, D. Kaminski, J. Zegenhagen, O. M. Magnussen
  Gordon Research Conference on Electrodeposition
  New London, NH, August 2010

- ***In situ* surface x-ray diffraction studies of the adsorption of the Cl-PEG complex and of Cu electrodeposition on Cu(001)**
  F. Golks, Y. Gründer, A. Drünkler, J. Stettner, K. Krug, D. Kaminski, J. Roy, J. Zegenhagen, O. M. Magnussen
  20$^{\text{th}}$ Higher European Research Course for Users of Large Experimental Systems (HERCULES)
  Grenoble/Paris, March 2010

- ***In situ* surface x-ray diffraction studies of the influence of the Cl-PEG complex on Cu electrodeposition on Cu(001) and Cu(111)**
  F. Golks, Y. Gründer, A. Drünkler, J. Stettner, K. Krug, D. Kaminski, G. Wijts, J. Roy, J. Zegenhagen, O. M. Magnussen
  Deutsche Tagung für Forschung mit Synchrotronstrahlung, Neutronen und Ionenstrahlen and Großgeräten
  Berlin, February 2010

- ***In situ* surface x-ray diffraction studies of the adsorption of the Cl-PEG complex and of Cu electrodeposition on Cu(001)**
  F. Golks, Y. Gründer, A. Drünkler, J. Stettner, K. Krug, D. Kaminski, J. Roy, J. Zegenhagen, O. M. Magnussen
  ESRF Usermeeting
  Grenoble, February 2010

- ***In situ* surface x-ray diffraction studies of Cl and PEG adsorption and of Cu electrodeposition on low index Cu electrode surfaces**
  F. Golks, Y. Gründer, A. Drünkler, J. Stettner, K. Krug, D. Kaminski, G. Wijts, J. Roy, J. Zegenhagen, O. M. Magnussen
  216$^{\text{th}}$ Meeting of the Electrochemical Society (ECS)
  Vienna, October 2009

- ***In situ* surface x-ray diffraction studies of electrodeposition on Cu(100) in HCl and H_2SO_4**
  F. Golks, K. Krug, D. Kaminski, Y. Gründer, J. Stettner, O. M. Magnussen
  Conference on electrochemistry: Crossing Boundaries (by GDCh *et al.*)
  Gießen, October 2008

- ***In situ* surface x-ray diffraction studies of electrodeposition on Cu(100) in HCl and H_2SO_4**
  F. Golks, K. Krug, D. Kaminski, J. Stettner, O. M. Magnussen
  10^{th} International Conference on Surface X-Ray and Neutron Scattering (SXNS)
  Paris, July 2008

Oral Presentations

- ***In situ* diffraction studies of homoepitaxial growth of Cu(001) from aqueous electrolyte**
  F. Golks, Y. Gründer, J. Stettner, K. Krug, J. Zegenhagen, O. M. Magnussen
  Deutsche Physikalische Gesellschaft, Frühjahrstagung
  Dresden, March 2011

- ***In situ* diffraction studies of homoepitaxial growth of Cu(001) from aqueous electrolyte**
  F. Golks, Y. Gründer, J. Stettner, K. Krug, J. Zegenhagen, O. M. Magnussen
  Workshop on 'Réactivité des surfaces et synchrotron' at Centre National de la Recherche Scientifique (CNRS)
  Grenoble, January 2011

- ***In situ* surface x-ray diffraction studies of homoepitaxial growth of Cu(001) from aqueous electrolyte**
  F. Golks, Y. Gründer, J. Stettner, K. Krug, J. Zegenhagen, O. M. Magnussen
  ESRF Science and Students Day
  Grenoble, October 2010

- ***In situ* surface x-ray diffraction studies of the adsorption of the Cl/PEG complex and of Cu electrodeposition on Cu(001)**
  ESRF Workshop on '*In situ* x-ray methods for electrochemical interfaces'
  Grenoble, February 2010

Invited Talks

- ***In situ* diffraction studies of homoepitaxial growth of Cu(001) from aqueous electrolyte**
  Workshop on 'Réactivité des surfaces et synchrotron' at Centre National de la Recherche Scientifique (CNRS)
  Grenoble, January 2011

Awards

- **ECS Poster Prize in Electrochemical Science & Technology**
  216$^{\text{th}}$ Meeting of the Electrochemical Society (ECS)
  Vienna, October 2009

Miscellaneous

- **Publication of cover art for the article 'High-speed *in situ* surface x-ray diffraction studies of the electrochemical dissolution of Au(001)'**
  Journal of the American Chemical Society, volume 133, issue 11, 2011

Curriculum Vitae

Frederik Golks

Address	Felix-Mendelssohn-Str. 2 D - 24768 Rendsburg
Date of Birth	August 18th 1983 in Neumünster, son of Helgard and Hans-Werner Golks
Nationality	German

Education

Apr. 2008 - present	Cooperative PhD project in the groups of Prof. Dr. O. M. Magnussen, Institute of Experimental and Applied Physics, University Kiel (Germany), and of Priv.-Doz. Dr. J. Zegenhagen, European Synchrotron Radiation Facility, Grenoble (France): 'In situ Surface X-ray Diffraction Studies of the Copper-Electrolyte Interface: Atomic Structure and Homoepitaxial Growth'
Oct. 2003 - Mar. 2008	Undergraduate Course in physics at University of Kiel (Germany): 04/2007 - 03/2008: Diploma thesis in the group of Prof. Dr. O. M. Magnussen, 'In-Situ Surface X-Ray Diffraction Studies of Metal/Electrolyte Interfaces', one month visiting scientist at the European Synchrotron Radiation Facility, Grenoble (France), in the group of Dr. J. Zegenhagen 06/2006 - 10/2006: Internship at the European Synchrotron Radiation Facility, Grenoble (France), in the group of Dr. J. Zegenhagen 06/2005: Intermediate diploma ('Vordiplom')
Aug. 1994 - Jul. 2003	Herderschule (High School), Rendsburg
Aug. 1990 - Jul. 1994	Altstadtschule (Elementary School), Rendsburg

Kiel, 27th of April 2011

Acknowledgements

After all the years of work you look back and recognize that the success, fortune and good time you had is based on the contribution of many people. I would like to thank all of them for their part, for guidance, support and encouragement. I cordially thank ...

- ... my thesis advisers Prof. Dr. Olaf Magnussen and Priv.-Doz. Dr. Jörg Zegenhagen who gave me the chance to work in a highly interesting and inspiring scientific environment both at the university and at the ESRF. I am grateful for their confidence, patience and particularly their willingness to helpful advice and discussion at any time.

- ... Dr. Jochim Stettner for the numerous discussions, for sharing his experience and for cooperation far in excess of many beamtimes spent together.

- ... Dr. Yvonne Gründer and Dr. Klaus Krug for a lot of sleepless night shifts slogged together, for sharing their knowledge and for teaching me the methodical approach to successful synchrotron experiments. Sincere thanks to Yvonne for her enthusiastic collaboration in our shared project!

- ... the diploma/master students Arne Drünkler, Geert Wijts, and Martin Ruge for their interest in the project accompanied by valuable and enjoyable support in the experiments.

- ... Dr. Jérôme Roy for his help at the beamline, his advice in all ESRF, `SPEC` and Linux related questions and, not to be missed, for his persistent effort in trying to teach me the real nature of matter: round and square atoms ☺.

- ... the ID32 beamline staff members Dr. Parasmani Rajput and Dr. Blanka Detlefs for their support during the experiments as well as Dr. Helena Isern, Lionel André, Matthias Greve, Arnd Seeger, Manuel Perez, and Lucien Petit for an excellent support in technical and computing issues.

- ... all engineers in the mechanical workshop Kiel as well as Wilfried Krüger and Martin Goduscheit for an excellent work on customized equipment, without which most experiments would not have been feasible.

- ... Monika Seeger, Linda Sommer, and Rosemarie Müller-Puffe for their inestimable help concerning administrative, organizational and social affairs.

- ... my office mates, group colleagues and friends in Kiel and Grenoble for interesting and fruitful discussions, and especially for an enjoyable atmosphere all the time! Special thanks to Belinda Baisch, Benjamin Runge, Christoph Schlueter, Christian Haak, Erik Tancini, Rita Giordano, Dr. Tamzin Lafford, Dr. Thomas Cornelius, Thomas Scheler, and Dr. Yaiza Gonzalez Garcia.

- ... my friends in the karate club, especially Florian Bark, for persisting encouragement and collaboration in regard of perfecting our skills.

- . . . my friends and fellow students Mathias Mann, Stephan Hilgenfeldt, and Malte Ogurreck for innumerable valuable hours spent together.

Finally, most gratitude goes to my friends and my family. Especially my parents and Anna supported me personally during all the years with patience, help and love.

Kiel, 27$^{\text{th}}$ of April 2011

Eidesstattliche Erklärung

Hiermit versichere ich, dass ich die vorgelegte Dissertation, abgesehen von der Beratung durch meine Betreuer Prof. Dr. O. Magnussen und Priv.-Doz. Dr. J. Zegenhagen, selbständig verfasst und keine anderen als die angegebenen Quellen und Hilfsmittel verwendet habe. Die Arbeit ist unter Einhaltung der Regeln guter wissenschaftlicher Praxis entstanden. Teile der Arbeit sind bereits veröffentlicht oder als Manuskript zur Veröffentlichung eingereicht worden. Meine den Veröffentlichungen und Manuskripten zugrunde liegenden Beiträge sind im Folgenden genauer aufgeschlüsselt:

JACS 133, 3772-3775 (2011), Kapitel 4: Implementierung des Mythen 1K Detektors in bestehenden experimentellen Aufbau des Messplatzes ID32, incl. Konstruktion des Detektorhalters und Schreiben der notwendigen Software. Hauptteile der Vorbereitung und Planung der Messzeit sowie maßgebliche Beteiligung an der experimentellen Durchführung. Durchführung der Hauptteile der Auswertung aufbauend auf Vorarbeiten von Dr. K. Krug. Anfertigung der Grafiken durch mich, Verfassen des Manuskriptes durch Prof. Dr. O. M. Magnussen. Maßgebliche Beteiligung an Interpretation der Auswertungen und Diskussion der Publikation.

PRB 81, 174114 (2010), Kapitel 5.1: Beteiligung an der Messzeitvorbereitung. Maßgebliche Beteiligung an den Röntgendiffraktions- und *ex situ* elektrochemischen Experimenten sowie deren physikalischer Auswertung. Die Modellierung der Gitterabbruchstäbe wurde von Dr. Y. Gründer und Dr. D. Kaminski durchgeführt. Die DFT-Rechnungen für das Cl/Cu(001) System wurden in der Gruppe von Prof. Dr. E. Pehlke durchgeführt. Verfassung des Manuskriptes durch Dr. Y. Gründer und A. Franke. Beteiligung an der Diskussion des Manuskriptes.

Manuskript eingereicht für Surface Science, Kapitel 5.2: Maßgebliche Beteiligung an Vorbereitung und Planung der Messzeiten sowie an deren experimenteller Durchführung. Die Hauptteile der *ex situ* elektrochemischen Charakterisierung wurden von Dr. Y. Gründer und A. Drünkler durchgeführt, ebenso die Hauptteile der Auswertung. Verfassung des Manuskriptes durch Dr. Y. Gründer. Beteiligung an der Diskussion des Manuskriptes und der Interpretation der Auswertungen.

Manuskripte (einzureichen), Kapitel 6 & 7: Hauptteile der Vorbereitung und Planung der Messzeiten sowie maßgebliche Beteiligung an der experimentellen Durchführung. Durchführung der Auswertung. Verfassung der Manuskripte. Maßgebliche Beteiligung an Interpretation der Auswertungen und Diskussion der Manuskripte.

Ich versichere, dass die vorliegende Dissertation weder ganz noch in Teilen Bestandteil einer anderen Studien- oder Prüfungsleistung war. Des Weiteren bestätige ich, keine früheren Promotionsversuche unternommen zu haben. Mir ist bewusst, dass Zuwiderhandlungen gegen diese Erklärung den Ausschluss von der Prüfung zur Folge haben können.

Kiel, den 27. April 2011